Imperial College London

DEPARTMENT OF PHYSICS
Centre for Cold Matter

single quantum emitters: resonance fluorescence and emission enhancement

Report submitted in partial fulfillment of the requirements of the degree of Doctor of Philosophy

candidate
Samuele Grandi

advisors
Edward A. Hinds
Alex S. Clark

April 2017

Doing what little one can to increase the general stock of knowledge
is as respectable an object of life, as one can
in any likelihood pursue.

— Charles Darwin

"Oramai convien che tu così ti spoltre",
disse 'l maestro; "ché, seggendo in piuma,
in fama non si vien, né sotto coltre;

senza la qual chi sua vita consuma,
cotal vestigio in terra di sé lascia,
qual fummo in aere e in acqua la schiuma".

— Dante, Inferno XXIV

Sammy,
uno può girare tutto il mondo
e comunque non aver capito niente.

— mia mamma

ACKNOWLEDGMENTS

Firstly, I would like to thank my examiners, Prof. Myungshik Kim and Prof. Mete Atature, for the time and effort they put into reading and correcting this thesis.

In these years I was lucky enough to be part of the great research group that is the Centre for Cold Matter here at Imperial. It has been a constant source of inspiration and motivation. My most sincere thanks to its director, and my supervisor, Prof. Ed Hinds, for the constant support, perpetual enthusiasms and for his brilliant insight. A big thank you to the DBT team, and especially to Alex Clark, for his great passion and vision in leading the group. Thanks also to other members, Kyle Major, Claudio Polisseni and Seb Boissier, for all your help and advice, and for making this a truly inspiring environment.

For all their invaluable work behind the scene of science and academia, and for making science and academia a much smoother process, thank you to to Sanja Maricic, Judith Baylis and Marcia Salviato.

My luck was not finished, as I was also part of the FQT initial training network, an exciting research environment that greatly benefited my PhD far beyond what was written in the grant proposal. Prof. Kim deserved an additional mention as the coordinator of the program, and I would like to thank him and the board. My warmest thanks also to Doug Plato, for the continuous effort he put in the FQT project and for his great support as mentor. Of course, my warmest thanks to my fellow FQT members of the first cohort, Allan, Paloma, Frederik and Moritz, for being amazing friends and colleagues, sharing great moments too long to be listed, and for withstanding my constant rants about the weather, the food, and the coffee.

I also had the great opportunity of spending some months at the NTT laboratories in Japan, and I would like to thank Dr. Masaya Notomi for making this possible. I would like to thank Prof. William Munro and Dr. Devin Smith for their support, insight and supervision, and all the Photonic Nanostructure Research Group for their warm welcome.

Many people contributed in making these years a memorable experience, and also took their share of whining and, sometimes excessive, physics talking. To my flatmates through the years, Siba, Emilie, Chantal and Caroline, you are to thank for making me feel at home in London.

To David and Felix, thank you for being great friends, and for all the memorable evenings spent at Racton 13. To Javier, thank you for all your precious help and support, in real life as much as in physics. I must thank Tessa, Maia, Jess and Anne, for all the great time at Langham, at quiz, and especially for letting me basically squat at your house, while withstanding my thesis writing. Achi and Stefania, thank you for bringing here a bit of Italy and Florence, and for sharing with me the long winters. Queralt and Laura, you definitely helped me in feeling more at home by missing the South with me, but you also made me appreciate the good you can find here. Warmest thanks to Gio and Villi, for having shared with me a good deal of great time, and having the power of cheering me up, no matter what. I will never forget my time in Japan either; Maxi, Watti, Kos, Risa, Mari: aside from being as welcoming as you can possibly be, you basically saved me. To all of you, and to all those that I have forgotten, thanks.

Finally, my parents, my sister, my brother and my family deserves my warmest thanks. You are a never ending source of inspiration, support and comfort. And here perhaps resides my bigger fortune.

DECLARATION

I declare that all the material in this thesis is my own unless otherwise stated and referenced.

The copyright of this thesis rests with the author and is made available under a Creative Commons Attribution Non-Commercial no Derivatives licence. Researchers are free to copy, distribute or transmit the thesis on the condition that they attribute it, that they do not use it for commercial purposes and that the do not alter, transform or build upon it. For any reuse or redistribution, researchers must make clear to other the licence terms of this work.

ABSTRACT

Single photons are highly desirable for encoding, sending and processing quantum information. Suitable engineering of single quantum emitters and their environment can lead to a reliable single photon source and to mediated photon-photon interactions, essential assets for quantum communication and computation purposes.

Dye molecules, our chosen single quantum emitter, have attracted much attention in recent years due to their high photostability and narrow emission lines. In this thesis I present a detailed analysis of the optical properties of single dibenzoterrylene molecules in an anthracene matrix. Single photon emission is demonstrated at room and cryogenic temperatures. In the latter case, an analysis of the second-order correlation function of the emission of a single molecule is studied at various temperatures. The data agree with a full solution of the optical Bloch equations over a wide range of temperature, and provide some insight into the dephasing process of the molecules.

I then present a technique for integrating single dye molecules with nano-photonic devices. These are hybrid plasmonic waveguides, designed to guide light and to enhance the interaction with a single emitter by a tight confinement of the waveguide mode. Single molecules are deposited over the waveguides and a first evidence of coupling is presented. I conclude with proposed improvements to the optical setup and to the deposition methods.

Finally, I present another type of integrated device, where the light matter interaction is enhanced by inserting single quantum emitters into coupled optical resonators. The theoretical description for the case of resonant two-photon absorption from single atoms in coupled photonic crystal cavities is developed. I conclude by proposing a possible realisation of this system, and describing the first steps towards the fabrication of such a device.

CONTENTS

LIST OF SYMBOLS xiii

LIST OF FIGURES xvii

1 INTRODUCTION 1

1.1 Photons 1

1.2 Sources 3

1.3 Emission enhancement 8

1.4 Dibenzoterrylene in Anthracene 12

1.4.1 Optical Properties 12

1.4.2 DBT in Ac as a single photon source 15

1.5 Thesis guide 17

I RESONANCE FLUORESCENCE OF SINGLE MOLECULES 19

2 THEORY OF RESONANCE FLUORESCENCE 21

2.1 Modelling the molecule 21

2.1.1 Steady-state solution 22

2.1.2 Analytical solution 24

2.1.3 $g^{(2)}(\tau)$ and antibunching 28

2.2 Alternative schemes 32

2.2.1 Triplet state analysis 32

2.2.2 Blue-detuned pumping 34

3 SPECTROSCOPY AND PHOTOPHYSICS OF SINGLE MOLECULES 37

3.1 The confocal microscope 37

3.2 Sample preparation and characterisation 46

3.2.1 Growth of DBT-doped Ac crystals 46

3.2.2 Optical measurements 48

3.3 Cryogenic regime 55

3.3.1 Spectroscopy 55

3.3.2 Saturation and power broadening 58

3.3.3 Emission Spectrum 59

3.3.4 Triplet state 60

3.4 Coherent Control 62

3.4.1 Temperature-induced dephasing 62

3.4.2 $g^{(2)}$ and dephasing 64

3.4.3 Literature comparison 66

3.5 Summary and Outlook 72

II COUPLING AND ENHANCEMENT 75

4 HYBRID PLASMONIC WAVEGUIDES 77
4.1 Plasmonics and photonics 77
4.2 Hybrid Plasmonic Waveguides 79
4.2.1 Design 79
4.2.2 Fabrication 84
4.3 Sample preparation 88
4.3.1 Optical setup 88
4.3.2 Crystal growth 90
4.3.3 Characterisation 92
4.4 Single molecules coupled to HPW 94
4.4.1 Contamination 94
4.4.2 Coupling procedure 98
4.4.3 First success 101
4.5 Summary and Outlook 103
4.5.1 Towards cryogenic temperatures 103

5 RESONANT PROCESSES IN PHOTONIC CRYSTAL DEVICES 107
5.1 Motivation 107
5.1.1 CROWs 107
5.1.2 Erbium oxide 112
5.2 Theoretical Modeling 117
5.3 Experimental Results 124
5.4 Summary and Outlook 130

6 SUMMARY AND CONCLUSIONS 133

III APPENDIX AND BACKMATTER 135

A APPENDIX TO CHAPTER 2 137
A.1 Solving the optical Bloch equations 137
A.2 The scattered field 142
A.2.1 Open systems 143
A.2.2 Master equation for resonance fluorescence 146
A.2.3 $G^{(1)}(\tau)$ and fluorescence spectrum 152
A.2.4 $G^{(2)}(\tau)$ and antibunching 157

B APPENDIX TO CHAPTER 3 159

C APPENDIX TO CHAPTER 4 161
C.1 Local field corrections 162
C.2 Collection efficiency: dipole emission 165

LIST OF PUBLICATIONS 169

REFERENCES 171

INDEX 194

LIST OF SYMBOLS

In this thesis I have tried to maintain a strict consistency of notation. In particular, **bold** letters are used for vectors, in capital letters if it is a matrix. Small capital letters are used for parameters in experimental fits. To lighten the notation, I have avoided the use of "hats" for quantum mechanical operators. However, I have reserved the use of the letters a and b for bosonic operators, and other operators are specified in the list underneath. Note that I used the symbol $\imath$ for the imaginary unit.

With regards to figures, crossed axes are used when plotting analytical functions or prediction, while full frames are used for experimental data. In this case, dots are used for "bare" data, like counts from an APD, a measured power or the coincidences in a correlation measurement. Derived quantities, like linewidths, saturation intensities or sum of raster scans are reported with empty markers, like empty circles or triangles.

$\mathcal{A}$	mode area.
a, $a^\dagger$ and b, $b^\dagger$	bosonic annihilation and creation operators.
A, B, C,	fit parameters.
a, b, c,	crystallographic axes.
$D(\omega)$	density of states.
$\mathbf{E}$	electric field.
$\mathcal{F}_p$	Purcell factor.
$g^{(1)}(\tau)$, $g^{(2)}(\tau)$	first and second order correlation functions.
$g_{i,j}$	coupling constant between cavities.
$\mathcal{H}$	Hamiltonian operator.
$\mathbb{H}$	Hilbert space.
K	pumping rate in rate equations.
$\mathbf{k}$	wave vector.
I	electric field intensity.
I_{sat}	saturation intensity.
$\mathbf{I}$	identity matrix.
$\imath$	imaginary unit.

$\mathcal{L}_i$	Lindblad operator.
$\mathcal{L}[f](s)$	Laplace transform of the function $f(t)$.
n	refractive index, or photon number.
n_g	group index.
NA	objective numerical aperture.
P	power.
R	rate of emission of photons.
$\mathcal{S}$	emission spectrum.
S	saturation parameter.
$S_{\mu,\nu}$	ν-th vibrational level of the μ-th electronic manifold for DBT in Ac.
T	temperature.
u, v	in phase and quadrature components of the dipole.
V	volume.
v_g	group velocity.
W	density operator for system and reservoir.

$\boldsymbol{\alpha}$, $\boldsymbol{\beta}$	angles of the anthracene crystals.
β	waveguide coupling factor.
Γ_i	decay rates, usually molecular transition rates.
γ_i	master equation loss parameters.
Δ	detuning from resonance frequency.
$\Delta\nu$	transition linewidth in frequency units.
$\Delta\omega$	transition linewidth in angular frequency units.
$\delta_{i,j}$, $\delta(x)$	Kronecker delta and delta function.
ϵ	polarisation versor.
η	collection efficiency.
λ	wavelength.
Λ	reservoir operators.
$\boldsymbol{\mu}$	dipole moment.
ν	frequency.
ρ	density matrix.
σ_i	dipole operators.
σ_{TPA}	two-photon absorption cross-section

Ω Rabi frequency.

ω angular frequency.

LIST OF FIGURES

Figure 1.1 visual representation of a photon. 2
Figure 1.2 schematic of the optimal single photon source. 4
Figure 1.3 schematic of quantum dots and NV centres. 6
Figure 1.4 most common dye molecules and matrices. 7
Figure 1.5 working principle of a plasmonic device. 10
Figure 1.6 working principle of a photonic crystal. 11
Figure 1.7 level scheme of DBT in Ac. 13
Figure 1.8 absorption and emission spectra for a molecule-host system. 14
Figure 2.1 steady-state solution of the optical Bloch equations. 24
Figure 2.2 plots of $\rho_{22}(t) - \rho_{11}(t)$ for resonance fluorescence, at different values of saturation parameter S and dephasing Γ_2. 27
Figure 2.3 detuning dependent plot of $\rho_{22}(t)$. 29
Figure 2.4 $g^{(2)}(\tau)$ for resonance fluorescence, at different values of saturation parameter S and dephasing Γ_2. 31
Figure 2.5 $g^{(2)}(\tau)$ for a three level system of fig. 1.7. 33
Figure 2.6 $\rho_{22}(t)$ for increasing S in the incoherent pumping regime. 35
Figure 2.7 $g^{(2)}_{\text{blue}}(\tau)$ for increasing saturation S. 36
Figure 3.1 scheme of a confocal microscope. 38
Figure 3.2 scheme of the Montana cryostation, and of the sample holder design. 40
Figure 3.3 temperature tests on the cryostation. 42
Figure 3.4 schematic of the laser locking system. 44
Figure 3.5 cosublimation Ac crystals. 47
Figure 3.6 optical properties of single DBT molecules at room temperature. 49
Figure 3.7 TCSPC measurement of a molecule. 53
Figure 3.8 optical properties of a DBT molecule below 4 K. 57
Figure 3.9 fluorescence spectrum of a single DBT molecule. 59
Figure 3.10 long-times histogram $C(\tau)$ for a single DBT. 61
Figure 3.11 single molecule spectroscopy with controlled, temperature-induced dephasing. 63

Figure 3.12 antibunching histogram, for increasing temperature and saturation. 65
Figure 3.13 experimental resonance fluorescence of a single DBT molecule, at various saturations and temperatures. 66
Figure 3.14 plot of $\mathcal{D}_s$. 68
Figure 3.15 comparison of literature expression of $g^{(2)}(\tau)$. 69
Figure 3.16 resonance fluorescence of DBT at 30 K. 70
Figure 3.17 resonance fluorescence of a DBT on the $S_{0,0} \rightarrow S_{1,3}$ line. 71
Figure 3.18 resonance excitation of a single molecule close to the Rb transition. 73
Figure 4.1 schematic of a surface plasmon polariton. 78
Figure 4.2 design and main properties of the HPW. 80
Figure 4.3 plots of mode area and Purcell factor for varying gap widths. 83
Figure 4.4 fabrication of the HPW. 85
Figure 4.5 SEM images of the HPW. 86
Figure 4.6 schematic of the confocal microscope used with the HPW. 89
Figure 4.7 supersaturation Ac crystals. 91
Figure 4.8 values of grating efficiency as a function of wavelength. 93
Figure 4.9 analysis of contaminants in the HPW samples. 95
Figure 4.10 histogram $C(\tau)$ for the contaminant emitter of fig. 4.9. 96
Figure 4.11 plasma cleaning of the HPW. 98
Figure 4.12 wavelength response of several optical elements, and the effect on the collected single molecule spectrum. 100
Figure 4.13 preliminary coupling of a single DBT molecule to a waveguide. 102
Figure 4.14 low temperature study of supersaturation crystals. 104
Figure 4.15 new regular supersaturation Ac crystals. 105
Figure 5.1 schematic and SEM images of CROWs. 108
Figure 5.2 transmission spectrum for an $n = 5$ CROW. 110
Figure 5.3 optical properties of Er_2O_3. 113
Figure 5.4 suggested application of Er_2O_3 for quantum information. 115
Figure 5.5 time-domain populations of an $n = 5$ CROW. 120
Figure 5.6 steady-state populations of an $n = 3$ CROW. 122
Figure 5.7 optical and SEM images of fabricated CROWs. 124

Figure 5.8 transmission spectrum of a ridge waveguide with erbium coating. 125
Figure 5.9 effects of laser dicing on erbium-coated devices. 127
Figure 5.10 transmission spectrum of devices after FIB milling. 128
Figure 5.11 analysis of the crystallinity of the Er_2O_3 oxide layer. 129
Figure 5.12 transmission as a function of TPA 131
Figure A.1 diagram of the open system composed of a two-level atom and three reservoirs R. 144
Figure A.2 $S_{inc}(\omega)$ for varying saturation S and dephasing Γ_2. 156
Figure B.1 Detailed scheme of the setup for SMS. 160
Figure C.1 detailed scheme of the setup for the HPW. 162
Figure C.2 study of different local field correction $n^{\alpha}l^{\beta}(n)$. 165
Figure C.3 dipole emission patterns of DBT in Ac for various substrates. 166

1 INTRODUCTION

The title of this thesis spawns a lot of questions. Why do we need quantum emitters, and why do they have to be single? What is special about resonant excitation, and how can we enhance it? Last, and perhaps most fundamentally, what is a photon? The aim of this introductory chapter is to answer some of these questions and explain the *raison d'être* of the quest for a single photon source.

1.1 PHOTONS

I start with the last, and perhaps with the most difficult question: what is a photon? One way to start answering this question is considering a box of finite size, with perfectly reflecting walls [1, p. 1]. The electromagnetic field inside this box can be described by a harmonic oscillator, with an infinite and discrete set of modes dictated by the boundary conditions at the walls. If we consider one mode as a quantum harmonic oscillator with frequency ω, then the eigenenergies of this mode are integer multiples of $\hbar\omega$. We can thus identify one photon as the elementary excitation of a single standing-wave mode inside this box, described by a harmonic oscillator in its first excited state, as pictured in figure 1.1. This definition can then be extended to traveling modes of radiation, for example describing the mode of a laser beam, by allowing the box to have a periodic boundary condition and letting its size go to infinity. Now the modes have a different spatial distribution, but the eigenenergies are still quantised in units of $\hbar\omega$. If we consider the problem from a more experimental point of view instead, we find that photons can be localised in time and space: at the moment of detection [2, Ch. 3]. After it has been generated, for example by the de-excitation of an atom [3, Ch. II.A], the photon travels until a detecting device destroys it in the measurement process. This event could then be used to localise the photon, as a particle-like object[1]. The connection between extended wavefunction that propagates and loc-

[1] In the inverse process, an atom could be use to inspect the box mentioned earlier, making a 3D map of the probability of excitation of the atom as a function of its position. The result is the closest visual representation of the "shape" of a photon.

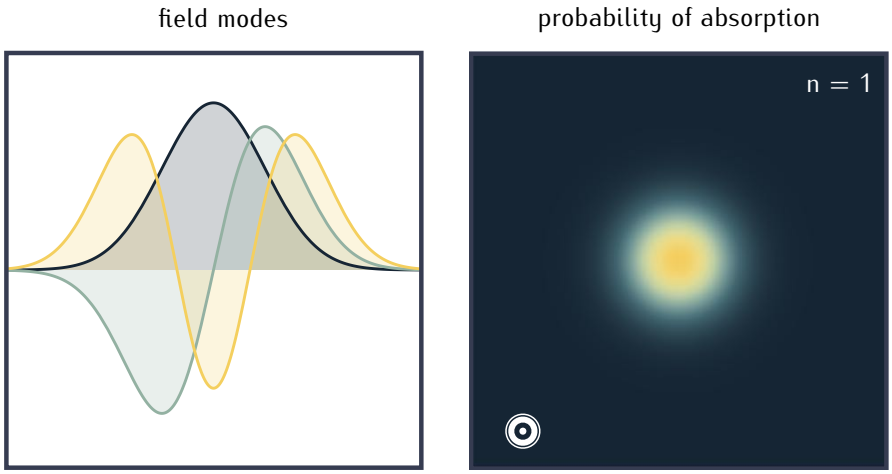


Figure 1.1 Visual representation of the photon, as the first excited state of an oscillator describing the electromagnetic field in a box (represented on the left, up to $n = 3$). The field can be inspected by a resonant atom, plotting the probability of excitation (represented on the right). This can be interpreted as a visualisation of the photon wavepacket.

alised particle that is detected is reconciled in the framework of quantum mechanics, and has been widely confirmed experimentally.

The concept of photons was introduced for the first time by Planck [4], but the name "photon" was actually coined by Lewis [5]. They are characterised by their wavelength λ, and carry a momentum $\hbar k$, with $k = 2\pi/\lambda$ as the associated wave-number. Photons can be guided in optical fibres for long distances, due to their low interaction probability. This resilience against decoherence together with the possibility of manipulating photons through simple (that is, linear) optical means is at the origin of the surge in the last decades in the study, generation and detection of photons. These properties make photons particularly useful in the fast growing field of quantum information and computation.

The core concept of this field is the encoding of information in quantum mechanical objects, for computation or communication purposes [6]. Some physical property with two eigenstates is used to represent the mathematical concept of a "qubit", the quantum equivalent of the classical bit of information. While a bit could assume only the two values of "0" or "1", the qubit has access to the continuum of superposition states in between. Considerable advantages over classical information theory can be gained, for example in the security of communications or in the efficiency of computation.

Quantum information could be encoded in the state of single photons, using for example the horizontal or vertical polarisation as the "0" and "1"

elements of a basis. Logical operations can be performed on these qubits by making the photons interact with each other, for example through coupling to atoms [7, 8] or to non-linear media [9]. While photons alone could be sufficient to perform computational tasks [10] (using quantum interference, as elaborated later in this chapter), such a scheme would unfortunately suffer from the low interaction probability of photons, and by possible losses during the process. Other systems could be employed as qubits, such as chains of ions in traps [11, 12], quantised charges or magnetic flux in superconducting junctions [13, 14], nuclear spins [15–19] or even spin of single quantum objects [20–22]. While advances are made in these directions, and new candidates are added to the list of possible physical realisations of the qubit [23], one requirement remains constant: the need to link different qubits, or even different quantum computers [24]. This network might be distributed over long distances, that could nevertheless be easily covered by light-speed fast photons, carrying and exchanging information as "flying qubits".

1.2 SOURCES

We now have a basic understanding of what photons are, and what makes them suitable candidates for quantum information processing. I will summarise here the main methods that have been devised for generating single photons: spontaneous parametric down conversion and attenuated laser pulses; single atoms and ions in traps; quantum dots, colour centres in crystals and dye molecules. I will review each one, comparing them with the requirements that an ideal single-photon source (SPS) should meet [25, 26].

The name itself suggests the first characteristic a source needs to have: the ability to emit *single* photons. This property can be verified with a simple experiment. A stream of single photons impinging on a 50/50 beam splitter will be divided equally between the two output ports. Two single photon detectors, placed on each of these two paths and equidistant from the beam splitter, will never detect simultaneous photons, precisely due to the presence of only one photon at a time at the beam splitter. A histogram of coincidences as a function of the delay τ between the two paths will then present a dip towards the region of $\tau = 0$, whose depth can be used to infer how well separated the photons are [27]. A second important characteristic of an ideal SPS is the possibility of controlling the emission of photons in time, turning it "on" and "off" at will. Such a

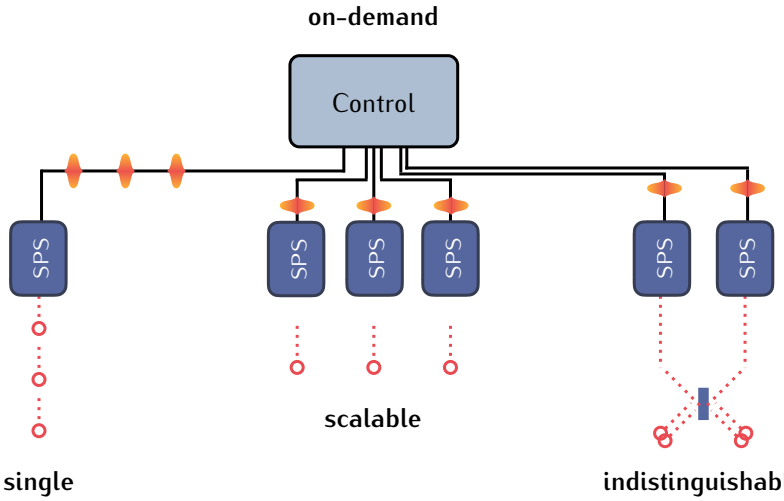


Figure 1.2 Schematic of the optimal single photon source; on-demand and scalable, generating indistinguishable photons with high purity.

deterministic source will then emit a single photon whenever it receives a trigger.

With these conditions in mind, two types of source prove unsatisfactory as SPS: faint laser pulses and spontaneous parametric down conversion. The first of these techniques relies on a strong attenuation of laser pulses, trying to reach the goal of only 1 photon per laser pulse. By increasing the attenuation it is possible to exclude almost completely the possibility of having more than one photon in a pulse, but only by attenuating so far that the average number of photons per pulse is close to zero. Therefore, despite the occasional emission of a photon in the desired time slot the normal output is nothing at all [28]. The spontaneous parametric down conversion source has a somewhat similar problem. Such sources are based on the interaction of a pump laser with a nonlinear crystal, such as barium borate (BBO). Occasionally, one pump photon is split into a signal and an idler photon, whose frequency has to satisfy energy conservation and phase matching conditions [29, 30]. The photon pair generated in this way has strong correlations in polarisation and wavelength, and since the photons are emitted at the same time, the detection of one can be used to herald the presence of the other. These properties make sources based on parametric down conversion good candidates for quantum communication, quantum cryptography and quantum computation [31–34]. However, the spontaneous emission of photon pairs is a random process, so to avoid the possibility of accidentally having two pairs one must once again settle for the occasional pair, with no pairs most of the time.

In addition to wanting fast, reliable production of single photons, one ideally wants many source acting in parallel so that many identical photons can be made available at the same time. This is called *scalability*. This requirement is key to the final goal of having several single photons sources on the same device, easily accessible and controllable. However, scalability can be very challenging to accomplish, and for certain systems is simply not possible. This is the case for atoms and ions in gas phase in traps, for example. Transitions in atoms and ions can be very narrow, have been thoroughly studied and are highly reproducible. Single photons can be generated from atoms and ions with high purity. Atoms could also be employed for the generation of pairs of photons during atomic transition cascades. The polarisations of the two photons, each one generated in back to back transitions, present strong correlations, in a similar fashion as pairs from parametric down conversion. Photons from atomic cascades have been used for many tests of fundamental importance [35–38]. However, all these properties are valid only for atoms and ions in gas form, isolated and held in place in a trap [39–44]. It is precisely the setup required for trapping and manipulation of atoms and ions that makes them a problematic candidate for single photon emission. The traps have to be kept at high vacuum levels, and superconductive magnets are sometimes required for trapping ions. Moreover, high precision lasers tuned to the atomic transition have to be stabilised to address the narrow atomic transitions. The simultaneous control of several individual atoms for single photon generation is at the forefront of research in this field.

A last key property of photons required in many quantum information processes is their *indistinguishability*. If we consider a SPS as emitting always in the same spatial and polarisation mode, the photons are said to be indistinguishable, and they can be described by the same coherent wavepacket. Under these conditions, the spectrum of the SPS, obtained accumulating multiple spectra of single photons, is equal to the Fourier transform of the time profile of the single photons: the source is Fourier-transform limited, or lifetime-limited. Perfectly indistinguishable photons incident on the two ports of a beam splitter are at the origin of a uniquely quantum effect. If upon detection it is not possible to tell which photon took which path from their time of arrival, mode or any other measure, then the probability amplitudes of the two photons will interfere [32, 45–50]. The photons "bunch together", both being detected at the same port. No coincidence count will be recorded at the detectors, and a histogram of coincidences as a function of time delay between the two

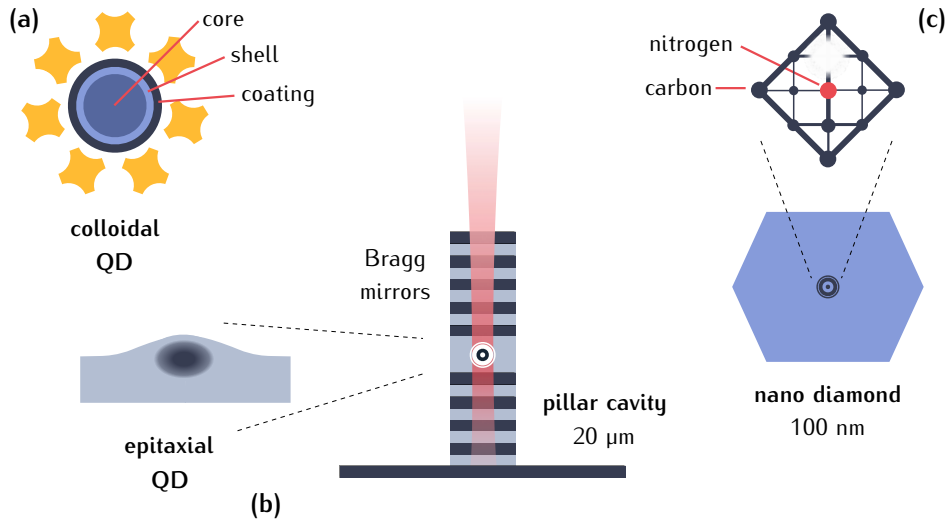


Figure 1.3 Schematic of QD and NV centres. a) colloidal quantum dot. b) epitaxial quantum dot, with a common pillar-type cavity. c) schematic of the nitrogen vacancy centre in a nano diamond.

paths will present a dip. This dip is a measure of the distinguishability of the wavepackets of the two photons, and is affected by any dephasing of the source [45, 51, 52]. Photons from atoms and ions possess a high degree of indistinguishability, but these sources were discarded due to their scalability. Indistinguishability can then be used as another measure for the next three kinds of SPS: quantum dots, colour-centres and organic molecules.

Quantum dots come in two main forms: colloidal and self assembled. The first is composed of nanocrystals of II-VI semiconductors, fabricated through chemical synthesis [53, 54]. Nanocrystals emit through the recombination of an electron-hole pair generated by photon absorption, and they can be used to generate single photons on demand both at room and at cryogenic temperatures. However, the spectrum of colloidal quantum dots is severely broadened, and does not reach the Fourier-limit even at low temperature. They are still widely used to test photonic structures, or for biological purposes due to the possibility of initialising their external coating, but these limitations make them unsuitable as SPS.

Self-assembled quantum dots are more promising candidates. They are composed of a small island of III-V semiconductors, embedded in a matrix of another semiconductor with a higher band gap, grown on a single-crystalline substrate. They have a narrower emission than colloidal quantum dots [55, 56], and they have successfully been included in photonic structures such as photonic crystals, micropillars and microcavities [47, 57, 58]. Cryogenic temperatures are needed to reach Fourier-

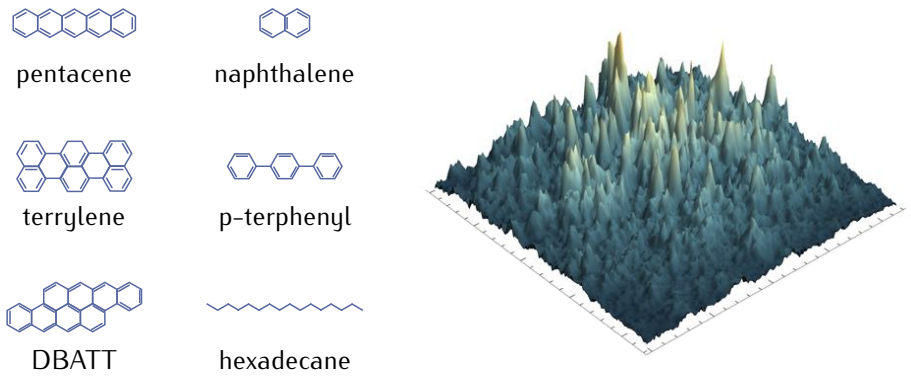


Figure 1.4 Some common dyes and matrices. The right panel reports an image of the fluorescence of several single molecules, at room temperature.

limited emission, and that might affect the scalability of these devices. Indistinguishable photons from different quantum dots require an exquisite control over the solid state surroundings of the emitters, either by placing them in a resonator, or controlling the charge state of the quantum dot [58–61]. Novel designs and refined fabrication techniques are constantly pushing ahead the quality of quantum dots devices [62]. Moreover, the properties of single quantum dots can be engineered, and recently this has led to devices with microwave [63] or telecom-band emission [64] or with an emission profile that could be interfaced in hybrid structures [65].

Colour-centres in diamonds are another promising candidate for a SPS. Impurities and defects in the diamond lattice can create localised structures with atom-like levels. The most common colour centres are the Nitrogen-Vacancy (NV) centre [66–68], the Nickel-Nitrogen (NE8) centre [69, 70], and the Silicon-Vacancy (SiV) centre [71–73]. The hardness of the lattice gives colour centres a high stability; they show an electronic transition, that in some cases is so narrow that it can be distinguished at room temperature and is Fourier-limited at cryogenic temperatures. The efficiency of emission on this line is unfortunately limited, with a maximum of 4% for NV-centres [66], while it is as high as 70% for SiV- and NE8-centres [50, 69]. However, this vacancy does not reach the Fourier-limit, and present a substructure in the emission spectrum [50]. All these vacancies present spin structures with long lived states, that could be extremely useful for quantum information processing [21, 74]. The advent of nanodiamonds with a few centres in each one, besides increasing the collection efficiency, allowed an easier inclusion of diamond vacancies into photonic structures [75, 76]. Several kinds of colour centres are being explored in diamond [77], as well as in other materials [78–81].

Single organic molecules close this list of candidate SPS. Several dye molecules are suitable for single photon emission, such as terrylene, pentacene, dibenzanthanthrene (DBATT) and dibenzoterrylene (DBT), the latter being the main subject of this thesis. These are usually embedded in a hydrocarbon crystalline matrix, such as p-terphenyl, naphtalene or anthracene. The combination of molecule and matrix can provide a strong, narrow optical transition connecting the ground and first electronic excited states [82, 83]. An intermediate triplet state is also present, with a spin-forbidden transition to the ground state, whose rate depends on the particular combination of dopant and host [84]. The allowed transition is purely radiative, so photons are efficiently generated on demand. The decay can go to vibrationally excited levels of the ground state, producing red sidebands in addition to the purely electronic transition known as the zero-phonon line or ZPL. The ZPL branch is typically $30-50\,\%$ of the total decay rate [85]. Microcavities have been used to improve this ratio [86, 87]. Single photon emission has been demonstrated at room and cryogenic temperatures [88–91], the latter being needed for Fourier-limited photons. A strong nonlinear susceptibility of a single molecule has already been proven [92, 93] making this a promising way to mediate interactions between individual photons. The crystalline matrix surrounding the molecule gives it good photostability, but can also limit the interfacing of molecules with external structures, such as photonic crystal cavities or plasmonic structures, due to their high refractive index [94]. On the other hand, different host matrices can be used to tailor the emission properties of dye molecules, as well as exploiting different plastic properties of their surrounding matrix [95–97], making them a versatile tool for quantum photonics.

1.3 EMISSION ENHANCEMENT

The quantum picture of spontaneous emission can be described quite straightforwardly. An atom or molecule destroys a photon in the electromagnetic field of a light beam, simultaneously transferring an electron from the ground state to an excited state. After a while a vacuum fluctuation of the electromagnetic field causes the electron to jump back to the ground state, emitting a photon whose mode is determined by that of the fluctuation. This view involves a quantum treatment of the atom (to have quantised energy levels) and of the field (to have photons and a vacuum fluctuations). While the Einstein coefficients were able to treat

the main features of both stimulated and spontaneous emission through thermodynamical considerations alone, Dirac was the first to derive a fully quantum treatment of spontaneous emission, making use of second quantisation [98]. Milonni [99] gives an interesting comparison of classical and quantum views of spontaneous emission.

The main result of Dirac's work, dubbed by Fermi[2] "golden rule n°2", is the calculation of the probability of transition γ between any two states of a quantum system:

$$\Gamma = \frac{2\pi}{\hbar^2} |\mathbf{M}_{if}|^2 \, D(\omega) \tag{1–1}$$

where $\mathbf{M}_{if} = \langle f| \mathcal{H} |i\rangle$ is the matrix element of the perturbation $\mathcal{H}$ connecting initial state $|i\rangle$ to final state $|f\rangle$. $D(\omega)$ is the density of available final states per unit angular frequency. This is valid when the spectrum of the perturbation is flat over the frequency range corresponding to the width of the resonance line.

For the case of a single atom or molecule in vacuum, with a resonance frequency ω_0, the perturbation is the interaction of the atomic or molecular dipole $\boldsymbol{\mu}$ with the electric field $\mathbf{E}$. This takes the form of $\mathcal{H} = -\boldsymbol{\mu} \cdot \mathbf{E}$. We can then write the matrix element as $\mathbf{M}_{if} = -\mu_{if} E$, where $\mu_{if} = \langle f| \mu |i\rangle$, with μ being the component of $\boldsymbol{\mu}$ along the direction of $\mathbf{E}$, and E is the absolute value of $\mathbf{E}$.

For the electromagnetic vacuum in a large space of volume V, $D(\omega) = V\omega^2/\pi^2 c^3$ modes of the field per unit volume. This result was first used by Weisskopf and Wigner [100] to calculate the spontaneous emission rate of an atom in vacuum:

$$\Gamma = \frac{\mu_{if}^2 \omega^3}{3\pi\varepsilon_0 \hbar c^3}. \tag{1–2}$$

We note that the unspecified volume V has disappeared from this expression because $E^2 \propto 1/V$. However, moving the atom from vacuum to a homogenous medium adds a factor of n to the transition probability Γ, where n is the medium refractive index[3]. This points at a close interaction between an atom and its environment.

By tailoring of the density of states one can engineer strong modifications of spontaneous emission rate, polarisation and directionality [101–103]. Often, the modification of the emission rate is quantified by the ratio of the new spontaneous emission rate to the vacuum value of eq. (1–2). This ratio $\mathcal{F}_p$ is called Purcell factor, as E. Purcell was the first one to sug-

[2] And hence called "Fermi's golden rule".

[3] This is a "zero-th order" correction to Γ, as the interaction of a two level system with the environment is more complicated. This topic is treated in detail in Appendix C.1.

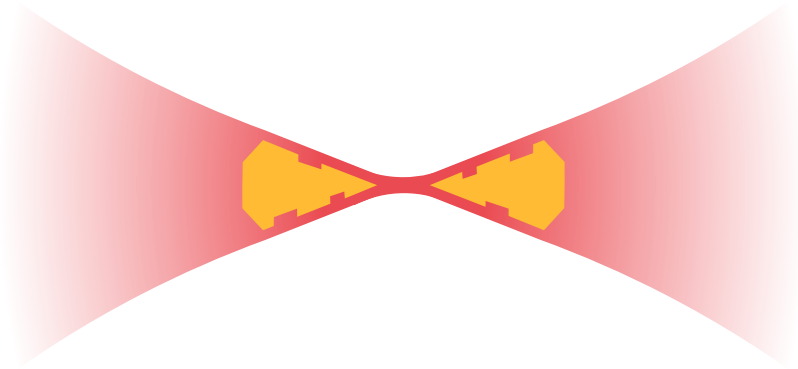


Figure 1.5 Working principle of a plasmonic device. Metallic structures can redirect and confine light to an area comparable with a single emitter.

gest that the spontaneous emission could be affected by its environment, at the time with radiofrequency transitions [101].

Let us consider the case of a single emitter, positioned near a waveguide, that is, a 1-D continuum of states. There is great interest in this particular case, as an an-chip source of single photon is instrumental in the widespread use of quantum information and communication protocols. In this case the Purcell factor has the form

$$\mathcal{F}_p \propto \frac{1}{v_g}\frac{\lambda^2}{\mathcal{A}} \tag{1–3}$$

where λ is the emission wavelength and $\mathcal{A}$ and v_g are the area and group velocity of the optical mode. Later in chapter 3 a full derivation of this expression is presented. Let us consider how one could maximise $\mathcal{F}_p$. The wavelength λ is more or less fixed by the choice of the emitter. That leaves two options: reducing the transverse mode area $\mathcal{A}$ or the group velocity v_g. Both options have been widely investigated, and have led to the rapid development of the fields of plasmonics and photonic crystals [104].

Plasmonics involves placing single emitters close to specially designed metallic structures. The emitter's dipole couples to the electrons on the metal surfaces where the density of modes can be very high and the mode size can be very small. The coherent coupling is between the light and surface charge waves, called plasmons. Figure 1.5 shows a schematic of the operation of a plasmonic device, in which the transverse size of the propagating mode is strongly compressed as it passes the metal and the propagation is also slowed down by the coupling.

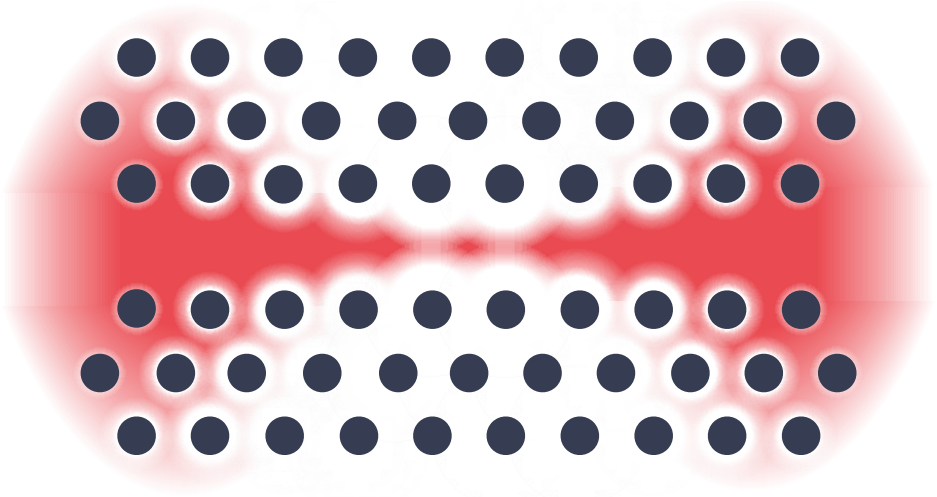


Figure 1.6 Working principle of a photonic crystal. Bragg scattering from a periodic modulation of light inhibits light from traveling through the lattice, while allowed modes are formed within the gap, with a heavily reduced group velocity.

In photonics, a periodic modulation of the refractive index in the surroundings of the emitter can achieve a similar effect. When this modulation is on the order of the wavelength of light, for example by etching holes in a uniform slab, a photonic band-gap, similar to the conduction-band gap in semiconductors, is formed within the structure. Propagation in the structure is inhibited for a range of frequencies, thereby reducing $D(\omega)$. If a defect is inserted into the periodic structure, and if that defect's modes are within the band gap, then emission into these modes is enhanced due to a reshuffling of $D(\omega)$ from the forbidden region to newly formed modes. Figure 1.6 shows the principle of operation of a photonic crystal. The region perforated by small holes has a low average refractive index and therefore the incident light is funneled into the high-index region in the centre where the cross sectional area $\mathcal{A}$ of the mode can be small. As this guide becomes small enough to approach cutoff, both the phase velocity and the group velocity decrease, approaching zero in the limit of cutoff.

Each technique can be tailored to address specific experimental requirements. Compared to plasmonics, only moderate enhancements have been achieved with photonic crystals, but the fluorescence from a single emitter can be efficiently channeled into photonic strictures [105], leading to demonstrated coupling to a single mode of a waveguide up to 99% [106]. On the other hand, the tight confinement of plasmonic structures has lead to considerable enhancements in single photon emission, with Purcell enhancements of several thousand [107]. However, the emission yield of an

emitter can be severely compromised by coupling to dissipative plasmon modes.

1.4 DIBENZOTERRYLENE IN ANTHRACENE

This section details our system of choice in the quest for an efficient single photon source.

Dibenzoterrylene (DBT) and anthracene (Ac) are both polycyclic aromatic hydrocarbons, organic compounds made of benzene rings bonded together. The molecule of DBT ($C_{38}H_{20}$) is composed of 10 benzene rings, while Ac ($C_{14}H_{10}$) has only three. Several other matrices are suitable hosts for DBT, including other aromatic compounds such as naphthalene [108–110], 2,3-dimethylnaphtalene [111] and para-dichlorobenzene [112], or polymers such as n-hexadecane or methyl methacrylate [97]. In recent years, the combination of DBT in Ac has attracted much attention as a potential single photon source [48, 90, 91, 94, 113–119].

Its potential application as an organic semiconductor has spurred an in-depth study of anthracene [120]. Crystals of anthracene can be grown by co-sublimation [121], supersaturation [94], or evaporation through spin coating [91] or melting [119]. The crystal presents three principal optical axes, each with a different refractive index. These have been measured for light at a wavelength of 546 nm [122], with values $n_x = 1.570$, $n_y = 1.817$ and $n_z = 2.220$. Relating these to the three crystallographic axes a, b and c, the n_y axis lies parallel to the b axis. A measurement at 589 nm [123] gives $n_x = 1.55$, $n_y = 1.775$ and $n_z = 2.04$. When the molecule of DBT is included in a crystal, it replaces three anthracene molecules with its optical dipole oriented along the b axis [124]. For that reason n_y is the index of interest for the field emitted by DBT molecules in anthracene. Extrapolating from these two wavelegnths to the 785 nm of interest for this work, we find that it is adequate to take n_y as 1.8.

1.4.1 Optical Properties

The energy level scheme of a DBT molecule in Ac is sketched in figure 1.7. The molecule of DBT has a strong transition between the first two singlet states, also called the highest occupied molecular orbital (HOMO), and lowest unoccupied molecular orbital (LUMO). The transition is associated to the promotion of one electron to the LUMO, and the alignment of the spin of the promoted electron and of the hole in HOMO

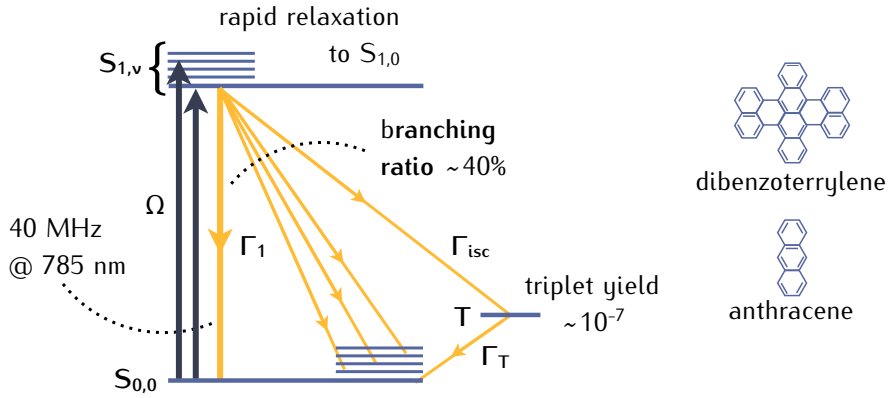


Figure 1.7 Energy level scheme and molecular structure of DBT molecules in anthracene. The main optical properties and the transition rates are highlighted.

give the singlet or triplet nature of the level. The singlet transition is the ZPL, and for a DBT molecule in anthracene this line has a wavelength of ~ 785 nm. Different host materials produce different ZPL wavelengths, ranging from 744 nm to 785 nm [108, 110, 112, 113, 125], due to different spatial configurations of the molecule in the lattice. The natural width of the transition in our anthracene crystals is typically 45 MHz, corresponding to an upper state lifetime of 3.5 ns. This can range from 30 to 50 MHz because local variations in the anthracene host strain the molecule. These local variations also spread the transition frequency over a range of several GHz. This is called inhomogeneous broadening. At room temperature, the molecules interact with thermal phonons, which dephase the optical dipole very rapidly, producing a (homogeneous) thermal width of several THz.

In addition to the ZPL there are vibrational sidebands. It is convenient to use the notation $S_{\mu,\nu}$ to indicate the singlet state with electronic level μ and vibrational level ν. The ZPL will then connect the two levels $S_{0,0}$ and $S_{1,0}$. An excitation to a higher vibrational level $S_{1,\nu}$ is followed by a rapid relaxation back to $S_{1,0}$. The time scale for this process is a few picoseconds, giving a linewidth of several tens of GHz [90]. Absorption lines have been identified, with excess energies of several hundred cm^{-1}. Among these, the $S_{0,0} \rightarrow S_{1,3}$ presents the strongest absorption, and has an excess energy corresponding to ~ 300 cm^{-1} [85, 126]. Any of these transitions can be driven by a laser, indicated by Ω in figure 1.7, after which the molecule rapidly relaxes to state $S_{1,0}$.

From $S_{1,0}$ the molecule can decay to any $S_{0,\nu}$. The spacing of these spectral lines is the same as the spacing in the absorption spectrum. A schematic of the emission spectrum is presented in figure 1.8. After the

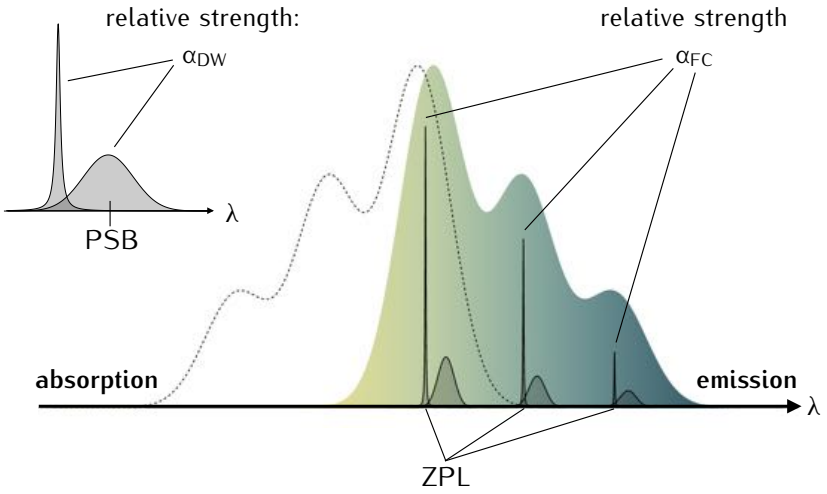


Figure 1.8 Absorption and emission spectra for a molecule-host system. The plot shows the molecular emission lines merging into one profile as room temperature is reached.

ZPL, the brightest line is the one decaying to the third vibrational level $S_{0,3}$. The relative strength between the absorption lines is primarily due to the Franck-Condon factors, i.e. to the vibrational overlap integrals for the initial and final states of a transition. A useful quantity to define is the branching ratio, the ratio of the probability of emission on the ZPL with respect to all others. For the case of DBT in Ac it varies between 30% and 50% [90, 109].

All these transitions have side-bands [127]. During the absorption or emission of a photon, a phonon of the anthracene crystal can also be generated or absorbed. An exact expression for the relationship between the electronic transition and the phonon side-band can be obtained by calculating the Debye-Waller factor

$$\alpha_{DW} = \frac{I_{ZP}}{I_{ZP} + I_{PSB}}. \tag{1–4}$$

This factor expresses the fraction of emission I_{ZP} from an electronic transition $S_{1,0} \rightarrow S_{0,\nu}$ with respect to the emission I_{PSB} on the phonon side-band.

At cryogenic temperatures all the transitions are well separated, as shown in figure 1.8. As the temperature is increased the linewdith of each transition is increased, until at room temperature they overlap, and it is not possible to distinguish between them. The emission spectrum presents a single profile, resulting in a total emission several Terahertz wide [91, 94] as noted above.

Many dye molecules have a triplet state $T_{1,\nu}$ between the first two singlet states. Upon excitation to $S_{1,0}$, the molecule decays to $T_{1,\nu}$ with a probability given by the intersystem crossing rate Γ_{isc}. Finally the molecule decays back to $S_{0,\nu}$ with a rate Γ_T. This is the case for DBT. The energy of the triplet state for the DBT-Ac couplet has never been measured, but an estimate of 5 400 nm has been given for the transition to $S_{0,0}$ of DBT in 2,3-dimethylnaphthalene [111]. The conformation of DBT in this polymer is similar to the case of Ac, so we could reasonably guess $\sim$ 900 nm for the wavelength of the $S_{1,0} \rightarrow T_{1,0}$ transition. However Sadeq and Sipe [128] have recently calculated that the triplet state of DBT in Ac lies almost half way between the ground state and the first excited singlet, with a transition wavelength for $S_{1,0} \rightarrow T_{1,0}$ of $\sim$ 1500 nm. A measurement is needed to determine a reliable value.

The lifetime of the triplet state is roughly four orders of magnitude longer than that of the excited state $S_{1,0}$, therefore transitions to $T_{1,\nu}$ can be identified by constantly exciting the molecule to the $S_{1,\nu}$ manifold. A transition to the triplet state takes the molecule out of the main cycle, resulting in periods of time where no photoluminescence is emitted from the molecule [129]. This phenomenon is called *blinking*, and is common in many solid-state single-photon emitters [130, 131]. The length of these "dark" periods is how we know the triplet lifetime $1/\Gamma_T$. We have performed a measurement of this lifetime, presented in chapter 3 of this thesis. In our system Γ_{isc} is particularly low; an upper bound of $10^{-7}\Gamma_1$ has been found [126]. Such a low intersystem crossing probability results in a steady emission of photons from the molecule, that only rarely blinks.

1.4.2 DBT in Ac as a single photon source

At the beginning of this chapter I have listed the desired characteristics of an ideal single-photon source. The photophysical properties of DBT in anthracene can now be reviewed, in light of its use as a potential single photon source.

Due to the narrow absorption lines and the wide inhomogeneous broadening, each molecule can be addressed individually. A single mode laser can be scanned across the inhomogeneous width, exciting a single molecule at a time, avoiding crosstalk and maintaining the purity of emission. However, these conditions are only met in case of a proper inclusion of the molecule in the crystal of Ac, and after the sample has been cooled

below 4 K [125]. In fact, the linewidth of the ZPL increases exponentially with temperature [125, 126], rapidly leaving the Fourier-limited regime.

Dye molecules in their excited states are highly prone to oxidation, and hence to bleaching. By excluding oxygen, the anthracene protects the molecule from bleaching. When the crystal is grown in a nitrogen atmosphere, DBT molecules can be excited over a trillion times without any change in photophysical properties [91, 94]. The specific inclusion of DBT in the anthracene crystal, where the molecular dipole is aligned with the crystallographic b axis, could spur a new control over the emission. A preferential direction of growth has been shown for anthracene crystals grown on crystalline substrates, such as lithium niobate [132]. A suitable disposition of crystalline axis and photonic nanotructures could be used to harness the emission of the molecule in a desired guided mode with maximal efficiency.

As we have discussed above, only about half the spontaneous emissions are on the ZPL, the rest being on the red-shifted Raman sidebands. The yield on the ZPL could be improved by placing the molecule inside a high-finesse cavity tuned to the ZPL [116, 133]. This would allow a nearly continuous stream of photons, to be produced with high fidelity by pulsed excitation of the strong absorption line $S_{0,0} \rightarrow S_{1,3}$ [90].

Quantum dots, colour centres and dye molecules are all promising candidates for single photon emission. The choice among them can only be made according to the particular goal one is aiming for. Besides single photon generation, our group is also interested in nonlinear effects of single molecules and their possible application to quantum gates. Single DBT molecules in anthracene crystals are a good choice for these purposes. Their small size makes them suitable to be included in microcavities [116, 133, 134]. Once coupled to a cavity, single DBT molecules could be used to imprint a π phase shift on a single photon, in a manner similar to single atoms in cavities. Alternatively, a single DBT molecule could be coupled to dielectric or plasmonic waveguides [94, 97, 118, 119], for reliable single photon generation and a possible use in quantum communication protocols, or linear photonic quantum computing. Additionally, the existing expertise of the group with rubidium atoms could be used to interface molecules and atoms in a hybrid system [135].

1.5 THESIS GUIDE

The rest of this thesis is divided into two parts. The first part is devoted to the resonant excitation of single DBT molecules. The SECOND chapter defines the theoretical framework for resonance fluorescence, introducing the optical Bloch equations relevant for a single molecule in a crystalline matrix. These are solved for varying levels of saturation and dephasing of the single emitter to give a general expression for the second order correlation function of resonance fluorescence.

The theory is then experimentally tested, as reported in the THIRD chapter. The optical properties of DBT molecules in Ac are thoroughly tested at room and cryogenic temperatures. Values of saturation intensity and linewidth are obtained for both cases. Finally, a single DBT molecule is used to perform resonance fluorescence at different temperatures where the thermal dephasing varies widely. I find that the curve for the second order correlation function obtained in the first chapter fits the data perfectly. I use the results to obtain some insight into the mechanism of dephasing.

The second part of this thesis deals with the manipulation of the spontaneous emission of a single quantum object. The FOURTH chapter is devoted to the use of plasmonic enhancements. The properties of a hybrid plasmonic waveguide are presented, as well as its fabrication and the process developed to deposit DBT in Ac over the devices. Preliminary results, showing a single molecule coupled to a device, are presented, together with an outline of the calculation of the coupling efficiency.

Finally, the FIFTH chapter presents an application of photonic crystals to integrated devices. A series of coupled photonic crystals cavities is coated with an active material, with the aim of enhancing light matter interaction. Preliminary experimental results are presented, together with a theoretical treatment of the experiment, as a dissipative open quantum system.

Part I

RESONANCE FLUORESCENCE OF SINGLE MOLECULES

2 THEORY OF RESONANCE FLUORESCENCE

In the previous section we have introduced the optical and photophysical properties of DBT molecules in an anthracene crystal. We have seen its optical properties, and the particular role of dephasing in the properties of the emitted photons. We need now a mathematical model of a DBT molecule that would allow us to predict the experimental results, obtained by collecting the molecular fluorescence, under any excitation parameter. Therefore, we are interested in a time-dependent expression for the amplitudes of the ground and excited states, and in the coherence of the excitation process. As we can gauge these quantities only through the molecular emission, we need to focus on how the scattered field relates to the dynamics of the two-level system.

2.1 MODELLING THE MOLECULE

Let's start by introducing the two pure states $|1\rangle$ and $|2\rangle$ corresponding to the molecular states $S_{0,0}$ and $S_{1,0}$ introduced in section 1.4. A general description of the state of the molecule is given by the density operator $\rho = |\psi\rangle\langle\psi|$, where $|\psi\rangle = c_1 |1\rangle + c_2 |2\rangle$ and c_i are complex amplitudes. The matrix elements $\rho_{i,j} = \langle i| \rho |j\rangle$ of this operator constitute the density matrix. The diagonal terms ρ_{11} and ρ_{22} are the probability of occupation of each level, while the off-diagonal terms ρ_{12} and ρ_{21}, often called "the coherences", describe the ensemble-averaged optical dipole. The temporal evolution of these observables is dictated by the Optical Bloch Equations (OBEqs) [1, sec. 2.7]. These are a closed system of differential equations describing the interaction between a classical field $\mathbf{E}$ and an atomic system, in our case a single DBT molecule. If we recall figure 1.7, and that

the intersystem crossing rate Γ_{isc} for DBT in Ac is negligible, we can write these equations as

$$\begin{cases} \dot{\rho}_{22} = -\Gamma_1 \rho_{22} + \frac{1}{2} \imath \Omega_0 (\rho_{21} - \rho_{12}) \\ \dot{\rho}_{12} = (\imath \Delta - \Gamma_2)\, \rho_{12} - \frac{1}{2} \imath \Omega_0\, (\rho_{22} - \rho_{11}) \\ \dot{\rho}_{11} = -\dot{\rho}_{22} \\ \dot{\rho}_{21} = \dot{\rho}_{12}^* \\ \rho_{11} + \rho_{22} = 1, \end{cases} \tag{2–1}$$

where subscripts 1 and 2 refer to states $S_{0,0}$ and $S_{1,0}$ respectively. Γ_1 is the total decay rate for population leaving the state $S_{1,0}$ by all of the transitions $S_{1,0} \to S_{0,\nu}$. It is assumed that all this population returns to $S_{0,0}$. Further, the relaxation from $S_{0,\nu}$ to $S_{0,0}$ is so rapid that the levels $S_{0,\nu}$ play no role in eq. (2–1). Γ_2 is the coherence decay rate of the $|2\rangle \to |1\rangle$ transition. $\Omega_0 = \frac{\mu_{12} E}{\hbar}$ is the Rabi frequency, where E is the absolute value of the amplitude of the electric field $\mathbf{E}$ and μ_{12} is the projection of the transition dipole moment along the direction of $\mathbf{E}$. $\Delta = \omega - \omega_0$ is the detuning between the exciting field and the $|2\rangle \to |1\rangle$ transition, which is resonant at frequency ω_0. Equation (2–1) also makes the rotating wave approximation and adopts an appropriate interaction picture to eliminate the time-dependence of the interaction [1, sec. 2.7].

When illuminated by a laser tuned to the transition frequency, the molecule starts to cycle between ground and excited state, emitting a photon each time it decays, either spontaneously at a rate Γ_1, or by stimulated emission back into the laser mode. The cycling rate is controlled by Ω_0. Sometimes the decay goes to a vibrationally excited ground state, but these relax very rapidly to $S_{1,0}$. We are therefore interested in a solution of the system (2–1) that would allow us to track the behaviour of populations ρ_{11} and ρ_{22} and of the coherences ρ_{12} and ρ_{21} for different values of excitation intensity (i.e. of Ω_0) and dephasing (i.e. Γ_2).

2.1.1 Steady-state solution

Let us start by considering the dynamics described by the OBEqs at long times, when the molecule is in dynamic equilibrium with the exciting field. The solutions for ρ_{11} and ρ_{22} will reveal the most immediate properties of a driven two-level system in the case of continuous excita-

tion. By considering the steady-state regime[1] of the eqs. (2–1) we obtain the expressions

$$\rho_{12}^{(ss)} = \imath\frac{1}{2}\frac{\frac{\Gamma_1}{\Omega_0}\frac{\Omega_0^2}{\Gamma_1\Gamma_2}\left(1-\imath\frac{\Delta}{\Gamma_2}\right)}{1+\frac{\Delta^2}{\Gamma_2^2}+\frac{\Omega_0^2}{\Gamma_1\Gamma_2}} \tag{2–2a}$$

$$\rho_{22}^{(ss)} = \frac{1}{2}\frac{\frac{\Omega_0^2}{\Gamma_1\Gamma_2}}{1+\frac{\Delta^2}{\Gamma_2^2}+\frac{\Omega_0^2}{\Gamma_1\Gamma_2}} \tag{2–2b}$$

$$\rho_{11}^{(ss)} = 1-\rho_{22} \tag{2–2c}$$

where we have isolated the saturation parameter $S = \frac{\Omega_0^2}{\Gamma_1\Gamma_2}$. For resonant excitation $\Delta = 0$ and we have the more compact forms

$$\rho_{12}^{(ss)} = \frac{\imath}{2}\frac{S}{1+S}\frac{\Gamma_1}{\Omega_0} \tag{2–3a}$$

$$\rho_{22}^{(ss)} = \frac{1}{2}\frac{S}{1+S} \tag{2–3b}$$

By recalling the expression for the on-resonance Rabi frequency we can express S as a function of excitation intensity:

$$S = \frac{\mu_{12}^2}{\varepsilon\varepsilon_0 c\hbar^2}\frac{2}{\Gamma_1\Gamma_2}I = \frac{I}{I_{sat}} \tag{2–4}$$

where the saturation intensity I_{sat} is defined as

$$I_{sat} = \frac{\varepsilon\varepsilon_0 c\hbar^2}{\mu_{12}^2}\frac{\Gamma_1\Gamma_2}{2} \tag{2–5}$$

The steady-state solutions given in eqs. (2–3) are plotted as a function of saturation parameter in figure 2.1. For low values of S, the excitation probability ρ_{22} increases linearly, but this begins to saturate around $S = 1$, reaching the limiting value of 1/2. Then, at high intensity the two-level system approaches an equal probability of occupation for $|1\rangle$ or $|2\rangle$. Spontaneous emission randomises the dipole and prevents the population from becoming inverted. The spontaneous emission rate $R(I)$ is just the product of decay rate Γ_1 and the excited state population ρ_{22}, so that, in the steady-state at resonance,

$$R(I) = \Gamma_1\rho_{22}^{(ss)} = \frac{1}{2}\Gamma_1\frac{S}{1+S}. \tag{2–6}$$

[1] Appendix A.1 contains a detailed derivation.

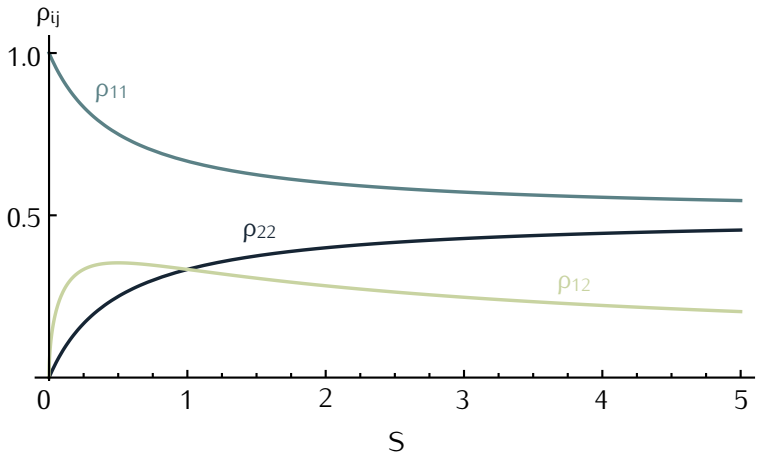


Figure 2.1 Plots of the steady-state solution of the optical Bloch equations for ρ_{11}, ρ_{22} and ρ_{12} as a function of the saturation S.

In chapter 3 we will make use of this formula to extract information on the saturation intensity of single molecules.

If we look back at eq. (2–2) and how it changes with frequency, we see that the population ρ_{22} has a Lorentzian line shape, whose full width at half maximum (FWHM) depends on both Γ_2 and the saturation parameter S:

$$\Delta\omega(I) = 2\Gamma_2\sqrt{1 + I/I_{sat}} = \Delta\omega(0)\sqrt{1+S}. \tag{2–7}$$

Here $\Delta\omega(0) = 2\Gamma_2$ is the FWHM of the scattering resonance at low power (in angular frequency units). We can see that the linewidth increases with intensity, and the effect is called power broadening. This occurs because the scattering rate near resonance is limited by saturation, while it continues to increase in the wings of the resonance. By tuning the excitation light across the transition and collecting the photoluminescence, we can measure this lineshape to gain information about the dephasing rate Γ_2 and the saturation intensity I_{sat}.

2.1.2 Analytical solution

The steady-state solution of the Optical Bloch equations (eq. (2–2)) allows us to describe the photoluminescence collected from a molecule over long times $t \gtrsim \Gamma_1^{-1}$, but we are also interested in the transient evolution over shorter times of the populations $\rho_{ii}(t)$ and of the coherences $\rho_{ij}(t)$. While partial solutions of the problem have been presented in literature [88], I have not found a full solution, so I present one here.

Let us solve the case of a molecule initially in the ground state, excited by resonant light ($\Delta = 0$). By isolating the real and imaginary parts of ρ_{12}, identified by

$$\begin{aligned} u &= \rho_{12} + \rho_{21} \\ v &= -\imath\,(\rho_{12} - \rho_{21}) \end{aligned} \tag{2–8}$$

we can simplify eqs. (2–1) to

$$\begin{cases} \dot{\rho}_{22} = -\Gamma_1 \rho_{22} + \dfrac{1}{2}\Omega_0 v \\ \dot{v} = -\Gamma_2 v - \Omega_0\,(\rho_{22} - \rho_{11}) \\ \dot{\rho}_{11} = -\dot{\rho}_{22}. \end{cases} \tag{2–9}$$

In this notation, u and v represent the in-phase and the quadrature component of the dipole, in the rotating wave approximation. $u(t)$, the real part of $\rho_{12}(t)$, is not present in this new system of equations. This is due to the resonant nature of the pumping, since under these conditions the driven dipole is in quadrature with the driving field. The system of equations (2–9) is most easily solved by taking the Laplace transform, under which $\rho(t) \to \tilde{\rho}(s)$ and $\dot{\rho}(t) \to s\tilde{\rho}(s) - \rho(0)$. This converts the differential equations to a simple set of algebraic equations:

$$\begin{cases} s\tilde{\rho}_{22}(s) = -\Gamma_1 \tilde{\rho}_{22}(s) + \dfrac{1}{2}\Omega_0 \tilde{v}(s) \\ \tilde{v}(s) = -\Gamma_2 \tilde{v}(s) - \Omega_0\,(\tilde{\rho}_{22}(s) - \tilde{\rho}_{11}(s)) \\ s\tilde{\rho}_{11}(s) - 1 = -s\tilde{\rho}_{22}(s) \end{cases} \tag{2–10}$$

recalling that $\rho_{11}(0) = 1$. These equations are readily solved to find $\tilde{\rho}(s)$. After applying the inverse Laplace transform to the solutions $\tilde{\rho}_{ij}(s)$ and simplifying the terms we are left with the final expressions

$$\rho_{12}(t) = \frac{\imath}{2}\frac{\Omega_0\Gamma_1}{\Gamma_1\Gamma_2 + \Omega_0^2}\left[1 + \frac{d-q}{2q}e^{-(p-q)t} - \frac{d+q}{2q}e^{-(p+q)t}\right] \tag{2–11a}$$

$$\rho_{22}(t) = \frac{1}{2}\frac{\Omega_0^2}{\Gamma_1\Gamma_2 + \Omega_0^2}\left[1 - \frac{p+q}{2q}e^{-(p-q)t} + \frac{p-q}{2q}e^{-(p+q)t}\right] \tag{2–11b}$$

where we have used the substitutions

$$\begin{aligned} d &= \frac{\Omega_0^2}{\Gamma_1} - \frac{\Gamma_1 - \Gamma_2}{2} \\ p &= \frac{\Gamma_1 + \Gamma_2}{2} \\ q &= \sqrt{\frac{(\Gamma_1 - \Gamma_2)^2}{4} - \Omega_0^2}. \end{aligned} \tag{2–12}$$

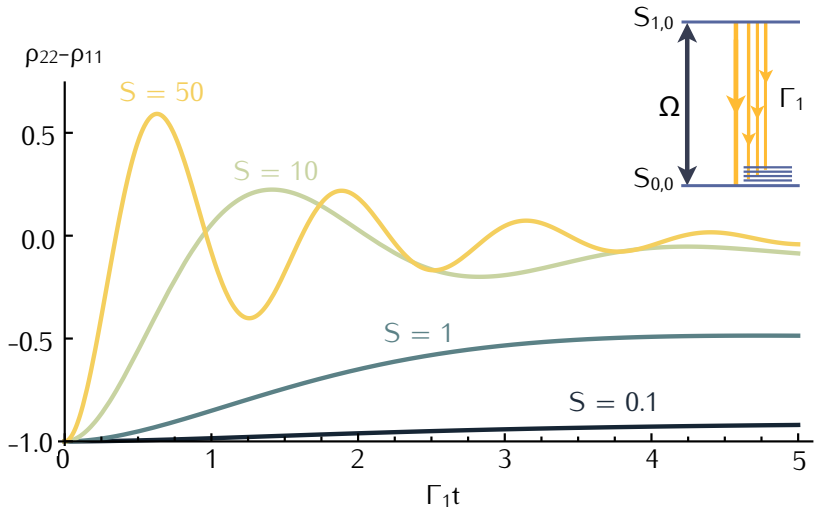
This derivation is detailed fully in Appendix A.1. In the limit of $t \to \infty$, the exponentials in eqs. (2–11) damp away and we are left with eqs. (2–3).

Let us look first at the case of $\Gamma_2 = \Gamma_1/2$ and observe $\rho_{22} - \rho_{11}$ for different values of the saturation parameter S, as plotted in figure 2.2a. We can first notice that as the power is increased, the equilibrium (i.e. the behaviour at $t \gg \Gamma_1$) approaches equally populated states, as we already found in eqs. (2–3). In addition, however, we now see at shorter times the appearance of an oscillatory behaviour in the population. This is due to the coherent nature of the excitation light, which can drive Rabi oscillations provided $4\Omega_0^2 > (\Gamma_1 - \Gamma_2)^2$. As one can see in eq. (2–12) this is the condition for q to become imaginary. At low excitation intensities there is no oscillation, and the populations approach equilibrium exponentially.

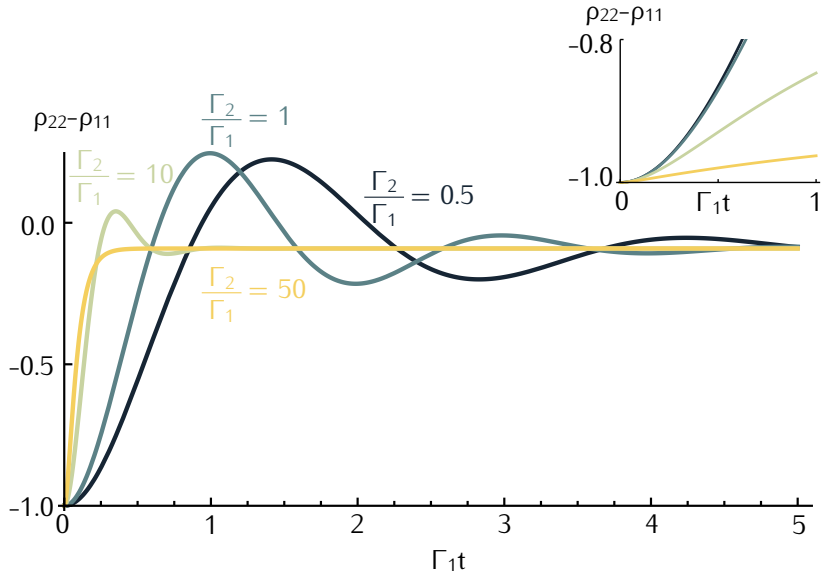
It is possible to see that the peaks and troughs in figure 2.2a appear when $\Omega_0 t$ is close to an integer multiple of π, so we can visualise $\Omega_0 t$ as a polar angle on the Bloch sphere. Spontaneous emission, and any additional dephasing mechanism, progressively randomises the phase of the Rabi oscillations, thereby washing out the coherence. This behaviour can be best viewed by a different form of eq. (2–11b). With the alternative expression $q = \imath\sqrt{\Omega_0^2 - \frac{1}{4}(\Gamma_1 - \Gamma_2)^2}$, the exponentials can be expressed as the sum of sin and cos functions. The new expression for $\rho_{22}(t)$ is

$$\rho_{22}(t) = \frac{1}{2}\frac{S}{1+S}\left[1 - e^{-pt}\left(\cos(qt) + \frac{p}{q}\sin(qt)\right)\right]. \tag{2–13}$$

In this new form it is easy to identify the oscillatory behaviour, with the modified Rabi frequency $\Omega' = \sqrt{\Omega_0^2 - \frac{1}{4}(\Gamma_1 - \Gamma_2)^2}$ defining the frequency of the oscillations. The Rabi oscillations are then damped by the exponential term, with the time constant given by p. We see then that both the stimulated emission and the dephasing rates Γ_1 and Γ_2 take part in the damping.



(a) Case of $\Gamma_2 = \Gamma_1/2$, and increasing saturation values as indicated in the plot. As the saturation parameter S increases stimulated emission starts to competewith the damping, resulting in the oscillatory behaviour visible in the figure. Inset: a reminder of the pumping scheme.



(b) In this plot the saturation is constant at $S = 10$. The level of dephasing Γ_2/Γ_1 is increased as indicated in the plot. As the system undergoes cycles of absorption and emission, the damping due to Γ_1 and Γ_2 dephases the Rabi oscillations, that progressively disappear. At the same time a higher Rabi frequency Ω_0 is required to reach the same saturation. Inset: the Rabi frequency is now kept constant, to show the decrease in population due to increasing dephasing. The excitation process is also slower, as shown by the derivative of the plots.

Figure 2.2 Plots of the population difference $\rho_{22}(t) - \rho_{11}(t)$ in the case of resonance fluorescence, for different values of saturation parameter S and dephasing Γ_2.

The role of the dephasing rate is particularly important, as we have mentioned in section 1.4. Figure 2.2b shows the population dynamics at a fixed saturation parameter of 10, taking several different values for the ratio Γ_2/Γ_1. When the only dephasing is due to the spontaneous decay of population, $\Gamma_2 = \Gamma_1/2$, and this (dark blue) curve reproduces the $S = 10$ (green) curve of figure 2.2a. An increase in Γ_2 requires a proportional increase in Ω_0^2 in order to maintain $S = 10$ and this causes the Rabi oscillations to become faster. At the same time, the total damping rate grows even more quickly and the oscillations cease all together when q becomes real - i.e. when $(\Gamma_2 - \Gamma_1)^2 > 4\Omega_0^2$. This can be seen in figure 2.2b, where the green curve for $\Gamma_2/\Gamma_1 = 10$ shows the remnant of an oscillations, while the yellow curve for $\Gamma_2/\Gamma_1 = 50$ is purely exponential.

So far in this section we have focused on the case of resonance fluorescence, where the excitation field is at the resonance frequency and the analytical formulae are reasonably simple. However, I have also used the same Laplace transform method to obtain a solution for ρ_{12} and ρ_{22} that allows a nonzero detuning Δ as well. This was done using Mathematica. The expressions are too complicated to duplicate here, but I wanted to record that an analytic solution does exist. Figure 2.3 plots the analytical solution for $\rho_{22} - \rho_{11}$ with $S = 10$ and various values of detuning. These curves agree with numerical simulations of the same optical Bloch equations. One sees with detuning that the Rabi oscillations become nutations of higher frequency and smaller amplitude as the detuning is increased. As long as the damping rate remains small compared with the frequency of these oscillations, their frequency is close to the generalised Rabi frequency $\Omega = \sqrt{\Omega_0^2 + \Delta^2}$, familiar from the case of an undamped two-level system [1, sec. 2.7]. The equilibrium value of the population decrease accordingly, until the excitation light is too far from resonance and the molecule is not excited any more. I do not make any further use of this general solution in the rest of my thesis.

2.1.3 $g^{(2)}(\tau)$ and antibunching

Equation (2–11) fully specify the dynamics of a two-level system. It is now necessary to find a way to experimentally gauge this behaviour. This can be done by studying the fluorescence scattered by the two-level system[2].

[2]The detailed derivation of the connection between the scattered electromagnetic field and the dynamics of the two-level system is presented in appendix A.2.2.

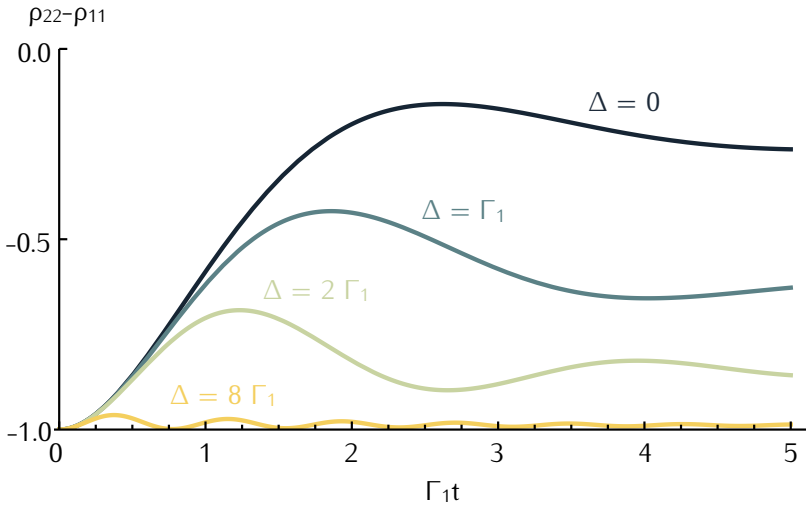


Figure 2.3 Plots of $\rho_{22}(t)$ for constant $S = 10$ and $\Gamma_2 = \Gamma_1/2$, but increasing detuning Δ. As the exciting field is detuned from resonance, faster oscillations deplete the excited state population due to the increased generalised Rabi frequency Ω. At the same time the probability of excitation decreases, and the system is eventually never excited by the field.

As we have seen in the previous section, a photon is emitted whenever the system decays from state $|2\rangle$ to state $|1\rangle$, that is, the ground state manifold. The probability of emission is therefore proportional to the probability of occupation of state $|2\rangle$, that is ρ_{22}. This can then be reconstructed by considering the time interval between two consecutive detections. The histogram built accumulating several detection events, once normalised, is a sampling of the second-order correlation function $g^{(2)}(\tau)$:

$$g^{(2)}(\tau) = 1 - \frac{p+q}{2q} e^{-(p-q)\tau} + \frac{p-q}{2q} e^{-(p+q)\tau}. \tag{2–14}$$

The expression of eq. (2–14) is equivalent to the expression of the population $\rho_{22}(\tau)$ presented in eq. (2–11b). This is due to the fact that $g^{(2)}(\tau)$ can be interpreted as the probability of detecting a photon at time $t = \tau$, given that a first one was detected at $t = 0$. As the molecule has to transit to the excited state before it can emit a photon, the probability of detection is proportional to the population ρ_{22}.

The function $g^{(2)}(\tau)$ can be measured by use of the Hanbury-Brown-Twiss setup, originally presented to measure the diameter of stars [27] and briefly described in section 1.2. A formula for $g^{(2)}(\tau)$ for the scattered field from a two-level system was first introduced by Carmichael and Walls [136, 137], and the first direct observation was carried out on an atomic beam of sodium by Kimble, Dagenais and Mandel [138]. Due

to its direct connection with the population of the excited state ρ_{22}, it has been used to study the internal dynamics of single quantum systems, especially in the case of single organic molecules [82, 88, 139].

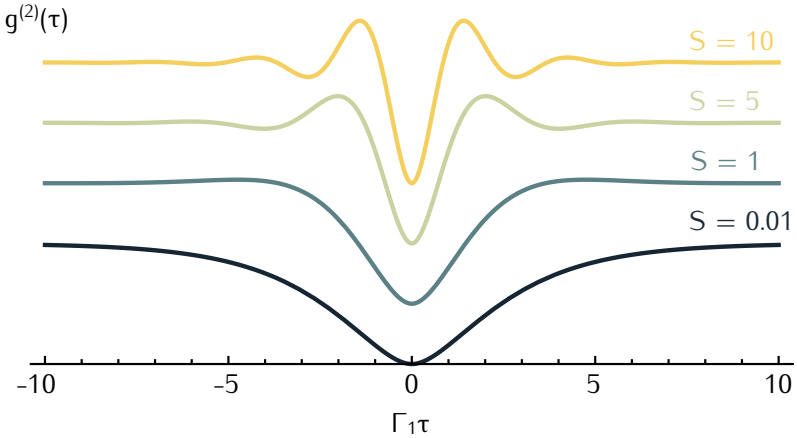
In figure 2.4 we show plots of eq. (2–14) for different values of saturation and dephasing. The plots are exactly equivalent to those in figure 2.2a because $\rho_{11} + \rho_{22} = 1$. As $g^{(2)}(\tau)$ is proportional to the probability of detecting photons at different times, the oscillations of figure 2.4a shows periodical peaks in the arrival of photons at the detector, with frequency increasing with saturation. Recalling figure 2.2a, those peaks are associated with a population inversion of the two levels, where there is a higher probability of emission. In figure 2.4b we instead fix the excitation power and increase the dephasing. This shows the transition from damped Rabi flopping to overdamped exponential time evolution. In both regimes, the antibunching dip present at $\tau = 0$ marks the radiation emitted by the molecule as clearly non-classical for any dephasing rate Γ_2.

The Cauchy-Schwartz inequality for the anticorrelation function states that $g^{(2)}(0) \geqslant g^{(2)}(\tau)$ for any τ [1, sec. 6.5], setting the limit for classical and non-classical light. In figure 2.4 $g^{(2)}(0) < g^{(2)}(\tau)$; this property is called *antibunching*. It is also possible to demonstrate that $g^{(2)}(0) \geqslant 1$, and this inequality can be related to the photon number distribution of the field [1, sec. 6.10]. The fluorescence from a quantum emitter is composed of single, well separated photons, and this is reflected in the value of the correlation function near the origin, where $g^{(2)}(\tau) < 1$. This is a signature of a sub-poissonian statistics of the field, and is again a characteristic a non-classical state[3]. For the case of resonance fluorescence $g^{(2)}(0) < g^{(2)}(\tau)$ and $g^{(2)}(0) = 0$. In general,

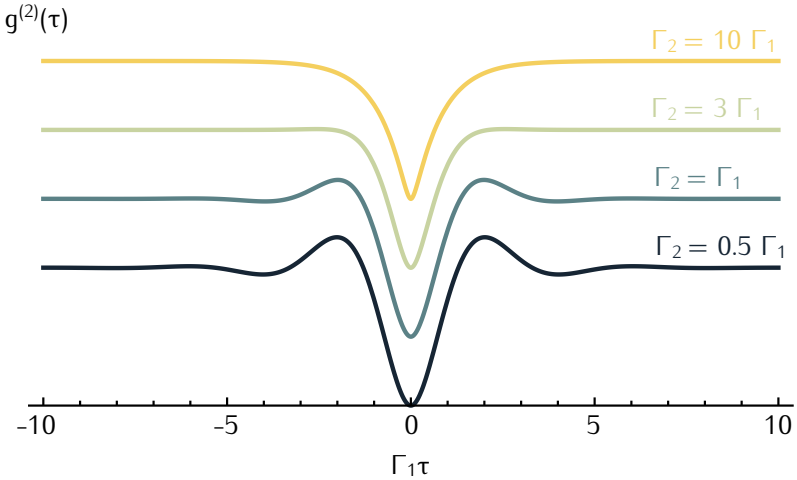
$$g^{(2)}(0) = 1 - \frac{1}{\bar{n}} \tag{2–15}$$

where $\bar{n}$ is the mean number of photons in the field, or the number of contributing single emitters [142, sec. 3.7]. After accounting for experimental fluctuations, is then possible to set $g^{(2)}(0) < 0.5$ as the threshold for single photon generation from a potential quantum emitter.

[3] It is important to notice that, while in our case sub-poissonian statistics and antibunching are correlated, it is not true in general [140, 141].



(a) As the excitation intensity increases the population is transferred to the excited state. When $\Omega_0 \approx \Gamma_1$ the population starts to oscillate, with higher probability of emission of photons and consequent bunching.



(b) The system transit rapidly from coherent to incoherent regime, as the dephasing is increased. Here the Rabi frequency is kept at a constant value $\Omega_0 \approx 2\Gamma_1$ while Γ_2 is increased according to the values in the plot. Rabi oscillations are washed out by the dephasing, but the antibunching is not affected.

Figure 2.4 Plots $g^{(2)}(\tau)$ in the case of resonance fluorescence, for different values of saturation parameter S and dephasing Γ_2.

2.2 ALTERNATIVE SCHEMES

The optical Bloch equations introduced in this chapter are a powerful tool to investigate the dynamics of a two-level system. The equations can also be easily re-arranged to describe more complicated systems. In this section I present two cases relevant for our study of single organic molecules, where we consider the effect of the triplet state and we analyse blue-detuned pumping to a higher vibrational level.

2.2.1 Triplet state analysis

We can easily modify the OBEq (2–1) to include the triplet state mentioned in section 1.4. These take the form

$$\begin{cases} \dot{\rho}_{11} = \Gamma_1 \rho_{22} + \Gamma_T \rho_T + \frac{1}{2} \imath \Omega_0 \left(\rho_{21} + \rho_{12} \right) \\ \dot{\rho}_{22} = -\left(\Gamma_1 + \Gamma_{isc} \right) \rho_{22} + \frac{1}{2} \imath \Omega_0 \left(\rho_{21} + \rho_{12} \right) \\ \dot{\rho}_{12} = \left(\imath \Delta - \Gamma_2 \right) \rho_{12} + \frac{1}{2} \imath \Omega_0 \left(\rho_{22} - \rho_{11} \right) \\ \dot{\rho}_T = \Gamma_{isc} \rho_{22} - \Gamma_T \rho_T \\ \rho_{11} + \rho_{22} + \rho_T = 1 \end{cases} \tag{2–16}$$

where, following the notation of figure 1.7, Γ_{isc} is the spontaneous decay rate from state $|2\rangle$ to the triplet state. ρ_T is the population of the triplet state, that has a spontaneous decay rate of Γ_T to the ground state. It is possible to neglect the dipole coupling to the triplet because of the large detuning between the $S_{0,0} \rightarrow S_{1,0}$ transition and the triplet transitions $S_{0,0} \rightarrow T_{0,0}$ and $S_{1,0} \rightarrow T_{0,0}$.

From the steady-state solution of eqs. (2–16) we obtain a similar expression for ρ_{22} [143], with the difference that the saturation parameter now has the expression

$$S = \frac{1}{2} \frac{2 + \frac{\Gamma_{isc}}{\Gamma_T}}{\left(\Gamma_1 + \Gamma_{isc} \right) \Gamma_2} \Omega^2. \tag{2–17}$$

From this we can obtain the value for saturation intensity

$$I_{sat} = \frac{\varepsilon \varepsilon_0 c \hbar^2}{\mu_{12}^2} \frac{(\Gamma_1 + \Gamma_{isc}) \Gamma_2}{(2 + \frac{\Gamma_{isc}}{\Gamma_T})} \tag{2–18}$$

that reduces to (2–5) for $\Gamma_{isc} \rightarrow 0$. We can identify additional parameters to characterise this system. Looking at eq. (2–17), we can isolate the ratio $\mathcal{B} = \Gamma_{isc}/\Gamma_T$. This is the triplet "bottle-neck" parameter, and it regulates

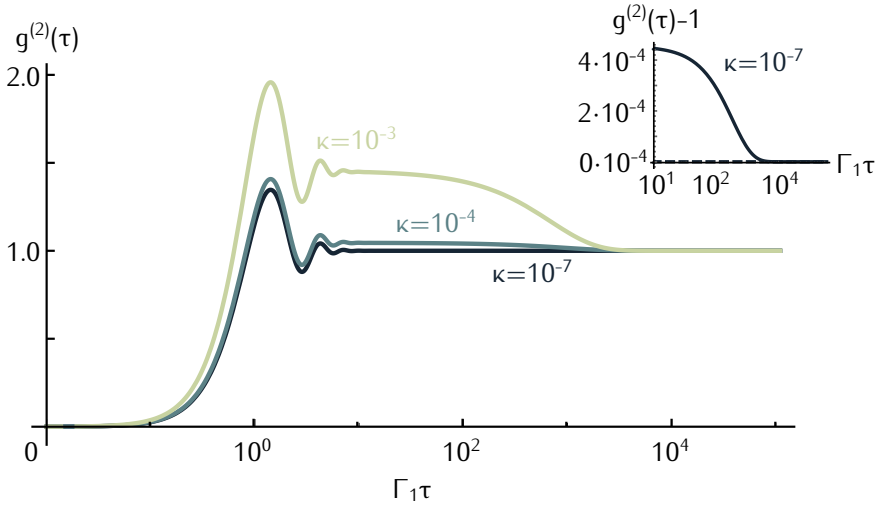


Figure 2.5 Plot of $g^{(2)}(\tau)$ for the level scheme of fig. 1.7 and different κ. Saturation $S = 10$ and $\Gamma_T = 10^{-3}\,\Gamma_1$. It is possible to notice the bunching due to the triplet bottle-neck for times $\tau \sim \Gamma_T$. The inset compares the cases $\kappa = 10^{-7}$ and $\kappa = 0$ (dashed), showing the almost negligible difference.

the population in the triplet, relative to that in state $S_{1,0}$. We can also define the branching ratio $\kappa = \Gamma_{isc}/\Gamma_1$ which expresses the relative probability of spontaneous decay from $S_{1,0}$ to the triplet and to the ground state.

Following the Laplace transform method it is possible to obtain a time-dependent solution for ρ_{22}, and therefore for $g^{(2)}(\tau)$ [88]. The most notable effect of the triplet state is to stop the fluorescence of the molecule for times of the order of Γ_T, the previously mentioned blinking effect. Therefore, when analysed over long times, the fluorescence consists of a stream of photons with dark periods of length $\sim \Gamma_T^{-1}$, and this is reflected in $g^{(2)}(\tau) > 1$ for $\tau \sim \Gamma_T^{-1}$. In contrast with the antibunching close to the origin, here the $g^{(2)}(\tau)$ shows bunching, due to the separation of the fluorescence into bright and dark periods. Figure 2.5 is a plot of $g^{(2)}(\tau)$ for three values of the triplet-singlet decay branching ratio κ, while saturation is kept constant. The triplet state lifetime was set to the plausible value of $10^3\,\Gamma_1^{-1}$. As is clear from the inset, the bunching is almost negligible for the estimated $\kappa = 10^{-7}$ of DBT in Ac. By considering realistic values for the decay rates, $g^{(2)}(\tau)$ can be simplified. As the lifetime of the triplet state for organic molecules is in the microsecond regime [116, 126], and the branching ratio κ for DBT in Ac has an upper limit of $10^{-7}\,\Gamma_1$ [126], we can write $g^{(2)}(\tau)$ for long times as [82]

$$g^{(2)}(\tau) \approx 1 + \frac{\mathcal{B}}{2} e^{-\Gamma_T \tau}. \tag{2–19}$$

2.2.2 Blue-detuned pumping

So far we have treated the case of resonance fluorescence, where the molecule is excited resonantly on the ZPL. This case is suitable for coherent control of the state of the system, as is required for use in quantum gates [144] or memory devices [145]. However, if we keep in mind the goal of efficient single photon generation, this scheme is not the most favourable. Due to the resonant nature of the pumping, population inversion cannot be achieved in a continuous excitation mode, as we see in eqs. (2–3). Moreover, the emitted photons cannot be distinguished from the pump light on the basis of wavelength. It is better in this case to pump the molecule into a vibrationally excited state $S_{1,\nu}$, which then relaxes rapidly to $S_{1,0}$. This permits full population inversion, and separate the pump and the emission frequencies, as discussed more fully in section 1.4.

The rate of the (nonradiative) vibrational relaxation Γ_{nrad} is of the order of 10^{12} s^{-1} [90]. The precise value of Γ_{nrad} is different for every molecule, and can be deduced from the linewidth of the $S_{1,\nu} \to S_{0,0}$ transition. We have mentioned that a strong absorption has been observed for pumping to $S_{1,3}$, and that is what we use for this purpose. The energy level scheme for this new regime is presented in figure 2.6.

With the same formalism used before, and with ρ_{33} as the population of $S_{1,3}$, the new optical Bloch equations are

$$\begin{cases} \dot{\rho}_{33} = -\left(\Gamma_3 + \Gamma_{\text{nrad}}\right)\rho_{33} - \frac{1}{2}\imath\Omega_0(\rho_{31} - \rho_{13}) \\ \dot{\rho}_{22} = \Gamma_{\text{nrad}}\rho_{33} - \Gamma_1\rho_{22} \\ \dot{\rho}_{13} = -\left(\imath\Delta + \frac{1}{2}\left(\Gamma_3 + \Gamma_{\text{nrad}}\right)\right)\rho_{13} + \frac{1}{2}\imath\Omega_0(\rho_{33} - \rho_{11}) \\ \dot{\rho}_{23} = -\left(\imath\Delta + \frac{1}{2}\left(\Gamma_3 + \Gamma_{\text{nrad}} + 2\Gamma_2\right)\right)\rho_{23} + \frac{1}{2}\imath\Omega_0\rho_{21} \\ \dot{\rho}_{12} = -\left(\imath\Delta + \Gamma_2\right)\rho_{12} - \frac{1}{2}\imath\Omega_0\rho_{23}. \end{cases} \tag{2–20}$$

where again $\rho_{13} = \rho_{31}^*$, $\rho_{23} = \rho_{32}^*$ and the population is conserved $\rho_{11} + \rho_{22} + \rho_{33} = 1$. Γ_3 is the spontaneous radiative decay rate of the $S_{1,3} \to S_{0,0}$ transition.

This system can be solved with the same procedure described in the previous section, but an equivalent, and easier, solution for ρ_{22} can be obtained if we consider the timescales of the different decay processes. As the molecule is excited to $S_{1,3}$, the quick non-radiative decay Γ_{nrad} transfers the population from ρ_{33} to ρ_{22}. This process is much faster

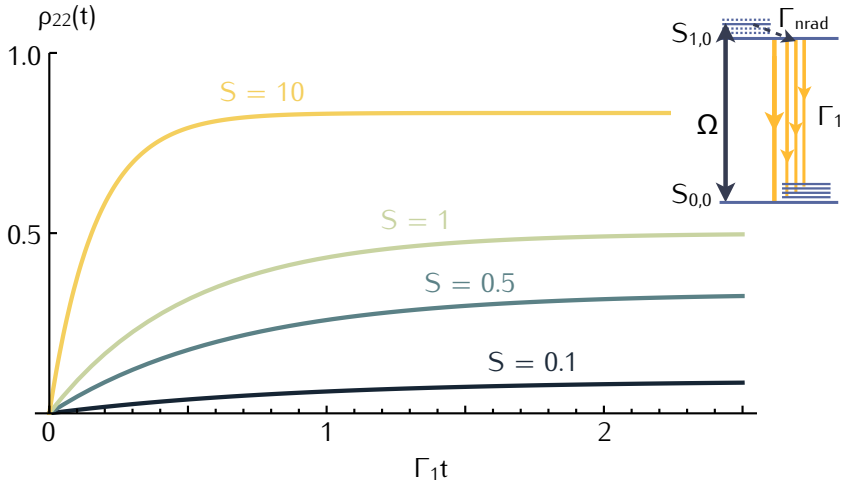


Figure 2.6 Plot of $\rho_{22}(t)$ for increasing S in the incoherent pumping regime described by eqs. (2–20). The exponential rise of ρ_{22} becomes sharper and sharper as the system is pumped harder. Inset: energy level scheme for blue-detuned pumping. The non-radiative relaxation rate Γ_{nrad} quickly transfer the population from $S_{1,3}$ to $S_{1,0}$.

than the damping rate Γ_3, that can therefore be discarded. In addition, the emission rate Γ_1, that will take the molecule back to $S_{0,0}$ is also much slower than Γ_{nrad}; any coherence between ρ_{33}, ρ_{22} and ρ_{11} is washed out. We can therefore move to a system of rate equations for a three-level system, where ρ_{33} is populated with a rate K, and all the off-diagonal terms of the density matrix are null:

$$\begin{cases} \dot{\rho}_{11} = -K\rho_{11} + \Gamma_1\rho_{22} \\ \dot{\rho}_{22} = -\Gamma_1\rho_{22} + \Gamma_{nrad}\rho_{33} \\ \dot{\rho}_{33} = K\rho_{11} - \Gamma_{nrad}\rho_{33}. \end{cases} \tag{2–21}$$

Given that $\Gamma_{nrad} \gg \Gamma_1$, Γ_3 and K, the time-dependent solution for $\rho_{22}(t)$ of this closed system can be readily found as

$$\begin{aligned} \rho_{22}(t) &= \frac{K}{K+\Gamma_1}\left(1 - e^{-(\Gamma_1+K)t}\right) \\ &= \frac{S_{blue}}{1+S_{blue}}\left(1 - e^{-\Gamma_1(1+S_{blue})t}\right) \end{aligned} \tag{2–22}$$

where $S_{blue} = K/\Gamma_1$. This shows an approach to full population inversion at high saturation. Plots of ρ_{22} for different level of saturation are reported in figure 2.6.

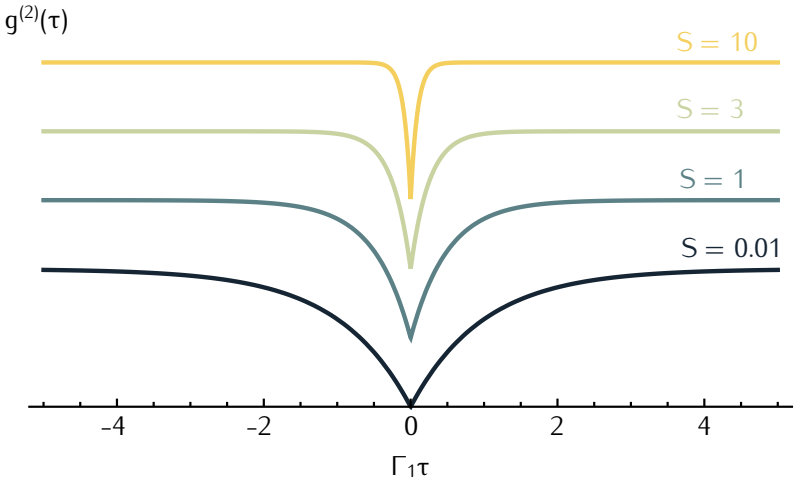


Figure 2.7 Plot of $g^{(2)}_{\text{blue}}(\tau)$ for increasing saturation S. As the excitation intensity is increased the antibunching dip narrows, with no effect on $g^{(2)}_{\text{blue}}(0)$.

The same asymptote can also be obtained by solving eqs. (2–20) in the steady state regime. They are solved explicitly in Appendix A.1, and we report here only the useful result relating S_{blue} to the Rabi frequency

$$S_{\text{blue}} = \frac{\Omega_0^2}{2\Gamma_1\Gamma_{\text{nrad}}}. \tag{2–23}$$

On comparing this with the expression $S = \frac{\Omega_0^2}{\Gamma_1\Gamma_2}$, given just below eq. (2–2), we see that the blue-detuned pump needs more power by a factor of $2\Gamma_{\text{nrad}}/\Gamma_2$ to reach the same level of saturation.

From the population ρ_{22} we obtain a formula for the second-order correlation function, which is nothing more than eq. (2–22) normalised to long times:

$$g^{(2)}_{\text{blue}}(\tau) = 1 - e^{-\Gamma_1(1+S_{\text{blue}})\tau}. \tag{2–24}$$

Plots of $g^{(2)}(\tau)_{\text{blue}}$ for different values of saturation S are presented in figure 2.7. As the excitation power is increased the antibunching dip narrows because the equilibrium is approached at a rate $\Gamma_1\,(1 + S_{\text{blue}})$. While $g^{(2)}_{\text{blue}}(0)$ is unaffected by the increasing power, the steep rise of $g^{(2)}_{\text{blue}}(\tau)$ can be hard to detect. The jitter in the detection signal can easily smooth the antibunching dip, sometimes bringing $g^{(2)}_{\text{blue}}(\tau)$ above the 0.5 limit. A convolution of the correlation function with the correct instrument response function is then necessary [125].

3 SPECTROSCOPY AND PHOTOPHYSICS OF SINGLE MOLECULES

This chapter details the experimental analysis of single molecules in anthracene. Its optical properties are probed at room temperature, before exploring the cryogenic regime. The theory derived in the previous chapter is used to extract useful information about the molecules, such as dephasing rate, saturation intensity and triplet state lifetime. Finally, the role of temperature-induced dephasing on the second order correlation function $g^{(2)}(\tau)$ of the molecule is explored. I use these results to compare the full solution introduced in the previous chapter with several approximations presented in the literature.

3.1 THE CONFOCAL MICROSCOPE

The optical setup uses the well-established technique of confocal microscopy. This is widely used in several fields of science, from high resolution imaging to the observation of biological processes, and it is the work horse of single molecule microscopy and spectroscopy [146–148]. The usual setup has two optical paths, both going through an objective lens. One is used for illumination, usually with a collimated laser beam, and the other for collection of the sample emission. Discrimination between the excitation light and the sample fluorescence is achieved by separating the two due to their differences in polarisation, spectral properties or spatial profile.

Our setup follows the same principles, and a sketch[1] of it is reported in figure 3.1. Light from a tuneable laser is spatially filtered by coupling it into a polarisation-maintaining fibre (PMF) and used as the excitation light. On a separated optical table the laser light is collimated again and is then filtered in polarisation and wavelength by means of a polariser (P) and a band-pass filter (BP, Thorlabs). A further half wave plate (HWP) is used to vary the polarisation of the excitation light.

The beam is then directed into an objective lens (Karl-Zeiss Epiplan Neofluar, 100x magnification) that focuses on the sample plane, to a spot

[1] A more detailed description of the experimental setup is shown in Appendix B.

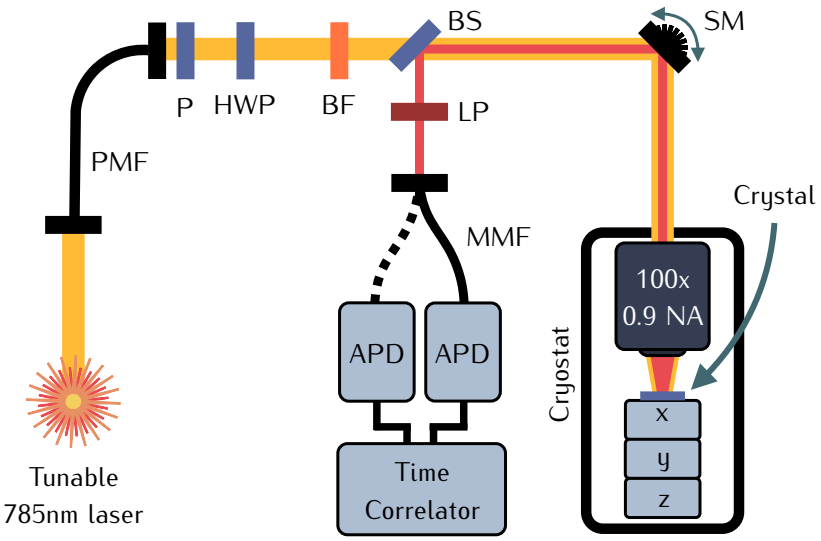


Figure 3.1 Schematic of the confocal microscope used for cryogenic spectroscopy of single molecules. PMF: polarisation-maintaining fibre. P: polariser. HWP: half-wave plate. BF: band-pass filter. BS: beam splitter. SM: scanning mirrors. LP: long-pass filter. MMF: multimode fibre. APD: avalanche photodiode.

with a FWHM of 550 nm. This result is in close agreement with the expected diffraction-limit value given by [149]

$$D = 1.22 \frac{\lambda}{NA} \tag{3–1}$$

where D is the spot diameter, λ is the wavelength of the laser light and NA is the numerical aperture of the objective. This is defined as

$$NA = n \sin\theta \tag{3–2}$$

where n is the refractive index of the medium in which the light propagates (in our case air or vacuum), and θ is the maximum angle of deviation from vertical incidence at which light enters or exits the lens. For our objective NA $= 0.9$, therefore the maximum angle of incidence of light in air is about $64°$. The diffraction-limited condition of eq. (3–1) is achieved only in case of perfectly collimated laser light, but a more decisive factor is the filling parameter, the ratio between the beam diameter and the back aperture of the objective lens [150, Sec. 3.6]. To ensure that this aperture is filled, the laser beam is expanded by a telescopic system of lenses to a FWHM of 2.98(3) mm.

The fluorescence emitted by the sample, as well as back-scattered excitation light, is collected by the same objective lens. The portion of radiation that is within the numerical aperture of the objective is col-

limated, and propagates back along the same path. It is then spatially separated from the pump on a 50:50 cube beam splitter, and spectrally filtered by means of two long-pass filters (HQ 800LP Chroma). Finally, the beam is focused into a multi-mode fibre, that can be coupled to an avalanche photo-diode detector (APD, Perkin Elmer), to a spectrometer (Andor Shamrock 303i, with Newton 791-FI CCD) or to a fibre beam splitter (Thorlabs) connected to two APDs for time correlation measurements. It is usual in confocal microscopy to have a pinhole at the focal plane of the last focussing lens, as an additional spatial filter. The diameter of the pinhole is used to define the depth of field of the microscope by rejecting light from outside of the focal plane of the objective [151]. In our case the core of the multimode fibre serves as the pinhole. With a diameter of $\varnothing = 62.5\ \mu m$, the fibre collects light from an area

$$\frac{f_{obj}}{f_{lens}}\varnothing \approx 10\,\mu m^2 \tag{3–3}$$

where f_{obj} and f_{lens} are the focal lengths of the objective lens and of the collection lens. This area can seem too wide, especially when considering the dimensions of the laser spot. However, due to the low power usually used in single-molecule microscopy, this large collection is not a limiting factor nor does it affect the signal-to-noise-ratio, and instead highly simplifies the alignment of the collection optics.

Images of the sample are obtained by raster-scanning the laser spot, and collecting the fluorescence from the sample. This is accomplished by changing the angle of incidence of the laser onto the objective, that then focuses the light to a different position. Two galvanometric mirrors (Thorlabs) are put to this use. An image limited to about $25\times25\ \mu m$ can be collected before the beam is clipped by the back aperture of the objective, diminishing excitation and collection efficiency. In addition, the setup allows white-light imaging. A white light source[2], is first collimated, and then superimposed onto the confocal path on a beam splitter. Another beam splitter picks off the reflected light, that is then imaged with a CCD camera (Andor Luca 785 MONO). Two irises, one after the white-light source and one after the camera beam splitter, are used to optimise the brightness of the image.

[2]Reported in figure B.1.

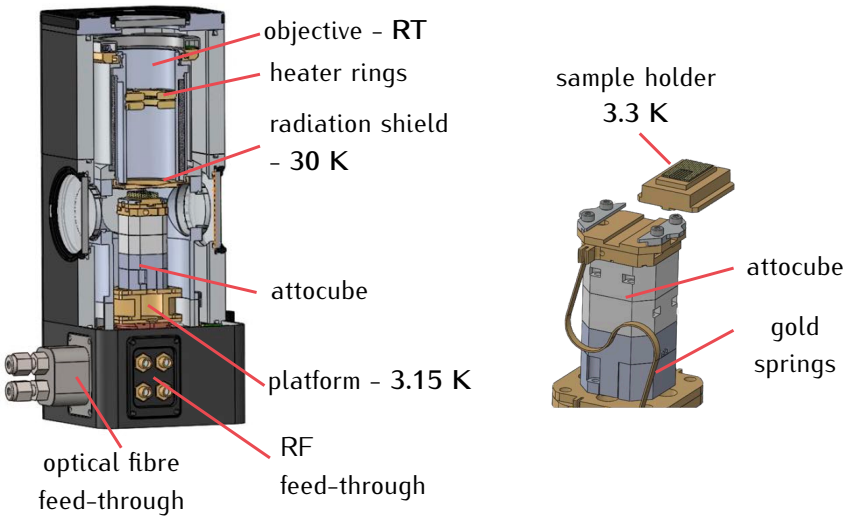


Figure 3.2 Scheme of the Montana cryostation, and of the sample holder design.

Cooling the molecules

Interactions between the DBT and its host environment can greatly increase the spectral width of the emitted light. To reach the natural linewidth the molecules have to be cooled to below 4 K. This was accomplished using a close-cycle Montana cryostation, illustrated in figure 3.2.

Helium gas is compressed in two stages, and is then evaporated onto a metal cold-finger, that reaches a temperature of 2.5 K. The cold finger then extends to the main chamber, that is kept under vacuum (pressure < 0.1 mTorr). Here a base platform is cooled to 3.15 K, the difference in temperature with the cold finger owing to imperfect thermal connections. A 3D piezo-positioning stage is placed on the platform, on top of which the sample holder housing is located. Heat is transferred from the platform to the sample by a system of metal springs. These bring the sample holder at the top of the attocube to a temperature of about 3.3 K, while still allowing free movement in all three directions. The platform and the sample holder temperatures are monitored by thermometers. The sample chamber is separated from the objective by a radiation shield that is kept, together with the chamber walls, at a temperature of 30 K. As the objective is not suitable for cryogenic purposes, and it is kept at room temperature by a heater ring, the shield is necessary to isolate the sample. The radiation shield is placed 200 µm below the objective, and features a 2 mm hole aligned with the objective to allow imaging. Since the objective has a working distance of 300 µm, only 100 µm are left between the focal plane and the radiation shield. Therefore, the confocal image can

at Platform	None	Glass Slip	Wafer	Quartz
Varnish	3.6	7.49	8.98	7.34
Silver paint - CMR	3.5	10.33	10.63	13.14
Silver paint - Elec	3.15	5.25		
Silver paint - Agar	3.15	3.93	4.19	6.56

at Sample	None	Glass Slip	Wafer	Silicon
Silver paint - Agar	3.15	4.17	3.94	3.92

Table 1 Temperatures read by the thermometer placed in the test copper block, connected with different cement and substrates to the cryostat platform or sample.

only be in focus down to 100 µm below the top surface of the sample, and this has to be taken into account when designing samples.

The sample holder is divided into two pieces, one of which removable. Individual samples are attached to the removable part by a cement; different samples can be easily swapped by exchanging sample holders, while keeping their thermal connection intact. This is indeed a crucial factor: as the sample is not immersed in liquid helium, and the temperature of the sample holder is already at the limit of what is needed for single molecule spectroscopy, an optimal thermal connection had to be achieved.

For this purpose I ran a series of tests with different cements and substrates, with the aim of measuring the minimum temperature of the surface of a substrate once thermally connected to the sample-holder. As the Ac crystal would be deposited on it, and considering that the platform itself is already at 3.3 K, I had to make sure that molecules would be cooled to below 4 K. I removed the thermometer controlling the sample holder from its casing, and I inserted it into a copper block as reported in figure 3.3. By connecting this block to the cryostation using different cements, and interposing different substrates between the block and the cryostat, I tested what temperature could be attained for every combination. We tested the following substrates:

- a glass microscope cover slip, with a thickness of 120 µm;
- a quartz slide, with a thickness of 2 mm;
- a portion of a silicon substrate, with a thickness of 550 µm;
- a silicon wafer, with a multiple coating of 2 µm of silica (SiO_2) and 120 nm of silicon nitride (Si_3N_4), for a total thickness of 550 µm.

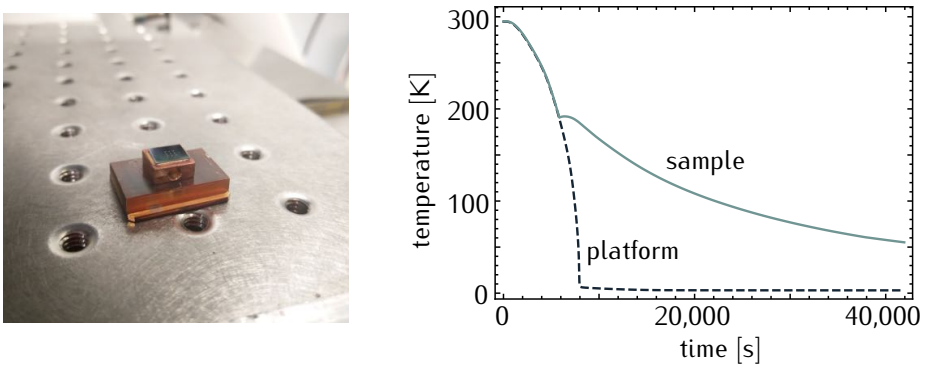


Figure 3.3 On the left, picture of the copper block housing the sample thermometer, used to tests the thermal conductivity of substrates and cements. The right plot reports the typical temperature measurement for the case of thermal grease.

Initial tests were performed removing the attocube and connecting the thermometer directly with the platform. At first we tested the thermal grease provided by Montana. This is a carbon-based grease that provides a good thermal contact, especially for metal-metal interfaces. However, around ~ 200 K the grease solidifies, usually causing the sample to detach from the sample mount. This is clearly visible in figure 3.3, where a sharp separation appears between the temperature reading of the sample and the platform.

I therefore looked for other cements, giving better thermal connection with the sample. Together with thermal grease, Montana supplied us with varnish-based glue. This requires curing at 70° C for 25 minutes to reach optimal conditions of strength and thermal conductivity. At the same time, I purchased two different kinds of silver paint, easily available from commercial websites, such as RS. While the specific conditions varied between products, they all required curing to reach optimum performances. I tested these cements by placing the thermometer block directly in contact with the platform, with and without each of the substrates listed before. The results are reported in table 1. When the thermometer block was glued to the platform, almost every cement gave a good thermal connection, with sample and platform temperature readings showing the same result (even for thermal grease). However, once any substrate was placed between the cryostat and the copper block each combination gave a different, sometimes surprising, result. Of particular interest were the first tests obtained with silver paint. This kind of cement was deemed to be the most reliable, but the temperature reached with the first batch of silver paint [3] was far from optimal, and even higher than what was

[3] CMR conductive silver paint RS186.

achievable with varnish. In many cases the sample flicked off the mount during the cool down. A second batch of silver paint[4], with a lower concentration of silver, was more successful. A temperature below 6 K was achieved with a glass slide inserted between the thermometer block and the platform. Following this positive result, a new silver paint[5] was purchased. Despite having a moderate silver content (~ 60%), the large size of the silver flakes proved to be key for an ideal thermal connection. After the attocube was placed back inside the chamber, we measured the sample temperatures listed in the last row of table 1. Even with this additional thermal load on the cryostation, a temperature of ~ 4 K was achieved with most of the substrates. This crucial dependance on the nature of the silver paint was attributed to the considerable strain put on the cryostat. As the temperature of the sample mount is already as high as 3.2 K, a maximum of 0.8 K can be lost across the substrate and through the anthracene crystal in order to attain lifetime-limited emission from single DBT molecules.

Laser sources

As reported in section 1.4, once the molecules are brought to liquid helium temperatures the interaction with lattice phonons is suppressed and the coherence lifetime is only limited by population decay. In these conditions the ZPL has a lifetime-limited linewidth of 40 MHz, distributed over about 1 THz due to differences in the local environment of the individual molecules. In order to address a single emitter, the source of the excitation light in the confocal microscope has to be specifically tailored. In particular, it has to feature a narrow linewidth ($\leqslant$ 1 MHz) that can be scanned over the whole inhomogeneous width. Three distributed-feedback (DFB) diode lasers, centred at 785 nm (Eagleyard), 780 nm (Eagleyard) and 767 nm (Toptica) fulfilled these requirements.

The temperature and the current of the diodes can be controlled, to scan and stabilise the emission wavelength. In order to monitor the laser frequency, a portion of the excitation light is subtracted from the main beam and focused into a PM-fibre. The light is then collimated, and re-focused into a Fabry-Perot cavity (Thorlabs SA210-5B) with a lens of focal distance 10 cm. A silicon photodiode (Thorlabs) collects the light transmitted through the cavity. The length of the cavity is changed by controlling the voltage sent to a piezoelectric attached to one of the two cavity mirrors. Whenever the length of the cavity changes by an integer

[4] Electrolube conductive silver paint.
[5] Agar Scientific.

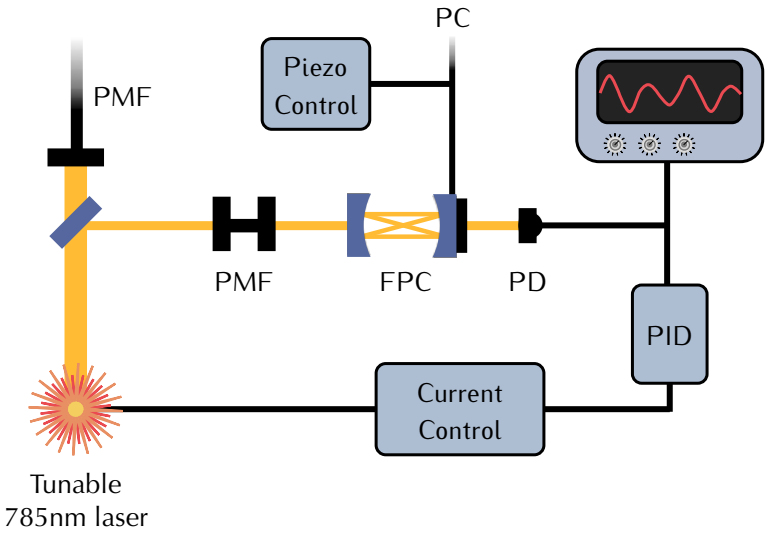


Figure 3.4 Schematic of the setup for the stabilisation and the control of the laser diode wavelength. FPC: Fabry-Perot cavity. PD: silicon photodiode. PID: Proportional-Integro-Derivative loop.

multiple of the light wavelength there is a new maximum transmission, detected by the photodiode.

This particular cavity is confocal: two equal spherical mirrors are separated by a spacing L that is equal to their radius of curvature, and the free spectral range is FSR $= c/(2L) = 20$ GHz. The odd and even transverse modes are equally spaced, giving the appearance of a 10 GHz FSR, but when the input is well centred and symmetrical the odd modes disappear. Observing this is a good indication that the light is well aligned with the cavity. When the cavity length is accurately confocal, the even modes are exactly degenerate and then the linewidth is determined by the cavity finesse, which in this case is ~ 100.

The piezolectric mirror of the cavity was controlled by a voltage driver (Thorlabs MDT693A), and the cavity length was adjusted to reach half of transmission peak by looking at the transmitted light with the photodiode and an oscilloscope. The photodiode signal was fed to a Proportional-Integro-Derivative (PID) loop (Stanford Scientific SIM960), that in turn controls the voltage sent to the current controller (Thorlabs LDC205C) of the laser diode. If an external voltage was applied to the cavity, the PID loop changed the wavelength of the laser light to match the change in cavity length, and therefore restored the same level of transmission. A change in voltage of 1 V translated into a change of about 1 GHz in laser frequency.

As the diode laser current was changed to produce a frequency scan, so too did the power emitted by the laser. As the molecules are expected to

be as narrow as 30 MHz, no effect on the shape of the molecular transition was anticipated, and no other error on the frequency of the laser was noticed. Nonetheless, in case of features with a wider excitation spectrum, or for background purposes, one should take into account this change in power.

The temperature of the diode laser was also monitored and controlled (Thorlabs TE200), because the temperature of the diode affects the laser frequency. The diode can operate between 8 °C and 40 °C. This does not offer a practical way to scan the laser because the thermalisation time is long, but it does allow coarse tuning of the centre frequency.

In addition to three DFB diode lasers, I employed a pulsed diode laser (PicoQuant). It features a central wavelength of 755 nm, a pulse length of 150 ps and a maximum repetition rate of 40 MHz. This laser was used in the time-correlated single-photon counting (TCSPC) measurements, presented in section 3.2.2.

3.2 SAMPLE PREPARATION AND CHARACTERISATION

3.2.1 Growth of DBT-doped Ac crystals

Anthracene and DBT have been widely studied, both separately and as a host-dopant configuration, and many growth techniques have been developed. The one that best suited our needs is co-sublimation: DBT and anthracene are heated below their melting points, and the two vapours mix and crystallise on a collection plate. Co-sublimated crystals have been used in most of the recent studies on single-photon emission in DBT [90, 117, 126, 152].

Our crystals grow in a home-made co-sublimation oven [116, 121]. The main chamber is composed of a cylindrical stainless-steel mount, that is evacuated and filled with nitrogen. The temperature of the chamber is controlled by a tape heater wrapped around it, with layers of fibreglass wool and aluminium foil to provide thermal insulation. Inside the oven there are two aluminium crucibles, one containing the anthracene and the other the DBT molecules. To ensure good temperature control each is actively stabilised. A first coarse control is provided by cartridge heaters, that bring the temperature within 3 °C of the desired value. A thermoelectric component provides the final and finer adjustment of the temperature, with a precision up to 0.1 °C. The cartridge and the thermoelectric heaters are thermally linked to each other and to the crucible using a high temperature paste and are monitored by resistance thermometers. The top cover of the oven is the copper collection plate. Its temperature is controlled in the same manner as the two crucibles, but as it needs to be at a lower temperature an additional cooling is supplied by water, connected through copper piping to the top of the cartridge.

A standard growth takes about 4.5 hours [116]. The crucible of DBT is filled with 1 ml of a 1 mMol solution of DBT molecules[6] in toluene, that lasts for multiple growths. The anthracene crucible is filled with 1 g of Ac powder[7], that is replaced after every growth. The oven is then pumped and purged with nitrogen four times, and finally left with a nitrogen atmosphere at 225 mbar. The exclusion of oxygen from the environment minimises the probability of photobleaching for the DBT molecules, as explained in section 1.4. The heater tape is then turned on, bringing the walls to 160 °C; this is essential to avoid growing crystals on the side walls. At the same time the copper collection plate is brought to 102 °C.

[6] 17.8,15.16-dibenzoterrylene supplied by the Institute for PAH-Research, Greifenberg, Bavaria

[7] CAS: 120.12.7, > 99% purity, Aldrich.

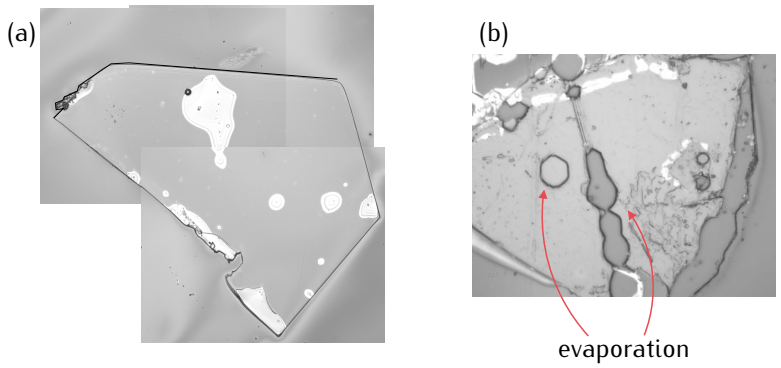


Figure 3.5 Crystal of Ac from cosublimation. (a) Half of the hexagon is clearly visible. (b) An improperly covered crystal. Considerable portions of the crystals have already evaporated, leaving holes that present the same hexagonal shape as the crystals themselves.

After an hour of stabilisation, the temperature controls of the crucibles are turned on. The Ac crucible is brought to 130 °C, while the DBT crucible can be adjusted between 130 °C and 200 °C to control the concentration of molecules in the Ac crystal. In the following 2 hours crystals start growing on the top collection plate. After this time the cartridges of the two crucibles are turned off, and when their temperatures equal that of the collection plate everything is shut down, to allow a uniform cooling of the entire oven back to room temperature.

Each growth yields tens of thin anthracene crystals that hang from the top collection plate from one of the vertices of their hexagonal shape, and are typically a few mm across. A typical example is shown in figure 3.5(a). A crystal is collected with tweezers, and then placed on a glass cover slip or silicon substrate for optical analysis. The Ac crystal is held together by weak Van der Waals forces, and quickly sublimes at room temperature if not protected, as illustrated in figure 3.5(b), so we spin coat a thin layer of polyvinyl alcohol (PVA). A solution of 4 m/m PVA (Aldritch) is heated to 80 °C for an hour to let it dissolve, and then stored in a fridge. For each crystal 20 µl of PVA were deposited on the sample, that is then spun at 6000 rpm for a minute. This creates a thin layer (~ 50 nm) of PVA that protects the crystal from sublimation.

3.2.2 Optical measurements

Our first task is to check at room temperature that there are DBT emitters at a useful concentration by making a raster scan of the confocal microscope with excitation at 785 nm, as shown in figure 3.6a. There we see about 40 bright spots in a region of about 100 square microns. This is enough for the current testing of the optical properties of single molecules. Next we need to confirm that the light is indeed scattered by DBT and not by contaminants or defects. We confirm this by looking at the polarisation of the scatterers, the saturation of their scattering rate, and the antibunching of their emission.

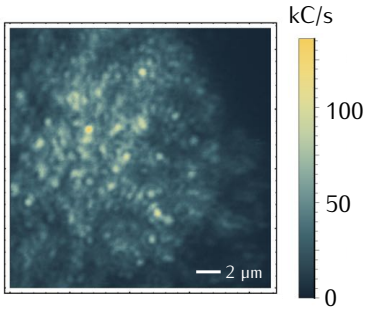
Polarimetry

As discussed in section 1.4, DBT molecules align along the b axis of an anthracene crystal, and this is also the direction of the optical transition dipole $\boldsymbol{\mu}$. Varying the polarisation of the excitation light changes the $\boldsymbol{\mu} \cdot \mathbf{E}$ term of the Rabi frequency, completely extinguishing the excitation when the two are perpendicular. This is not the normal behaviour of contaminant molecules or defects that may also scatter the light. Figure 3.6b shows two raster scans of a doped anthracene crystal, taken with linear polarisations of the excitation light that are 90° apart. Most of the bright spots become very dim as the angle between the molecular dipole and the laser light was increased. The residual light was probably due to imperfect linear polarisation of the excitation light. Another possibility are clusters of DBT molecules that were not well included in the Ac crystal and therefore showed a different response to polarisation.

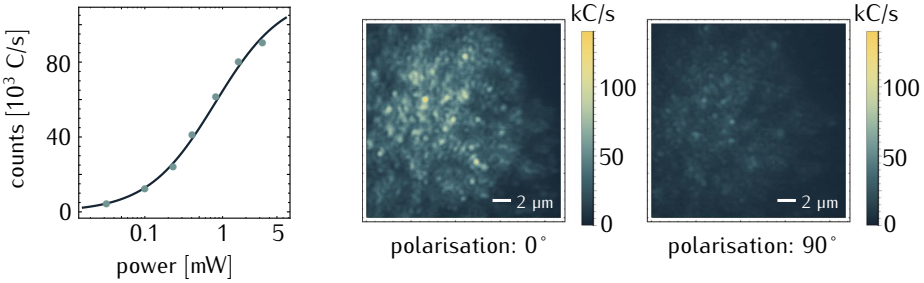
Saturation

As expressed in eqs. (2–3) and (2–22), the probability of populating the excited state of the molecule eventually saturates with increasing power. This is a consequence of the non-linear nature of a two-level system. If we look back at the expression of the saturation intensity of eq. (2–5), we can estimate a rough value for I_{sat}. Considering a radiative lifetime $1/\Gamma_1$ of a few nanoseconds [91, 94, 121, 126], and a typical dipole moment for a dye molecule of a few debye [126], then

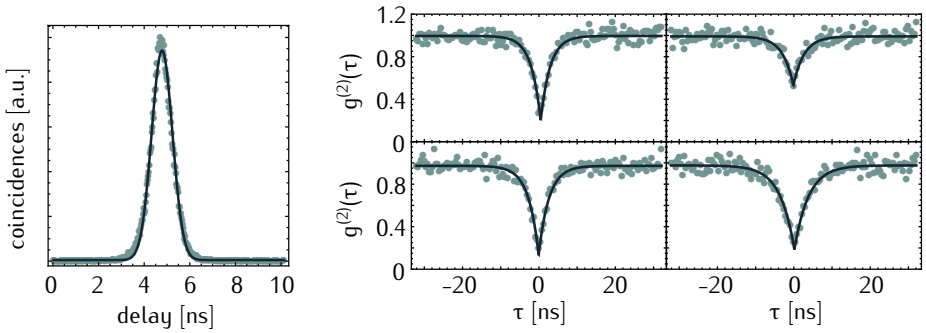
$$\frac{I_{sat}}{\Gamma_2} = \frac{\varepsilon \varepsilon_0 c \hbar^2}{\mu_{12}^2} \frac{\Gamma_1}{2} \approx 10^{-8}\,\mathrm{W/cm^2/Hz} \tag{3–4}$$



(a) Example of a confocal scan of a co-sublimated crystal of Ac, showing about 40 individual DBT molecules. The edge of the crystal is visible in the top right corner.



(b) Test of single photon emission. The panel on the left shows a saturation trace for a single molecule. The scans on the right are taken with the polarisation light 90° apart. As the DBT molecules are all aligned along the same crystallographic axis, as the excitation polarisation is changed the emission rate is modulated.



(c) Left: instrumental timing resolution, using 250 ps - wide pulses of the Picoquant laser. Right: antibunching measurements of 4 different molecules, notice the top right that is actually two molecules.

Figure 3.6 Optical properties of single DBT molecules at room temperature.

This means that, considering the room temperature spectrum of DBT of ~ 10 THz [91], at room temperature $I_{sat} \approx 10^6$ W/cm^2. For a Gaussian beam of spot size w_0 the maximum intensity is given by

$$I = \frac{2P}{\pi w_0^2}. \tag{3–5}$$

Then, with our spot size of 467 nm, saturation is reached with an incident power of $P_{sat} \approx 10^{-2}$ W. If we take into account additional losses due to optical elements, like beam splitters, filters, polarisers or the windows of the cryostation, then a significantly higher laser power is needed at the output of the optical fibre.

At such high power, the emission from the molecule is mixed with a high background, coming from scattered laser light and emission from the substrate. It is therefore necessary to measure this background, that shows a linear behaviour. This background can then be added to eq. (2–6), giving the formula:

$$R_{exp}(I) = a\frac{S}{S+1} + b\,I \tag{3–6}$$

for the detected emission rate, with $S = I/I_{sat}$ as before. The additional term $b\,I$ is the linear background contribution to the total count rate, and b is taken from the linear fit of the background. A saturation trace of a single molecule (where the background is already subtracted), is shown in the left panel of figure 3.6b. The saturation of the collected fluorescence identifies the emitter as a two-level system. We measured typical values for I_{sat} of $\sim 2 \cdot 10^5$ W/cm^2 and maximum count rates in the order of ~ 100 kC/s.

It is worth noticing that from this saturation data one could extract the total collection efficiency of the apparatus. The parameter a gives the maximum count rate in collection. By comparing it with the expression given in eq. (2–6), we see that the ratio $2a/\Gamma_1$ is equal to the total collection efficiency η of the setup[8]. We will see later in this section and in the next one how Γ_1 can be determined. For the moment, considering the reported values of $1/\Gamma_1$ of a few ns [91, 94, 126], by considering the detector efficiencies, losses due to optical elements and filters, we estimate a maximum value of collection efficiency of $\eta \leqslant 10^{-3}$.

[8] It is important to remember that η is highly affected by the filters used in collection, especially in the case of molecules at cryogenic temperatures. Moreover, at room temperature it can change with the excitation wavelength. Cf. appendix A.1 for a complete analysis.

Antibunching

After saturation and polarisation analysis most false positives are usually identified. However, some contaminants or impurities could still show polarisation dependent emission as well as saturation. The final test is to check the photon statistics of the emitted radiation, and confirm that it is a stream of single photon. This means measuring the second order correlation function $g^{(2)}(\tau)$ introduced in section 2.1.3, in an antibunching measurement accomplished with the setup of figure 3.1. The fluorescence from the microscope, separated from the pump, is coupled into a fibre beam splitter, and the two outputs are monitored with APDs[9]. The signal from the detectors is sent to a time-correlator (PicoQuant TimeHarp 260), that monitors the arrival times of pulses in the two channels.

One detector, the *start*, sets the clock in motion, while the other, called *sync*, gives the timing reference and stops the clock. It is then possible to build a histogram $C(\tau)$ of the lengths of the time intervals between detection events. When the time τ between two detection events exactly matches the path difference between the two channels, then the histogram should show a dip in case of a single photon emitter because it is impossible for one photon to be detected simultaneously on two different paths.

The histogram $C(\tau)$ is then proportional to the joint probability $p_{next}(\tau) = p(\tau|0)$ of detecting a photon at time $t = \tau$, given that the previous one was detected at time $t = 0$. $C(\tau)$ is equivalent to $g^{(2)}(\tau)$ in the case of low count rates on both channels [54]. In fact, $g^{(2)}(\tau)$ is proportional to the probability $p(t+\tau|t)$ of detecting a photon at time $t+\tau$ given that a photon, not necessarily the previous one, was detected at time t. The histogram $C(\tau)$ can be normalised to long times, so that it oscillates around 1 away from the antibunching dip, and then it can be fitted with the appropriate $g^{(2)}(\tau)$.

Because the photon stream is split between two detectors, the antibunching dip can be seen even when it is narrower than the dead-time of the detectors [153]. However, the jitter in the timing of the TTL pulse from the APD after the detection of a photon can compromise the dip significantly. To this purpose, we set out to measure the time-jitter of our setup. Using as excitation the pulsed diode laser, heavily attenuated, we removed the long-pass filter and collected the scattered light from the sample, measuring $C(\tau)$. The result is shown in the left panel of figure 3.6c. While ideally $C(\tau)$ would be a delta function for this case, due

[9] Of course, $g^{(2)}(\tau)$ could be measured using only one number-resolving detector, with a negligible electronic response time and detection efficiency close to unity.

to the time jitter of the detectors it can be fitted by a Gaussian. For our case, we measured a variance of 455 ns. This Gaussian is then used to convolve $g^{(2)}(\tau)$, before fitting to experimental data. The recorded histogram $C(\tau)$ is convolved with the instrument response function of the combined *BS-APDs-TimeCorrelator* setup. The sharp exponential rise of the antibunching function is smoothed by the convolution, and $g^{(2)}(0)$ rises above 0. This is particularly evident for $g^{(2)}(\tau)$ in case of large dephasing, or for the blue pumping presented in eq. (2–24).

We then proceeded to measure $g^{(2)}(\tau)$ for several emitters in the crystal, to check whether they were single molecules. Figure 3.6c reports antibunching plots for four of them. The dip on the top right only goes down to $g^{(2)}(0) \approx 1/2$, suggesting, through eq. (2–15), that this emitter is made up of two molecules. Since these measurements were carried out at room temperature, and therefore with large values of dephasing, a single exponential rise is visible, confirming the prediction of figure 2.4b for high values of Γ_2/Γ_1.

The other dips in figure 3.6c, despite being lower than the 0.5 threshold for single photon emitters, do not go down to zero at $\tau = 0$. The detector response contributes to this, but another effect has to be taken into account, that is the presence of background photons in the detection channels. These can come from unfiltered scattering from the laser, background from the medium surrounding the single emitter or from the detector dark counts. For the case of silicon APDs, the latter can be disregarded. However, our imperfect signal-to-background ratio can be an issue for solid state single photon emitters. When calculating the effect on $g^{(2)}(0)$ of accidental counts, we have to consider two contributions [67, 154]. The first is an accidental correlation between background counts, whose probability is the square of the probability of detecting a single background photon. This is given by $P_{bg} = R_{bg}/(R_{bg} + R_{sig})$, where R_{bg} is the background count rate, and R_{sig} is the signal count rate. Secondly, correlations between accidentals and signal photons must also be taken into account. In a similar fashion, these are given by the product of P_{bg} with the probability $P_{sig} = R_{sig}/(R_{bg} + R_{sig})$ of detecting a signal photon. The adjusted value for the $g^{(2)}(0)$ is then given by

$$g^{(2)}(0) = P_{bg}^2 + 2P_{bg}P_{sig} = \frac{R_{bg}^2}{(R_{bg} + R_{sig})^2} + 2\frac{R_{bg}R_{sig}}{(R_{bg} + R_{sig})^2}. \qquad (3\text{–}7)$$

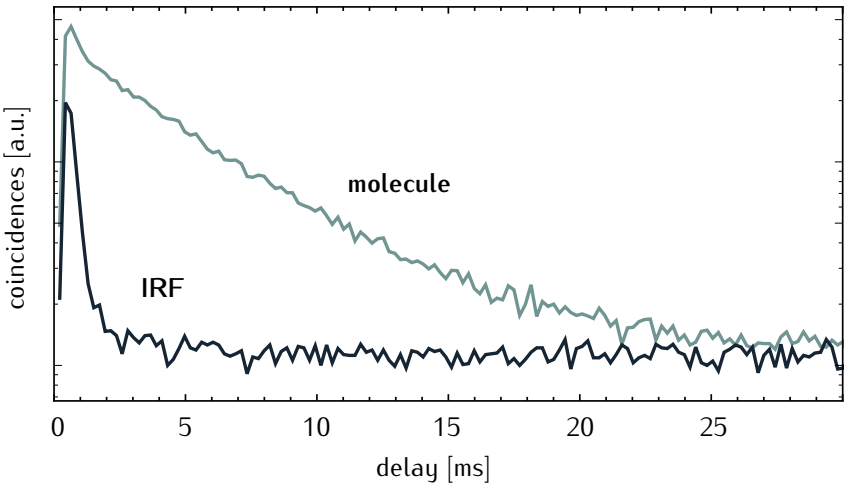


Figure 3.7 Example of a TCSPC measurement. The delay represents the time of arrival of single photons with respect to the 150 ps excitation laser pulse. The instrumental response function (IRF), measured using scattered laser light, is shown in black.

It is then important to record the count rates of both detection channels, as well as the background level. This can have a major contribution in case of room temperature antibunching measurements[10].

Time-Correlated Single Photon Counting measurement

The final characterisation of a single DBT molecule is to measure directly the lifetime of the excited state $S_{1,0}$. We know that the probability of spontaneous emission from $S_{1,0}$ to $S_{0,0}$ follows an exponential decay $\propto e^{-\Gamma_1 t}$. Therefore, by making a histogram of the emission times following a pulsed excitation it is possible to reconstruct this profile and determine Γ_1.

For this excitation we make use of the pulsed diode laser. Our diode laser has a pulse length of 150 ps, that is considerably shorter than the lifetime of the excited state. A molecule excited by this laser is subject to an almost instantaneous transfer to the excited state. Moreover, the laser repetition rate naturally provides the reference signal from which to start measuring the time of arrivals of the emitted photons.

The setup is similar to the one used for measuring the second-order correlation function. This time the *sync* signal is provided by the laser, while the fluorescence from the molecule is entirely used for the *start* channel. The time-correlator then builds the usual histogram $C(\tau)$, this time measuring the difference in time of arrival between the laser refer-

[10] While this contribution is almost negligible in this case, it will be crucial in the next chapter.

ence signal and the first APD pulse. $C(\tau)$ then exhibits the exponential decay due to spontaneous emission.

This procedure, called Time-Correlated Single Photon Counting (TCSPC), is a much faster way to determine the lifetime than measuring $g^{(2)}(\tau)$, as it does not require a coincidence count between two detectors. Here too, though, it is necessary to account for the instrumental response.

We measure this function by performing a TCSPC measurement on a portion of the sample that does not contain any fluorophores, but does scatter some light. That response is then convolved with the exponential decay of spontaneous emission, and used for fitting $C(\tau)$. In figure 3.7 we report a typical TCSPC measurement for a single DBT molecule. The signal from the molecule, after the background signal is subtracted, shows the expected linear behaviour on a semi-logarithmic scale, for times long compared with the response time. We have measured lifetimes between 2.8 and 5.2 ns, matching previous measurements in similar crystals [121, 126].

3.3 CRYOGENIC REGIME

Bright emission spots in the crystals of anthracene grown with the co-sublimation technique presented all the optical signatures of single DBT molecules at room temperature, as presented in the last section. Satisfied that these were indeed single emitters of DBT, we then cooled them to the base temperature of the cryostation (~ 4 K), to perform further study of resonance fluorescence and coherent control.

3.3.1 Spectroscopy

When the molecules are cold, the scattering resonance of a single DBT is only $30 - 40$ MHz wide, whereas the range of local field shifts is many tens of GHz. This makes it challenging to find molecules by their fluorescence when there are only a few tens of molecules in the field of view, as we normally choose to have.

Figure 3.8a shows 3 raster scans of a crystal of Ac. The panel on the left is a scan at room temperature, similar to figure 3.6a, where many bright spots can be identified. As the temperature is lowered and finally reaches the ~ 4 K conditions, barely a a single molecule is visible because the lines are now so narrow. In the scan on the right, the molecules have been recovered by moving the excitation wavelength to the blue, so that the scattering resonances are broadened by the fast relaxation from $S_{1,\nu}$ to $S_{1,0}$.

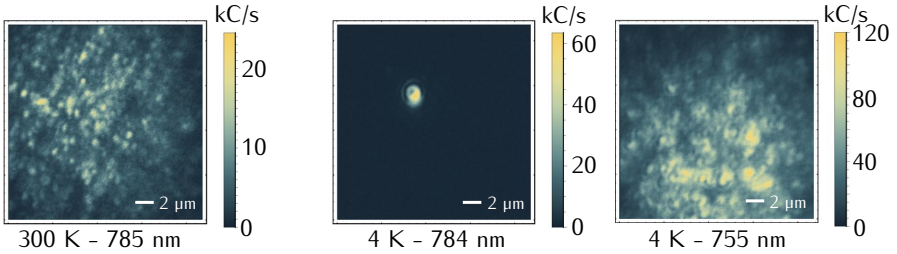
To find the centre of the inhomogeneous distribution of the ZPL, the sample was cooled to a temperature of ~ 50 K. I performed a series of raster scans on the same crystal region, changing the laser frequency after each acquisition. The total amount of counts collected in each scan was plotted against the laser frequency, and fitted to a Gaussian, obtaining a standard deviation of $93(1)$ GHz, and a central value of 784 nm (382.388 THz). This is more than a nanometer away from the values reported in literature, a shift of about 10^5 the linewidth of a cold DBT molecule, and this shift is expected to increase as the temperature is lowered. It is clear then how important it is to track the ZPL at different temperatures[11].

Having found the new centre of the inhomogeneous broadening, the sample was brought to base temperature. The same measurements were repeated, this time with a higher frequency resolution and at a high laser

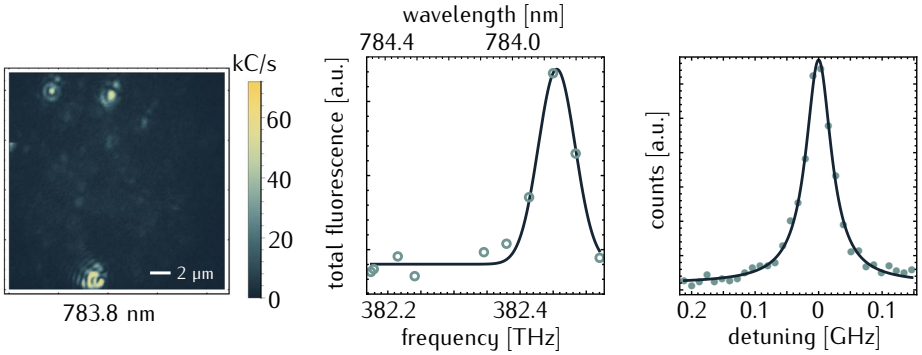
[11] We recently performed a similar analysis on a different crystal with a higher thickness, and found a central value of 784.68 nm (381.94 THz) with a FWHM of 200 GHz, at a temperature of 10 K.

power (expected saturation parameter $S \approx 30$). In this way the absorption spectra of the molecules were considerably power broadened (see eq. (2–7)), making them easier to see, as shown on the left of figure 3.8b. Again, I measured the total fluorescence from the sample as a function of excitation frequency, as plotted in the centre panel of figure 3.8b. This is centred at 783.86(1) nm (382.455 THz), with a standard deviation of 27.8(2) GHz, obtained from a Gaussian fit. The right hand panel of figure 3.8b shows the resonant scan of a single DBT molecule, at 4 K. The width of this line is only 50(2) MHz, corresponding to the natural linewidth due to the radiative lifetime. This was a crucial result, that validated our efforts in sample fabrication and mount design. The lifetime limit, as we have seen in chapter 1, is a fundamental requirement for a single photon source, and with this measurement we proved the quality of our system.

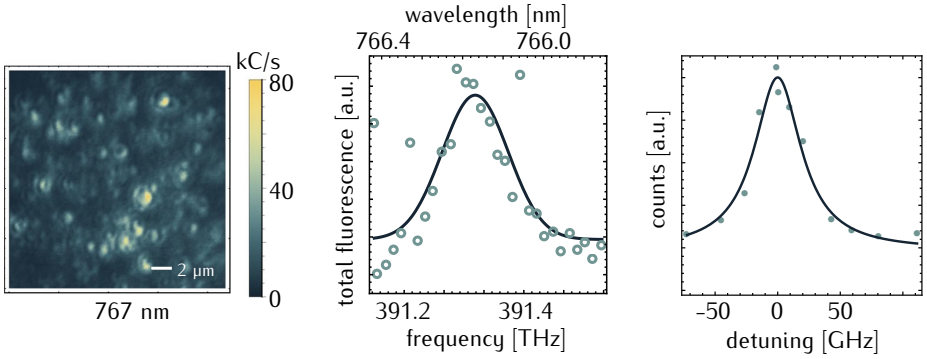
In a similar fashion, we set out to measure the absorption spectra and the distribution of the $S_{0,0} \rightarrow S_{1,3}$ transition. I took a series of raster scan of the sample, this time using the 767 nm diode laser, as shown on the left of figure 3.8c. As on the right of figure 3.8a, many molecules are seen because of the broad scattering resonance. By plotting the total collected counts against the laser frequency, I map out the inhomogeneous distribution of the $S_{0,0} \rightarrow S_{1,3}$ transition in the centre of figure 3.8c. This is consistent with a Gaussian, having a central value of 766.16(1) nm (391.289 THz) and standard deviation $\sigma = 41(1)$ GHz. The central value of the distribution is comparable with the literature values [90]. The additional noise in the plot is due to the appearance of bright emitters, that are likely to be single DBT molecules with blue-detuned ZPLs. The right hand panel of figure 3.8c shows the scattering resonance line for a single molecule. This shows the wide resonance width (40 GHz) which results from the fast relaxation (~ 4 ps) of the $S_{1,3}$ state.



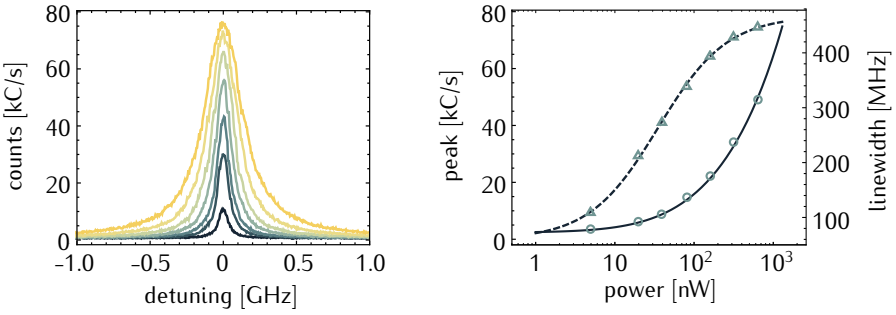
(a) Three raster scans, taken at room temperature (left), and at 4 K, with excitation light at 784 nm (centre) and 755 nm (right)



(b) Analysis of the inhomogeneous broadening for the $S_{0,0} \rightarrow S_{1,0}$ transition at 4 K. Left: high power raster scan at 783.8 nm (383 THz). Centre: total fluorescence collected as a function of excitation frequency. Right: resonant scan of the ZPL of a single DBT molecule.



(c) Analysis of the inhomogeneous broadening for the $S_{0,0} \rightarrow S_{1,3}$ transition. Left: raster scan. Centre: total fluorescence collected as a function of excitation frequency. Right: resonant scan of the $S_{0,0} \rightarrow S_{1,3}$ line of a single molecule.



(d) Effect of power on the linewidth of a single emitter. Left: resonant scans of a single molecule, taken for increasing excitation power incident on the vacuum window. Right: width (FWHM, circles) and peak scattering rate (triangles), versus power.

Figure 3.8 Optical properties of a DBT molecule below 4 K.

3.3.2 Saturation and power broadening

Next we investigated the ZPL scattering resonance of a single molecule in more detail. The panel on the left of figure 3.8d shows a set of resonance lines taken over a range of light intensities. These lines fit so perfectly to the Lorentzian form that the fits are not shown - they lie exactly on top of the data. We began by looking at the width of the resonance, which according to eq. (2–7) is

$$\Delta\nu(I) = \Delta\nu(0)\sqrt{1 + I/I_{sat}} \tag{3–8}$$

where $\Delta\nu(I)$ is the width of the line at intensity I, and $\Delta\nu(0)$ is the width at low intensity. The circles in the panel on the right of figure 3.8d show the widths versus the laser power incident on the vacuum window, and the line is the fit to eq. (3–8). For this particular molecule, the fit gave a saturation power of $P_{sat} = 34.6(5)$ nW. Looking at ten different molecules we obtained values in the range $30 - 50$ nW.

By inserting a power meter right underneath the microscope objective and comparing the power there with the power incident on the vacuum window, I managed to measure a total transmission of $\sim 60\%$. Taking the transmission and the spot size of 467 nm, I determined that the saturation intensity I_{sat} incident on the surface of the anthracene is $6.07(7)$ W/cm^2. Measurements on other molecules gave a range of I_{sat} of $5 - 9$ W/cm^2.

Next, we turned to the peak scattering rates, which are plotted by the triangles in the right hand panel of figure 3.8d. These should follow the form $S/(1+S)$ given in eq. (2–6), and the line in the figure shows the fit to this form. There is no need to allow for a background here (as I did in eq. (3–6)) because the excitation intensity is much lower in this cryogenic case. This particular curve gave $I_{sat} = 6.16(7)$ W/cm^2, consistent with our conclusion from the analysis of the widths. We can see that the two methods are equally sensitive, but note also that there is an additional calibration uncertainty in both, due to the conversion from power (outside the cryostat) to intensity (incident on the anthracene), which is of order 10%.

Turning to the saturation of the $S_{0,0} \rightarrow S_{1,3}$ transition, this line is too wide to be scanned with the diode laser, so I just looked at saturation of the scattering rate. The fluorescence from the molecule was collected with the APD, and averaged over a few second. This was repeated at increasing excitation power, and the result fitted to eq. (2–6). A value of $\sim 10(1)$ kW/cm^2 was obtained for a single molecule, in good agreement with eq. (3–4) considering the ~ 40 GHz linewidth of the transition.

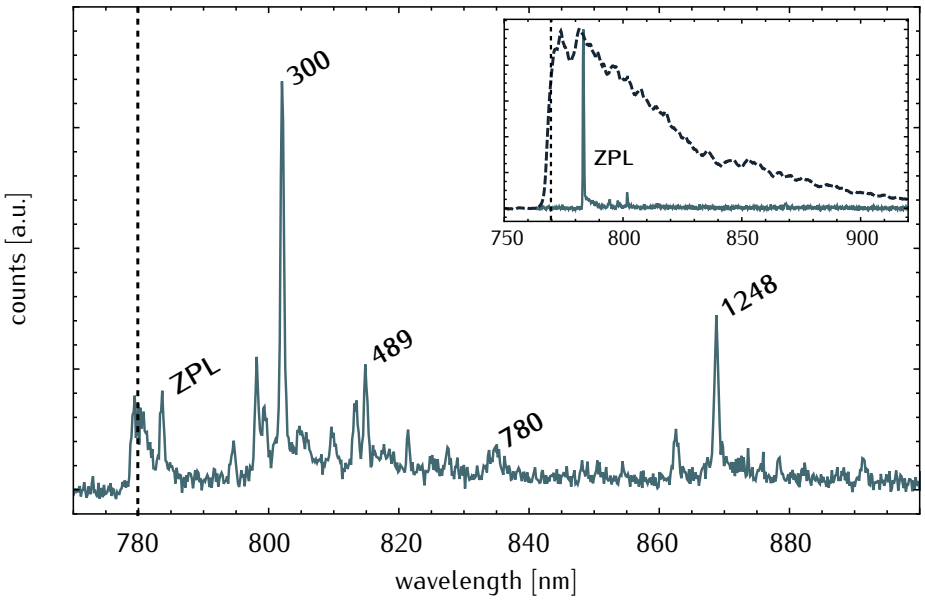


Figure 3.9 Fluorescence spectrum of a single DBT molecule. The main plot shows the single lines due to emission to the vibrational manifold of the molecular ground state: the number is the distance from the ZPL in cm^{-1}. The dashed line represents the filter edge. The inset spectrum on the right shows the ZPL, not blocked by the filter on this case. Dashed is a room temperature fluorescence spectrum for a single DBT molecule in Ac, for comparison.

3.3.3 Emission Spectrum

Finally, I set out to measure the fluorescence spectrum of a single DBT molecule. At first I excited the molecule resonantly on the $S_{0,0} \rightarrow S_{1,3}$ transition, and collected the red-shifted fluorescence though a 780 nm long-pass filter. This was then sent to a spectrometer. The spectrum, shown in figure 3.9 showed all the expected emission lines for DBT in anthracene, as reported by Nicolet et al. [126]. Confirming previous results, the strongest vibrational emission line is the one to $S_{0,3}$, mirroring the $S_{0,0} \rightarrow S_{1,3}$ transition. This is marked in the figure with its separation from the ZPL, in cm^{-1}. Other strong emission lines are marked in the figure. These correspond to transitions to $S_{0,6}$ (the transition excited by the pulsed 755 nm laser), $S_{0,12}$ and $S_{0,17}$.

After this measurement I excited the same molecule, this time filtering the fluorescence with a 770 nm long-pass filter, allowing the ZPL to pass. The new spectrum, shown in the inset of figure 3.9, shows clearly the bright peak of the ZPL. By integrating the spectrum over the ZPL, and comparing it with the rest of the emission, I calculated that the branch-

ing ratio for this particular molecule to radiate on the ZPL is ~ 50%, a promising value for single-photon generation.

3.3.4 Triplet state

I have so far excluded the triplet state from my analysis because Γ_{isc} has an upper bound of $10^{-7}\,\Gamma_1$. However, we are very interested in working with the triplet, because it could provide a powerful additional degree of freedom. Due its long lifetime, photons could be stored in the triplet state for several microseconds. Manipulation of the spin of the triplet could add a new dimension to the possible uses of DBT in quantum information and communication protocols, such as quantum memory, or entanglement swapping [74, 155].

The triplet state lies below $S_{1,0}$ and with a branching ratio of ~ 10^{-7} the excited molecule will decay to the triplet, causing dark periods in the fluorescence. We have seen in figure 2.5 that this makes a small modification to the $g^{(2)}(\tau)$. Here I measure that effect to determine the lifetime of the triplet.

For values of $\tau \gg 1/\Gamma_1$ the histogram $C(\tau)$ approaches zero. This is because, in the case of low count rates, the time between the detection of two consecutive photons follows a Poissonian statistic. The molecule is excited with a probability $\frac{1}{2}\frac{S}{S+1}$ given by eq. (2–3b). This factor multiplies the spontaneous emission rate Γ_1, giving the photon emission rate R, that finally has to be multiplied by the collection efficiency η. Since η is very low (usually $\eta \leqslant 10^{-3}$), most photons are lost and not detected. Therefore the detection events are uncorrelated from each other, and follow a Poissonian statistics, with time constant given by $\Gamma_\eta = \frac{S}{S+1}\frac{\Gamma_1}{2}\eta$.

The presence of a triplet state alters this behaviour. When a molecule transits to the triplet state it has to wait a time of the order of $1/\Gamma_T$ before another photon can be emitted. This increases the average time between two consecutive photons and superimposes another exponential decay due to the triplet state emission on top of the decay due to Γ_1.

Figure 3.10 presents an antibunching measurement with long detection times to show this effect. A single molecule was excited resonantly at a temperature of 3.5 K, and with a power corresponding to $S = 10$. Correlations over the difference in time of arrival of consecutively detected photons were analysed, measuring delays up to 1 ms. Two exponential decays are clearly visible. The data is fitted with a function of the form

$$f(t) = a\,e^{-\Gamma_\eta t} + b\,e^{-\Gamma_T t} + c. \tag{3–9}$$

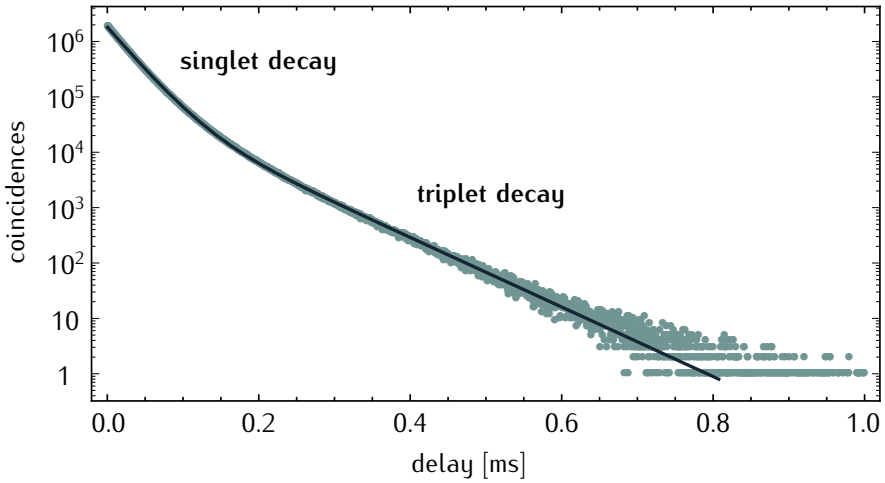


Figure 3.10 Histogram $C(\tau)$ for a single DBT molecules. The analysis at long times reveals the presence of two different exponential decays, due to the collection efficiency and to the presence of the triplet state of the molecule.

From this fit I estimated a triplet state lifetime $1/\Gamma_T$ of 68(1) µs. This disagrees with the value of 1.5 µs reported by Toninelli et al. [91], but agrees well with the range $40 - 200$ µs reported by Nicolet et al. [126].

3.4 COHERENT CONTROL

At this point, we wanted to test the effect of controlled, temperature-induced dephasing on the second-order correlation function of a single molecule[12]. Temperature-induced dephasing is an important phenomenon in single photon emission. It can limit the indistinguishability of the source by broadening its spectrum beyond the lifetime limit.

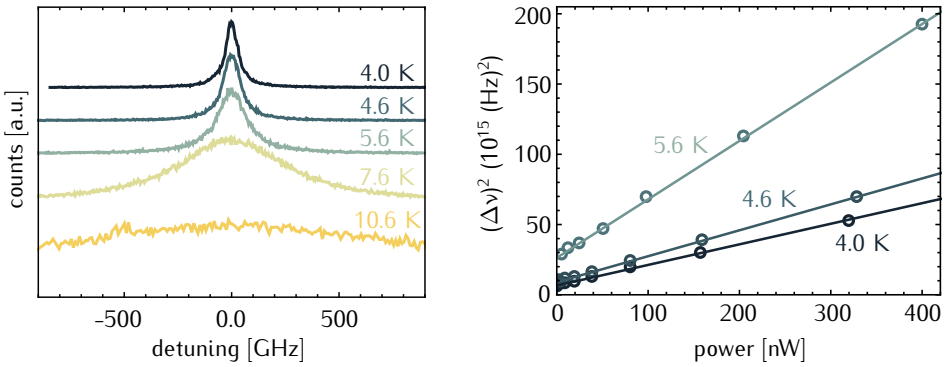
3.4.1 Temperature-induced dephasing

I started by selecting a single DBT molecule, dubbed "Artemis". I performed the spectroscopic analysis described before, collecting its fluorescence as I scanned the excitation light across its ZPL, and repeating the process for different powers. We were thus able to extract a natural linewidth $\Delta\nu(0)$ of 80.9(2) MHz, slightly on the red side of the inhomogeneous broadening. The saturation intensity was 7.8(1) W/cm^2, corresponding to 44 nW of power incident on the vacuum window of the cryostat.

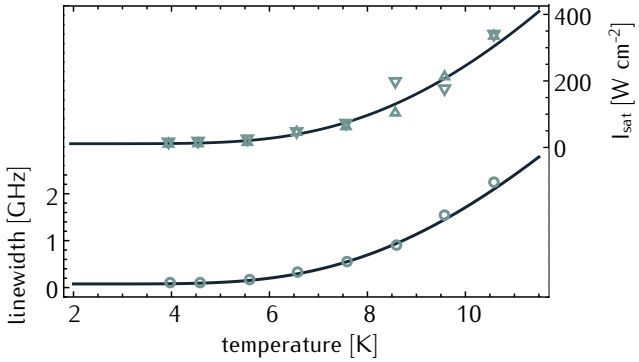
We then used heaters placed in the platform of the cryostation, right underneath the attocube, to control the temperature of the sample. This is more efficient than controlling the rate at which the helium is evaporated on the cold finger. Heating the sample mount while leaving the rest of the parameters constant allowed for a quick change of the sample temperature that quickly stabilised. Most importantly, the relative distances between components in the cryostation remained unchanged, leaving no need to adjust the focus of the objective.

I scanned though the scattering resonance many times, while varying both the intensity of the light and the temperature of the sample. The left panel of figure 3.11a shows a set of scans, all taken at an intensity corresponding to $S \sim 0.1$, for a variety of temperatures. It is immediately clear that the linewidth increases with increasing temperature, rising from 80 MHz at 4 K to over 2 GHz at a temperature of 10.6 K. By plotting the linewidth as a function of excitation intensity, as shown in the right panel of figure 3.11a, and fitting to eq. (3–8), I was able to determine the zero-power linewidth as a function of temperature, plotted in figure 3.11b. This data can be used to provide information about the dephasing of the DBT molecules in anthracene [156, 157].

[12] This work has been partially published in Physical Review A [125].



(a) Resonant scan of a single DBT molecule, for different temperatures. The left panel highlights the temperature-induced broadening of the ZPL. The right panel reports the power-broadening effect on the same molecule, for different temperatures.



(b) Effect of temperature on $\Delta\nu$ (circles) and I_{sat} (triangles). Values for I_{sat} are derived from the power broadening of the line (upright triangles) and from the saturation of the fluorescence rate (inverted triangles). The error bars on each point are smaller than the point size.

Figure 3.11 Single molecule spectroscopy with controlled, temperature-induced dephasing.

A theory of such thermal line broadening is presented by Hesselink and Wiersma [157], who propose dephasing by phonons and suggest an Arrhenius law

$$\Delta\nu(T) = \Delta\nu(0) + a\, e^{-\frac{T_0}{T}} \tag{3–10}$$

where T_0 is the activation temperature of the phonons responsible for the dephasing. On fitting the data of figure 3.11b to this equation, I obtained the values $T_0 = 39(1)$ K and $\Delta\nu(0) = 77.6(2)$ MHz. The temperature dependence is well described by this formula, lending some credibility to the model of a single local phonon causing phase interruptions of the optical dipole. In figure 3.11b we see that the temperature-dependence of I_{sat} is very similar to that of $\Delta\nu$. Indeed, on fitting these data to the same form

$$I_{sat}(T) = I_{sat}(0) + a\, e^{-\frac{T_0}{T}}. \tag{3–11}$$

we find $T_0 = 41(3)$ K, which is consistent with the result from the widths. Since $I_{sat} \propto \Gamma_1\Gamma_2$, the common value of T_0 indicates that Γ_1 does not vary significantly over this temperature range and that the change in I_{sat} is just due to the increase in Γ_2 with temperature.

This value of activation temperature is consistent with the lower bound of 35 K reported by Nicolet et al. [124]. Expressing it in wavenumbers, $\nu_P = k_B T_0/hc$ we find $\nu_P = 27$ cm^{-1} (370 μm), about half the frequency of the surface phonon of the Ac crystal [158, 159]. This result is in good agreement with the theory of dephasing presented by Hesselink and Wiersma [157]. In their work, the authors studied the process of dephasing for pentacene molecules in various matrices. They suggested that, owing to the exponential increase of dephasing with temperature, a localised phonon state is present in the system. By spectroscopic analysis, they also suggested that the process of dephasing involved two quanta of the local phonon mode. At cryogenic temperatures, anthracene shows active phonon modes at 49 cm^{-1} and 56^{-1}, that could then take active part in the dephasing process.

3.4.2 $g^{(2)}$ and dephasing

We then investigated the second order correlation function $g^{(2)}(\tau)$ as a function of both saturation and dephasing. As we have seen in section 2.1.3, $g^{(2)}(\tau)$ provides a direct witness of the molecular dynamics dictated by eq. (2–11b). As the Rabi frequency increases, stimulated emission competes with spontaneous emission, and coherent oscillations appear in the population of the molecule, mirrored by oscillations in the fluorescence, as reported in figure 2.4a. This behaviour is perfectly displayed in my experimental data, reported in the left panel of figure 3.12. These are five $g^{(2)}(\tau)$ curves taken for increasing values of saturation, from ~ 0.5 to ~ 5, keeping "Artemis" at the base temperature of 4 K.

Next, I looked at the behaviour of the molecule for increasing values of temperature (and hence dephasing rate Γ_2). As the temperature is increased, we expect the Rabi oscillations to be quickly brought out of phase by the increased dephasing rate Γ_2, and the dynamics to shift to an incoherent regime. I increased the temperature of the molecule up to 10.6 K. At each temperature I measured the linewidth and the saturation intensity of the molecule. I then recorded $g^{(2)}(\tau)$ for saturation values $S \approx 5$. The results are reported in the right panel of figure 3.12. The behaviour again mirrors the expectation in figure 2.4b.

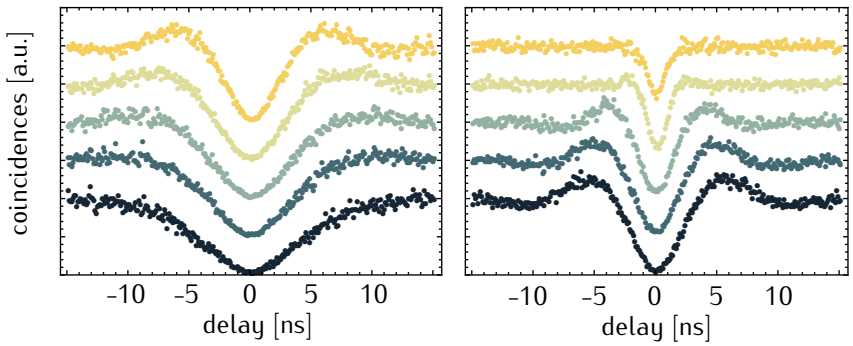


Figure 3.12 Two sets of $C(\tau)$ histograms, taken for increasing saturation and base temperature (left) and for fixed saturation and increasing temperature (right). Note the similarities with figs. 2.4a and 2.4b.

This complex behaviour is all contained in eq. (2–14), that we recall now:

$$\begin{aligned} g^{(2)}(\tau) &= 1 - \frac{p+q}{2q} e^{-(p-q)\tau} + \frac{p-q}{2q} e^{-(p+q)\tau} \\ p &= \frac{\Gamma_1 + \Gamma_2}{2} \\ q &= \sqrt{\frac{(\Gamma_1 - \Gamma_2)^2}{4} - \Omega_0^2}. \end{aligned} \tag{3–12}$$

We can now compare this equation with the experimental data. The only unknown parameter is the lifetime of this particular molecule. TCSPC would be a natural way to determine Γ_1, but our short-pulse laser at 755 nm also excited other, nearby molecules, as can be seen[13] in figure 3.8a. We therefore selected an antibunching curve and fitted with eq. (3–12), to measure Γ_1. That curve, shown in panel (b) of figure 3.13, gave $1/\Gamma_1 = 3.8(1)$ ns. As the saturation intensities and the zero-power linewidth at each temperature were already known, no additional parameter was needed. The remaining panels of figure 3.13 show 5 other antibunching curves, with the corresponding $g^{(2)}(\tau)$ in good agreement with the data. It is important to notice that the values of $g^{(2)}(0)$ reached the expected values for our signal-to-background ratio and for our instrument response function.

As a final remark, we can now use the newly found value of the population decay rate Γ_1 to have an estimate of the total collection efficiency η. From the saturation traces of section 3.3.2 we measured a high-power asymptote for the detected fluorescence rate of $\eta\,\Gamma_1/2 \sim 110$ kC/s (this

[13] Indeed the three scans presented in figure 3.8a were taken in the same region of the crystal.

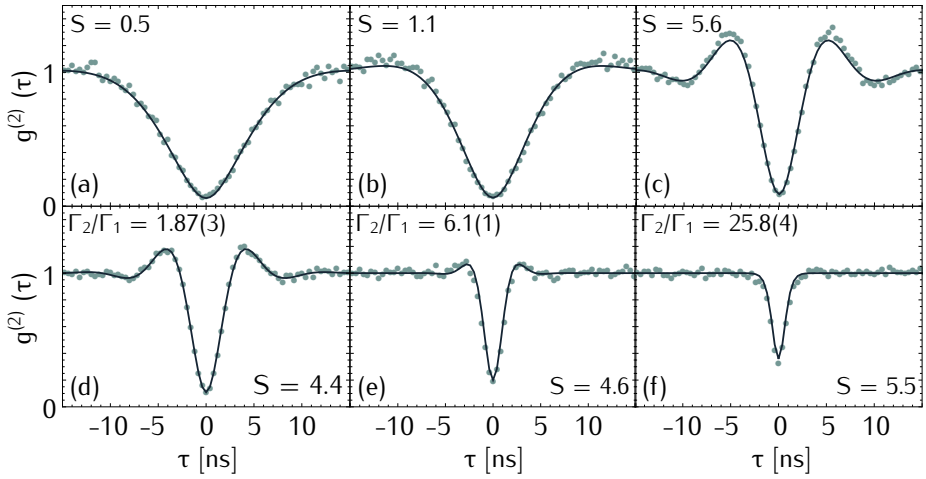


Figure 3.13 Resonance fluorescence of a single DBT molecule, at constant temperature and increasing excitation power (top row) and vice versa (bottom row). Values of saturation and dephasing were obtained with the data reported in fig. 3.11, while the lifetime $1/\Gamma_1$ was obtained with the data of panel (b). The rest of the panels present the relative $g^{(2)}(\tau)$ functions with no free parameters.

is fairly constant for all the temperatures, confirming that Γ_1 does not change with temperature, as surmised below eq. (3–11)). Comparing this with the 3.8 ns lifetime, we deduce that we detect a fraction $8.7(5) \cdot 10^{-4}$ of the emitted photons.

3.4.3 Literature comparison

The function $g^{(2)}(\tau)$ in eq. (3–12) that we have used to fit the data of figure 3.12 is valid for all values of saturation and dephasing. However, certain approximations, such as low excitation power or high levels of dephasing, can be made to fit particular experimental conditions and to obtain a simpler form of eq. (3–12).

Let us begin with the common case of lifetime-limited emitters. The rate of dephasing of the coherences is then half the decay rate of the excited state population, so that $\Gamma_2 = \Gamma_1/2$. Inserting this equality into eq. (3–12), and expressing the sum of exponentials as a sum of periodic functions, we obtain:

$$\lim_{\Gamma_2 \to \Gamma_1/2} g^{(2)}(\tau) = 1 - e^{-\frac{3\Gamma_1}{4}t}\left(\cos\left(q't\right) + \frac{3\Gamma_1}{4q'}\sin\left(q't\right)\right) \qquad (3\text{–}13)$$

where $q' = \sqrt{\frac{\Gamma_1^2}{16} - \Omega_0^2}$. This is the expression that was first introduced by Carmichael and Walls [136, eq. 6.5], and then used in the first experiments with atomic beams [138], single atoms [160] and stored ions [161].

This formula can be simplified even further if we consider the case of low saturation, with $\Omega \ll \Gamma_1$. Under this assumption, we have that

$$q' = \sqrt{\frac{\Gamma_1^2}{16} - \Omega_0^2} \to \frac{\Gamma_1}{4}\left(1 - \frac{8\Omega^2}{\Gamma_1^2}\right) \approx \frac{\Gamma_1}{4}. \tag{3–14}$$

If we now substitute this into eq. (3–12), again assuming $\Gamma_2 = \Gamma_1/2$, we obtain

$$\lim_{\substack{S\to 0 \\ \Gamma_2 \to \Gamma_1/2}} g^{(2)}(\tau) = \left(1 - e^{-\frac{\Gamma_1}{2}\tau}\right)^2, \tag{3–15}$$

an expression presented in the same work by Carmichael and Walls [136, eq. 6.7].

The previous expressions are all valid for the case of resonance fluorescence. However, many quantum emitters rely on pumping to a higher energy level. Excitation is usually followed by a rapid non-radiative relaxation to a lower state, from which the system decays back to the ground state and a photon is emitted. The timescale $1/\Gamma_2$ for the evolution of coherences is then much faster than $1/\Gamma_1$, the timescale for the evolution of the populations: the pumping is incoherent. This is the case we have seen in section 2.2.2 for single molecules, and it has been used for other systems as well [54, 162]. Starting again from q we see that

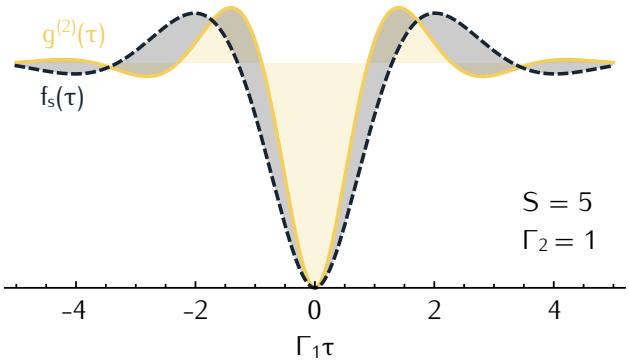
$$q = \sqrt{\frac{(\Gamma_1 - \Gamma_2)^2}{4} - \Omega_0^2} \longrightarrow \frac{\Gamma_2}{2} - \frac{\Gamma_1}{2}(1 + 2S) \tag{3–16}$$

when considering that $\Gamma_1/\Gamma_2 \ll 1$ and that $\Omega_0^2 = S\Gamma_1\Gamma_2$. By substituting this into eq. (2–12), we have the limits

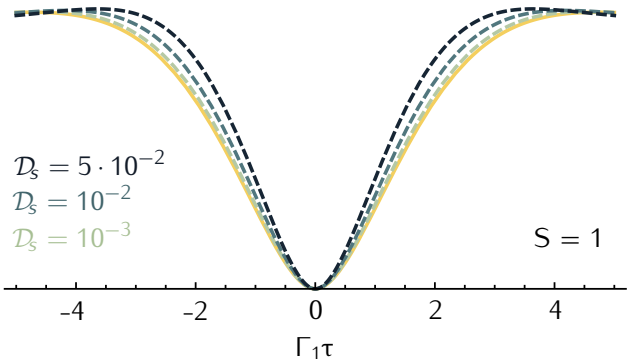
$$\begin{aligned} \lim_{\Gamma_1/\Gamma_2 \to 0} \frac{p - q}{2q} &= 0 \\ \lim_{\Gamma_1/\Gamma_2 \to 0} \frac{p + q}{2q} &= 1 \\ \lim_{\Gamma_1/\Gamma_2 \to 0} -(p + q) &= -(1 + S)\Gamma_1 \end{aligned} \tag{3–17}$$

that once inserted into eq. (3–12) gives

$$\lim_{\Gamma_2 \gg \{\Gamma_1, \Omega_0\}} g^{(2)}(\tau) = 1 - e^{-(1+S)\Gamma_1\tau} \tag{3–18}$$



(a) Graphic representation of function $\mathcal{D}_s$, comparing $g^{(2)}(\tau)$ (solid yellow) with one of its approximations (dashed dark blue). The numerator of eq. (3–19) is represented by the dark shaded area between the two functions. The denominator is the yellow shaded area, where $g^{(2)}(\tau)$ is different from 1. Level of saturation and dephasing are reported in the plot.



(b) Comparison between antibunching curves for $S = 1$ (dashed), with dephasing adjusted to reach values of $\mathcal{D}_s = 10^{-3}, 10^{-2}, 5 \cdot 10^{-2}$ with respect to the solid yellow curve.

Figure 3.14 Analysis of the function $\mathcal{D}_s$, for $f_s(\tau)$ with the form of eq. (3–13).

which has the same form of eq. (2–24). It is necessary to impose the additional condition that the dephasing rate is faster than the system dynamics to cancel out every coherence, and to obtain the single exponential rise.

As each of eqs. (3–13), (3–15) and (3–18) is valid under specific conditions of dephasing rate and saturation, let us consider the region in which each one can be used reliably. As a figure of merit we take the function:

$$\mathcal{D}_s\left(S, \frac{\Gamma_2}{\Gamma_1}\right) = \frac{\int_{-\infty}^{+\infty} d\tau \left[g^{(2)}(\tau) - f_s(\tau)\right]^2}{\int_{-\infty}^{+\infty} d\tau \left[1 - g^{(2)}(\tau)\right]^2} \tag{3–19}$$

The idea is illustrated in figure 3.14a, where the solid yellow line shows $g^{(2)}(\tau)$, the dashed blue line shows one of the approximate functions, the grey shaded area is then the numerator of $\mathcal{D}_s$, while the yellow shaded area is the denominator. We see that this comparison gives weight to approximate the regions where $g^{(2)}(\tau)$ differs from 1. The limit of valid-

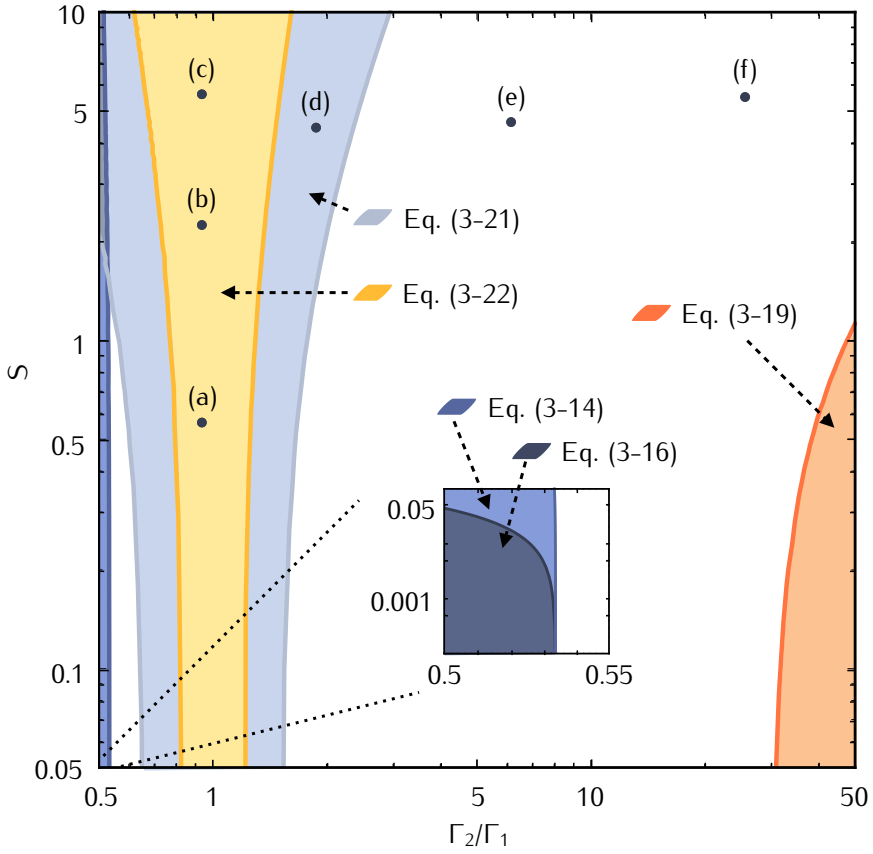


Figure 3.15 Areas in the parameter space of saturation S and dephasing Γ_2/Γ_1 where each of eqs. (3–13), (3–15), (3–18), (3–20) and (3–21) gives a reliable description of the system dynamics. The points (a)-(f) correspond to the measurements reported in figure 3.13.

ity of a function $f_s(\tau)$ was chosen to be $\mathcal{D}_s < 10^{-3}$. This is the limit under which $f_s(\tau)$ and $g^{(2)}(\tau)$ are virtually indistinguishable. An example is reported in figure 3.14b, that shows three curves for which $\mathcal{D}_s = 10^{-3}, 10^{-2}, 5 \cdot 10^{-2}$.

We used $\mathcal{D}_s$ to calculate the region of validity of the approximations presented before. Figure 3.15 presents the area where $\mathcal{D}_s < 10^{-3}$ for eqs. (3–13), (3–15) and (3–18) for a wide range of values of dephasing Γ_2/Γ_1 and saturation parameter S.

There is a slender region on the left where eq. (3–15) is reliable. Equation (3–13) works over an even smaller region, shown inset. On the right, at high Γ_2/Γ_1, eq. (3–18) becomes valid. At high power, this limit is pushed even further away.

Two additional regions in figure 3.15 show the ranges of reliability for two other expressions found in the literature. The yellow portion is re-

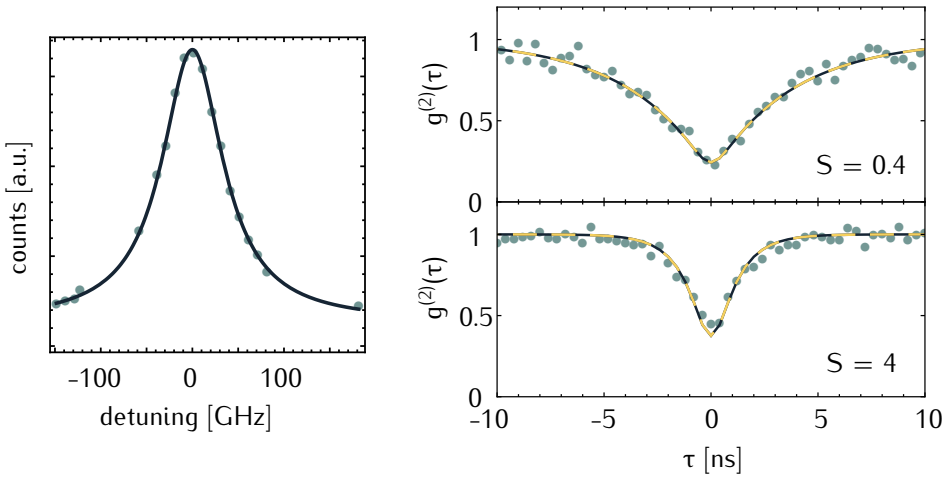


Figure 3.16 Resonance fluorescence for a single molecule at T ~ 30 K. Left: resonant scan of the ZPL is reported on the left (FWHM 45 GHz). Right: two antibunching measurements, showing the equivalence between eq. (3–12) (solid, dark) and eq. (3–18) (dashed yellow) at this temperature.

lated to the function presented by Batalov et al. [163, eq. (1)] for NV centres:

$$g^{(2)}_{\text{Batalov}}(\tau) = 1 - e^{\frac{\Gamma_1+\Gamma_2}{2}}\left[\cos(\Omega\tau) + \frac{\Gamma_1+\Gamma_2}{2\Omega}\sin(\Omega\tau)\right]. \tag{3–20}$$

This is another approximation of the full solution of the optical Bloch equations. A similar case is valid for the function presented by Flagg et al. [164, eq. (2)] for quantum dots:

$$g^{(2)}_{\text{Flagg}}(\tau) = 1 - e^{\frac{\Gamma_1+\Gamma_2}{2}}\left[\cos(q''\tau) + \frac{\Gamma_1+\Gamma_2}{2q''}\sin(q''\tau)\right] \tag{3–21}$$

with $q'' = \sqrt{\Omega_0^2 + (\Gamma_1 - \Gamma_2)^2}$. These two functions have the peculiar property of reducing to eq. (3–12) when $\Gamma_2 = \Gamma_1$. They are valid over a limited portion of the parameter space around this condition.

We have also highlighted the points corresponding to each of the panels of figure 3.13. For this particular molecule, points (a) to (c) can be described by eqs. (3–20) and (3–21). As the dephasing is increased, eq. (3–20) can be used to model point (d), but points (e) and (f) can only be described by the full solution in eq. (3–12). We think these two points are the first critical test of the optical Bloch equations in this intermediate condition between coherence and incoherence. The validity of eq. (3–13) has been tested on several systems. The transition to eq. (3–18) is much more interesting, and it has been the centrepiece of this first part of this

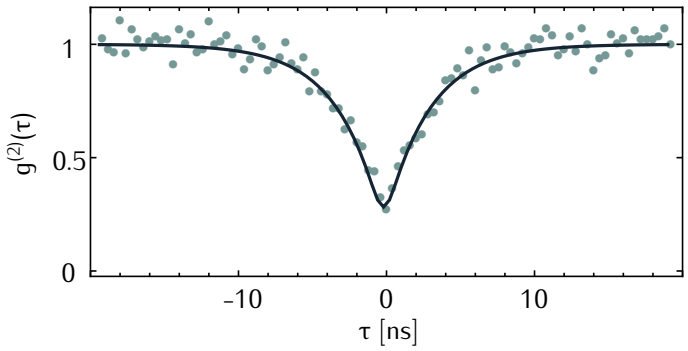


Figure 3.17 Resonant scan (left) and antibunching measurement (right) for a single DBT molecule, excited on the $S_{0,0} \rightarrow S_{1,3}$ line. The antibunching data were fitted with eq. (2–24), validating the rate-equations approach of section 2.2.2.

thesis. While looking at "Artemis" we managed to reach only a dephasing of $\Gamma_2/\Gamma_1 \approx 20$. As we have learned from figure 3.15 this is not enough to reach the area of validity of eq. (3–18). We couldn't achieve a higher dephasing for this molecule, due to presence of other DBT molecules in its proximity, whose spectrum overlapped with "Artemis" as the temperature was raised above 10 K.

I therefore raised the temperature to about $\sim$ 30 K, and looked for another single emitter. I performed the usual spectroscopy measurement on a new single emitter, a typical resonance line being shown on the left of figure 3.16. I found a zero-intensity linewidth $\Delta\nu = 81.0(1)$ GHz and a saturation intensity $I_{sat} = 4.2(2)$ kW/cm^2. As Γ_2/Γ_1 was of the order of $\sim 10^3$, we expect the high dephasing approximation to hold perfectly. To test this hypothesis I acquired $g^{(2)}(\tau)$ for 5 different levels of saturation, two of which are shown on the right hand side of figure 3.16. Again the only unknown parameter was Γ_1: to obtain it I used the least-square algorithm, comparing the 5 curves with eq. (3–12) with Γ_1 as the common parameter. I then used this value to plot eq. (3–18) on top of the data, shown as the dashed yellow line on the right of figure 3.16. It fits the data perfectly. I have also plotted eq. (3–12) as a solid line. The two curves are indistinguishable, proving the validity of the high-dephasing approximation.

In section 2.2.2 a similar expression for $g^{(2)}(\tau)$ was obtained for the case of blue-detuned pumping. The same single exponential has been used to fit the result of an antibunching measurement on a single DBT molecule, excited on the $S_{0,0} \rightarrow S_{1,3}$ line. The result is shown in figure 3.17. The molecule absorption spectrum, centred at 766.12 nm (391.312 THz), presents a Lorentzian profile with a linewidth $\Delta\nu = 45.4(6)$ GHz, in good

agreement with the expected few picosecond-long relaxation to $S_{1,0}$. The $g^{(2)}(\tau)$ function again shows the single exponential rise, as non-radiative processes wash out any coherence from the dynamics.

3.5 SUMMARY AND OUTLOOK

The results presented in this chapter fully characterise the behaviour of a single DBT molecule in an anthracene matrix. After optimising parameters for the cryostation and for the optical setup, I performed a full spectroscopic analysis of single molecules, at room temperature as well as at cryogenic temperatures. This last analysis in particular allowed me to gain information regarding the dephasing of single DBT molecules, and its relationship with phonons in the Ac lattice.

As this was the first time (near) lifetime-limited molecules were observed in our lab, precious information was collected. This newly acquired knowledge is particularly beneficial, especially due to the considerable difference between the measured centre of the inhomogeneous frequency distribution and its value as reported in the literature. Immediately this information is going to be used in the other research lines carried out in our group, and in particular in the inclusion of anthracene crystals and single DBT molecules in a fibre-coupled micro cavity [116]. Due to the design of the cavity, no optical access external to the cavity is possible, requiring a good knowledge of the spectral position of single molecules.

Once included in a cavity, DBT molecules would provide a tremendous source of indistinguishable single photons. The narrow photons, as mentioned in the introduction, are suitable for integration with atomic systems. DBATT in a solid state matrix [135], has already produced photons that can couple to sodium atoms and it is natural to wonder if photons from DBT might couple to rubidium atoms. Recently a single quantum dot has been interfaced with hot rubidium vapours [65, 165], that were used as a memory for single photons.

In this direction, I set to investigate whether single DBT molecules could be found at the 780 nm rubidium D2 wavelength. For this purpose I used an additional diode laser, tuneable over several nm, and centred on 779 nm. As the density of molecules is much lower at this wavelength, a long series of raster scans was set up. After the acquisition of each raster scan, the laser frequency was changed, eventually covering a full range of 20 GHz in steps of 200 MHz. A high laser power was used, to

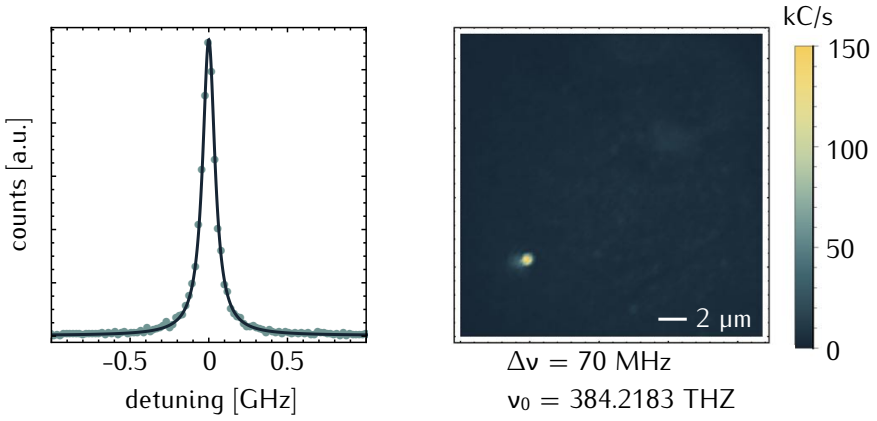


Figure 3.18 Resonance excitation of a single molecule close to the Rb transition.

increase the linewidth of single molecules and therefore increase the allowed frequency interval between consecutive scans. Figure 3.18 reports a successful scan, with a single DBT molecule clearly visible. It had a linewidth of 70(1) MHz, centred at 780.271 nm (384.216 THz).

The rubidium D_2 line lies at 384.230 THz, only 15 GHz away from the molecule. While this distance is too wide to bridge by Stark tuning the molecule [48, 166], the sample in question presented a low concentration of emitters. Only one molecule was found in a 20 GHz scan: a higher doping concentration could increase this number. Tuning electrodes have already been designed: anthracene crystals could be deposited over the electrodes, trying to shift the ZPL and overlap it with the rubidium transition.

Part II

COUPLING AND ENHANCEMENT

4 HYBRID PLASMONIC WAVEGUIDES

In the introduction I briefly described how light-matter interactions can be enhanced by nano-photonics techniques. This chapter focuses on the integration of single DBT molecules with plasmonic structures. This flourishing field of nano-photonics has already shown progress in coupling to several quantum emitters. In this chapter I present my progress towards integrating a single molecule with a new hybrid design of plasmonic waveguide, developed in collaboration with the experimental solid state group of Imperial College. Preliminary results are described, showing coupling between a waveguide and a single DBT molecule.

4.1 PLASMONICS AND PHOTONICS

The coupling of light to electrons in metal was first witnessed more than a hundred years ago [167]. Before the end of the last century a comprehensive theory had been developed for the coupling between photons and plasma waves - coherent oscillations of the electron gas with respect to the ions in the lattice of the metal [168, 169]. In particular the term surface plasmon polariton (SPP) was introduced to identify the traveling quasi-particle of coupled light and electrons at a metal/dielectric interface [170]. As a superposition of photons and plasmons, SPP shows bosonic behaviour [162, 171–173]. Wave-particle duality was also demonstrated for SPP [174], as well as entanglement [175–177] and squeezing [178].

The first to suggest, and observe, that SPP could be used to confine light beyond the diffraction limit were Takahara et al. [179]. They suggested that, in the case of any material or interface where the dielectric function is negative, the usual diffraction limits of confinement are not valid. The initial results were hampered by losses, and showed only modest confinement. It was however noted that the photonic density of states could be modified by the nearby plasmonic structures [180], and they observed a minor speed-up in the spontaneous emission rate of a quantum emitter [181]. Advances in fabrication technologies over the last few decades, to-

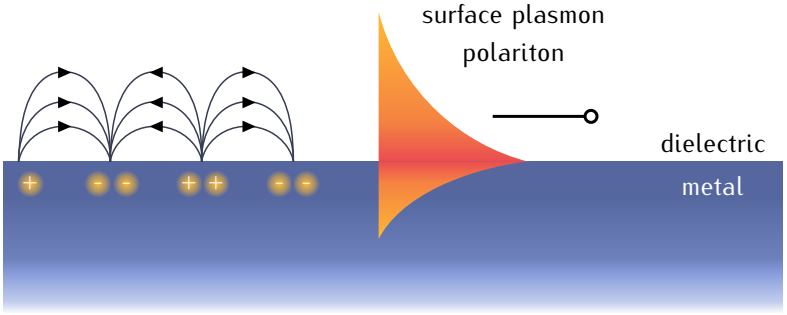


Figure 4.1 Schematic of a surface plasmon polariton.

gether with new efforts from the photonics community, have resulted in more precise, more refined and more effective structures.

The modification of the photonic density of states has the immediate effect of modifying the interaction between light and matter [180]. Also, the high confinement of the plasmonic field increases the elementary polariton field, and hence, the transition matrix element. Therefore an emitter placed close to a plasmonic structure can have its dynamics radically changed [101], allowing photons to be produced very rapidly. These types of structures can theoretically reach Purcell enhancements on the order of several hundreds [182] and up to a thousand [107]. The absence of cavities makes them relatively broadband, and allows them to respond rapidly, which could be an obvious advantage in quantum communication or information processing.

Usually the damping of the plasmon is so fast one cannot see Rabi flopping of the excitation between the photon and the plasmon [104, 183]. This is analogous to the case of coupling to an optical cavity of low Q, where the cavity ringdown time is shorter than the Rabi period, a situation often called weak coupling [184]. If the coupling can be made faster than the damping, then the emitter and the cavity are said to be "strongly coupled", and Rabi oscillations occur as energy is coherently transferred between the emitter and the SPP. Strong coupling to an SPP is highly desirable, as it could be used to engineer photon-photon interaction through photon blockade [185], enabling a single-photon transistor [182, 186–188]. It is however challenging to achieve, and was only recently demonstrated [189, 190].

The small volume of confinement of the optical mode comes with two drawbacks. First, one needs precise positioning because the coupling can change by several orders of magnitude in the space of a few tens of nanometers. Single emitters have to be placed with accuracy in the hot spots of antennas, or otherwise these have to be carefully designed

around them, without destroying the emitter itself. Second, the positioning requirement is exacerbated by the phenomenon of quenching: when an emitter is too close to a metal surface, most of its emission is coupled to non-radiative modes of the metal, that are rapidly dissipated. there is therefore an optimal region of positioning for the emitter.

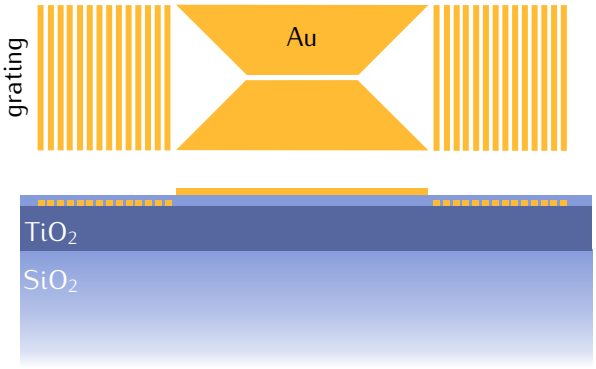
Optical waveguide- and antenna-like structures have been coupled to several single emitters, and new designs and materials are constantly being explored. Of particular interest are SPP in non-metallic materials, such as graphene, that shows low ohmic losses [191]. Highly efficient antennas have already been fabricated in dielectric materials [192], and very recently a new dielectric device was developed in gallium arsenide, showing high field enhancement without the ohmic losses [193].

4.2 HYBRID PLASMONIC WAVEGUIDES

In this section I describe the modelling and the realisation of plasmonic devices designed to couple to single DBT molecules in Ac.

4.2.1 Design

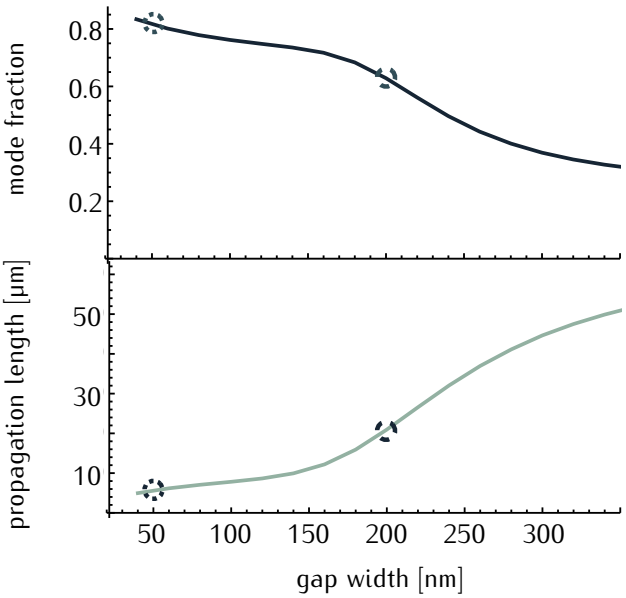
Our HPW are based on a design introduced by Lafone, Sidiropoulos and Oulton [194] and first fabricated and studied by Nielsen et al. [195]. Figure 4.2a shows a schematic and cross section of the device, sitting on a substrate of SiO_2. The semiconductor core of the waveguide is a layer of titanium dioxide (TiO_2), deposited on the substrate, and covered by a layer of SiO_2. Finally, two gold slabs are deposited on top of the SiO_2.



(a) Top-view and cross section of the HPW.



(b) Density plots for the cross section of the HPW, showing the electric field intensity $|E|^2$.



(c) Fraction of the electric field contained in the gap, and propagation length, as a function of gap width.

Figure 4.2 Design and main properties of the HPW. Markers are used to track the properties of the hybrid mode at different locations in the device, and for different gap widths.

A gold grating on either side of the structures brings light into (or out of) the TiO_2 layer, where it propagates towards the channel between the gold islands, roughly as a TE mode [196, pag. 387-389]. As the light approaches the channel the mode becomes increasingly hybridised with the plasmon mode on the edges of the gold islands. Figure 4.2b shows the distribution of electric field energy density[1] in channels of three different widths. On the left, the gold edges are separated by 1000 nm and the energy is mostly in the TiO_2 layer. In the middle panel, half the energy has moved up to he edges of the gold, while on the right - the narrowest channel - most of the energy is near the gold. The fraction of the field energy near the gold is plotted in figure 4.2c, where the abscissa is the spacing between the gold edges in each cross section. There is no dielectric confinement of the mode in the lateral direction, but the field is prevented from spreading laterally by its coupling to the plasmon. This requires careful adjustment of the thickness of the SiO_2 spacer layer. By controlling the hybridisation in this way, it is possible to benefit from the field confinement, while still retaining a long enough decay length[2] that the field can emerge from the structure and be coupled out the other side. Figure 4.2c shows the propagation length, which decreases from 50 μm to 5 μm over the three widths considered. Thus we expect that the field can pass though the narrowest structure as long as the channel is short compared with 5 μm.

As we introduced in chapter 1, the transverse confinement affects the electric field of a photon. Let us now calculate that explicitly. The energy of a single photon is given by

$$\hbar\omega = \int dV\, U, \tag{4–1}$$

where $U = \frac{1}{2}\epsilon\epsilon_0 |E_0|^2$ is the energy density, and ϵ is the dielectric constant at the position of the emitter. We can write the quantisation volume V as $\mathcal{A}_m L$, where $\mathcal{A}_m$ is the mode area and L is a quantisation length. The field at the site of the emitter is then given by

$$|E_0|^2 = \frac{2\hbar\omega}{\epsilon\epsilon_0 \mathcal{A}_m L}. \tag{4–2}$$

[1] I am indebted to Michael Nielsen for performing the Comsol simulations shown in this figure.

[2] Depending on the metal-dielectric interface, the propagation length in a fully plasmonic mode could be much shorter.

This provides the definition of the mode area. Assuming a single transverse mode, the density of states comes just from the 1D density with a periodic boundary condition:

$$D(\omega) = 2 \cdot \frac{d}{d\omega}\left(k\frac{L}{2\pi}\right) = \frac{n_g L}{\pi c}, \tag{4–3}$$

where n_g is the group index of the mode. The factor of 2 is to include both directions of propagation. For a molecule whose optical dipole is parallel to the field of the mode, Fermi's Golden rule gives the modified transition rate as

$$\begin{aligned}\Gamma_1' &= \frac{\pi}{2\hbar^2}\mu_{12}^2 |E_0|^2 D(\omega) \\ &= \frac{\mu_{12}^2 \omega}{n^2 \epsilon_0 \hbar c}\frac{n_g}{\mathcal{A}_m}\end{aligned} \tag{4–4}$$

The molecule in a homogeneous medium of refractive index n would radiate at a rate of approximately[3] $n\Gamma$, where Γ is the free space rate given in eq. (1–2). The ratio of these is the Purcell factor

$$\mathcal{F}_p = \frac{3}{\pi}\frac{n_g}{n^3}\frac{(\lambda/2)^2}{\mathcal{A}_m}. \tag{4–5}$$

The final term $(\lambda/2)^2/\mathcal{A}_m$ can be considered as the ratio between a diffraction-limited mode area and the new reduced waveguide mode area. The mode area in the central channel is plotted in the upper panel of figure 4.3 as a function of the separation between the gold islands, with the assumption that the molecule is placed at the maximum of the field. We see that the area shrinks by about a factor of 10 as the channel width is reduced from 300 to 50 nm, at which point it is ~ 200 times smaller than $(\lambda/2)^2$. The bottom panel of figure 4.3 shows an estimate of the corresponding Purcell factors. That was done at just two widths; 100 nm, where $n_g = 3.2$ and 200 nm, where $n_g = 2.5$. The Purcell factor indicated in the dashed line was then estimated assuming a simple line variation of n_g with gap.

The gratings that couple light in and out of the TiO_2 layer are approximately 5 μm wide. This field is funnelled into the channel by the tapering distance between the two gold islands. The angle of the taper has to be chosen carefully. Too shallow and the field will have to propagate further

[3] I do not here go into the question of the local field correction. The literature presents an ample analysis of the problem, and the reader is pointed to appendix C.1 for a more in depth study. Here we can neglect the corrections as we are comparing emission in two media with the same refractive index.

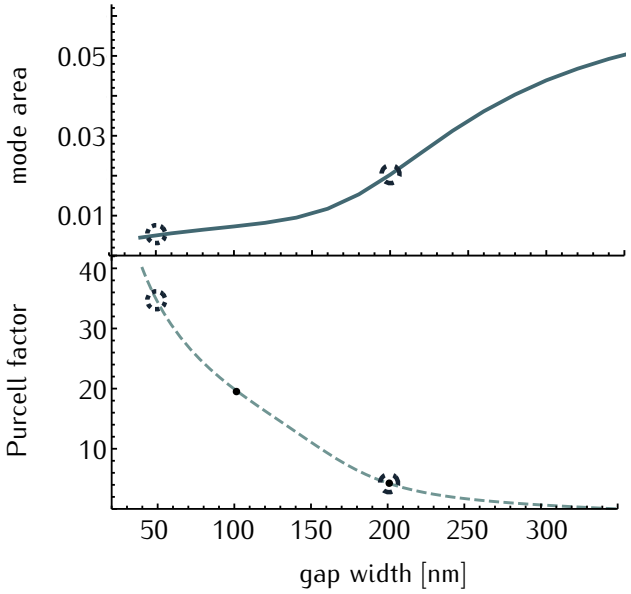


Figure 4.3 Plots of mode area and Purcell factor for varying gap widths. In the bottom panel, the solid points show where the guide index was calculated. The markers on both plots refer to those in fig. 4.2b. The dashed line is an estimated extrapolation from those points.

than one would like in this lossy guide. Too steep and the change will be non adiabatic [197], causing the field to be reflected instead of entering the channel.

The final result is an extremely versatile device. By clever use of tapers the properties of the waveguide mode can be shifted towards the photonic or the plasmonic regime. A low-loss, low-confinement mode can be used to guide the light, that can then be shifted to the high-loss but high confinement mode whenever light-matter interaction is required. One can visualise a device with several active regions, where the mode is highly plasmonic and non-linear elements, like single DBT molecules, mediate efficient photon-photon interaction.

4.2.2 Fabrication

The HPW were designed and fabricated to cover a wide range of parameters:

- the waveguide channels varied in:

  LENGTH: 6 different lengths, from 0 to 10 μm;

  WIDTH: 11 different gap widths, from 60 to 240 nm;

- the grating couplers varied in:

  PERIOD: 3 different periods, from 335 to 370 nm;

  FILL FACTOR: 2 different values for each period;

Fabrication was carried out locally, in the laboratories of the EXSS group at Imperial College[4]. The first fabrication steps are illustrated in figure 4.4. The starting point was a silica microscope slip where 300 nm of TiO_2 was deposited by evaporation (panel (a)). Next, PMMA[5] was spin coated to create a layer of 200 nm that provided the resist for electron beam lithography (EBL). The electron beam printed the grating structure on the PMMA by developing certain areas of the resist (panel (b)). The sample was then immersed for 30 s in a solvent[6] to remove the exposed parts ("developing" phase, panel (c)), and then washed for 30 s in IPA. This procedure created a negative image of the gratings in the PMMA. Before moving on, the trenches were cleaned in an oven with oxygen plasma, for 20 s at 40% of the maximum power.

[4] I am indebted to Javier Cambiasso for performing the fabrication of these devices.
[5] Poly(methyl methacrylate), A4 950k EM Resist.
[6] A 1:3 solution of methyl isobutyl ketone (MIBK) and isopropyl alcohol (IPA).

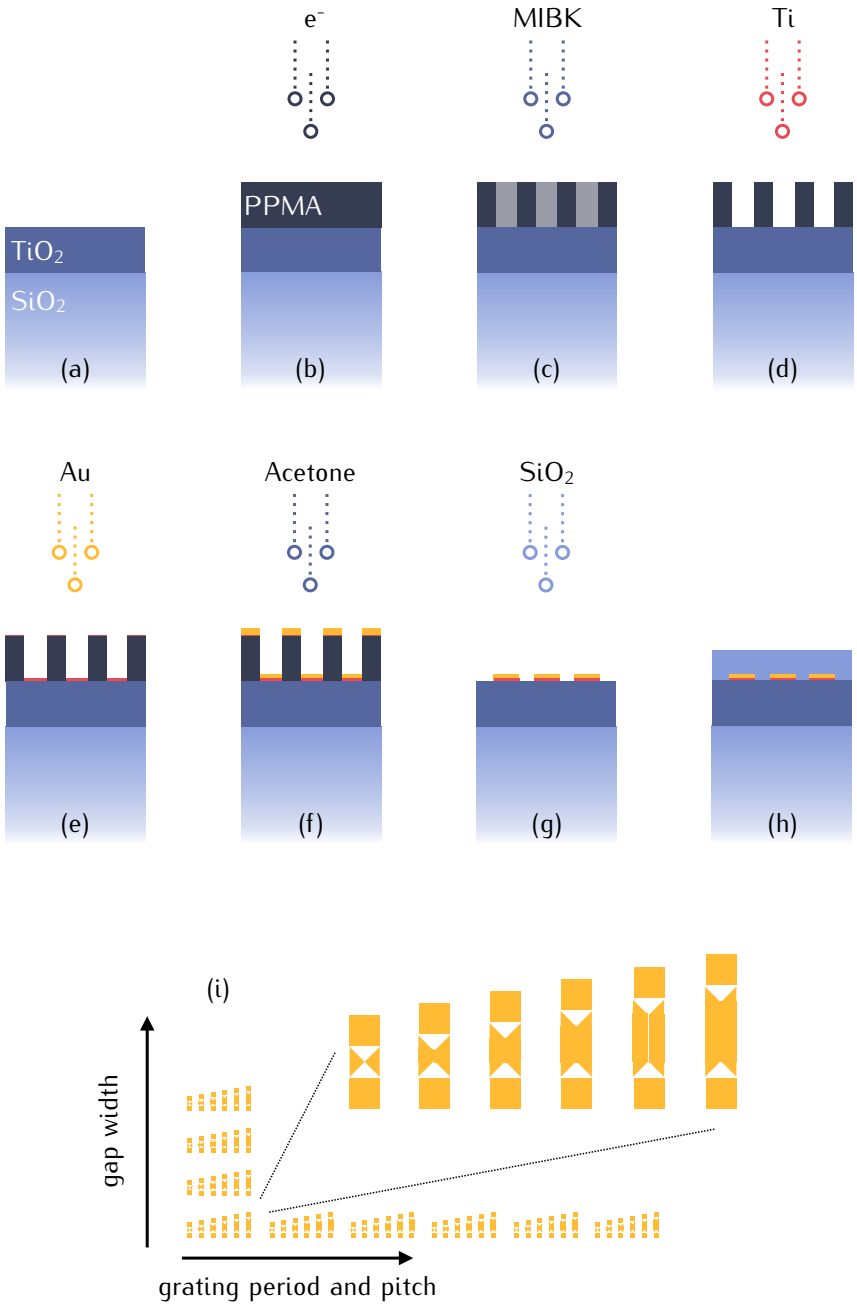
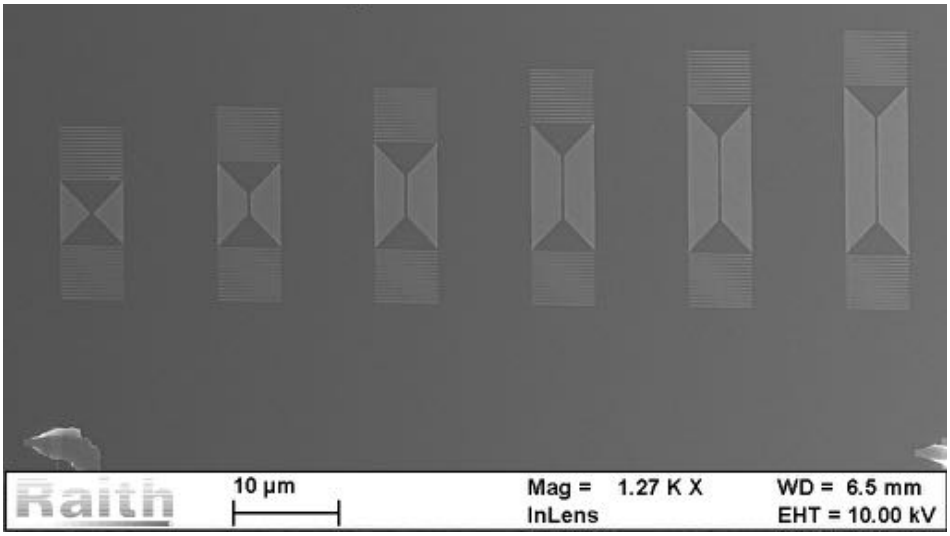
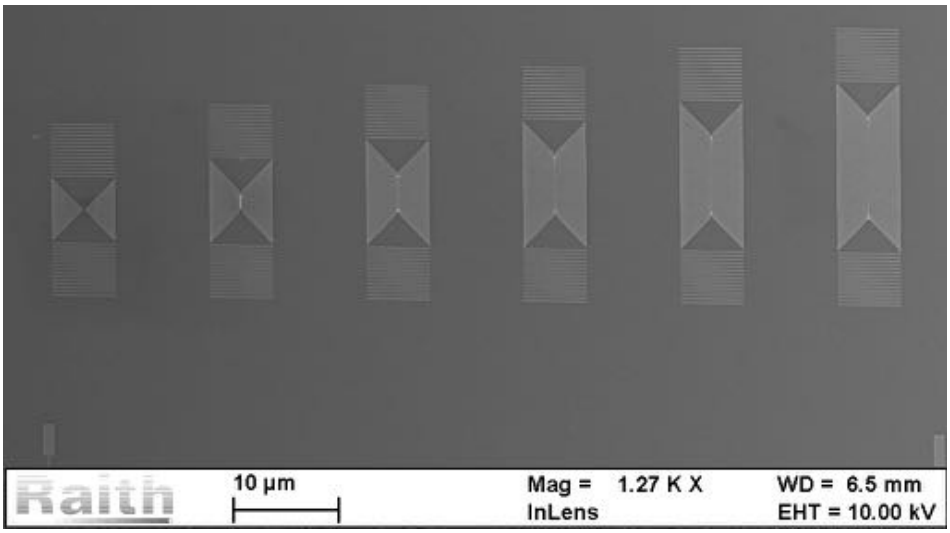


Figure 4.4 Fabrication of the HPW. Panels (a) to (h) present the different fabrication steps to deposit the gratings. Steps (b) through (f) were repeated to deposit the gold slabs, with a SAM used instead of Ti in step (d). The different combinations of waveguide width and length and grating period and filling factor are arranged according to panel (i). e^-: electrons. MIBK: PPMA solvent.



(a) Perfectly developed gold plates and waveguides, for case with the widest gap width.



(b) While the gold plates present the desired shape, the PMMA was removed from the gap region during the developing phase (step (c) of fig. 4.4), which was thereof filled with gold.

Figure 4.5 SEM images of the HPW, for two sets with different waveguide width.

To improve the deposition efficiency of the gold parts, a thin layer of titanium of about 5 nm was evaporated onto the sample (panel (d)). The titanium binds well with its oxide, and provided a good substrate for gold deposition. This was then thermally evaporated on the sample (panel (e)), creating a uniform layer of about 35 nm. Finally, the sample was immersed in acetone ("lift-off" phase, panel (f)). The acetone dissolved the remaining PMMA, at the same time removing the gold and the titanium deposited on top. At the end of the process only the gratings and a clean layer of TiO_2 were left. Lastly, 80 nm of SiO_2 were deposited on the sample through sputtering, creating the spacing layer (panel (g)).

Fabrication of the waveguides followed a similar procedure. PMMA was deposited again on the sample and exposed in the EBL. The developing phase was longer, about 1 min, to ensure that the sharp edges of the gold plates were removed completely. At the same time, caution had to be exercised in choosing this time, as an excessive immersion in the solvent could remove the thinner gaps between the gold plates. The sample was cleaned again in the plasma oven (12 s, at 40% power). Instead of titanium, a thin layer of a self-assembled monolayer[7] (SAM) was spin coated on the sample to facilitate gold adhesion to the SiO_2. A 40 nm layer of gold was evaporated on the sample, followed by another lift-off in acetone.

The samples were arranged as shown in panel (i) of figure 4.4. The full pattern of waveguides contained 396 individual devices, each one with a unique combination of waveguide length and width, as well as grating period and fill factor. In total, 12 copies of the full pattern were fabricated on a single substrate, leaving us with an ample range of devices to inspect.

Images of waveguides after fabrication, taken with a scanning electron microscope (SEM), are reported in figure 4.5. Only waveguides with gap widths greater than 105 nm developed efficiently. Devices with smaller gap widths featured incomplete, or even absent gaps between the gold plates, as visible in figure 4.5b. The developing phase has to be tuned, to ensure a good rendition of the devices, but at the same time maintain its minute features. The PMMA portion of the gap was too thin, and was dissolved in the MIBK solution.

[7] (3-Mercaptopropyl)trimethoxysilane (MPTMS).

4.3 SAMPLE PREPARATION

4.3.1 Optical setup

The setup followed the basic principles of confocal microscopy described in chapter 3, but modified to allow imaging of the grating couplers. A schematic of the setup is presented in figure 4.6.

Previously the excitation beam was directly hitting the objective lens. The sample scans were limited to a few tens of μm due to the back aperture of the objective clipping the beam when this was moved too far by the scanning mirrors. The new setup included 2 lenses assembled in a telescopic system. In this configuration, the two lenses were separated from a distance equal to the sum of their focal lengths, and the objective and the steering mirrors were placed in the focal plane of the last and first lens respectively. The lenses were arranged to share the same optical axis with the objective. In this way, if a beam was entering the telescopic system along the optical axis, it would leave it unchanged, hitting the objective perpendicularly. A change in its angle, usually provided by a pair of galvanometric mirrors, was transmitted through the lenses according to Fourier optics. The first lens changed the angle into position, focusing the beam at a distance h from the optic axis. The second lens then collimated the beam again, and transformed the position back into angle. In this manner it was possible to change the angle of incidence of the beam onto the optical plane of the objective, while keeping it centred on the back aperture. Moreover, the beam spot was magnified by the ratio between the two focal lengths, and could then be matched to the back aperture of the objective.

The rest of the setup followed the same principles described in section 3.1. Here the pump and the fluorescence were separated by means of a dichroic beam splitter (Chroma). In addition to increasing the signal-to-background ratio, the dichroic had the advantage over the BS of deflecting, and then wasting, a smaller fraction of the excitation light. Room temperature single-molecule spectroscopy requires high power excitation light, a demand that can be challenging once losses due to optical elements begin to accumulate. The objective lens (Nikon ApoPlan Fluo) had the same NA $= 0.9$ and magnification of 100x of the previous objective.

The setup was adjusted to include in- and out-coupling from the gratings. This was achieved by inserting a pellicle BS between the objective and the last lens in the telescopic system[8]. The BS thus provided an addi-

[8] A detailed scheme of the setup is reported in figure C.1.

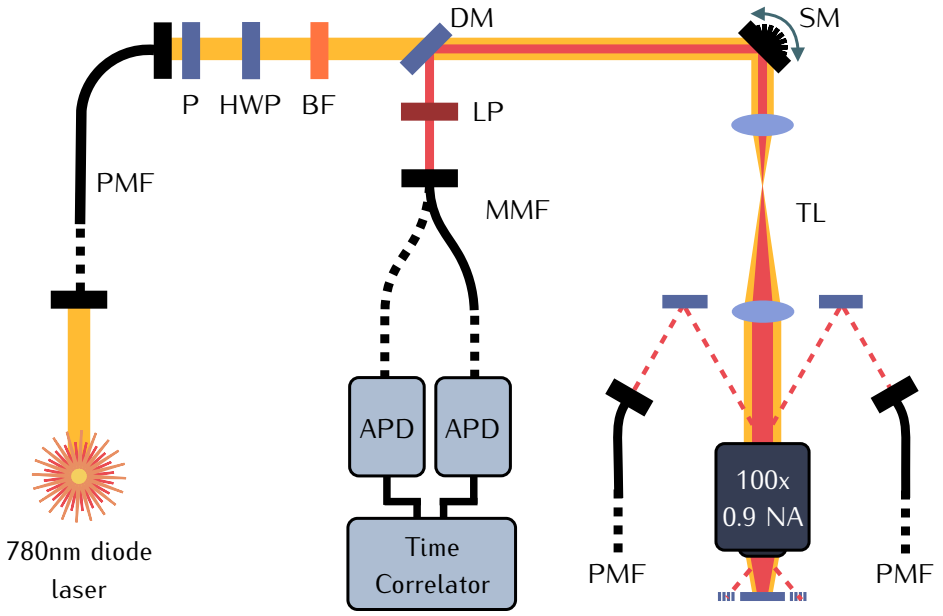


Figure 4.6 Schematic of the confocal microscope used to study coupling of single molecules to hybrid plasmonic waveguides. PMF: polarisation-maintaining fibre. P: polariser. HWP: half-wave plate. BF: band-pass filter. DM: dichroic mirror. SM: steering mirrors. TL: telescopic lenses. LP: long-pass filter. MMF: multi-mode fibre. APD: avalanche photodiode.

tional access to the objective and to the sample, completely independent from the main confocal path. This BS gave access to two additional beam paths, one for each grating. These could be used to couple light into or to collect the fluorescence from a grating: each beam path featured a fixed-length collimator connected to a PMF, and, according to the case, a half-wave plate or a long-pass filter.

The excitation light was supplied by an external cavity diode laser (Toptica), with a central frequency of 780 nm, or by a pulsed diode laser (PicoQuant), similar to one used in the previous chapter but with a central frequency of 780 nm. Both lasers were coupled into a PMF, that was then butt-coupled to a PMF connecting to the main confocal path or to one of the two grating ports.

This layout allowed two different modes of operation. Excitation light can be provided through the main confocal path, with the molecular fluorescence collected simultaneously through the confocal path and through both gratings. Each channel was monitored with an APD, and a raster scan image was built from the collected fluorescence. This configuration is ideal for measuring the optical properties of single DBT molecules, and for estimating the coupling to the waveguide.

Alternatively, the excitation light can be coupled to the waveguide through one of the gratings, while molecular fluorescence can be collected from the other grating. At the same time, the sample can be raster scanned using the confocal microscope. The scan should be dark, with only the molecules coupled to the waveguide appearing as bright emitters.

4.3.2 Crystal growth

The Ac crystals described in the previous chapter are not ideal for nanophotonics purposes. Despite the excellent optical properties, their thickness of ~ 1 µm combined with the high refractive index of Ac turn these crystals into a less than ideal candidate for bringing a single photon emitter close to a waveguide structure [94]. The main challenge is to place anthracene, and in particular single DBT molecules, into the narrow gap of the HPW.

I employed a method recently developed in our group for coupling single DBT molecules to dielectric waveguides [94, 132]. Contrary to the co-sublimation technique described before, this method uses a supersaturated anthracene vapour to grow very thin crystals, as required to couple molecules with our small devices.

A vial is filled with Ac powder, and placed on a hot plate, that melts the anthracene. The sample closes off the top of the vial; being colder than the bottom, close to the sample the vapour is supersaturated. Under this condition, uniformly thin crystals grow flat on the surface with large transverse dimensions. It was shown [94] that single crystals, with a thickness ~ 100 nm, can be repeatedly grown on different surfaces. When DBT molecules are spin coated onto the sample prior to crystal deposition, these are incorporated into the crystal, where they lie parallel to the surface with their optical dipoles along the b axis, and are photo-stable.

I started with a stock solution of DBT in toluene, with a a concentration of 1 mMol. I diluted it in diethyl ether, reaching a volume ratio of 1:2000. I then spin-coated our sample with 20 µl of this solution, ramping up until 2000 rpm over 5 s and holding for 60 s.

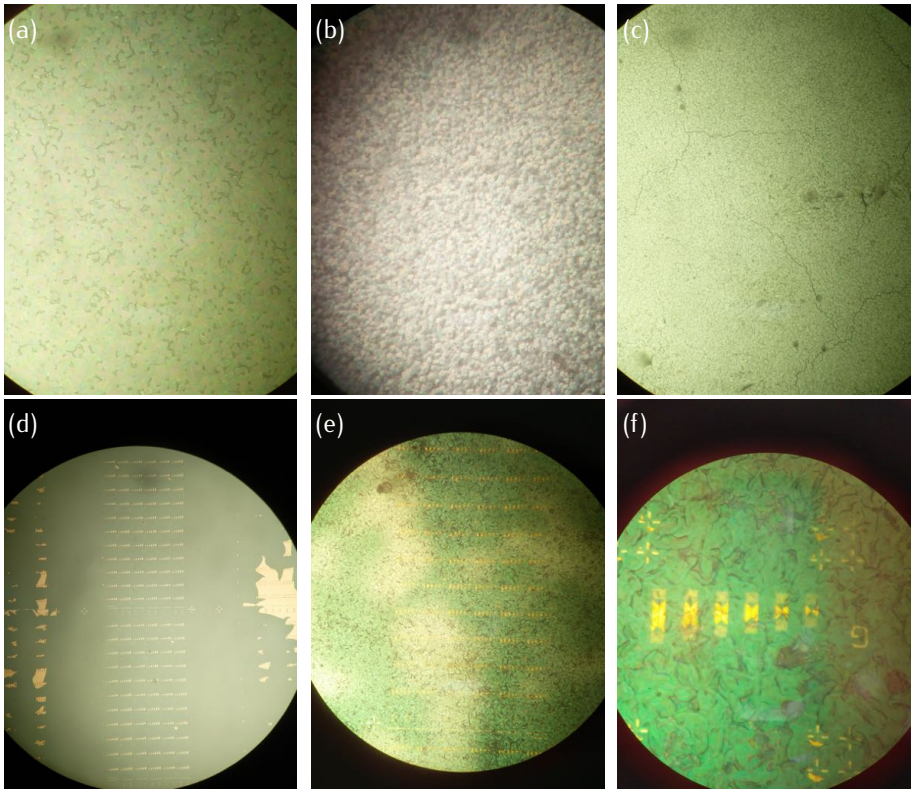


Figure 4.7 Crystals of Ac from supersaturation regime. Panel (a) shows a typical growth, with a uniform coverage of Ac over the whole surface. The nature of the crystal sheet is put into relief by the cross-polarisation image of panel (b). The single neighbouring crystals are clearly visible. If the growth time is increased over 3 minutes, then cracks in the crystal sheet start to appear, as reported in panel (c). Panels (d) and (e) show the sample before and after crystal growth, with the individual devices visible. A single set of waveguides is reported in panel (f).

A glass vial was filled with 2 g of finely ground Ac powder[9], and placed, together with the sample, inside a glove box. This was purged of oxygen by a pump and purge procedure with nitrogen gas (as also done for co-sublimation) to decrease the chance of the molecules photobleaching.

A hot plate, connected with a PID loop to a copper block that hosts the vial, was placed inside the glove box and heated until the copper block was at a temperature of 240 °C. This was slightly lower than the temperat-

[9]While the Ac was the same one used for co-sublimation, I noticed a difference between individual orders from our supplier (VWR). The batches seemed to be different in grain size, but especially in colours, ranging from pearly white to bright yellow. This last batch proved to be the most suited for supersaturation growth. A company inquiry is still open, but they suggest the difference could be due to a difference in water concentration.

ure reported in [94] (optimised for the growth of single, isolated crystals of anthracene) because I found that it gave a more complete coverage of the surface of anthracene. When the desired temperature was reached, the vial was placed in the copper block and covered with a glass microscope cover slip. After roughly 2 minutes the cover slip was removed and the sample was put in its place. A growth time of about 2 minutes provided the desired coverage of anthracene crystals.

I found the growth parameters to be robust, and the growth to be repeatable. Typical results are provided in figure 4.7. The seemingly uniform coverage shown in panel (a) is revealed, using crossed polarisation, to be made up of many contiguous single crystals (b). I observed after prolonged growth times that the crystal sheet became stressed and eventually cracked, as shown in figure 4.7(c). Panels (d)-(f) show waveguide chips before and after crystal growth. During the preliminary tests we found that the anthracene was reluctant to grow on gold, growing mostly around the devices. However, as visible in figure 4.7(f), longer growth times than those reported in [94] finally yielded a complete covering.

After crystal growth, the samples were rapidly checked under an optical microscope and in the confocal setup. If the desired coverage and density of emitters had been achieved than the sample was protected with PVA, as described in sec. 3.2.1, in order to suppress sublimation of the crystal.

4.3.3 Characterisation

Before testing the coupling of single molecules to the HPW, I characterised the losses due to grating coupling and waveguide propagation in individual samples.

At first, I tested the coupling efficiency of the gratings as a function of wavelength. This was essential because room temperature emission spectrum of a DBT molecule (shown in figure 3.9) is several THz wide, and from a peak at 790 nm extends past 900 nm. The spectrum and the grating efficiency had to be combined to get a correct estimate of the fraction of molecular emission that is harnessed in the waveguide.

The grating efficiency was obtained by means of throughput measurements on the test gratings. A different confocal microscope was used for these measurements, employing an objective with a lower $NA = 0.4$. The emission from the grating has a well defined angular spread, that is well contained even in this small numerical aperture, and the measurement

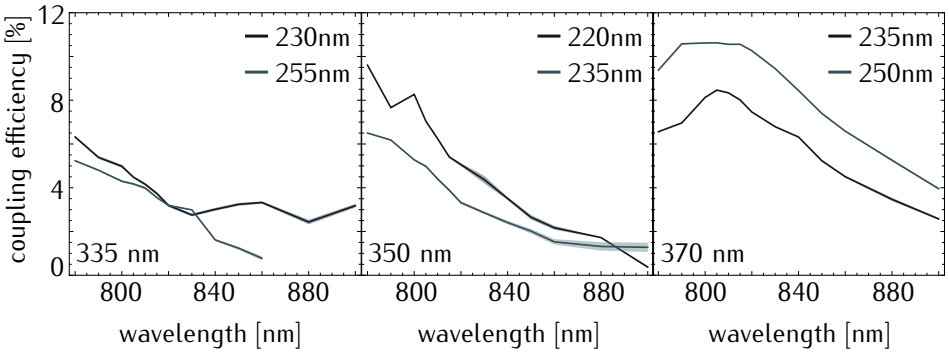


Figure 4.8 Values of grating efficiency as a function of wavelength. The three panels represent the three grating periods used in our sample, as reported in the bottom left corner. For each plot we report the two curves corresponding to the two filling parameters. The shaded areas represent the statistical error.

actually benefited by the increased spot size of the focused laser beam (cf. eq. (3–1)).

The laser beam was supplied by a broadly tuneable Ti:Sapph laser (Coherent Chameleon), providing an excitation wavelength from 780 nm to 900 nm. The laser, with an incident power of ~ 2 mW, was focused on one of the gratings, and the light coupled out from the other grating was collected from the objective and measured with a power meter, P_{out}. This was repeated for different excitation wavelengths. The background power levels P_{bg} were obtained by moving the excitation beam away from the grating, while keeping the collection path unchanged. The values of $P_{out}(\lambda)$ were then compared with the amount of light $P_{Au}(\lambda)$ reflected back through the setup by shining the laser light on a gold surface, that acted as a mirror. Assuming that the device is symmetrical, the efficiency for coupling the incident light into the centre of the device is given by

$$\eta_{grat}(\lambda) = \sqrt{\frac{P_{out}(\lambda) - P_{bg}(\lambda)}{P_{Au}(\lambda)}}. \tag{4–6}$$

The results are plotted in figure 4.8. It can be seen that the increase in the period of the gratings shifts the peak wavelength of the efficiency curve towards the red. For out-coupling photons therefore the best case was the one corresponding to the third panel, with a period of 370 nm and a bar width of 250 nm.

4.4 SINGLE MOLECULES COUPLED TO HPW

After the initial characterisation I began the search for a single molecule coupled to a device.

4.4.1 Contamination

The first tests on the HPW revealed a high level of contaminants. Figure 4.9(a) shows a confocal raster scan on a region of the sample devoid of Ac crystals. The many bright spots present on the scan are all probably contaminant bodies. They were identified as such from their heavy blinking, and from their low photostability.

All the solvents used for cleaning and growth purposes were of high purity, so I surmised that the source of the contamination was probably in the fabrication process, where the general requirements for purity are lower. I guessed that the contaminants were probably of organic origin, and therefore easily removed by an oxygen plasma. Before doing so, I decided to use these contaminants as a first probe of the waveguides.

A typical raster scan of a device is reproduced in figure 4.9(c), showing many bright spots. As they didn't display any polarisation dependence, nor an antibunching signature, they were identified as contaminants. Nonetheless, I tried to measure the coupling to the waveguide. As a first test, I took a raster scan of the sample, at the same time collecting the fluorescence from both gratings through the two additional ports. Each port was aligned by coupling a laser into the PMF fibre, and moving the laser spot on the grating, using the CCD camera. The spot was then aligned on the collection grating; an 800LP filter was placed in front of the collection lens and the PMF was moved from the laser to an APD. By monitoring the fluorescence from the confocal microscope and from each grating I was able to correlate spots on the grating scan with possible emitters in the confocal scan. Such a scan is reported in figure 4.9. A clear bright spot is visible in the grating scan of panel (e), corresponding to the bright signal circled in the raster scan of panel (c).

The count rates collected for this particular emitter are reported in panels (b) and (d) for the confocal path and the grating respectively. We can immediately see that the two rates were perfectly correlated with each other, even in case of extremely bright bursts of fluorescence[10]. The ratio between the two rates, plotted in panel (f), gave an almost constant split-

[10] These are so far of unknown origin.

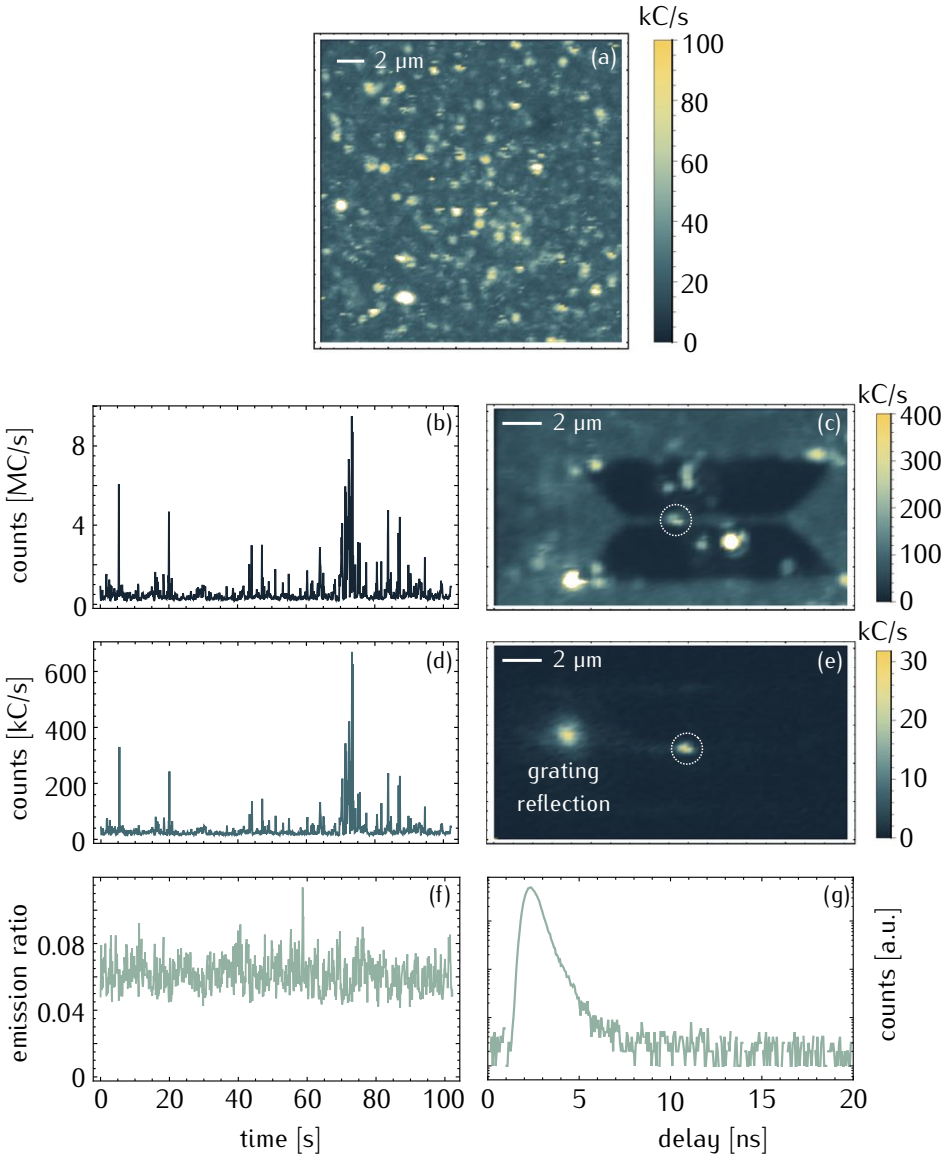


Figure 4.9 Analysis of contaminants in the HPW samples, with a typical raster scan (panel (a)). The fluorescence rate for the same emitter is shown in panels (b) and (d), for collection through the confocal path or through the grating ports. The emitter is highlighted in the confocal and grating raster scans of panels (c) and (e). The ratio between the two emission rates is reported in panel (f), while a TCSPC measurement is reported in panel (g).

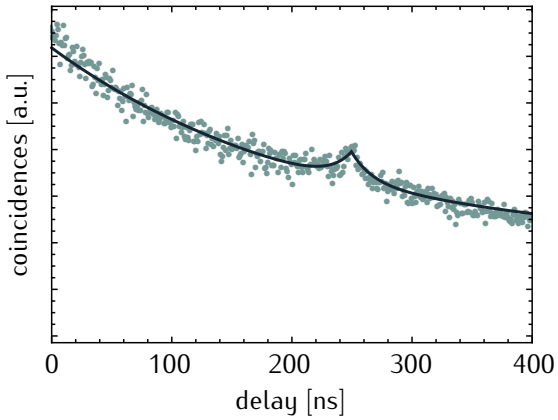


Figure 4.10 Histogram $C(t)$ for the contaminant emitter of fig. 4.9, recorded from the confocal microscope, as in (b). here the time is the electronic delay between the two detection paths. The bunching at $t \sim 250$ ns is presumably due to the high radiation bursts. The exponential decaying baseline is due to the high background count rate.

ting ratio of 0.07 between photons collected by the confocal and photons collected through the grating.

While I could not yet estimate the collection efficiency of our setup, this was nonetheless a promising result. If we consider the collection efficiencies to be equal for the confocal microscope and the gratings, then we are seeing 7% coupling to the guide, in one direction.

To inspect more closely the nature of the emitter I analysed the radiation with the time-correlator, performing a TCSPC and an antibunching measurement on the radiation collected from the main confocal path. The histogram built for the first measurement was aimed at measuring the lifetime of the emitter, to compare it with the lifetime of a DBT molecule. The result is shown in panel (g) of figure 4.9. Surprisingly, the exponential decay showed had a time constant of 0.55 ns, well outside the normal range for DBT in Ac. The sample in question had a channel gap of 200 nm, so it should not produce the Purcell enhancement needed to reach such a short lifetime. The signal-to-background ratio seemed high enough to confirm the validity of the measurement, and the exponential decay extended well past the jitter of the detectors (cf. figure 3.7).

The coincidence histogram for this particle is plotted in figure 4.10, where the x-axis represents the electronic delay between consecutive detection events[11]. In the plot, one sees a peak, rather than a dip, where the path difference between the two channels is zero ($t \sim 250$ ns). This

[11] To recover the same plots previously presented, it is sufficient to translate the x axis, setting the origin at the bunching peak, at $t \sim 250$ ns

is presumably associated with the bright radiation bursts seen also in figure 4.9(b,d). On fitting the data between 200 and 300 ns to the form

$$f(\tau) = a + b\,t + c\,e^{-\Gamma_B|t-t_0|} \tag{4–7}$$

I obtained a bunching time $1/\Gamma_B \approx 8$ ns. This adds further weight to the idea that these are not DBT molecules. We were unable to see the temporal structure of the bursts directly because the card used to record figure 4.9(b) did not have a sufficient temporal resolution.

As a final note, a bright emission spot can be seen on each corner of the gold plates in figure 4.9. This was probably due to other organic molecules placed close to the gold plates. The sharp edges of the plates made the HPW act as an antenna, concentrating the field at the vertex and enhancing the fluorescence of any emitter in the vicinity. The emission from these bright spots showed the same irregular time trace of panels (b) and (d) of figure 4.9.

This analysis of the contaminants had given useful information regarding the efficiency of our setup, and provided a first estimate of the coupling efficiency of the HPW, so I proceeded in cleaning the sample.

At first it was placed in distilled water at 70 °C to dissolve the PVA cover, after which it was washed in high-purity toluene, acetone and methanol in succession. It was not advisable to clean the sample in a supersonic bath for fear of damaging the gold plates structure. Instead, it was placed in an oven, to be cleaned with oxygen plasma (shown in figure 4.11(a)). After this cleaning, I obtained the almost featureless raster scan in figure 4.11(b), which is spectacularly different from the scan of the uncleaned chip in figure 4.9(a).

While most of the single emitters had been removed by the plasma ashes, this cleaning could only affect the surface of the sample. Any contaminant that was deposited on the sample before the sputtering of the buffer SiO_2 layer would be trapped underneath. This was indeed the case, as can be seen in figure 4.11(c). While no single emitter could be identified, the background levels of $\sim$ 100 kC/s were too high to be due to only scattered laser light. I compared this sample with a similar one previously fabricated, and noticed that there is no such fluorescence. The samples were fabricated in the same manner, within 2 months from each other. Probably a new batch of solvent in the fabrication process carried a high dose of contaminants, that were then encapsulated in the sample. An additional plasma cleaning step is then needed, before the gold plates of the HPW are deposited.

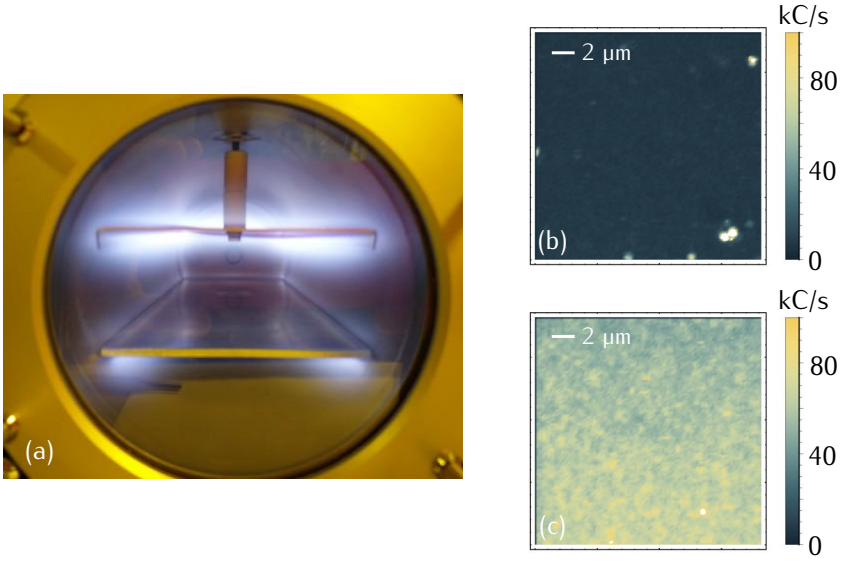


Figure 4.11 Plasma cleaning of the HPW. Panel (a) is plasma-oven used to clean the sample from organic contamination. The purple glow comes from the oxygen radicals. Panels (b) and (c) reports two samples after cleaning, with the latter showing signs of contaminants encapsulated in the underlying substrates.

4.4.2 Coupling procedure

The procedure to find a molecule coupled to a HPW closely follows the one presented in section 3.2 to identify single DBT molecules.

POLARIMETRY: two raster scans of the sample, taken with polarisation 45 ° apart. Emission from single DBT molecules would show modulation.

GRATING COUPLING : another series of raster scans at different polarisation could be taken, monitoring the fluorescence emitted from the gratings. Any correlation with the main confocal scan is a signature of an emitter coupled to the waveguide.

SATURATION SCAN: a measure of the saturation intensity I_{sat} of the single emitter is used to estimate the coupling efficiency. The fluorescence is collected as a function of excitation intensity, monitoring both the gratings and the confocal microscope.

ANTIBUNCHING MEASUREMENT: an antibunching dip is the definitive signature of single photon emission. This measurement is carried out by splitting the microscope signal or the grating signal and then measuring the time correlations as usual. Alternatively, the waveguide itself is used as a beam splitter, with the photons from the con-

focal path being used as the *stop*, while the grating signal provides the *start*. This last method has the virtue that the time trace of both channels gives a first measurement of the coupling efficiency.

TCSPC MEASUREMENT: the final measurement is a TCSPC determination of the lifetime of the excited state of the molecule. While this is already indicated by the antibunching measurements, the TCSPC provides a direct, independent and quick measurement of the lifetime.

Once all these tests are performed, the coupling efficiency of the emitter to the waveguide can be estimated from the collected fluorescence rate. The coupling factor β is defined as

$$\beta = \frac{\Gamma_{wg}}{\Gamma_{tot}} \tag{4–8}$$

where Γ_{wg} is the rate of emission of photons into the waveguide, while $\Gamma_{tot} = S/(1+S) \cdot \Gamma_1/2$ is the total emission rate[12] for a molecule driven on resonance with saturation parameter S. Thus the coupling factor is

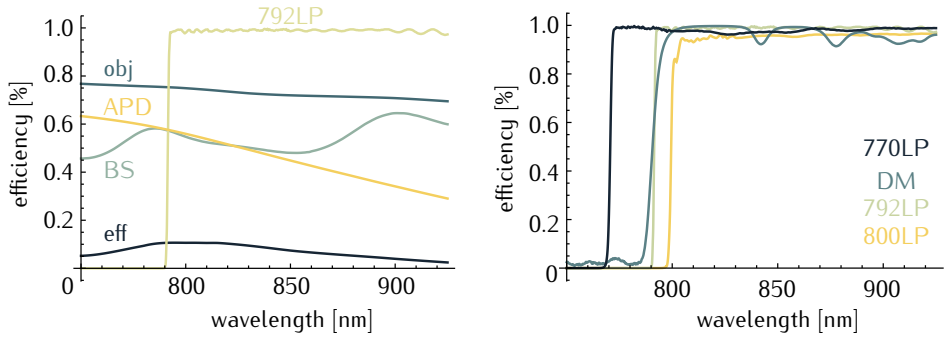
$$\beta = 2\frac{S+1}{S\,\Gamma_1}\frac{R_{wg}}{\eta_{wg}}. \tag{4–9}$$

R_{wg} is the count rate collected from the grating, with detection efficiency η_{wg}.

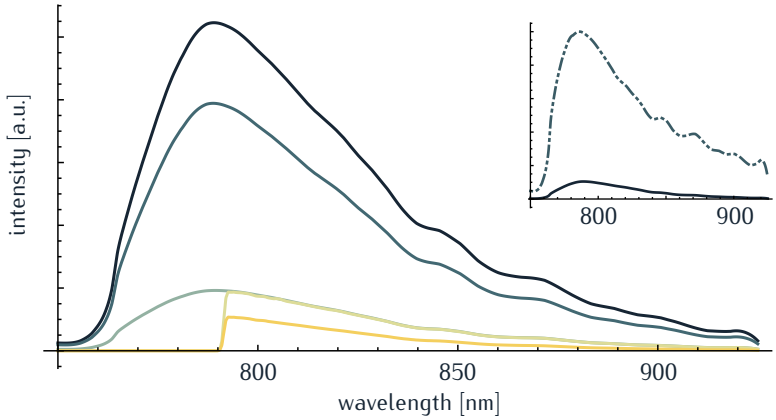
The detection efficiency η_{wg} has multiple contributions. First, one has to take into account the fraction of light that was coupled out of the grating and the fraction that is collected from the objective, together with the transmission through the objective itself. All these factors have been measured with the throughput measurement of section 4.3.3. These results have to be combined with the wavelength response of the gratings themselves, obtained also in section 4.3.3. All the other optical elements, such as beam splitters, filters or dichroic mirrors, also introduce losses. Finally, we have to consider losses due to fibre coupling, and then the efficiency of the silicon APD detectors.

When calculating the total value of coupling efficiency we have to go further than simple multiplication. The emission spectrum for a DBT molecule at room temperature, shown in figure 3.9, is about 20 THz wide and extends well into the infrared. Contrary to the low temperature measurement, it is now necessary to take into account the spectral response

[12] I point again to appendix A.1 for a treatment of room temperature resonant excitation of DBT molecules.



(a) Efficiency as a function of wavelength for various optical components. Left: transmission spectra for the objective (obj), gratings (eff), pellicle beam splitter (BS), APD and long-pass filter. Right: transmission spectra for more filters and the dichroic mirror used in the confocal path.



(b) Modification of the spectrum of a single DBT molecules, as it goes through different optical elements. The colour of the different curves is matched with the left panel of fig. 4.12a, so that, in order, they represent light as it goes through: the gratings, the objective, the pellicle BS, the long-pass filter and finally is detected from the APD. The inset compares the upper curve of the main plot (the effect of the grating couplers) with the original spectrum, that is shown dashed.

Figure 4.12 Wavelength response of several optical elements, and the effect on the collected single molecule spectrum.

of all the components in the setup. Figure 4.12a reports the spectral responses of several optical elements, including the efficiency of the gratings, already reported in figure 4.8.

We multiply the spectrum of DBT in Ac by these transmission functions to calculate the net detection efficiency. The spectrum measured in our setup was taken with a long-pass filter that removed the fluorescence below 770 nm. Recalling figure 1.8 the total emission spectrum is expected to extend well below the ZPL as well, due to interaction with lattice phonons. I therefore used as a starting point the spectrum presented in [91], obtained by exciting the molecule at a wavelength of 725 nm, and collecting the whole spectrum of fluorescence. I had to deconvolve from that spectrum the wavelength-dependent efficiency of the spectro-

meter that recorded it. I did so using the response of the spectrometer in our laboratory, which is very similar to the one in [91]. I then applied to this spectrum the transmission functions presented in figure 4.12a, and calculated the changes in the emission spectrum from emission to collection. Figure 4.12b plots the fluorescence spectrum as it is out-coupled from the grating, collected and transmitted through the objective, passes through two beam splitters, is filtered and finally detected from the APD. In measuring the coupling efficiency, we excite the molecule at 780 nm, and therefore we use both a 792 nm and a 800 nm long-pass filter to suppress the unwanted scatter.

The main loss was due to the grating coupling efficiency, providing a cut of 80% in collection efficiency. The other main loss was 50%, due to detection efficiency of the APD. Finally, the spectral filtering before the APD accounted for 40% or 30% loss, for the 792 nm or the 800 nm long pass filter. The combination of all these losses cuts the net collection efficiency to $\eta_{wg} \approx 10^{-3}$. While this value is comparable with the detection efficiency measured for the confocal path in section 3.2.2, it has to be noted that the factors there are different. See appendix C.2 for a more in depth calculation of the collection efficiency.

4.4.3 First success

I searched for single molecules that were coupled to the waveguide, and found 4 in the 50 waveguides with the widest channel gap (200 nm). They all bleached before I was able to complete a full set of measurements, but one of them lasted long enough to provide a good subset of data. The confocal microscope scan in figure 4.13(a) shows that molecule, marked by a dotted circle, and panel (b) shows the antibunching of its fluorescence, detected through the confocal microscope. In figure 4.13(c) I show the same molecule, viewed instead through one of the gratings, again marked by a circle. In addition, this image has a bright spot on the right which is due to excitation light scattered from the grating. The antibunching curve in panel (d) shows the correlation of the light collected directly from the molecule with that from the grating. After correcting the two $g^{(2)}(\tau)$ curves for the background count rate ((3–7)), I obtained the values of $g^{(2)}(0) = 0.25(9)$ and $g^{(2)}(0) = 0.19(9)$. This is a direct proof that a single molecule was coupled to the guide. Unfortunately the molecule stopped fluorescing before a saturation trace could be recorded, and I had no saturation data from the other three molecules. Therefore I was not able to determine the coupling efficiency to the waveguide from

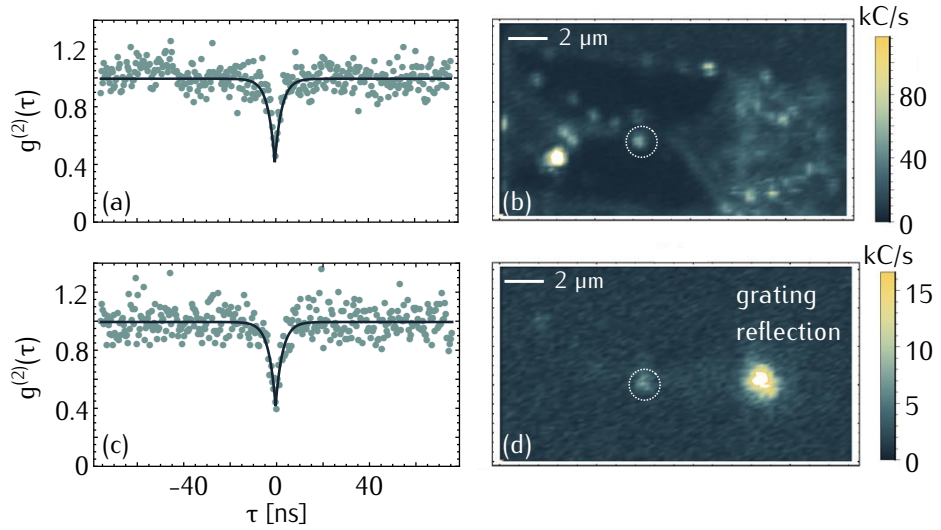


Figure 4.13 Preliminary coupling of a single DBT molecule to a waveguide. Panels (a) and (b) report an antibunching measurement and a confocal raster scan, with the emitter highlighted. Panels (c) and (d) report similar measurements, but taken through the grating couplers. In both cases the antibunching dip is visible, confirming the single photon nature of the radiation.

the data available. At this point I needed to stop taking data to write my thesis, so further progress on this will be for the next student.

Before bleaching, the fluorescence from the molecule became unstable in an unusual way, showing long dark periods of several tens of seconds. This is much longer than the expected blinking time due to transit to the triplet state. One possible explanation involves the position of the molecule in the Ac crystal. As the molecules are deposited on the devices before the crystals are grown, they may well sit only in a few monolayers inside the crystals, being close to the gold surfaces. These will inevitably get warm due to the continuous excitation with the laser. The thermal energy could be enough to rearrange the molecules of Ac in the crystal, giving the DBT sufficient mobility to move to the gold plates. As we have seen, below a certain distance from a metallic surface a single emitter enters a quenching regime, where most of its emission is coupled to the electrons in the metal and dissipated. This is what could have happened to the molecule coupled to the waveguide. The reappearance of its emission could be due to the molecule being in an intermediate position, and repeatedly lifting itself from the surface.

4.5 SUMMARY AND OUTLOOK

The results obtained so far for the HPW are very promising. I have recorded the emission from a single molecule coupled to a device, even for the widest gap where the coupling is weakest. I measured the second-order correlation function, both from the confocal arm alone, and using the waveguide coupling as the beamsplitter. In both cases the curves showed single-molecule antibunching.

My search for the molecules in the guide was very tedious and this could be improved in the future. The lengthiest part was the search for the emission through the grating couplers. This requires a PM fibre to be aligned on the grating and optimised for maximum collection. Given the low signal-to-background level, this positioning needs to be done precisely to avoid missing coupled molecules. These steps could be avoided with the use of our CCD camera. Its sensor features a Peltier element and water cooling, reaching a temperature of −80 °C. In this configuration it can reach single photon sensitivity. The light from the grating could be filtered and then sent directly to the CCD camera. Its field of view is wide enough to collect light from both gratings at the same time. After an emitter has been found on a waveguide, its coupling could be tested immediately by exciting it through the confocal path and observing its fluorescence with the CCD. This would be a quicker and more reliable procedure to test whether an emitter is coupled to a waveguide.

4.5.1 Towards cryogenic temperatures

The study in section 4.4.3 was carried out at room temperature. Ultimately, of course, we want to operate at cryogenic temperatures, where narrow, indistinguishable photons emitted on the molecule's ZPL could be suitable for quantum information and communication purposes. In preparation for this, I made some cryogenic tests of DBT-doped Ac crystals grown on a sapphire substrate using the method of section 4.3.2.

The temperature and growth time were modified, to match those explained in [94] in order to obtain single separated crystals. These were then cooled in the cryostation, and analysed in the setup described in figure 3.1. To single out narrow molecules we excited the same area of the sample first with a laser tuned to the ZPL, and then with the 767 nm laser. Because of their narrow ZPL, cold molecules were not expected to be resonant with the first laser, but should be excited through the broad

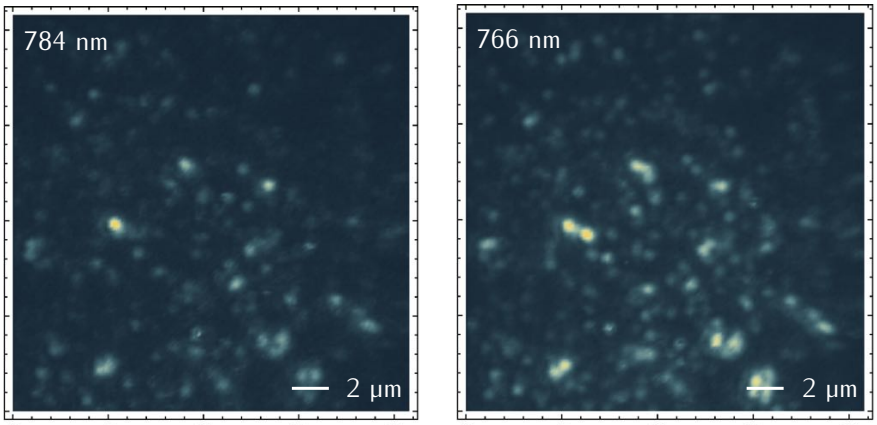


Figure 4.14 Two raster scans of the same area of the sample, with different excitation wavelength and similar saturation power. Additional emitters are visible on the right panel, as possible narrow DBT molecules, or simply scatterers with higher resonant frequency.

$S_{0,0} \rightarrow S_{1,3}$ transition. I therefore expected some additional emitters to appear in the 767 nm scan.

One example is shown in figure 4.14 where new spots do indeed appear in the shorter-wavelength scan. However, while I scanned that location with a wide range of frequencies around the ZPL, no narrow ZPL fluorescence was observed. These new emitters could be impurities, or highly-detuned molecule, with a resonant frequency around 767 nm. Other scans were equally unsuccessful. One might wonder if the crystals are too thin for the molecule to have a narrow line, however Gmeiner et al. [198] have seen lines of 100 MHz in crystals of similar thickness to ours (100 nm).

Wondering whether the crystals are good enough, we have refined our growth technique. The results are shown in figure 4.15. In the picture, taken from in an optical microscope with a 50x objective lens, several single crystalline structures are visible. Despite their modest size (several microns across), the resemblance with the co-sublimated crystals of figure 3.5 is striking. In particular I have highlighted one structure that presented the expected hexagonal shape. I have marked the two angles $\alpha = 109°$ and $\beta = 125°$ for the anthracene crystal [121, 199].

Several other structures presented a regular appearance. The obtuse angles of these structures (highlighted in the figure) matched the α angle for Ac crystals. Moreover, the acute angle proved to be equal to $2 \cdot (\beta - 90°)$. As the hexagonal crystal in figure 4.15 features a short side between the two β angles, we can imagine how the crystal growth will be directed. Moreover, we can immediately identify the *b*-axis of the crystals, and

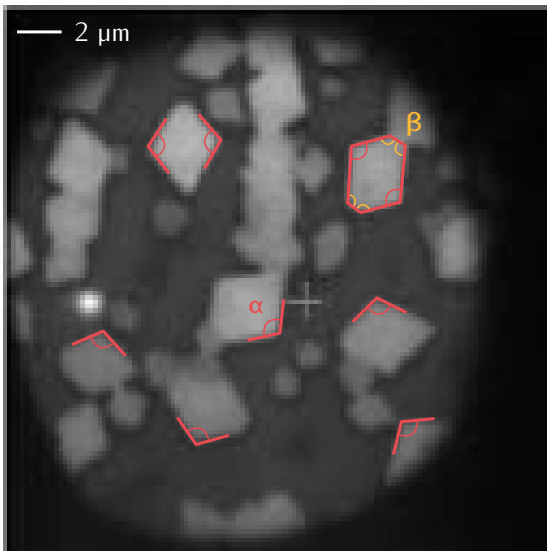


Figure 4.15 Picture of single crystals of anthracene showing regular shapes. We have highlighted the two angle for the Ac crystals, $\alpha = 109°$ and $\beta = 125°$.

with it the orientation of the dipole of embedded DBT molecules[13]. I conclude that the crystals themselves are indeed single crystals of high quality. As mentioned in section 4.4.3, there remains the possibility that the molecules, even though they are aligned with the b axis, may be too close to the surface to have narrow lines.

A final, more radical approach could be taken, by changing the Ac matrix. Recently, paradichlorobenzene (pDCB) showed great promise as a host for DBT [112]. The new combination gives lifetime-limited ZPL at 782 nm, that is entirely suitable for our devices. pDCB melts at only 50 °C, and it has recently been used to couple DBT to photonic nanostructures [119]. If pDCB could be spin coated or melted on a chip, it could provide a good alternative to the supersaturation growth. Tests of photostability and dephasing in this matrix will be crucial to the project.

[13] This claim has yet to be confirmed by experimental results.

5 RESONANT PROCESSES IN PHOTONIC CRYSTAL DEVICES

The previous chapter dealt with plasmonic enhancement. In this chapter I will expand on an alternative approach to emission enhancement, by integrating single emitters into an array of coupled optical cavities. In particular I will concentrate on resonant two-photon absorption in silicon devices.

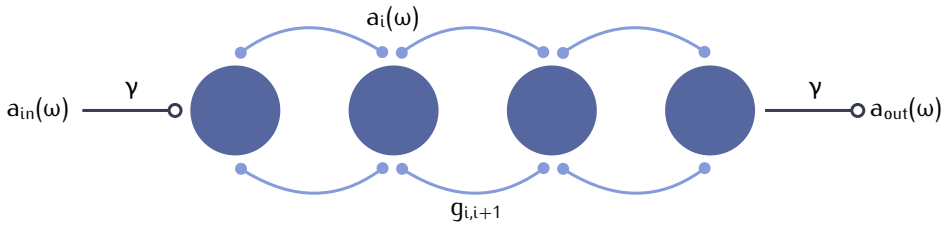
This final chapter presents the work I carried out during an internship at the Photonic Nanostructure Research Group, at the NTT Basic Research Laboratories [200]. The project combined the group expertise in fabricating high quality photonic crystals and in depositing crystalline layers of erbium oxides. Coating a series of coupled photonic crystal cavities with a layer of erbium oxide could enhance the interaction between coupled light and single ions in the oxide lattice. This would create a passive device with a highly enhanced light-matter interaction, that could be included in several quantum information protocols.

5.1 MOTIVATION

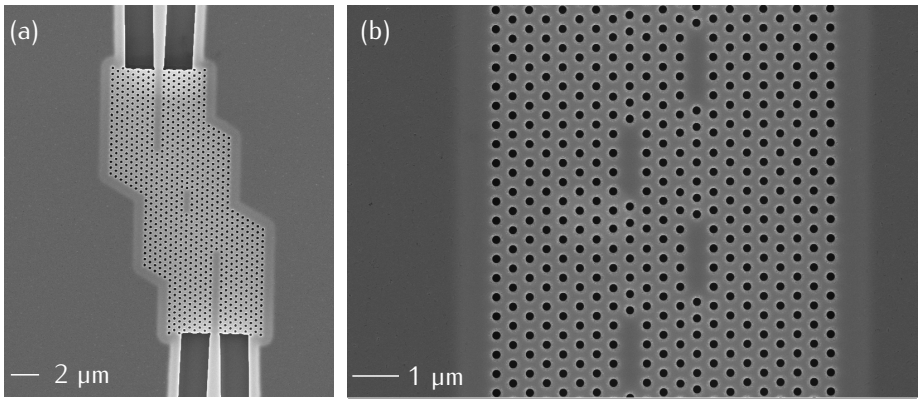
5.1.1 CROWs

Coupled resonator optical waveguides, or CROWs, are a powerful alternative to total internal reflection and Bragg wave-guiding [201]. A schematic of a CROW is reported in figure 5.1a. They consist of a series of optical resonators, coupled together in a chain. Light is coupled to the first optical resonator, and is then transmitted through the chain until the last cavity, from which is coupled out of the device. Several physical implementations have been suggested, like evanescent coupling between micro disk cavities [202], or, like in our case, defect cavities in a 2D photonic crystal [203, 204].

In figure 5.1b we report SEM images of the CROWs used during the course of the experiment. The regular pattern of holes in a silica slab creates a periodic modulation of the refractive index. This periodicity creates an interval of forbidden frequencies, a photonic band-gap, in a



(a) Schematic of a CROW. Input and output couplings are specified by γ, while g is the coupling constant between adjacent cavities.



(b) SEM images of the CROWs fabricated at NTT. The left panel shows two ridge waveguides coupled to an L3 cavity, the constituent element of the CROW. The right panel shows multiple L3 cavities, arranged in a CROW. The angle between the cavities is chosen to maximise the coupling between adjacent cavity modes, that have a peculiar x-shape.

Figure 5.1 Schematic of CROW, and SEM images of devices fabricated at NTT.

similar fashion as the gap between the valence and conduction band for semiconductors. Controlled disorder in the photonic crystal, like removing holes from the pattern, creates a localised defect with a high density of modes, within the band gap. Light is now allowed in the defect, but the group index of the allowed modes can be highly modified. The result is a slow propagation of light, that presents a highly reduced group velocity. Record values of $v_g = 10^{-2}c$ have been achieved, as well as optical cavities with high quality factors [106, 205, 206].

The single constituent of the CROW used for our experiment is a cavity obtained by removing three holes from a 2D photonic crystal. This design is also called an L3 cavity, and an example is reported on the left panel of figure 5.1b. The holes adjacent to the cavities can be adjusted in size and position to increase the quality factor of the cavity up to a value of $\sim 10^6$ [206]. A collection of these cavities can be arranged in a CROW, as reported in the right panel of figure 5.1b. Due to the particular profile of the mode, the cavities have to be arranged at an angle to maximise the coupling between consecutive resonators.

Due to their analogy with atomic electrons in a solid, CROWs can be treated using the tight-binding model of condensed matter physics. Under these assumptions, it is straightforward to derive the dispersion relation for the waveguide mode of the CROW as

$$\omega_k \approx \omega_0 \left(1 + g\cos(kC)\right) \tag{5–1}$$

where k is the wave vector restricted to the first Brillouin zone of the lattice, C is the dimension of the unit cell of the resonator (e.g. the cavity length), ω_0 is the resonance frequency of the resonators and g is the coupling constant between consecutive resonators [201]. We can then extract the group velocity of the CROW as

$$v_g(k) = \frac{d\,\omega_k}{d\,k} = -g\omega_0 C \sin(kC). \tag{5–2}$$

As this quantity is only dependent on the constant g, weakly coupled CROWs present a very low group velocity, with an almost flat dispersion diagram. By looking back at eq. (1–3), we can see that this is a highly desirable feature for nanophotonics, useful for harnessing and enhancing emission from a single quantum emitter [57, 207].

In the frame of quantum optics, CROW-like devices can be easily described by extending the input-output formalism for optical cavities [142, ch. 7]. The interaction Hamiltonian $\mathcal{H}_{SR}$ between a single mode of an optical cavity, governed by $\mathcal{H}_S$, and the external field, governed by $\mathcal{H}_R$, takes the form

$$\mathcal{H}_{SR} = \imath\hbar \int d\omega\, \kappa(\omega) \left[b\, a^\dagger - a\, b\right]. \tag{5–3}$$

where a ($a^\dagger$) and b ($b^\dagger$) are the bosonic annihilation (creation) operators for the electromagnetic field inside and outside the cavity. The function $\kappa(\omega)$ describes the coupling strength between the modes. The Heisenberg equations of motion for a and b, in the rotating wave approximation and in the interaction picture, are

$$\dot{b} = -\imath\omega b + \kappa(\omega) a \tag{5–4a}$$

$$\dot{a} = -\frac{\imath}{\hbar}\left[\mathcal{H}_S,\, a\right] - \int d\omega\, \kappa(\omega) b. \tag{5–4b}$$

Eq. (5–4a) can be solved given an initial or a final condition. When inserted into eq. (5–4b), two different solutions for $a(t)$ can be obtained. If we consider the coupling function $\kappa(\omega)$ to be constant over the relevant frequency range[1], and in particular to be $\kappa(\omega) = \sqrt{\gamma/2\pi}$, then we can re-

[1] Note that this approximation is not valid for the case of two-photon absorption.

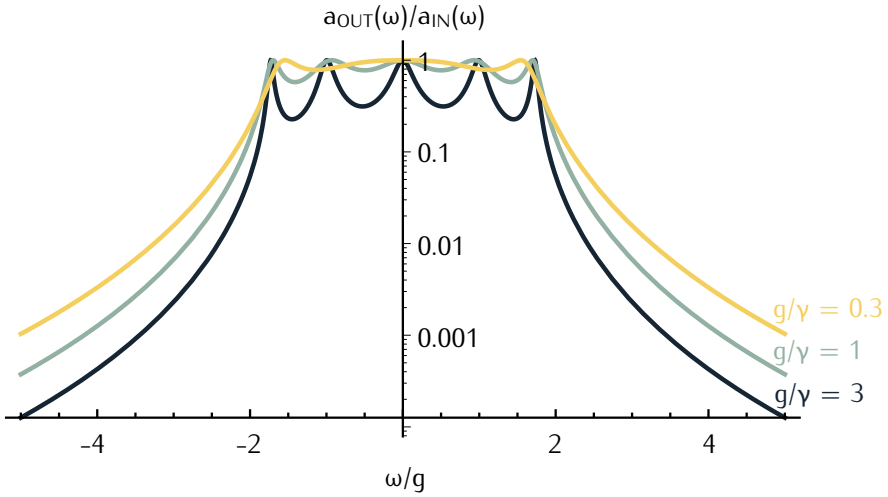


Figure 5.2 Transmission spectrum for an $n = 5$ CROW, for different values of loss parameter and coupling constant.

write eq. (5–4b) as a quantum stochastic differential equation, dependent on initial or final conditions of b:

$$\dot{a} = -\frac{\imath}{\hbar}[\mathcal{H}_S, a] - \frac{\gamma}{2}a + \sqrt{\gamma}a_{IN} \tag{5–5a}$$

$$\dot{a} = -\frac{\imath}{\hbar}[\mathcal{H}_S, a] + \frac{\gamma}{2}a - \sqrt{\gamma}a_{OUT} \tag{5–5b}$$

where we have defined the input and output field operators as

$$a_{IN}(t) = -\frac{1}{\sqrt{2\pi}}\int d\omega\, e^{-\imath\omega(t-t_0)}b_0(\omega) \tag{5–6a}$$

$$a_{OUT}(t) = \frac{1}{\sqrt{2\pi}}\int d\omega\, e^{-\imath\omega(t-t_1)}b_1(\omega) \tag{5–6b}$$

where $b_0(\omega) = b(t = t_0, \omega)$ and $b_1(\omega) = b(t = t_1, \omega)$ are the field operators for the initial ($t > t_0$) and final ($t < t_1$) conditions. The boundary condition that relates the field inside and outside the cavity is

$$a_{IN}(t) + a_{OUT}(t) = \sqrt{\gamma}a(t) \tag{5–7}$$

It is now possible to generalise this relationship, considering the case of n cavities coupled together. The system Hamiltonian has the form

$$\mathcal{H}_S = \hbar\sum_{j=1}^{n}\omega_j a_j^\dagger a_j + \imath\hbar\sum_{j=1}^{n-1} g_{j,j+1}\left(a_j^\dagger a_{j+1} - a_j a_{j,j+1}^\dagger\right) \tag{5–8}$$

where the j-th cavity is described by the operators a_j and $a_j^\dagger$, and cavities j and $j+1$ are coupled with strength $g_{j,j+1}$. Only the first and last cavities are coupled to the outside. From this expression, we can adapt eq. (5–5) to find the evolution of $\mathbf{a}(t) = \{a_i(t)\}$. For the i-th cavity, we find that

$$\dot{a}_i = -\imath\omega_i a_i - (g_{i-1,i}a_{i-1} - g_{i,i+1}a_{i+1}) - \frac{\gamma}{2}\delta_{i,c}a_i + \sqrt{\gamma}a_{IN,i}. \quad (5–9)$$

with $c = 1$ or n, to represent the input and output coupling of the first and last cavity.

We can express this equation in matrix form in the frequency space as

$$\mathbf{A}\mathbf{a}(\omega) = -\sqrt{\gamma}\mathbf{a}_{IN} \quad (5–10)$$

where $\mathbf{a}_{IN} = \{a_{IN\,i}\}$, and $\mathbf{A}$ is the matrix[2] that includes the three contributions of input and output field $\mathbf{I}/\mathbf{O}$, hopping between the modes $\mathbf{H}$ and the detuning $\mathbf{D}$. For a 5-cavity CROW, these have the form

$$\begin{aligned}\mathbf{A} &= \mathbf{D} + \mathbf{I}/\mathbf{O} + \mathbf{H} \\ &= \imath(\omega - \omega_0)\mathbf{I} + \begin{bmatrix} \frac{\gamma}{2} & 0 & 0 & 0 & 0 \\ 0 & 0 & 0 & 0 & 0 \\ 0 & 0 & 0 & 0 & 0 \\ 0 & 0 & 0 & 0 & 0 \\ 0 & 0 & 0 & 0 & \frac{\gamma}{2} \end{bmatrix} + \begin{bmatrix} 0 & -g & 0 & 0 & 0 \\ g & 0 & -g & 0 & 0 \\ 0 & g & 0 & -g & 0 \\ 0 & 0 & g & 0 & -g \\ 0 & 0 & 0 & g & 0 \end{bmatrix}\end{aligned} \quad (5–11)$$

where $\mathbf{I}$ is the identity matrix and we have imposed $g_{i,j} = g$ and $\omega_j = \omega_0$. Finally, by inserting eq. (5–7) into eq. (5–10), the input-output relation for a CROW are found to be

$$\mathbf{a}_{OUT}(\omega) = -\mathbf{A}^{-1}\left(\mathbf{A} + \gamma\mathbf{I}\right)\mathbf{a}_{IN}(\omega). \quad (5–12)$$

To calculate the field at the output of the last cavity, we need the last element of the vector $\mathbf{a}_{OUT}(\omega)$, for an input field that is non-zero only for the first cavity, $\mathbf{a}_{IN}(\omega) = (1, 0, 0, \ldots)$. $a_{OUT,n}(\omega)$ gives us information on the transmission spectrum of the CROW.

An example is reported in figure 5.2, for an $n = 5$ CROW and for different values of loss parameter and coupling constant. For $g > \gamma$ the spectrum presents n peaks where there is unity transmission, and a total bandwidth of $\sim n \cdot g$. The greater the ratio g/γ, the sharper these peaks are. The spectrum becomes almost flat as $g \sim \gamma$, to then feature $n-2$ peaks as $g < \gamma$, that also get sharper for increasing γ. By tuning the ratio

[2] Note that as $\mathbf{A}$ acts only on a, and not $a^\dagger$, it is non-hermitian.

g/γ is then possible to tailor the CROW, from a flat transmission line, and therefore less dispersion, to a very narrow, comb-like filter.

Lastly, I shall highlight another useful feature of the CROW. The resonators in the chain are (usually) positioned in the optimal configuration for cavity-cavity coupling. This configuration is not necessarily unique, but depends on the symmetry of the resonator. If we consider the case of whispering-gallery modes in micro disk resonators, then two consecutive cavities can be arranged at any angle between each other, still maintaining perfect coupling. In such a way a perfect, lossless bend of any angle can be made in the waveguide. On a more general level, a bend of angle $2\pi/i$ can be made in a CROW made of resonators with i-fold rotational symmetry. For our case of L3 cavities in a photonic crystal, two possible arrangements are available, giving lossless $\pi/2$ bends.

5.1.2 Erbium oxide

Erbium is at the forefront of integration between rare-earth elements and silicon devices. Its main application is light amplification in silicon at telecom wavelengths [208–210]. Recently erbium, and generally rare earth-doped materials have attracted renewed attention. Rare-earth elements present transitions within their 4f shell that are shielded from outer perturbations and lattice interactions. They thus provide another platform for coherent exchange of excitation between light an matter, owing also to their long-lived states [211, 212]. However, there are several downsides to the wide spread use of doping, starting from the low oscillator strength of a single ion. While relatively high doping can be achieved, and therefore a high concentration of emitters, this usually comes at the cost of emission quenching, due to the high number of defects in the crystal.

Some of these issues can be resolved by replacing doping techniques with naturally occurring compounds, such as, in our case, erbium oxide (Er_2O_3) [208, 213]. A single cell of Er_2O_3 contains 32 Er^{3+} ions, accounting to a remarkable $\sim 10^{22}$ Er/cm^3. Such a concentration of emitters, aside from being two orders of magnitude higher than what is reachable in erbium-doped glasses, does not affect the crystalline properties of the matrix, as the single ions do not reside in the lattice as an impurity. Er_2O_3 also benefits from a lattice constant that matches that of Si(111). An integrated, defect free layer of Er_2O_3 could be added to silicon devices, activating portions of optical chips for light-matter interaction.

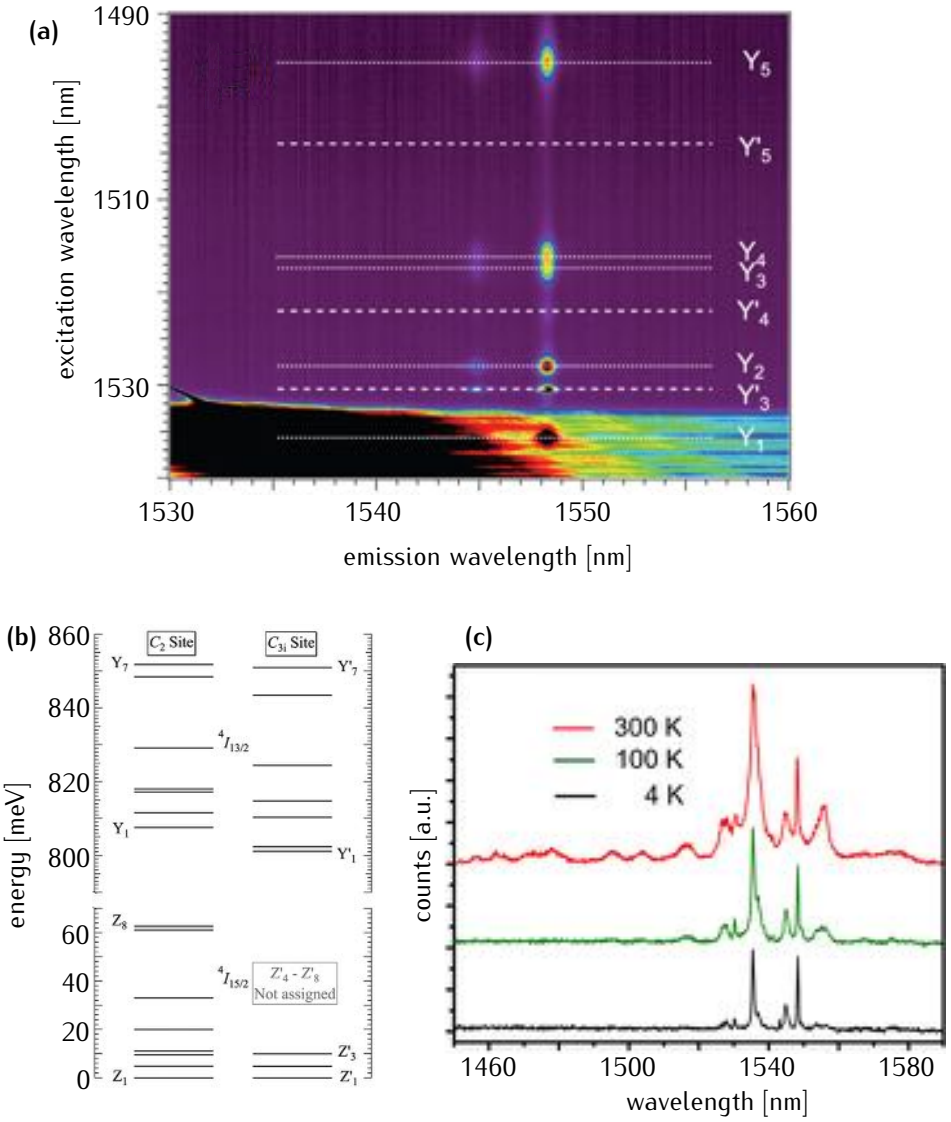


Figure 5.3 Optical properties of erbium oxide, reporting a) the emission spectrum as a function of excitation wavelength, b) the energy levels for the two insertion sites and c) the emission spectrum as a function of temperature. Images adapted with permission from [213] and [214].

The optical properties of erbium have long been reported in the literature [215]. The emission spectrum is dominated, in the telecom band, by the transition between the first excited state ($^4I_{13/2}$, Stark levels Y_i) and the ground state ($^4I_{15/2}$, Stark levels Z_i). In the emission process, one has to separate between the two insertion sites of the erbium ion in the lattice, identified as C2 and C3i sites, with the former being the most abundant. The two principal emission lines are at 1535 nm and 1548 nm, associated to the transitions $Y_1 \rightarrow Z_1$ for the C2 and C3i site respectively (the energy levels of the two sites are reported in figure 5.3(b)). Figure 5.3(a) shows the emission spectrum of erbium as a function of excitation wavelength. As is common in rare-earth ions, population is transferred between the two sites [214], assisted by phonons. The spectrum is then temperature dependent, as is shown in figure 5.3(c).

Absorption of a remarkable magnitude has been observed in Er_2O_3. The $Y_1 \rightarrow Z_1$ line has shown a reduction of 364 dB/cm in a micro disk resonator under resonant excitation [208]. Such a strong absorption, especially if enhanced by a cavity, is a useful asset for quantum information purposes. Allowed transitions could be selected from its many energy levels, to reach schemes suitable for non-linear interactions, such as electromagnetically-induced transparency or all-optical switching.

These non-linear interactions have already been demonstrated. Even at low powers, the interaction between weak pulses, or even single photons, is mediated by hot atomic vapours, or even single atoms. However, the necessity of trapping devices for the atoms, and the hot cells for the vapours are all in contrast with the scalability requirement mentioned in the introduction. By integrating the active element, the erbium oxide layer, directly on the photonic crystal it could be possible to take advantage of the tight confinement of optical cavities as well as of the slow light effect of photonic crystals. This would allow active manipulation of optical signals directly on a chip [216].

A possible application of Er_2O_3 and photonic crystal cavities is based on the work of Franson, Jacobs and Pittman [217]. The authors suggest placing three-level atoms inside a 50:50 fibre beam splitter, acting as two-photon absorbers in each of the fibre cores. When light of suitable wavelength is injected in the beam splitter, the atoms act as detectors for the presence of two photons in each channel. This continuous measurement of the state of the waveguide mode suppresses the probability of two photons being in the same fibre, in an optical analog of the quantum Zeno effect [218]. Therefore photons would behave as non-interacting fermions in this modified beam splitter.

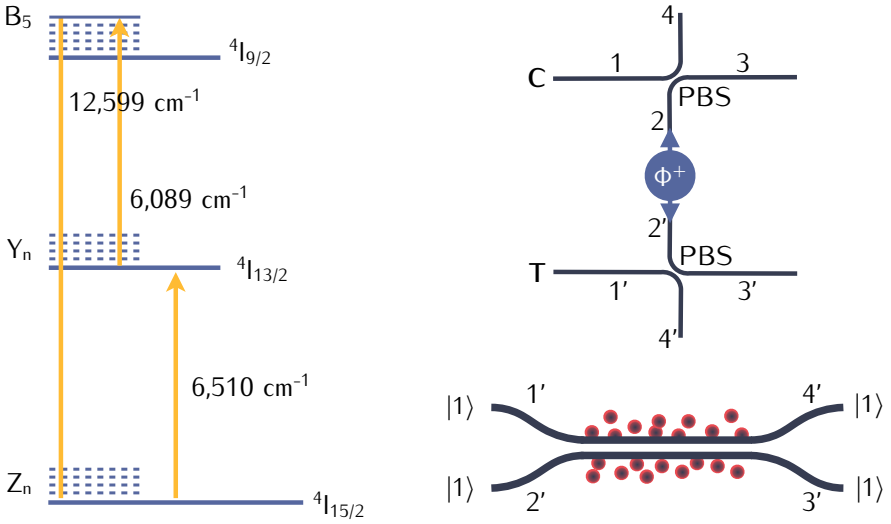


Figure 5.4 Suggested application of Er_2O_3 for quantum information purposes, through two-photon absorption. Left: level scheme of Er_2O_3, with highlighted the two transitions that could be used for TPA. Right: scheme for the probabilistic C-NOT gate suggested in [219], with the modified fibre beam splitter suggested in [217], with single absorbers in the fibre cores. C: control; T: target; PBS: polarising beam splitter.

An immediate application of this effect is in optical quantum computing [10]. Of the several suggested implementations, the probabilistic C-NOT gate suggested by Pittman, Jacobs and Franson [219], illustrated in the right panel of figure 5.4, would benefit from the quantum Zeno effect. In this scheme, the information is encoded in the polarisation of single photons. Each photon in the control and target channel is incident on a polarising beam splitter, at input ports 1 and 1′. The other input ports 2 and 2′ receive as input one photon from the entangled pair $\Phi^+ = (|HH\rangle + |VV\rangle)/\sqrt{2}$, where H and V stand for horizontal and vertical polarisation. The C-NOT operation is successfully applied whenever one and only one photon is detected at either of the two output ports 4 and 4′. In all other cases (two photons in the same mode, or none at all) the operation fails. This corresponds to the case of two photons of equal polarisation entering the beam splitter at the same time, and through quantum interference exiting the gate from the same port. Therefore, the gate has a 1/4 success probability. This can be increased by lowering the failure probability through the quantum Zeno effect. Placing two-photon absorbers in the polarising beam splitters, as shown in the right panel of figure 5.4, inhibits two-photon coalescence, so that two identical photons simultaneously incident on the beam splitter will leave from different ports.

Pittman, Jacobs and Franson's scheme is based on fibre beam splitters. Due to the limited concentration of absorber that can be achieved in these devices, and considering the limits on the size of the core of the fibres, a beam splitter of several meters in length would be necessary to achieve 100% success rate for the C-NOT gate. To overcome these problems, a different application was suggested, employing the quantum Zeno effect to implement all-optical switching. In two proposals the coupling of a laser beam to a resonator was modified by the presence of a pump beam. Whenever this control beam was present, an active material, like hot rubidium vapours surrounding a microdisk resonator [220] or a phase-matched crystal for difference-frequency generation in a Fabry-Pèrot cavity [221], would perform a continuous measurement on the state of the resonator, preventing the target light from coupling to it. A maximum contrast of 35:1 was observed in the latter case.

The left panel of figure 5.4 reports a potential use of the energy levels of Er_2O_3 for a similar application, using TPA between the marked levels to implement the continuous measurement for the Quantum Zeno effect. The combination of strong absorption in erbium and the enhanced light matter interaction in the CROWs could take these applications to chip-level.

5.2 THEORETICAL MODELING

This section develops a theoretical model for the process of resonant two-photon absorption in a CROW. The input-output formalism that was employed in the previous section is not valid in this context. The process of TPA is inherently frequency dependent and, in our description, incoherent. This problem has been solved by considering a master equation in the coherent state basis (that is, a Fokker-Planck equation), but only for the case of a single cavity [222]. The presence of additional cavities coupled together in a linear chain breaks the conditions under which an analytical solution can be reached [223]. Aside from a full numerical approach, several strategies could be employed to solve this problem [224, 225], but they exceed the scope of this thesis.

Instead, I present a mean-field approach to resonant TPA in coupled resonators. The system Hamiltonian[3] can be obtained from eq. (5–13) by adding a driving term to the first cavity:

$$\begin{aligned}\mathcal{H}_S = \hbar \sum_{j=1}^{n} \omega_j a_j^\dagger a_j + \imath\hbar \sum_{j=1}^{n-1} g_{j,j+1} \left(a_{j+1}^\dagger a_j - a_{j+1} a_j^\dagger \right) \\ + \frac{\imath}{2}\hbar\Omega \left(e^{\imath\omega_0 t} a_1^\dagger - e^{-\imath\omega_0 t} a_1 \right).\end{aligned} \tag{5–13}$$

The Hamiltonian $\mathcal{H}_S$ describes a series of n coupled harmonic oscillators, each of resonance frequency ω_j and coupling coefficients $g_{j,j+1}$, with a coherent driving on the first cavity. Note that the matrix $[g]_{j,k}$ doesn't include input and output coupling.

The master equation is derived in a parallel fashion with the resonance fluorescence case reported in appendix A.2.2. The reservoir interacting with the system is modelled as a bath of oscillators of the electromagnetic field:

$$\mathcal{H}_{R_1} = \hbar \sum_{k,j} \omega_k b_{k,j}^\dagger b_{k,j} \tag{5–14a}$$

$$\mathcal{H}_{SR_1} = \hbar \sum_{i=1}^{n} \sum_{k,j} \left(\kappa_{k,j,i}^* b_{k,j}^\dagger a_i + \kappa_{k,j,i} b_{k,j} a_i^\dagger \right). \tag{5–14b}$$

These introduce radiative losses on every cavity. The coupling constant $\kappa_{k,j,i}$ depends on the cavity index i as the first and last cavity in the CROW have additional loss channels from the input and output coupling. The crucial difference from the case treated in appendix A.2.2 is

[3] The system Hamiltonian was written so as to give only real terms in the evolution of ρ, hence the extra $\imath$ in the driving term.

the introduction of the two photon loss mechanism. It can be modelled by introducing an additional reservoir R_4 of atoms [226], coupled to the system only through exchange of two quanta of excitation. The Hamiltonians are

$$\mathcal{H}_{R4} = \hbar \sum_j \omega_j \sigma_{j,z} \tag{5–15a}$$

$$\mathcal{H}_{SR4} = \hbar \sum_{j=1}^{n} \chi(\omega) \left(a^{\dagger 2}_j \Lambda + a^2_j \Lambda^\dagger \right) \tag{5–15b}$$

where the reservoir operators are $\Lambda = \sum_k \sigma_{k,-}$, and $\chi(\omega)$ is the coupling constant of two-photon exchange. The Pauli matrices $\sigma_{j,z}$, $\sigma_{j,-}$ and $\sigma_{j,+}$ are the operators describing the excitation and de-excitation of the atoms.

The master equation for a linear chain of coupled cavities with dissipative two-photon loss is then

$$\dot{\rho} = -\frac{\imath}{\hbar} [\mathcal{H}_S, \rho] + \mathcal{L}_1 + \mathcal{L}_2 \tag{5–16a}$$

$$\begin{aligned} \mathcal{L}_i &= \sum_{j=1}^{n} \frac{\Gamma_{i,j}}{2} \left(2a^i_j \rho a^{\dagger i}_j - a^{\dagger i}_j a^i_j \rho - \rho a^{\dagger i}_j a^i_j \right) \\ \Gamma_{i,j} &= \begin{cases} \gamma_j & \text{for } i = 1 \\ \gamma_{TPA}(\omega) & \text{for } i = 2 \end{cases} \end{aligned} \tag{5–16b}$$

$\mathcal{L}_1$ is the 1-photon Lindblad term, with loss parameters γ_j that includes also the coupling to the outside: $\gamma_j = \gamma + \gamma_{ext}\delta_{j,c}$ with $c = 1$ or n, for input and output coupling. $\mathcal{L}_2$ is an additional Lindblad operator modelling the loss of two photons to the reservoir, in case their frequency matches the two-photon transition of the reservoir atoms. Both reservoirs are considered empty, to avoid the generation of two photons into the system.

The master equation can be used to calculate the evolution of any system operator O, as $\langle \dot{O} \rangle = \mathrm{Tr}[O\dot{\rho}]$. From the form of the Hamiltonian of eq. (5–13), we can identify the observables

$$\begin{aligned} N_i &= \left\langle a^\dagger_i a_i \right\rangle \\ D^{(\pm)}_i &= \imath^\pm \left\langle a^\dagger_i e^{\imath\omega_0 t} \pm a_i e^{-\imath\omega_0 t} \right\rangle \\ S^{(\pm,j)}_i &= \imath^\pm \left\langle a^\dagger_i a_{i+j} \pm a_i a^\dagger_{i+j} \right\rangle \end{aligned} \tag{5–17}$$

describing, respectively and for the i-th cavity, the mean number of photons, the driving and the exchange of excitations with the j-th cavity. Here $\imath^\pm$

is equal to 1 or ι, to ensure that the operators described in eq. (5–17) are self-adjoint.

The evolution of each of the observables of eq. (5–17) can be calculated through the master equation. However, due to the additional Lindblad term $\mathcal{L}_2$, the system of differential equations is not closed. Within the mean field frame, the following approximations:

$$\left\langle \left(a_i^\dagger a_i + a_{i+j}^\dagger a_{i+j}\right)\left(a_i^\dagger a_{i+j} + a_i a_{i+j}^\dagger\right)\right\rangle \to \left(N_i + N_{i+j}\right) S_i^{(+,j)} \tag{5–18a}$$

$$\left\langle a^\dagger{}_i a_i\, a^\dagger{}_i a_i\right\rangle \to N_i^2 \tag{5–18b}$$

simplify the dynamics, and close the evolution of N_i, $D_i^{(\pm)}$ and $S_i^{(\pm,j)}$. These assumptions are more lax than those usually employed in the mean field approximation [227]. The validity of the result is confined only to the case of strong pumping, that nonetheless can give useful insight into the behaviour of the system.

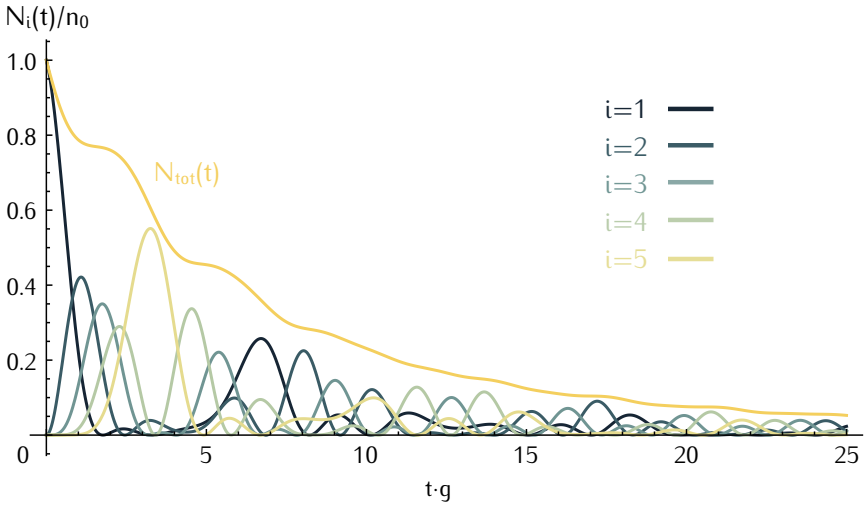
The temporal evolution of N_i, $D_i^{(\pm)}$ and $S_i^{(\pm,j)}$, under the above assumptions, is

$$\begin{aligned}
\dot{N}_i &= \frac{\Omega}{2} D_1^{(+)} \delta_{i,1} \\
&\quad + g\left(S_i^{(+,1)} - S_{i-1}^{(+,1)}\right) \\
&\quad - \gamma_i N_i + \gamma_{TPA}(\omega)\left(N_i - N_i^2\right)
\end{aligned} \tag{5–19a}$$

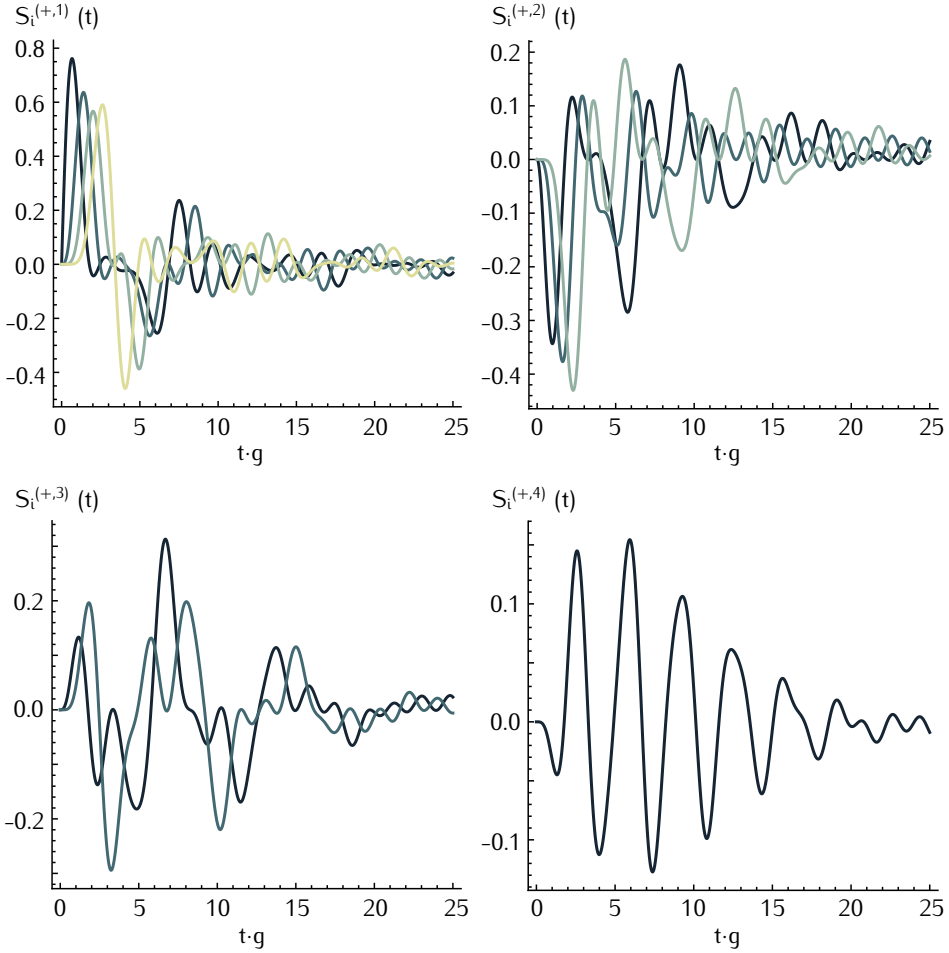
$$\begin{aligned}
\dot{D}_i^{(\pm)} &= \pm\omega_i D_i^{(\mp)} + \Omega\,\delta_{i,1}\delta_+ \\
&\quad + g\left(D_{i+1}^{(\pm)} - D_{i-1}^{(\pm)}\right) \\
&\quad - \frac{1}{2}\gamma_i D_i^{(\pm)} - \gamma_{TPA}(\omega) N_i D_i^{(\pm)}
\end{aligned} \tag{5–19b}$$

$$\begin{aligned}
\dot{S}_i^{(\pm,j)} &= \pm(\omega_i - \omega_{i+j}) S_i^{(\mp,j)} \\
&\quad + g\left(S_{i+1}^{(\pm,j-1)} - S_{i-1}^{(\pm,j-1)} + S_i^{(\pm,j+1)} - S_i^{(\pm,j-1)}\right) \\
&\quad - \gamma_i S_i^{(\pm,j)} + \gamma_{TPA}(\omega)\left(1 - N_i - N_{i+j}\right) S_i^{(\pm,j)}
\end{aligned} \tag{5–19c}$$

The index i goes from 1 to n. Eqs. (5–19a) to (5–19c) form a closed set of differential equations that can be numerically solved in the time domain. To soften the notation I have imposed equal coupling between the cavities, that is, $g_{i,j} = g$. Moreover, there are only $\{n\}$ relevant $N_i(t)$ and $D_i^{(\pm)}$ observables, and $\{n-j\}$ relevant $S_i^{(\pm,j)}$. Therefore, when calculating the evolution of these operators one should remember that $D_i^{(\pm)}(t) = 0$ and $N_i(t) = 0$ for $i = 0$ or $n+1$, and $S_i^{(\pm,j)} = 0$ for $i = 0$ or $i + j \geqslant n$.



(a) Plot of $N_i(t)$ and the total number of photons $N_{tot}(t)$, normalised to n_0. After the first bounces, $N_{tot}(t)$ presents the expected exponential decay.



(b) Plots of $S_i^{(+,j)}$. Notice that for odd j, $S_i^{(+,j)}$ have a zero mean value for $t \gg 1$, while for even j they approach 0 from above and below alternatively. All the plots are in units of n_0.

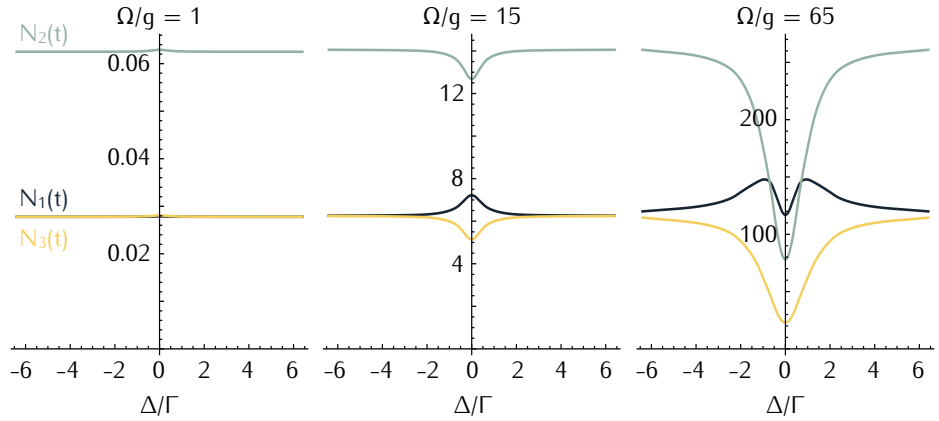
Figure 5.5 Plots of the observables presented in eqs. (5–19) for a $n = 5$ CROW, with $\gamma_{ext} = 1/3\,g$ and $\gamma = 10^{-6}g$. The first element of the CROW was loaded with n_0 photons, and no driving was present, $\Omega = 0$.

As a start, it is useful to consider the case of a highly coupled CROW, where $g > \gamma_{ext}$. In these conditions photons inside the device bounce between cavities several times before being lost. While it is not the ideal case for dispersion, it is a useful configuration to observe the in-cavity dynamics. The system is initialised with light only in the first cavity, $N_1(0) = n_0$, and no driving, $\Omega = 0$. The dynamics can be simplified by considering the CROW to be composed of identical cavities, $\omega_i = \omega_c$, and by taking the rotating wave approximation, $\omega_c = 0$. TPA is for now discarded ($\gamma_{TPA} = 0$), and there is therefore no need for the approximations of eq. (5–18a) and eq. (5–18b).

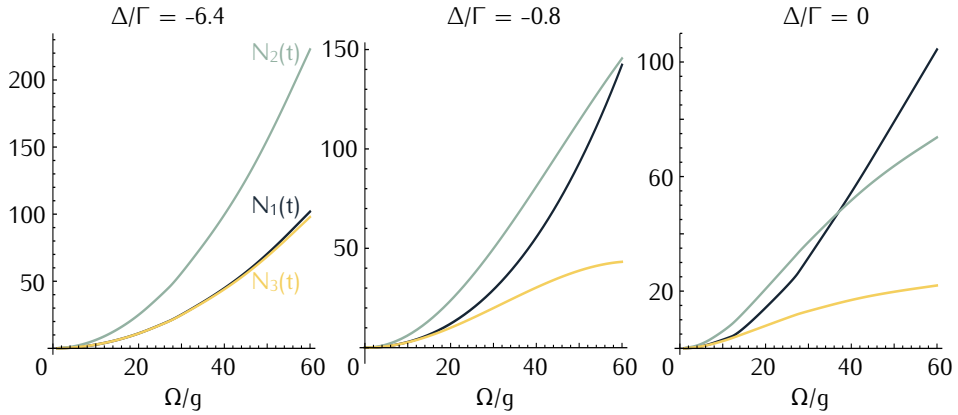
The result, for an $n = 5$ CROW ($\gamma_{ext} = 1/3\, g$, $\gamma = 10^{-6} g$,) is reported in figure 5.5. From the first cavity, the photons are progressively transferred through the CROW, until the last cavity is reached. As can be seen in figure 5.5a, a peak in the photon number of the last cavity is reached as light reaches the end of the CROW. The coherence of the oscillations is progressively lost due to out coupling losses, until the whole device is empty.

As no driving is present, $D_i^{(\pm)} \equiv 0$. Moreover, as $\omega_c = 0$, $S_i^{(-,j)}$ are decoupled from the dynamics, as they only couple to $S_i^{(+,j)}$ through the first line of eq. (5–19c). An interesting pattern can be observed in the $S_i^{(+,j)}$, that can be interpreted as the flux of photons between cavities. After a few bounces, the cavities are empty and $S_i^{(+,j)}$ tend to zero. While for odd j the mean of $S_i^{(+,j)}$ is zero, this is not the case for even j, as can be seen in figure 5.5b.

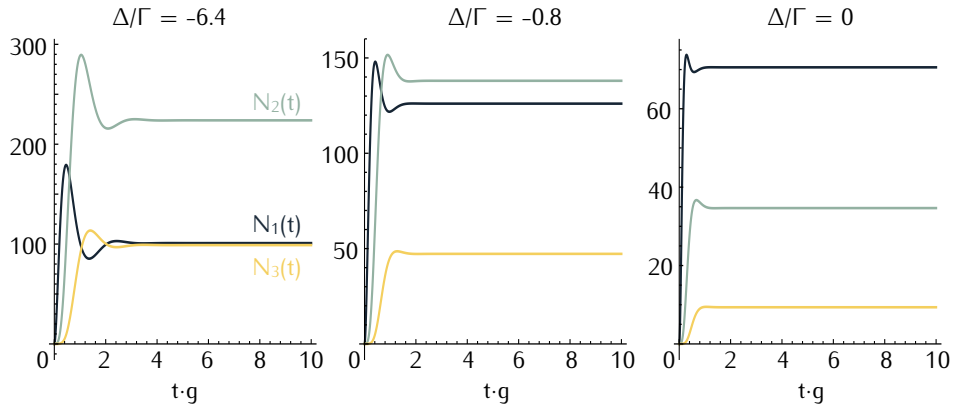
This could be interpreted as a preferential direction for the exchange of photons between cavities. The sign of $S_i^{(+,2)}$ for long times suggests that the exchange of photons between cavities in position i and $i+2$ is preferentially in the forward direction. The same observation on the sign of $S_i^{(+,4)}$ suggests the exchange between cavities in position i and $i+4$ is preferentially in the backwards direction. A complete analysis of the phenomenon would rely on calculating the temporal evolution of the $S_i^{(-,j)}$ as well. Then $S_i^{(+,j)}$ and $S_i^{(-,j)}$ can be treated as ladder operators for a harmonic oscillator.



(a) Plots of the cavity populations as a function of detuning between the excitation light and ω_{TPA}, for increasing values of excitation intensity.



(b) Plots of the cavity populations as a function of excitation intensity, for $\Omega/g = 60$ and for decreasing values of detuning. The values reported in the plot labels correspond to values of $\gamma_{TPA}(\Delta)$ of $10^{-5}, 10^{-3}$ and 10^{-2}.



(c) Plots of the cavity populations as a function of time, for $\Omega/g = 60$ and for decreasing values of detuning.

Figure 5.6 Plots of N_i for a $N = 3$ CROW, with $\gamma_{ext} = 3\,g$ and $\gamma = 10^{-6}g$. $\gamma_{TPA}(\omega)$ has a Lorentzian distribution centred on ω_{TPA}, with maximum value of $10^{-2}g$ and width Γ. All the populations $N_i(t)$ are expressed in terms of g.

Let us now move to the case of coherent loading of the first cavity. As the cavity photon number is now considerably high, and the laser provides a constant supply of photons, TPA is expected to have a stronger effect. In particular, $\gamma_{TPA}(\omega)$ is modelled with a Lorentzian curve[4] (FWHM Γ, and a maximum value of $10^{-2}g$) to represent dissipation from an atomic absorption line. Under these conditions a weakly coupled CROW is a more interesting candidate, due to its high dispersion and enhanced light-matter interaction. The system of eqs. (5–19) can be solved only in the steady-state regime. Figure 5.6 reports $N_i(t)$ for different values of Rabi frequency Ω and detuning Δ from the absorption frequency ω_{TPA} for an $n = 3$ CROW with $\gamma_{ext} = 3\,g$ and $\gamma = 10^{-6}g$.

As expected, the effect of TPA increases with power, as is visible in figure 5.6a. The three plots show the population of each cavity as the laser frequency is swept across the absorption line, for increasing in-coupling power. For weak coupling, the second cavity presents the highest population. However, as the increasing power accentuates the effect of TPA, it becomes almost empty. On the other hand, it is worth noticing that the population of the first cavity is actually increased for values of detuning $\Delta \approx \Gamma$.

A similar behaviour can be witnessed by fixing the laser detuning, and monitoring the populations for increasing power. As reported in figure 5.6b, N_i increases exponentially with Ω for large detuning, as TPA can be neglected. For smaller detuning this behaviour is altered, and eventually a saturation is reached. This can be interpreted as a balance between the cavity pump and the TPA losses.

The effect of TPA can also be witnessed in the time domain, as reported in figure 5.6c. Here the power is fixed, with $\Omega/g = 60$. As the detuning is decreased, equilibrium in the cavity populations is reached at shorter times, and with less pronounced oscillations with respect to large detuning values. This can be interpreted as a consequence of the introduction of disorder in the CROW, with the coherent oscillations of light disrupted by TPA.

[4] Power-broadening of the line is neglected here.

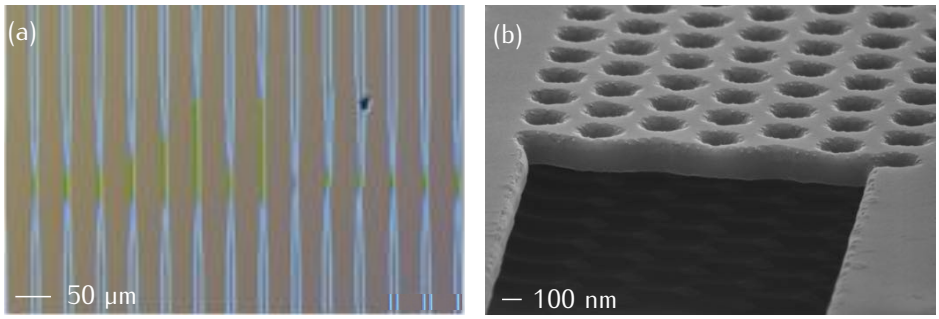


Figure 5.7 Images of the fabricated CROWs. a) optical image of one samples, showing the arrangement of the devices. b) SEM image of the photonic crystal, showing the under etching. The holes in the silicon present a roughened edge, due to the erbium oxide deposition.

5.3 EXPERIMENTAL RESULTS

A wide range of individual samples was fabricated, differing in size and separation of the holes, number of cavities and arrangement of the CROWs. In every sample, an initial ridge waveguide, with a width of 8 µm, is tapered down until it reaches single mode operation. Light was then coupled into a photonic crystal waveguide, itself coupled to a CROW. A specular design is repeated at the other side of the CROW, for a total length of a few millimetres. Light was coupled in and out of the device from either end using objective lenses. The devices were divided in groups with similar photonic crystals, each including CROWS of different number and design of cavities. An image of a portion of a device is reported in figure 5.7(a). A ridge waveguide and a photonic crystal cavity (L3) were added to every device, for calibration and alignment purposes.

The devices were fabricated at the NTT facilities, on a silicon-on-silica substrate. On a substrate of Si(111) a layer of 1 µm of SiO_2 was deposited, followed by another layer of Si(111), 200 nm thick. All the CROWs were under-etched, so that the photonic crystal was suspended in air, as visible in figure 5.7(b). This increased the confinement of light within the silicon slab. The entire set of devices was fabricated twice on two 2 cm $\times$ 2 cm silicon wafers, over which erbium oxide was epitaxially grown. The particular choice of silicon was made to provide a perfect match between the lattices of silicon and erbium oxide [214]. A single crystalline layer of erbium oxide was deposited on each device, for a total thickness 20 and 40 nm respectively.

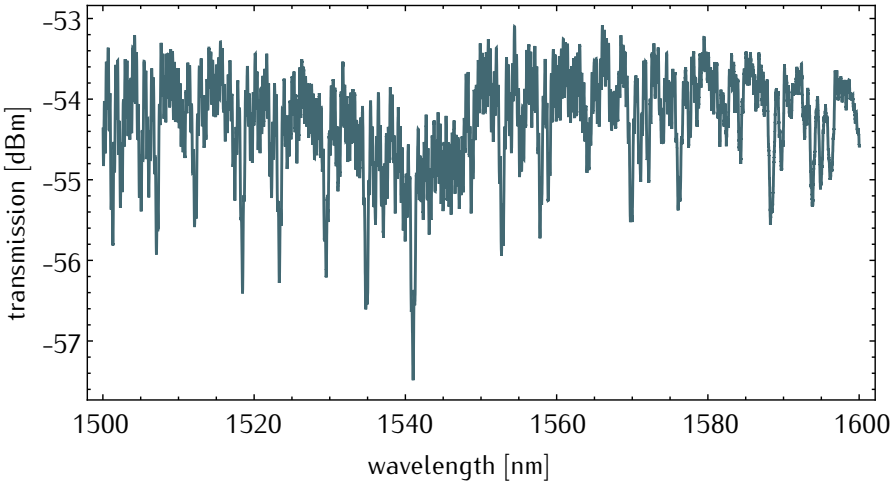


Figure 5.8 Transmission spectrum of a ridge waveguide, with 20 nm Er_2O_3 coating.

The most common silicon-based devices are usually grown on a Si(110) substrate, and can therefore be cut by applying a mechanical force in the desired position. The wafer then naturally breaks along the crystallographic axis, leaving a clean facet. Due to the different configuration, the crystal facets of silicon in the Si(111) were not favourable, and a different cutting procedure was necessary. While mechanical dicing with a diamond-saw is a common option, the quality of the resulting facets is not satisfying. Laser dicing instead provides a sharp and precise cut line. Moreover, the laser ablates a smaller portion of the sample with respect to mechanical dicing. This allowed a higher number of devices to be fabricated on a single wafer, with thinner and denser samples.

As a first test, I measured the transmission spectrum of a ridge waveguide with erbium coating. The excitation light was provided by a semiconductor laser, that was tuned from 1500 to 1600 nm. The laser was coupled into the devices from one end using a long working-distance objective, and collected in the same way from the other side. The collected light was then analysed by means of a power meter.

A measured transmission spectrum is reported in figure 5.8. While a wide plateau of almost unity transmission would be expected for a lossless silicon ridge waveguide, almost no transmission was recorded across the device. Fringes with a period of ~ 6 nm were observed, and a Fourier analysis of the data only revealed a minor resonance close to 260 pm. This excludes any internal reflection between the facets of the device. However, the low level of transmission makes the transmission measurement highly sensitive to any defect in the optical system, as for examples re-

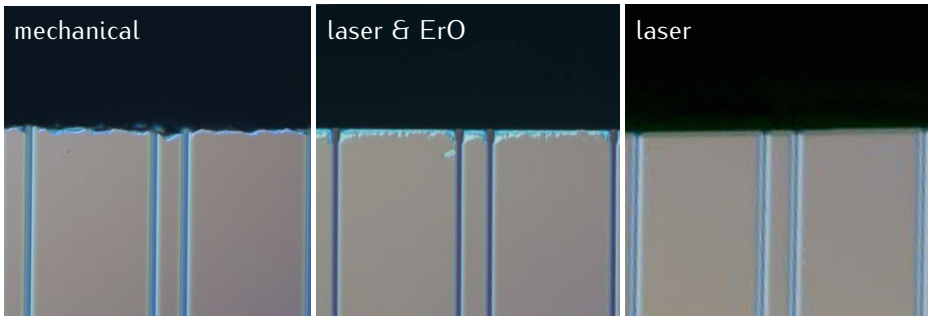
flection between optical elements. These could be at the origin of the oscillatory behaviour of figure 5.8.

I first identified the source of this low transmission in the quality of the facets of the device. An analysis with an optical microscope revealed that the quality of the dicing was lower than expected, and that the facets looked damaged. Some devices showed burn streaks on the cut lines, signs of multiple dicing attempts. This became even more evident when I compared them with a portion of the same device where the erbium had not been evaporated on, as it is visible in figure 5.9a. A sharp and clean edge was present in those cases, evidence for the problematic properties of erbium oxide.

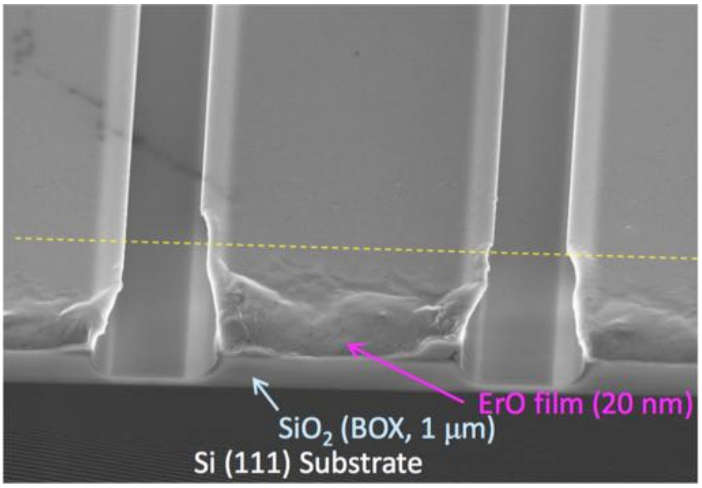
Indeed, the melting point of Er_2O_3 is 800 K higher than the melting point of either Si or SiO_2. Due to the relative high thickness of the devices ($\sim$ 3 mm) the erbium layer was too far from the focus of the cutting laser beam. Before the topmost layer could be vaporised, it was locally heated beyond the melting point of silicon, damaging the facets.

This hypothesis was confirmed by an SEM imaging of the facets, reported in figure 5.9b. Clearly the silicon slab had melted before the Er_2O_3 could be cut. To confirm that damage from the laser dicing was indeed the cause of the low transmission of figure 5.8, the facets of one device were selected for polishing. Focused ion beam (FIB) milling was employed to remove the first $\sim$ 8 µm on either end of a waveguide, leaving a new, sharp facet. The result is visible in figure 5.9c, that reports an SEM image of the milled waveguide, and another image, comparing it with the damaged one. The obtrusions inside the milled trench in the left panel of figure 5.9c are accumulations of gallium ions from the milling.

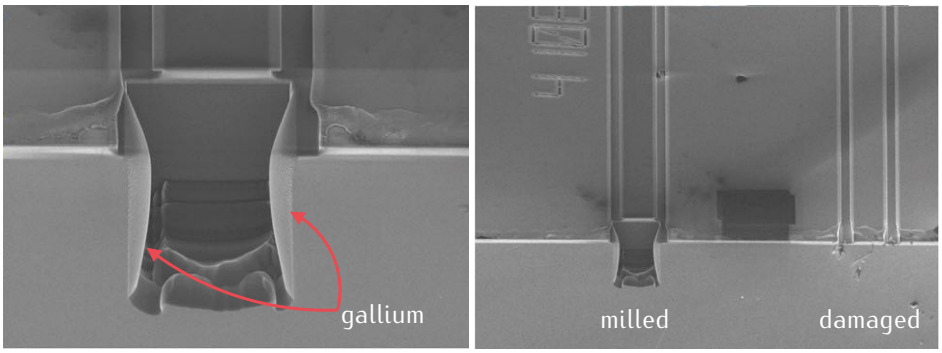
A ridge waveguide, an L3 cavity and a $n = 10$ CROW had their facets milled. Unfortunately, the new transmission spectra showed little improvement, with still no recognisable pattern, as is visible in figure 5.10. This result was confirmed by observing the region of the devices where the ridge waveguides coupled to the photonic crystal. Usually a CCD camera would detect some light scattering at this interface, but no such fluorescence was observed for the milled devices. The same behaviour could be seen in the sample reported in the right panel of figure 5.9c, that was only half-covered in erbium. The scattering fluorescence disappeared as the waveguide or the photonic crystal entered the region covered by Er_2O_3. The fluorescence disappeared altogether as another layer of Er_2O_3 was deposited over the whole sample.



(a) Results of different cutting techniques. The presence of the Er_2O_3 layer severely affects the efficiency of the laser dicing.



(b) SEM image of the silicon facets of the devices. It is possible to notice the damage close to the edges due to the high temperature of the cutting laser.



(c) Facets of a device after the FIB milling. Notice the accumulation of gallium ions close to the trench. The right panel reports the comparison with the damaged facet.

Figure 5.9 Effects of laser dicing on the silicon facets of the devices, and the results of FIB milling.

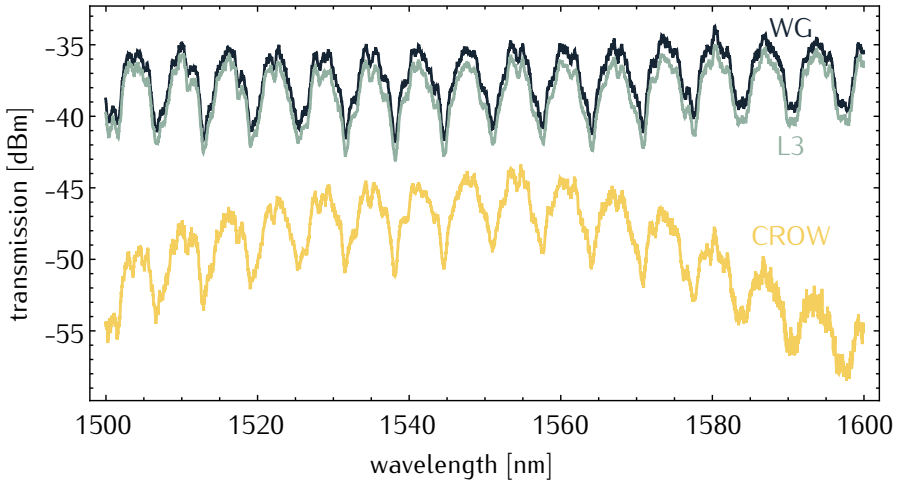


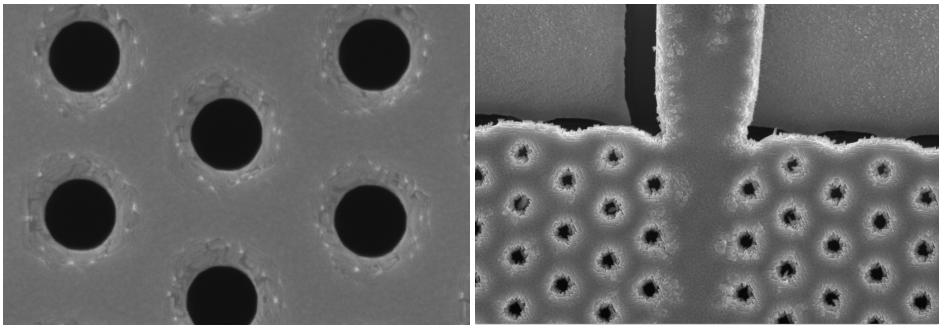
Figure 5.10 Transmission spectrum of a ridge waveguide, an L3 cavity and a CROW, after FIB milling. Still very little transmission can be detected.

This unexpected absorption effect of Er_2O_3 could have ben caused by defects in the deposition procedure. An amorphous layer of oxide could cause a high scattering of the photonic mode, hampering the transmission through the devices. To further study the effect of the coating of Er_2O_3 the samples were again inspected under the SEM.

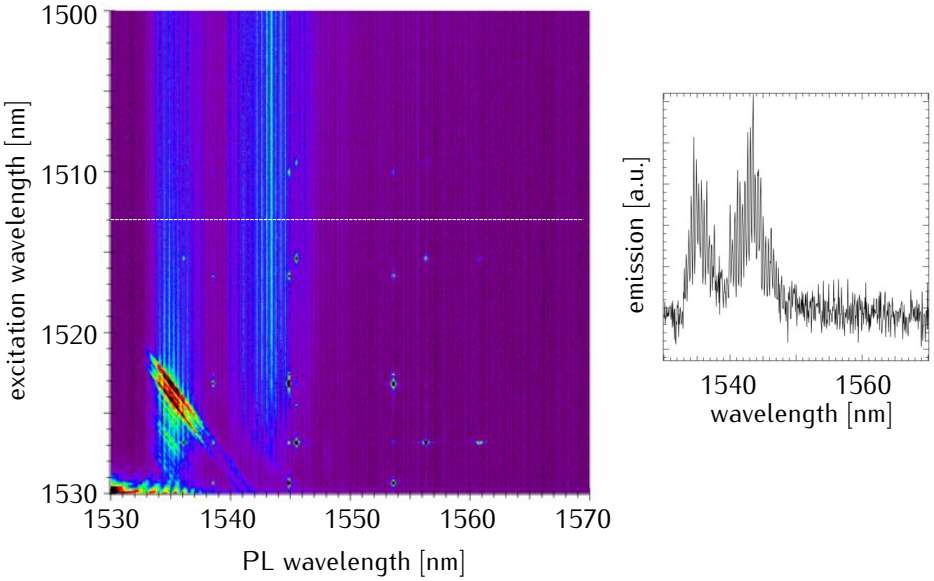
As reported in the left panel of figure 5.11a, the 20 nm Er_2O_3 layer looked flat, and single crystalline. The situation was radically different for the 40 nm layer, visible in the right panel of figure 5.11a. Single flakes of Er_2O_3 were clearly visible, confirming an unexpected growth of the oxide layer.

As the emission and absorption spectra of Er_2O_3 change with the crystallinity of the oxide, I studied the 20 nm Er_2O_3 layer at cryogenic temperatures to test the samples against the results reported in figure 5.3. The milled sample was placed inside a helium evaporation cryostat, and brought to a temperature of 3 K. The sample was mounted on a copper block in contact with the cold finger of the cryostat, and thermally connected with silver paint. The copper mount presented an angled edge, and the sample was pushed against it. In this way the topmost layer of the sample was in contact with the cold sample mount[5]. Fluorescence from the sample was collected from a confocal microscope and analysed with a spectrometer.

[5]A similar sample mount couldn't be used in chapter 3, as the distance between the radiation shield and the sample is ~ 100 µm. Instead, we spread the silver paint up the sides of the samples, to reach a similar effect.



(a) SEM images of the erbium oxide layer. Devices with 20 nm of Er_2O_3 (left panel) show a flat surface, while for the 40 nm case (left) the single crystallinity is compromised.



(b) Analysis of the photoluminescence of the 20 nm Er_2O_3 layer. The comparison with fig. 5.3 points towards an amorphous layer of oxide. The inset shows a cut of the emission spectrum along the dashed white line.

Figure 5.11 Analysis of the erbium oxide layer, revealing the differences with the case of crystalline erbium.

The fluorescence from the sample for different excitation wavelengths is reported in figure 5.11b. The contrast with figure 5.3 is striking, as none of the recognisable features of the emission of Er_2O_3 can be observed. The right panel of figure 5.11b reports the fluorescence on the white, dashed line of the left panel. This same fluorescence could be observed over a wide range of excitation wavelengths, in contrast with the expected trace of figure 5.3. None of the recognisable features of erbium oxide are visible, hinting at a problem in the erbium oxide deposition.

This result was rather unexpected, as the deposition of Er_2O_3 was based on a well-established and reliable technique, and the growth parameters were not changed from previous experiments. However, the amorphous, or at least non-crystalline, nature of the oxide layer could be at

the origin of the absence of transmission through the device, due to multiple scattering with crystalline units within the seemingly uniform Er_2O_3 layer.

5.4 SUMMARY AND OUTLOOK

In this chapter I have presented the advances towards a passive integrated device, capable of light-matter interaction through resonant TPA. I have presented the master equation relative to this system, and by taking a mean field approximation I have obtained a closed system of differential equations specifying the dynamics of the system. These were used to simulate the behaviour of a CROW in two different configurations of cavity-cavity coupling and driving. In the case of coherent loading of the CROW, I showed that already for a value of $\gamma_{TPA} = 10^{-2} g$ the effect of two-photon absorption becomes appreciable, leading to variations in the distribution of photons in the cavities.

The approximations of eqs. (5–18a) and (5–18b) are only a first attempt at solving the problem of dissipative two-photon loss in coupled cavities. More conservative approximations, like those introduced by Casteels et al. [227], are needed to obtain a reliable description of the system, especially when considering the case of single photon loading of the CROW and the problem of single-photon optical switching.

A crucial next step would consist in calculating a value for $\gamma_{TPA}(\omega)$. Following the master equation treatment, one could relate the expression of $\gamma_{TPA}(\omega)$ to the coupling constant of eq. (5–15b):

$$\gamma_{TPA} = \pi \int d^3k \, D_4(\mathbf{k}) \, |\chi(\mathbf{k})|^2 \, \delta(kc - \omega). \tag{5–20}$$

Here the density of states $D_4(\mathbf{k})$ for the reservoir modes can be replaced by the density $\mathcal{N}$ of erbium atoms. The coupling constant $\chi(\mathbf{k})$ could then be related to the TPA cross-section for erbium.

An extensive study of TPA has been carried out in the case of dye molecules [228]. For a collection of molecules in solution, the intensity of excitation light decreases with length according to the equation

$$\frac{\partial I}{\partial z} = -\mathcal{N} \, \sigma_{TPA} \, F \, I \tag{5–21}$$

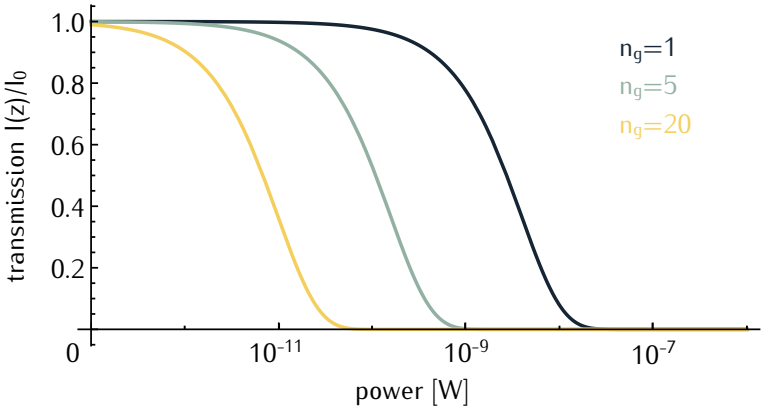


Figure 5.12 Plot of the transmission through a 1 mm long device coated in erbium, for different input powers, and for different group indices.

where $F = I/h\nu$ is the photon flux, and σ_{TPA} is the two-photon absorption cross section, defined as

$$\sigma_{TPA} = \frac{2\pi h\nu^2}{\epsilon_0^2 c^2 n^2} \frac{n_g^2 n^2}{\Gamma} \left(\frac{\mu_{gi}\, \mu_{if}}{\mathcal{E}_{gi} - h\nu} \right)^2 . \tag{5–22}$$

The cross section σ_{TPA} is expressed in Göppert-Mayer units, where 1 GM $= 10^{-50}$ cm$^4 \cdot$ s $\cdot$ photons^{-1} $\cdot$ molecule^{-1}. In eq. (5–22), Γ is the width of the TPA absorption band, in energy units. μ_{gi} and μ_{if} are the dipole moments of the two transitions between the ground and intermediate state, and between the intermediate and final state respectively. $\mathcal{E}_{gi}$ is the energy gap between the ground and the intermediate state. Finally, $n_g = c/v_g$ is the group index of the waveguide mode. We can now insert the values for the relevant erbium levels, as presented in figure 5.4. Considering the frequency of each transition, light with a wavelength of $\sim$ 1587 nm would undergo TPA between the ground state and the $^4I_{9/2}$ level. The $^4I_{15/2}$ state of erbium, here working as the intermediate state of TPA, has a long lifetime, of the order of $\sim 10^{-2}$ s. On the other hand, the $^4I_{9/2}$ manifold has a radiative lifetime of a few ms, due to fast multi-photon decay. The dipole moments of both transitions can be calculated form eq. (1–2). The refractive index of Er_2O_2 is $n = 1.9$. Considering an absorption line Γ of a few MHz and $n_g = 1$, then σ_{TPA} for erbium oxide is of order $\sim$ 100 GM, a value comparable with dye molecules in solution [228].

Starting from the solution to eq. (5–21), the attenuation of the field intensity due to TPA follows the relation

$$I(z) = I_0 e^{-\mathcal{N}\sigma_T \frac{P_0}{\hbar\omega\mathcal{A}} z} \tag{5–23}$$

where P_0 is the input power and $\mathcal{A}$ is the mode area. It is interesting to use eq. (5–23) to calculate the output intensity as a function of input power and group index for the case of a device of 1 mm in length, similar to the devices fabricated for the project. The result is shown in figure 5.12. At first, one should notice that the dissipation from TPA has a considerable effect, as with $n_g = 1$ an input signal of a few hundred nW is completely depleted at the end of the device. With increasing group index the minimum input power required for a complete extinction of the signal decreases, and reaches the fW level for $n_g = 20$. While this group index is feasible for a high quality photonic crystal, the results are based on a mode area corresponding to the waveguide cross-section, instead of the overlap between the waveguide mode and the erbium layer. A simulation of the waveguide mode is necessary to calculate a precise value of the attenuation.

Nonetheless, these preliminary results point at a considerable gain in TPA by integration in photonic crystal structures. Lack of time prevented a more thorough analysis of the devices fabricated at NTT. I believe that the anomalous transmission was caused by an improper deposition of erbium on the silicon substrate, especially considering the spectroscopic results of figure 5.11. A new batch of devices could be fabricated, first separating the samples with laser dicing, and then depositing a layer of erbium oxide. As an additional precaution, a layer of erbium oxide could be deposited on a pre-existing L3 cavity, checking wether the cavity modes are again disrupted by the erbium oxide, or, instead, enhanced.

6 SUMMARY AND CONCLUSIONS

In this thesis I have demonstrated efficient and reliable single photon emission from single DBT molecules in anthracene. A confocal microscope was assembled to characterise DBT-doped anthracene crystals; the density and orientation of the emitters, their saturation intensity, linewidth and spectrum were recorded. The molecules followed the behaviour dictated by the optical Bloch equations over the whole inspected range of temperature and saturation parameter, the first test of this kind on a single emitter in the solid state. At the same time I was able to characterise the dephasing process of the molecule, measuring the frequency of the local phonon field.

I also demonstrated the coupling of a single molecule to a photonic nanostructure for the first time in our group. I am not aware of any other experiment with single molecules coupled to hybrid plasmonic waveguides. The preliminary results obtained showed a clear antibunching curve from a single DBT molecule in a waveguide. As the device featured the weakest emission enhancement, these results represent the minimum achievable for these devices, and can only be improved by moving to smaller channel widths. I suggested improvements in deposition technique and optical inspection of the devices, that are currently being employed to further investigate these devices.

Together, these results confirm DBT as an excellent candidate for single photon generation. Moreover, molecules coupled to plasmonic waveguides or cavities can be used as integrated sources of optical non-linearity. Both applications are being explored in our group, and we hope to further establish dye molecules as a valuable tool of quantum nanophotonics.

Finally, I further explored the enhancement of light-matter interaction by studying two-photon absorption in coupled optical cavities. I presented a mean field approximation that allowed me to describe the dynamics of the system in case of coherent loading of the device. This analysis was used to design a series of coupled photonic crystal cavities, with a coating of erbium oxide as the active element. While no measurement could be carried out due to a fabrication problem, a calculation of the two-photon absorption cross section for these devices pointed to a potential application in quantum computation.

Part III

APPENDIX AND BACKMATTER

A APPENDIX TO CHAPTER 2

A.1 SOLVING THE OPTICAL BLOCH EQUATIONS

In this section I present the derivation of the solution of the optical Bloch equations. The solution of the steady-state regime is used to derive an expression for the collected fluorescence rate and for the saturation intensity. The Laplace transform method used to derive the analytical solution of eq. (2–14) is also outlined.

If we recall figure 1.7, and that the intersystem crossing rate Γ_{isc} for DBT in Ac is negligible, we can write these equations as

$$\begin{cases} \dot{\rho}_{22} = -\Gamma_1 \rho_{22} + \frac{1}{2}\imath\Omega_0(\rho_{21} - \rho_{12}) \\ \dot{\rho}_{12} = (\imath\Delta - \Gamma_2)\,\rho_{12} - \frac{1}{2}\imath\Omega_0\,(\rho_{22} - \rho_{11}) \\ \dot{\rho}_{11} = -\dot{\rho}_{22} \\ \dot{\rho}_{21} = \dot{\rho}_{12}^{*} \\ \rho_{11} + \rho_{22} = 1, \end{cases} \tag{A–1}$$

where subscripts 1 and 2 refer to states $S_{0,0}$ and $S_{1,0}$ respectively. Γ_1 is the total decay rate for population leaving the state $S_{1,0}$ by all of the transitions $S_{1,0} \to S_{0,\nu}$. It is assumed that all this population returns to $S_{0,0}$. Γ_2 is the coherence decay rate of the $|2\rangle \to |1\rangle$ transition. $\Omega_0 = \frac{\mu_{12} E}{\hbar}$ is the Rabi frequency, where E is the absolute value of the amplitude of the electric field $\mathbf{E}$ and μ_{12} is the projection of the transition dipole moment along the direction of $\mathbf{E}$. $\Delta = \omega - \omega_0$ is the detuning between the exciting field and the $|2\rangle \to |1\rangle$ transition, which is resonant at frequency ω_0. Equation (2–1) also makes the rotating wave approximation and adopts an appropriate interaction picture to eliminate the time-dependence of the interaction [1, sec. 2.7].

Steady-state regime

The steady state regime for eq. (A–1) is

$$\begin{cases} 0 = \Gamma_1 \rho_{22} + \dfrac{1}{2} \imath \Omega_0 (\rho_{21} + \rho_{12}) \\ 0 = -\Gamma_1 \rho_{22} + \dfrac{1}{2} \imath \Omega_0 (\rho_{21} + \rho_{12}) \\ 0 = (\imath \Delta - \Gamma_2)\, \rho_{12} + \dfrac{1}{2} \imath \Omega_0 (\rho_{22} - \rho_{11}) \end{cases} \tag{A–2}$$

Let us focus on the expression for the density matrix element ρ_{22}, describing the population of the excited state $S_{1,0}$. This can be easily obtained as

$$\begin{aligned} \rho_{22}^{ss} &= \frac{1}{2} \frac{\Gamma_2 \Omega_0^2}{\Gamma_1 \Gamma_2^2 + \Gamma_1 \Delta^2 + \Gamma_2 \Omega_0^2} \\ &= \frac{1}{2} \frac{\frac{\Omega_0^2}{\Gamma_1 \Gamma_2}}{1 + \frac{\Delta^2}{\Gamma_2^2} + \frac{\Omega_0^2}{\Gamma_1 \Gamma_2}} \end{aligned} \tag{A–3}$$

that has the expected Lorentzian response to frequency. We have already highlighted the saturation parameter $S = \frac{\Omega_0^2}{\Gamma_1 \Gamma_2}$. A more intuitive expression can be obtained if we include the expression for the on-resonance Rabi frequency $\Omega_0^2 = (\frac{\mu E}{\hbar})^2 = \frac{\mu^2}{\hbar^2} \frac{2I}{\epsilon \epsilon_0 c}$, with μ as the transition dipole moment, and E and I respectively as the electric field amplitude and intensity of the excitation field. For resonant excitation (i.e. $\Delta = 0$) eq. (A–3) becomes

$$\rho_{22}^{ss} = \frac{1}{2} \frac{\frac{2\mu^2}{\epsilon \epsilon_0 c \hbar^2} \frac{I}{\Gamma_1 \Gamma_2}}{1 + \frac{\Delta^2}{\Gamma_2^2} + \frac{2\mu^2}{\epsilon \epsilon_0 c \hbar^2} \frac{I}{\Gamma_1 \Gamma_2}} = \frac{1}{2} \frac{I/I_{sat}}{1 + I/I_{sat}}. \tag{A–4}$$

ρ_{22}^{ss} represent the probability of excitation of the molecule in steady-state. The rate of emission of photons R is then the product between ρ_{22}^{ss} and the spontaneous emission rate Γ_1.

Eq. (A–4) describes the population dynamics for a single molecule, as a function of the rates Γ_1, Γ_2 and Ω_0. We have seen in section 2.1.2 and figure 2.2 the different behaviours of the density matrix elements as saturation and dephasing rate are increased. These results are valid for our approximation of a single molecule as a pure two level system. While it is a sensible assumption at cryogenic temperature, this approximation breaks down at room temperature. The absorption profile of the ZPL and of the other $S_{0,0} \rightarrow S_{1,n}$ transitions are overlapped, with each having an unknown Franck-Condon and Debye-Waller factors (cf. figure 1.8).

We therefore have to assume that, while we can discard any coherence due to phonon interactions, a part of the excitation light is still resonant with the ZPL. The dynamics of the molecule can be described by the rate equations

$$\begin{cases} \dot{\rho}_{11} = -K\left(\rho_{11} - \alpha(\omega)\,\rho_{22}\right) + \Gamma_1\rho_{22} \\ \dot{\rho}_{22} = -\dot{\rho}_{11} \end{cases} \tag{A–5}$$

with $\rho_{22} + \rho_{11} = 1$. Here $K = S\Gamma_1$ is the pumping rate of the molecule from level $|1\rangle$ to level $|2\rangle$. The additional term $\alpha(\omega)K\,\rho_{22}$ represents the stimulated emission due to the resonance between the excitation light at frequency ω and the ZPL. This new set of rate equations gives the solution for the excited state population

$$\rho_{22}(t) = \frac{K}{(1+\alpha(\omega))K + \Gamma_1}\left(1 - e^{-((1+\alpha(\omega))K+\Gamma_1)t}\right). \tag{A–6}$$

with steady-state solution $\rho_{22}^{ss} = K((1+\alpha(\omega))K + \Gamma_1)$. We can assume that, for excitation light resonant with the ZPL, $\alpha(\omega)$ assumes its maximum value of 1, while it decreases for increased blue-detuned pumping. Eventually the overlap between the laser and the broadened ZPL is negligible, $\alpha(\omega) = 0$ and we recover the same result as eq. (2–22), with $\rho_{22}^{ss} = K/(K+\Gamma_1)$. On the other hand, if we assume perfectly resonant light, $\alpha(\omega) = 1$ and we recover the behaviour for $\Gamma_1/\Gamma_2 \to +\infty$, with $\rho_{22}^{ss} = K/(2K+\Gamma_1)$.

I am not aware of any measurement aimed at determining the parameter $\alpha(\omega)$. On one hand, an analysis of the absorption spectra of room-temperature DBT could provide an answer. A saturation scan taken at different wavelengths can provide a wavelength dependent R_{inf}. This could be compared with the lifetime of the emitter, according to the usual relation $R_{inf} = \eta\Gamma_1/(1+\alpha(\omega))$, where η is the collection efficiency. Due to the considerable uncertainty in the calculation of η and the small variation we are trying to oberserve, we need a comparison measurement. We expect the maximum detectable count rate to decrease as the excitation wavelength approaches the ZPL, until a minimum value is reached for maximally resonant light. We expect $\alpha(\omega) \approx 0$ when ω is above $\sim 2\pi c/760$ nm, as we expect the ZPL to be broadened to a maximum of 14 THz [132]. We can then calculate the ratio

$$\frac{R_{inf}(\omega)}{R_{inf}^{blue}} = \frac{\eta(1+\alpha(\omega))^{-1}\Gamma_1}{\eta\,\Gamma_1} = \frac{1}{1+\alpha(\omega)} \tag{A–7}$$

from which we can extract the behaviour of $\alpha(\omega)$.

An alternative method could be to compare R_{inf} at room and cryogenic temperatures. We know that the 2-level system approximation holds for a single DBT molecule excited resonantly at cryogenic temperatures. Therefore, $R_{inf}(T = 3\ K) = \eta\,\Gamma_1/2$. This time it is not possible to simplify the collection efficiency: as we have seen in figure 4.12 the collection efficiency is highly dependent on the spectrum of the molecule. A similar analysis could be carried out, once the position of the ZPL, the spectrum and the lifetime of the molecule are known. Eq. (A–7) takes the form

$$\frac{R_{inf}^{warm}(\omega)}{R_{inf}^{cold}} = \frac{\eta_{warm}(1+\alpha(\omega))^{-1}\Gamma_1}{\eta_{cold}\Gamma_1/2} = 2\frac{\eta_{warm}}{\eta_{cold}}\frac{1}{1+\alpha(\omega)}. \tag{A–8}$$

A precise knowledge of the collection efficiency of the setup is necessary. While it could be obtained in the same manner reported in section 4.4.2, its uncertainty could compromise the precision of the measurement. It is worth noticing that eq. (A–8) could work also for different molecules: in this case the spontaneous decay rates cannot be simplified, and have to be added to the final expression.

Analytical solution

The steady-state solution of the Optical Bloch equations allows us to describe the photoluminescence collected from a molecule over long times $t \gtrsim \Gamma_1^{-1}$, but we are also interested in the transit evolution over shorter times of the populations $\rho_{ii}(t)$ and of the coherences $\rho_{ij}(t)$. While partial solutions of the problem have been presented in the literature [88], I have not found a full solution, so I present one here.

The eqs. (A–1) are a closed set of differential equations. A direct attempt at solving them could result in involved calculations. The problem can be tackled more efficiently by making use of Laplace transforms [229]. Taking the Laplace transform of each equation of (A–1) turns differential equations into simple algebraic ones, due to the relation

$$\mathcal{L}\left[\dot{\rho}_{ij}\right](s) = s\tilde{\rho}_{ij}(s) - \rho_{ij}(0) \tag{A–9}$$

where $\tilde{\rho}_{ij}(s) = \mathcal{L}\left[\rho_{ij}\right](s)$ is the Laplace transform of the matrix element. Another property of Laplace transform states that

$$\mathcal{L}^{-1}\left[\sum_i \frac{c_i}{s - s_i}\right](t) = \sum_i c_i e^{s_i t}. \tag{A–10}$$

By solving the algebraic equations for $\tilde{\rho}_{ij}$, and expressing all the solutions according to eq. (A–10) an easy expression for the time-domain form can be achieved.

Let us concentrate on the population of the excited state. Considering a system described by the optical Bloch equations (A–1) and for resonant excitation, $\tilde{\rho}_{22}(s)$ has the form

$$\tilde{\rho}_{22}(s) = \frac{\Omega_0^2}{2s\left(s^2 + s\Gamma_1 + s\Gamma_2 + \Gamma_1\Gamma_2 + \Omega_0^2\right)}. \tag{A–11}$$

The denominator has 3 solutions s_j, therefore eq. (A–11) can be expressed as the sum of 3 fractions:

$$\begin{aligned} \tilde{\rho}_{22}(s) &= \Omega_0^2 \sum_{j=1}^{3} \frac{c_j}{s - s_j} \\ c_j &= \frac{1}{\prod_{i=1}^{3}(s_j - s_i)} \quad i \neq j. \end{aligned} \tag{A–12}$$

Using now eq. (A–10), it is possible to write $\rho_{22}(t)$ as

$$\rho_{22}(t) = \Omega_0^2\left(c_1 e^{s_1 t} + c_2 e^{s_2 t} + c_3 e^{s_3 t}\right). \tag{A–13}$$

By inserting the values for s_j and c_j (note that one solution is null), we reach the final expression:

$$\rho_{22}(t) = \frac{1}{2}\frac{\Omega_0^2}{\Gamma_1\Gamma_2 + \Omega_0^2}\left[1 - \frac{p+q}{2q}e^{-(p-q)t} + \frac{p-q}{2q}e^{-(p+q)t}\right] \tag{A–14}$$

where

$$\begin{aligned} p &= \frac{\Gamma_1 + \Gamma_2}{2} \\ q &= \sqrt{\frac{(\Gamma_1 - \Gamma_2)^2}{4} - \Omega_0^2}. \end{aligned} \tag{A–15}$$

The same process can be repeated to obtain ρ_{11} and ρ_{12}, introduced in eqs. (2–11).

A.2 THE SCATTERED FIELD

In the previous section we have obtained a solution for the OBEqs that allowed us to understand the population dynamics of a two-level system during absorption and emission. However, we are only able to gauge this behaviour by collecting the fluorescence emitted by our molecules. We need therefore a better understanding of the process of scattering of light, keeping in mind the quantum nature of the interaction between the exciting field and the molecular dipole.

A perturbative approach to the scattering process has indeed been attempted. In the case of weak exciting field, this approach is successful in describing the fluorescence spectrum of a driven two-level system [230]. However, due to the non-linear response to power of our system, soon this description becomes inadequate. Even when the system is in equilibrium with the exciting field, oscillations about this value must be accounted for. These oscillations separate the scattered field into a coherent and an incoherent component, the latter becoming more and more prominent at high excitations [231]. The picture of scattering that emerges is that of a coherent process of absorption and emission of photons, that cannot be treated as independent events.

A more definite witness of the non-classical nature of the interaction can be found if we analyse the photon statistics of the scattered field. Be recording the time of arrival of the photons, we would see that the probability of detecting two photons at the same time is negligible. This is due to a peculiar property of the harmonic oscillator we are using to model the two-level system. As there is only one available excited level, a maximum of one quantum of excitation can be present at any given time; two photons must be separated in time by an absorption event [232]. This particular phenomenon is called "antibunching", and requires the quantisation of the electromagnetic field to be accurately described [233].

We need to introduce new tools in order to study the properties of the scattered field. Both the non-linear behaviour of the fluorescence spectrum and the antibunching of the scattered field arise from the quantum nature of the system we are considering. The average values of the dipole operators $\langle \sigma_i \rangle$ are known up to an uncertainty given by their probabilistic nature. To take into account these stochastic effect, we introduce the first and second-order correlation functions

$$G^{(1)}(t, t+\tau) = \left\langle E^-(t)\, E^+(t+\tau) \right\rangle \tag{A–16a}$$

$$G^{(2)}(t, t+\tau) = \left\langle E^-(t)\, E^-(t+\tau)\, E^+(t+\tau)\, E^+(t) \right\rangle \tag{A–16b}$$

of the electric field operator $E(\mathbf{r},t) = E^+(\mathbf{r},t) + E^-(\mathbf{r},t)$ where $E^- = (E^+)^\dagger$, with special attention to the portion of $E(\mathbf{r},t)$ that is scattered by the two-level system.

In order to relate the correlation functions to the solutions of the Optical Bloch equations obtained before we have to take a step back. Given the state $|\psi\rangle$ of the molecule we have seen that writing the Schrödinger equation for the components of $\rho = |\psi\rangle\langle\psi|$ brings us to the optical Bloch equations (2–1) [1, sec. 2.7]. However, the same result can be obtained by writing the Heisenberg equation of motion. We will therefore start by introducing the formalism of the master equation, from which we will able to relate the dynamics of the two-level system with the scattered field.

A.2.1 Open systems

Let's start from the same assumption as before: a two-level system interacting with a classical driving field

$$\mathbf{E}(t) = \hat{e}E\cos(\omega t) \tag{A–17}$$

where $\hat{e}$ is the unit vector defining the polarisation of the field and E is the amplitude, oscillating at the frequency ω. The system is not isolated, but is interacting with the environment. This is modelled as a reservoir R_1, a bath of harmonic oscillators [234, sec. 2.3]. For the case of single molecules these oscillators are the mode of the electromagnetic field. Quanta of excitation can be exchanged from the system to the environment and vice-versa, but the state of the reservoir is unchanged (Markov approximation). Also, the reservoir and the system states are separable at any given time (Born approximation). Under these assumptions it is possible to recover the model of a driven two-level system. To fully account for our case of single molecules in a matrix, we need to include the dephasing effect of phonon interaction. To this purpose we introduce two additional reservoirs R_2 and R_3, each one in contact with one of the two levels of the molecule [234, sec. 2.2.4]. We are thus introducing interactions that conserve the number of excitations in the system, but destroy their phase.

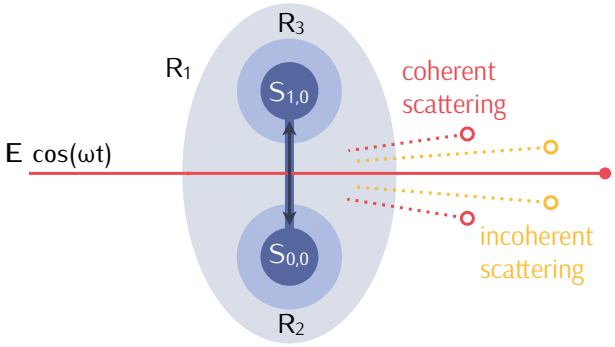


Figure A.1 Diagram of the open system composed of a two-level system and three reservoirs R. The different Hamiltonians $\mathcal{H}_{SR1}$, $\mathcal{H}_{SR2}$ and $\mathcal{H}_{SR2}$ model the interaction between the system and the reservoirs. The molecule is then driven with an external field $\mathbf{E}$, that is treated classically. To fully describe the radiation scattered by the molecule field quantisation is necessary.

We can express the Hamiltonians governing the two-level system S, the reservoirs R_1, R_2 and R_3, and the interactions $S \leftrightarrow R_1$, $S \leftrightarrow R_2$ and $S \leftrightarrow R_3$ as

$$\mathcal{H}_S = \frac{1}{2}\hbar\left(\omega_0 + \omega_p\right)\sigma_z + \imath\frac{1}{2}\Omega_0\left(e^{-\imath\omega t}\sigma_+ + e^{\imath\omega t}\sigma_-\right) \quad \text{(A–18a)}$$

$$\mathcal{H}_{R1} = \hbar\sum_{k,j}\omega_k a^\dagger_{k,j}a_{k,j} \quad \text{(A–18b)}$$

$$\mathcal{H}_{SR1} = \hbar\sum_{k,j}\left(\zeta^*_{k,j}a^\dagger_{k,j}\sigma_- + \zeta_{k,j}a_{k,j}\sigma_+\right) \quad \text{(A–18c)}$$

$$\mathcal{H}_{R2} + \mathcal{H}_{R3} = \hbar\sum_{j}\left(\nu_{1j}b^\dagger_{1j}b_{1j} + \nu_{2j}b^\dagger_{2j}b_{2j}\right) \quad \text{(A–18d)}$$

$$\begin{aligned}\mathcal{H}_{SR2} + \mathcal{H}_{SR3} = \hbar\sum_{i,j}\Big(&\xi_{1i,j}\left(b^\dagger_{1i}b_{1j} - \delta_{i,j}\bar{n}_{1i}\right)\sigma_-\sigma_+ \\ &+ \xi_{2i,j}\left(b^\dagger_{2i}b_{2j} - \delta_{i,j}\bar{n}_{2i}\right)\sigma_+\sigma_-\Big),\end{aligned} \quad \text{(A–18e)}$$

written in the rotating-wave approximation. We have introduced here the Pauli matrices $\sigma_- = |1\rangle\langle 2|$, $\sigma_+ = |2\rangle\langle 1|$ and $\sigma_z = |2\rangle\langle 2| - |1\rangle\langle 1|$, where σ_- and σ_+ are the operators for the excitation or de-excitation of a molecule, and σ_z is the population difference between states $|1\rangle$ and $|2\rangle$. ω_p is the frequency shift due to the phase-destroying processes. The operators $a^\dagger_{k,j}$ and $a_{k,j}$, and $b^\dagger_{ij}$ and b_{ij} are the creation and annihilation operators for the reservoirs. In the case of R_1 they are related to creation or annihilation of a photon of frequency ω_k, wave-vector $\mathbf{k}$, and polarisation mode $\hat{\mathbf{e}}_{k,j}$,

coupled to creation or annihilation of an atomic excitation. The coupling constant of this process is

$$\zeta_{\mathbf{k},j} = -\imath e^{\imath \mathbf{k}\cdot\mathbf{r}_A}\sqrt{\frac{\omega_k}{2\hbar\varepsilon_0 V}}\epsilon_{\mathbf{k},j}\cdot\boldsymbol{\mu} \tag{A–19}$$

where V is the quantisation volume and $\mathbf{r}_A$ is the position of the molecule. On the other hand, the interaction with the reservoirs R_2 or R_3 destroys the phase of the dipole by virtual processes that annihilate a phonon of energy $\hbar\nu_{1(2)i}$ and create one of energy $\hbar\nu_{1(2)j}$, but conserves the excitation of the system. The coupling constant is $\xi_{1(2)i,j}$. As the reservoirs are modelled by a collection of harmonic oscillators, it is possible to identify a mean number of excitations present in each one. At room temperature, the presence of optical photons can be disregarded, and R_1 is empty. This is not true for phonons. $\bar{n}_{1i}$ and $\bar{n}_{2i}$ express precisely this quantity, the mean number of phonons present in the reservoirs R_2 and R_3.

We are interested in how the scattered field is related to the dynamics of the two-level system. We can write the electric field $E(\mathbf{r},t)$ in terms of the operators of R_1 as

$$E^+(\mathbf{r},t) = \imath\sum_{\mathbf{k},j}\hat{\epsilon}_{\mathbf{k},j}e^{\imath\mathbf{k}\cdot\mathbf{r}}\sqrt{\frac{\hbar\omega_k}{2\varepsilon_0 V}}a_{\mathbf{k},j}(t) \tag{A–20}$$

in the Heisenberg picture. The field modes interact with the system through $\mathcal{H}_{SR_1}$, that governs also the evolution of the operators $a_{\mathbf{k},j}(t)$. The Heisenberg equations of motion are

$$\dot{a}_{\mathbf{k},j} = -\imath\omega_k a_{\mathbf{k},j} - \imath\zeta^*_{\mathbf{k},j}\sigma_- \tag{A–21}$$

that can be easily solved as

$$\tilde{a}_{\mathbf{k},j}(t) = a_{\mathbf{k},j}(0) - \imath\zeta^*_{\mathbf{k},j}\int_0^t dt'\,\tilde{\sigma}_-(t')e^{\imath(\omega_k-\omega_0)t'} \tag{A–22}$$

where $\tilde{a}_{\mathbf{k},j} = a_{\mathbf{k},j}e^{\imath\omega_k t}$ and $\tilde{\sigma}_- = \sigma_- e^{\imath\omega_0 t}$. From eqs. (A–20) and (A–22) we can see that $E^+(\mathbf{r},t)$ is divided into two components E_f and E_s, corresponding to the free evolution of the field and to the portion scattered by the two-level system. It is precisely this portion $\hat{E}_s(\mathbf{r},t)$ that we are looking for. We have already mentioned that we can consider the mean reservoir as empty. Therefore E_f, whose temporal evolution is proportional to $a_{\mathbf{k},j}(0)$, will not affect the correlation functions of eqs. (A–16). Substitut-

ing eq. (A–22) into eq. (A–20) and considering only the scattered portion, we can calculate the final expressions for $G^{(1)}(t, t+\tau)$ and $G^{(2)}(t, t+\tau)$:

$$G^{(1)}(\tau) = \langle \sigma_+(0)\sigma_-(\tau)\rangle_{ss} \tag{A–23a}$$

$$G^{(2)}(\tau) = \langle \sigma_+(0)\sigma_+(\tau)\sigma_-(\tau)\sigma_-(0)\rangle_{ss}\,. \tag{A–23b}$$

We are evaluating the expectation values in the steady-state because the case of interest is the one with the field in equilibrium with the dipole. By taking the limit for $t \to +\infty$ of eqs. (A–16) $G^{(1)}(t, t+\tau)$ and $G^{(2)}(t, t+\tau)$ are independent of the initial conditions, and we can consider τ as the only variable.

A.2.2 Master equation for resonance fluorescence

We have now transferred the properties of the scattered field from the reservoir operators $a_{k,j}$ to the dipole operators σ_i that regulate the dynamics of the two-level system. According to eqs. (A–23) we need to evaluate the temporal evolution of the expectation values of the Pauli matrices. These can be obtained by writing a master equation. This section details the steps necessary to obtain the master equation for resonance fluorescence. This same procedure was used to calculate the master equation for a CROW, presented in eq. (5–16a).

Let us consider a general case of system-reservoir interaction, that will then be adapted to the specific case described by the Hamiltonians of eq. (A–18). Let $W \in \mathbb{H}_S \otimes \mathbb{H}_R$ be the density matrix describing the system $\rho \in \mathbb{H}_S$ and the reservoir $R_1 \in \mathbb{H}_R$. The Hamiltonian $\mathcal{H} = \mathcal{H}_0 + \mathcal{H}_{SR}$ acts on W, and in the interaction picture the evolution of $\widetilde{W} = e^{\frac{\imath}{\hbar}\mathcal{H}_0 t} W(t) e^{-\frac{\imath}{\hbar}\mathcal{H}_0 t}$ is given by

$$\begin{aligned}\dot{\widetilde{W}} &= \frac{\imath}{\hbar}\left[\mathcal{H}_0, \widetilde{W}(t)\right] - \frac{\imath}{\hbar} e^{\frac{\imath}{\hbar}\mathcal{H}_0 t}\left[\mathcal{H}, W\right] e^{-\frac{\imath}{\hbar}\mathcal{H}_0 t} \\ &= -\frac{\imath}{\hbar}\left[\widetilde{\mathcal{H}}_{SR}, \widetilde{W}(t)\right].\end{aligned} \tag{A–24}$$

A solution for $\widetilde{W}(t)$ can be found integrating eq. (A–24). Replacing the solution back into eq. (A–24) leads to

$$\dot{\widetilde{W}} = -\frac{\imath}{\hbar}\left[\widetilde{H}_{SR}, W(0)\right] - \frac{1}{\hbar^2}\int_0^t dt' \left[\widetilde{H}_{SR}(t'), \left[\widetilde{H}_{SR}(t'), \widetilde{W}(t')\right]\right] \tag{A–25}$$

Considering an interaction that starts at $t = 0$, and that no previous coupling was present between the system and the reservoir, then W is separable, and can be factorised as $W = \rho(0) \otimes R_0$. Moreover, it is possible

to assume that any coupling that might arise between the system and the reservoir is weak, and does not affect the state of the reservoir. Under these assumptions

$$\widetilde{W}(t) = \tilde{\rho}(t) \otimes R_0 + \mathcal{O}(\widetilde{\mathcal{H}}_{SR}) \tag{A–26}$$

for all times. This is the *Born approximation*. Due to the weakness of the interaction, it is possible to discard all the higher order terms of $\widetilde{\mathcal{H}}_{SR}$. Eq. (A–25) can be simplified:

$$\dot{\tilde{\rho}} = -\frac{1}{\hbar^2}\int_0^t dt' \, \mathrm{Tr}_R\Big[\Big[\widetilde{H}_{SR}(t'), \Big[\widetilde{H}_{SR}(t'), \tilde{\rho}(t')\, R_0\Big]\Big]\Big] \tag{A–27}$$

where $\mathrm{Tr}[]$ is the trace operator. The term $\Big[\widetilde{\mathcal{H}}_{SR}, W(0)\Big]$ was discarded under the assumption that

$$\mathrm{Tr}_R\Big[\widetilde{\mathcal{H}}_{SR} R_0\Big] = 0, \tag{A–28}$$

as the operators coupling to the system have zero mean in $\mathbb{H}_R$. This condition can always be met by a rearrangement of the reservoir operators[1].

The Born approximation differentiates the system and the reservoir. This difference can be thought of as a "size" difference: any action that ρ could have on R is washed out, and lost. A second differentiation can be introduced, by considering two different time scales: a slow one for ρ, and a fast one for R. It is then possible to exclude any effect of ρ on itself. Information on the past states of ρ could only be stored in R, but this is again washed out by its fast evolution. This is the *Markov approximation*, under which $\tilde{\rho}(t') \to \tilde{\rho}(t)$ in eq. (A–27).

It is now possible to introduce a model for the system-reservoir interaction. The usual choice is to consider R as a bath of oscillators. The interaction is then described by

$$\widetilde{\mathcal{H}}_{SR} = \hbar \sum_j \tilde{s}_j(t)\widetilde{\Lambda}_j(t) \tag{A–29}$$

[1] This was already accomplished with $\mathcal{H}_{SR_3}$ and $\mathcal{H}_{SR_4}$, as the interaction between the molecule and the mean reservoir field was included directly in $\mathcal{H}_S$, so that $\mathcal{H}_{SR_3} + \mathcal{H}_{SR_4}$ would have a zero mean effect on ρ. Cf. [234, sec. 2.2.4].

where $\tilde{s}_j(t)$ is any system operator, while $\widetilde{\Lambda}_j(t)$ is a reservoir operator, both in the interaction picture. After straightforward algebra, eq. (A–27) can be written as

$$\dot{\tilde{\rho}} = -\sum_{ij}\int_0^t dt' \left\{ \left[\tilde{s}_i(t)\tilde{s}_j(t')\tilde{\rho}(t) - \tilde{s}_j(t')\tilde{\rho}(t)\tilde{s}_i(t)\right] \mathrm{Tr}_R\left[R_0\widetilde{\Lambda}_i(t)\widetilde{\Lambda}_j(t')\right] \right.$$
$$\left. \left[\tilde{\rho}(t)\tilde{s}_j(t')\tilde{s}_i(t) - \tilde{s}_i(t)\tilde{\rho}(t)\tilde{s}_j(t')\right] \mathrm{Tr}_R\left[R_0\widetilde{\Lambda}_j(t')\widetilde{\Lambda}_i(t)\right] \right\}. \tag{A–30}$$

Starting from eq. (A–30), it is possible to introduce the specific Hamiltonians for our case. It is important to notice that while $\widetilde{\mathcal{H}}_{SR} = \sum_j \widetilde{\mathcal{H}}_{SRj}$, simple calculations will show that any cross term $\widetilde{\mathcal{H}}_{SRj}\widetilde{\mathcal{H}}_{SRi}\widetilde{W}$ vanishes. The interaction with $\mathcal{H}_{SR1}$ of eq. (A–18c) is described by

$$\tilde{s}_1(t) = \sigma_- e^{-\imath\omega_0 t} \qquad \widetilde{\Lambda}_1(t) = \sum_{k,j} \zeta^*_{k,j} a^\dagger_{k,j} e^{\imath\omega_j t} \tag{A–31a}$$

$$\tilde{s}_2(t) = \sigma_+ e^{\imath\omega_0 t} \qquad \widetilde{\Lambda}_2(t) = \sum_{k,j} \zeta_{k,j} a_{k,j} e^{-\imath\omega_j t} \tag{A–31b}$$

while $\mathcal{H}_{SR2} + \mathcal{H}_{SR3}$ is related to

$$\tilde{s}_3(t) = \sigma_-\sigma_+ \qquad \widetilde{\Lambda}_3(t) = \sum_{i,j} \xi_{1i,j}\left(b^\dagger_{1i}b_{1j} - \delta_{i,j}\bar{n}_{1i}\right) \tag{A–32a}$$

$$\tilde{s}_4(t) = \sigma_+\sigma_- \qquad \widetilde{\Lambda}_4(t) = \sum_{i,j} \xi_{2i,j}\left(b^\dagger_{2i}b_{2j} - \delta_{i,j}\bar{n}_{2i}\right). \tag{A–32b}$$

It is worth noticing that the system operators $\tilde{s}_1(t)$ and $\tilde{s}_2(t)$ are an approximation, as they do not take into account the driving term of the Hamiltonian in eq. (A–18a). However, the final result would differ by less than 0.01% due to the great mismatch between optical frequencies and Ω. It is therefore possible to proceed with the definitions of eq. (A–31a) and (A–31b). An exhaustive treatment of the problem is reported in [234, sec. 2.3.2].

I shall now detail the derivation only for $\mathcal{H}_{SR_1}$, that can then be used as a guide for $\mathcal{H}_{SR_2} + \mathcal{H}_{SR_3}$. By noticing that $\widetilde{\Lambda}_2(t) = \widetilde{\Lambda}_1^\dagger(t)$, eq. (A–30) becomes

$$\begin{aligned}\dot{\tilde{\rho}} = -\int_0^t dt' \Big\{ &\left[\sigma_-\sigma_-\tilde{\rho}(t') - \sigma_-\tilde{\rho}(t')\sigma_-\right] e^{-i\omega_0(t+t')} \left\langle \widetilde{\Lambda}_1^\dagger(t)\widetilde{\Lambda}_1^\dagger(t')\right\rangle_{R_1} + \text{h.c.} \\ &\left[\tilde{\rho}(t')\sigma_-\sigma_- - \sigma_-\tilde{\rho}(t')\sigma_-\right] e^{-i\omega_0(t+t')} \left\langle \widetilde{\Lambda}_1^\dagger(t')\widetilde{\Lambda}_1^\dagger(t)\right\rangle_{R_1} + \text{h.c.} \\ &\left[\sigma_-\sigma_+\tilde{\rho}(t') - \sigma_+\tilde{\rho}(t')\sigma_-\right] e^{-i\omega_0(t-t')} \left\langle \widetilde{\Lambda}_1^\dagger(t)\widetilde{\Lambda}_1(t')\right\rangle_{R_1} + \text{h.c.} \\ &\left[\tilde{\rho}(t')\sigma_+\sigma_- - \sigma_-\tilde{\rho}(t')\sigma_+\right] e^{-i\omega_0(t-t')} \left\langle \widetilde{\Lambda}_1(t')\widetilde{\Lambda}_1^\dagger(t)\right\rangle_{R_1} + \text{h.c.}\Big\}\end{aligned} \tag{A–33}$$

where h.c. stands for the hermitian conjugate, and

$$\left\langle \widetilde{\Lambda}_1^\dagger(t)\widetilde{\Lambda}_1^\dagger(t')\right\rangle_{R_1} = \mathrm{Tr}_{R_1}\left[R\,\widetilde{\Lambda}_1^\dagger(t)\widetilde{\Lambda}_1^\dagger(t')\right]. \tag{A–34}$$

An analytical form for this correlation function can be found by explicitly considering the state of the reservoir, as a thermal bath:

$$\begin{aligned}R_1 &= \Pi_{k,j}\left(1 - e^{-\frac{\hbar\omega_j}{k_B T}}\right) e^{-\frac{\hbar\omega_j}{k_B T}\hat{a}_{k,j}^\dagger \hat{a}_{k,j}} \\ &= \sum_{n_{j,k}} \frac{1}{\bar{n}_1 + 1}\left(\frac{\bar{n}_1}{\bar{n}_1 + 1}\right)^{n_{j,k}} |n_{j,k}\rangle\langle n_{j,k}|\end{aligned} \tag{A–35}$$

from which easily follows

$$\left\langle \widetilde{\Lambda}_1^\dagger(t)\widetilde{\Lambda}_1^\dagger(t')\right\rangle_{R_1} = \left\langle \widetilde{\Lambda}_1(t)\widetilde{\Lambda}_1(t')\right\rangle_{R_1} = 0 \tag{A–36a}$$

$$\left\langle \widetilde{\Lambda}_1^\dagger(t)\widetilde{\Lambda}_1(t')\right\rangle_{R_1} = \sum_{k,j} |\zeta_{k,j}|^2 e^{i\omega_k(t-t')}\bar{n}_1(\omega_k, T) \tag{A–36b}$$

$$\left\langle \widetilde{\Lambda}_1(t)\widetilde{\Lambda}_1^\dagger(t')\right\rangle_{R_1} = \sum_{k,j} |\zeta_{k,j}|^2 e^{-i\omega_k(t-t')}\left[\bar{n}_1(\omega_k, T) + 1\right] \tag{A–36c}$$

where $\bar{n}_1(\omega_k, T)$ is the mean number of excitations of the reservoir modes of R_1.

The summations over the modes of the bath can now be replaced by an integration over a continuum of frequencies:

$$\sum_{k,j} |\zeta_{k,j}|^2 \to \sum_j \int_0^{+\infty} d^3k\, D_1(k)\, |\zeta(k,j)|^2 \tag{A–37}$$

where $D_1(k)$ is the density of the states for this particular reservoir.

With the change of variable $\tau = t - t'$, eq. (A–33) becomes

$$\begin{aligned}\dot{\tilde{\rho}} = -\int_0^t d\tau \Bigg\{ \Big[(\sigma_-\sigma_+\tilde{\rho}(t) - \sigma_+\tilde{\rho}(t)\sigma_-)\, e^{-\imath\omega_0\tau} \\ \sum_j \int d^3k\, D_1(\mathbf{k})\, |\zeta(\mathbf{k},j)|^2\, e^{\imath\omega_k\tau}\, \bar{n}_1(\omega_k, T) \Big] + \text{h.c.} + \\ \Big[(\tilde{\rho}(t)\sigma_+\sigma_- - \sigma_-\tilde{\rho}(t)\sigma_+)\, e^{\imath\omega_0\tau} \\ \sum_j \int d^3k\, D_1(\mathbf{k})\, |\zeta(\mathbf{k},j)|^2\, e^{-\imath\omega_k\tau}\, (\bar{n}_1(\omega_k, T) + 1) \Big] + \text{h.c.} \Bigg\}\end{aligned} \tag{A–38}$$

Recalling the Markov approximation, it is possible to extend the time integral until $-\infty$, as over the time scale of the interaction, dictated by τ, $\rho(t)$ can be considered constant. Eq. (A–38) is simplified to

$$\begin{aligned}\dot{\tilde{\rho}} =& \alpha\,(\sigma_-\tilde{\rho}(t)\sigma_+ - \sigma_+\sigma_-\tilde{\rho}(t)) + \\ & \beta\,(-\sigma_-\sigma_+\tilde{\rho}(t) + \sigma_+\tilde{\rho}(t)\sigma_- + \sigma_-\tilde{\rho}(t)\sigma_+ - \tilde{\rho}(t)\sigma_+\sigma_-) + \text{h.c.}\end{aligned} \tag{A–39}$$

where the constants α and β express the relationship with the density of states

$$\begin{aligned}\alpha &= \pi \sum_j \int d^3k\, D_1(\mathbf{k})\, |\zeta(\mathbf{k},j)|^2\, \delta(kc - \omega_0) + \imath\Delta_0 \\ &= \frac{\gamma}{2} + \imath\Delta_0 \qquad \text{(A–40a)} \\ \beta &= \pi \sum_j \int d^3k\, D_1(\mathbf{k})\, |\zeta(\mathbf{k},j)|^2\, \delta(kc - \omega_0)\, \bar{n}_1(kc, T) + \imath\Delta_0' \\ &= \bar{n}\frac{\gamma}{2} + \imath\Delta_0' \qquad \text{(A–40b)}\end{aligned}$$

where the two terms Δ_0 and Δ_0' are the principal part of the integrals:

$$\Delta_0 = \sum_j \mathcal{P}\left\{ \int d^3k\, \frac{1}{\omega_0 - kc} D_1(\mathbf{k})\, |\zeta(\mathbf{k},j)|^2 \right\} \tag{A–41a}$$

$$\Delta_0' = \sum_j \mathcal{P}\left\{ \int d^3k\, \frac{\bar{n}_1(kc, T)}{\omega_0 - kc} D_1(\mathbf{k})\, |\zeta(\mathbf{k},j)|^2 \right\} \tag{A–41b}$$

Inserting these results back into eq. (A–39), and recalling that $\sigma_\pm\sigma_\mp = \frac{1}{2}(1 \pm \sigma_z)$, simple algebra leads to

$$\begin{aligned}\dot{\tilde{\rho}} =& -\frac{\imath}{2}(2\Delta_0' + \Delta_0)\,[\sigma_z,\,\tilde{\rho}] \\ &+ \frac{\gamma}{2}(\bar{n}+1)\,(2\sigma_-\tilde{\rho}(t)\sigma_+ - \sigma_+\sigma_-\tilde{\rho}(t) - \tilde{\rho}(t)\sigma_+\sigma_-) \\ &+ \frac{\gamma}{2}\bar{n}\left(2\sigma_+\tilde{\rho}(t)\sigma_- - \sigma_-\sigma_+\tilde{\rho}(t) - \tilde{\rho}(t)\sigma_-\sigma_+\right)\end{aligned} \tag{A–42}$$

This procedure can be followed to solve for the interaction with reservoirs R3 and R4. Moreover, the master equation for coupled CROWS presented in eq. (5–16a) can be obtained by considering $\tilde{s}_1(t) = \hat{a}e^{-\imath\omega_c t}$ and $\tilde{s}_1(t) = \hat{a}^\dagger e^{-\imath\omega_c t}$, and recalling that $\bar{n}_1 = 0$ at optical frequencies.

The master equation can be obtained by summing all the contributions of the different reservoirs into eq. (A–42). By recalling that

$$\dot{\rho}(t) = -\frac{\imath}{\hbar}\,[\mathcal{H}_S,\,\rho(t)] + e^{-\frac{\imath}{\hbar}\mathcal{H}_S}\dot{\tilde{\rho}}(t)e^{\frac{\imath}{\hbar}\mathcal{H}_S}. \tag{A–43}$$

and solving for $\dot{\rho}$, one obtains the master equation for resonance fluorescence in the rotating wave approximation

$$\begin{aligned}\dot{\rho} =& -\frac{\imath}{2}\left(\omega_0 + 2\Delta_0' + \Delta_0 + \delta_p + \Delta_p\right)[\sigma_z,\,\rho] \\ &+ \imath\frac{1}{2}\Omega_0\left[e^{-\imath\omega t}\sigma_+ + e^{\imath\omega t}\sigma_-,\,\rho\right] \\ &+ \frac{\gamma}{2}\,(2\sigma_-\rho\sigma_+ - \sigma_+\sigma_-\rho - \rho\sigma_+\sigma_-) \\ &+ \frac{\gamma_p}{2}\,(\sigma_z\rho\sigma_z - \rho)\,.\end{aligned} \tag{A–44}$$

The terms δ_p and Δ_p are given by

$$\delta_p = \int_0^\infty d\omega\;\left(D_3(\omega)\xi_2(\omega,\,\omega) - D_2(\omega)\xi_1(\omega,\,\omega)\right)\bar{n}_2\,(\omega,\,T) \tag{A–45a}$$

$$\Delta_p = \mathcal{P}\left\{\iint_0^\infty d\omega d\omega'\,\frac{D_3(\omega)D_3(\omega')\,|\xi_2(\omega,\,\omega)|^2 - D_2(\omega)D_2(\omega')\,|\xi_1(\omega,\,\omega)|^2}{\omega - \omega'}\right\} \times \bar{n}_2\,(\omega,\,T)\,. \tag{A–45b}$$

where $\bar{n}_2\,(\omega,\,T)$ is the mean occupation number of the reservoirs R_3 and R_4. Together with Δ_0 and Δ_0', these terms shift the resonance frequency of the atom. The effect of δ_p and Δ_p can be observed in single molecule spectroscopy, as they are related to the Debye-Waller factor α_{DW}, regulating the relative strength between an electronic transition and its phonon side-band. Δ_0 and Δ_0' are instead harder to observe, and are generally neglected. However, they give a first approximation of the Lamb shift of

the resonance frequency for the two-level system. A more thorough calculation of the Lamb shifts would require a calculation outside the rotating wave approximation. I refer again to [234] and [235] for an exhaustive treatment of the problem.

The damping term γ, given by

$$\gamma = \pi \sum_j \int d^3k \, D_1(\mathbf{k}) \, |\zeta(\mathbf{k}, j)|^2 \, \delta(kc - \omega_0) \tag{A–46}$$

can be easily related to Γ_1 by recalling the expression for $\zeta(\mathbf{k}, j)$ introduced in eq. (A–19). Considering the density of states for each polarisation in k-space in a volume V

$$D_1(\mathbf{k}) d^3k = \frac{\omega^2 V}{8\pi^3 c^3} d\omega \sin\theta d\theta d\phi, \tag{A–47}$$

simple calculations show that, as expected, $\gamma = \Gamma_1$. Finally the damping term γ_p, given by

$$\begin{aligned} \gamma_p = \pi \int_0^\infty & \left(D_3^2(\omega) \, |\xi_2(\omega, \omega)|^2 + D_2^2(\omega) \, |\xi_1(\omega, \omega)|^2 \right) \\ & \times \bar{n}_2(\omega, T) \left(\bar{n}_2(\omega, T) + 1 \right), \end{aligned} \tag{A–48}$$

can be related to the excess dephasing due to interaction with phonons:

$$\gamma_p = \Gamma_1/2 - \Gamma_2. \tag{A–49}$$

A.2.3 $G^{(1)}(\tau)$ and fluorescence spectrum

Equation (A–44) is the master equation for resonance fluorescence. The temporal evolution of any system observable can be expressed as

$$\frac{d}{dt} \langle \hat{O} \rangle = \mathrm{Tr}\left[\hat{O} \dot{\rho} \right]. \tag{A–50}$$

Let's consider the case of the Pauli matrices. The temporal evolution of their expectation values can be obtained from eq. (A–50) and from the master equation (A–44). However, by recalling that

$$\rho = |\psi\rangle\langle\psi| = \begin{bmatrix} |c_1|^2 & c_1^* c_2 \\ c_1 c_2^* & |c_2|^2 \end{bmatrix} \tag{A–51}$$

and the matrix representation of dipole operators, we see that

$$\langle \sigma_- \rangle = c_1^* c_2 = \rho_{21} \tag{A–52a}$$
$$\langle \sigma_+ \rangle = c_1 c_2^* = \rho_{12} \tag{A–52b}$$
$$\langle \sigma_z \rangle = |c_2|^2 - |c_1|^2 = \rho_{22} - \rho_{11}. \tag{A–52c}$$

We can then use the solution of the Optical Bloch equations (2–1) found with the Laplace transform method. Recalling eqs. (2–11), we can write $\langle \sigma_z \rangle$ as

$$\rho_{22}(t) - \rho_{11}(t) = -\frac{\Gamma_1 \Gamma_2}{\Omega_0^2 + \Gamma_1 \Gamma_2} \left(1 + \frac{\Omega_0^2}{\Gamma_1 \Gamma_2} \left(\frac{p+q}{2q} e^{-(p-q)t} - \frac{p-q}{2q} e^{-(p+q)t} \right) \right). \tag{A–53}$$

We can now evaluate the correlation function of eq. (A–23a). As we are considering the steady-state regime for the Pauli matrices, we need to consider the fluctuations of the averages $\langle \sigma_i \rangle$. The Pauli matrices are now expressed as $\sigma_i = \langle \sigma_i \rangle_{ss} + \Delta\sigma_i$ where $\langle \sigma_i \rangle_{ss}$ is the steady-state limit. If we consider the vector $\boldsymbol{\sigma}$ that has the Pauli matrices has components, then from eqs. (2–11) and (A–53) we can write

$$\boldsymbol{\sigma} = \langle \boldsymbol{\sigma} \rangle_{ss} + \Delta\boldsymbol{\sigma} \tag{A–54a}$$
$$\langle \boldsymbol{\sigma} \rangle_{ss} = \begin{bmatrix} -\frac{\imath}{2} \frac{\Omega_0 \Gamma_1}{\Omega_0^2 + \Gamma_1 \Gamma_2} \\ \frac{\imath}{2} \frac{\Omega_0 \Gamma_1}{\Omega_0^2 + \Gamma_1 \Gamma_2} \\ -\frac{\Gamma_1 \Gamma_2}{\Omega_0^2 + \Gamma_1 \Gamma_2} \end{bmatrix}. \tag{A–54b}$$

We can now separate $G^{(1)}(\tau)$ into the coherent and incoherent components:

$$G^{(1)}(\tau) = \langle \langle \sigma_+ \rangle_{ss} \langle \sigma_- \rangle_{ss} \rangle_{ss} + \langle \Delta\sigma_+(0) \Delta\sigma_-(\tau) \rangle_{ss}. \tag{A–55}$$

The first part can be easily calculated from eq. (A–54). The second term instead requires a more involved analysis. We can calculate the evolution of $\Delta\boldsymbol{\sigma}$ from eq. (A–44) and eq. (A–54) singularly. We can then translate the evolution to the correlation function $\langle \Delta\sigma_+(0) \Delta\sigma_-(\tau) \rangle$ due to the quantum regression theorem, that states the equivalence between Heisen-

berg equations of motion for expectation values of system operators and for their correlation functions. We can then write

$$\frac{\mathrm{d}}{\mathrm{d}\tau}\left\langle \Delta\sigma_+(0)\Delta\boldsymbol{\sigma}(\tau)\right\rangle_{\mathrm{ss}} = \mathbf{M}\left\langle \Delta\sigma_+(0)\Delta\boldsymbol{\sigma}(\tau)\right\rangle_{\mathrm{ss}} \tag{A–56a}$$

$$\mathbf{M} = \begin{bmatrix} -\Gamma_2 & 0 & -\imath\frac{\Omega_0}{2} \\ 0 & -\Gamma_2 & \imath\frac{\Omega_0}{2} \\ -\imath\Omega_0 & \imath\Omega_0 & -\Gamma_1 \end{bmatrix} \tag{A–56b}$$

We can solve eq. (A–56a) by diagonalising the matrix $\mathbf{M}$. If we consider $\boldsymbol{\Lambda}$ as the matrix of the eigenvectors of $\mathbf{M}$, then $\left(\boldsymbol{\Lambda}^{\mathsf{T}}\right)^{-1}\mathbf{M}\,\boldsymbol{\Lambda}^{\mathsf{T}} = \boldsymbol{\lambda}$, where $\boldsymbol{\lambda}$ is a diagonal matrix with diagonal elements given by the eigenvalues of $\mathbf{M}$. $\boldsymbol{\Lambda}^{\mathsf{T}}$ is the transpose of $\boldsymbol{\Lambda}$. We have then

$$\begin{aligned}\frac{\mathrm{d}}{\mathrm{d}\tau}\left(\boldsymbol{\Lambda}^{\mathsf{T}}\right)^{-1}\left\langle \Delta\sigma_+(0)\Delta\boldsymbol{\sigma}(\tau)\right\rangle_{\mathrm{ss}} = \\ \left(\left(\boldsymbol{\Lambda}^{\mathsf{T}}\right)^{-1}\mathbf{M}\,\boldsymbol{\Lambda}^{\mathsf{T}}\right)\left(\boldsymbol{\Lambda}^{\mathsf{T}}\right)^{-1}\left\langle \Delta\sigma_+(0)\Delta\boldsymbol{\sigma}(\tau)\right\rangle_{\mathrm{ss}},\end{aligned} \tag{A–57}$$

from which easily follows

$$\left\langle \Delta\sigma_+(0)\Delta\boldsymbol{\sigma}(\tau)\right\rangle_{\mathrm{ss}} = \boldsymbol{\Lambda}^{\mathsf{T}} e^{\boldsymbol{\lambda} t}\left(\boldsymbol{\Lambda}^{\mathsf{T}}\right)^{-1}\left\langle \Delta\sigma_+\Delta\boldsymbol{\sigma}\right\rangle_{\mathrm{ss}}. \tag{A–58}$$

We can express the initial conditions $\left\langle \Delta\sigma_+\Delta\boldsymbol{\sigma}\right\rangle_{\mathrm{ss}}$ considering the steady-state limit of eqs. (2–3) as

$$\begin{aligned}\left\langle \Delta\sigma_+\Delta\boldsymbol{\sigma}\right\rangle_{\mathrm{ss}} &= \begin{bmatrix} \left\langle \sigma_+\sigma_-\right\rangle_{\mathrm{ss}} - \left\langle \sigma_+\right\rangle_{\infty}\left\langle \sigma_-\right\rangle_{\mathrm{ss}} \\ \left\langle \sigma_+\sigma_+\right\rangle_{\mathrm{ss}} - \left\langle \sigma_+\right\rangle_{\mathrm{ss}}^2 \\ \left\langle \sigma_+\sigma_z\right\rangle_{\mathrm{ss}} - \left\langle \sigma_+\right\rangle_{\mathrm{ss}}\left\langle \sigma_-\right\rangle_{\mathrm{ss}} \end{bmatrix} \\ &= \begin{bmatrix} \frac{1}{2}\left(1+\left\langle \sigma_z\right\rangle_{\mathrm{ss}}\right) - \left\langle \sigma_+\right\rangle_{\mathrm{ss}}\left\langle \sigma_-\right\rangle_{\mathrm{ss}} \\ -\left\langle \sigma_+\right\rangle_{\mathrm{ss}}^2 \\ -\left\langle \sigma_+\right\rangle_{\mathrm{ss}}\left(1+\left\langle \sigma_z\right\rangle_{\mathrm{ss}}\right) \end{bmatrix} \\ &= \frac{\Omega_0^2}{4\left(\Gamma_1\Gamma_2+\Omega_0^2\right)^2}\begin{bmatrix} 2\Omega_0^2 - \left(\Gamma_1-\Gamma_2\right)\Gamma_1 \\ \Gamma_1^2 \\ 2\imath\Gamma_1\Omega_0 \end{bmatrix}\end{aligned} \tag{A–59}$$

Going back to eq. (A–55), by inserting eqs. (A–54), (A–58) and (A–59) we obtain the expression for the *first-order correlation function for resonance fluorescence*

$$\begin{aligned}\mathrm{G}^{(1)}(\tau)\,e^{\imath\omega_0 t} = \mathrm{G}_{\mathrm{coh}} + \\ \alpha\left(e^{-\Gamma_2\tau} + \beta e^{-(p-q)\tau} + \gamma e^{-(p+q)\tau}\right)\end{aligned} \tag{A–60}$$

where we have used the substitutions

$$\alpha = \frac{\rho_{22}^{(ss)}}{4} \tag{A–61a}$$

$$\beta = \frac{\Gamma_1}{4\Omega_0^2}\rho_{22}^{(ss)}\left(2 + \frac{\Gamma_1 - \Gamma_2}{q}\right)(d - q) \tag{A–61b}$$

$$\gamma = \frac{\Gamma_1}{4\Omega_0^2}\rho_{22}^{(ss)}\left(2 - \frac{\Gamma_1 - \Gamma_2}{q}\right)(d + q) \tag{A–61c}$$

in addition to the usual definition of eq. (2–12). G_{coh} represents the fixed contribution of the coherent scattering to the first-order correlation function, and is expressed as

$$G_{coh} = \frac{\Gamma_1^2\Omega_0^2}{4\left(\Gamma_1\Gamma_2 + \Omega_0^2\right)^2} = \frac{\Gamma_1^2}{\Omega_0^2}\left(\rho_{22}^{(ss)}\right)^2 \tag{A–62}$$

This result is of particular importance, as we can use it to obtain the spectrum of resonance fluorescence $\mathcal{S}(\omega)$. This will also be separated into a coherent and incoherent component, originating from the two scattering processes. By taking the Fourier transform of eq. (A–60), we obtain the general expression

$$\mathcal{S}(\omega) = \mathcal{S}_{coh}(\omega) + \mathcal{S}_{inc}(\omega) \tag{A–63a}$$

$$\mathcal{S}_{coh}(\omega) = \frac{\Gamma_1^2}{2\pi\Omega_0^2}\left(\rho_{22}^{(ss)}\right)^2 \delta(\omega - \omega_0) \tag{A–63b}$$

$$\begin{aligned}\mathcal{S}_{inc}(\omega) = {} & \frac{\alpha}{\pi}\frac{\Gamma_2}{(\omega - \omega_0)^2 + \Gamma_2^2} \\ & + \frac{\alpha}{\pi}\Big(\beta\frac{p - q}{(\omega - \omega_0)^2 + (p - q)^2} + \\ & \quad + \gamma\frac{p + q}{(\omega - \omega_0)^2 + (p + q)^2}\Big)\end{aligned} \tag{A–63c}$$

This is a generalisation of the result obtained first by Mollow [231]. Following his work several approximation have been made, finding alternatives expression for eq. (A–63) under different conditions, especially weak and strong incident field [1, sec. 8.4] [236, Ch. 4] [237, Suppl. Inf.].

Let us again vary the saturation and study the behaviour of $\mathcal{S}(\omega)$, as reported in figure A.2. When the intensity of the excitation field is low, the coherent scattering prevails. This means that the emission spectrum does not present the spontaneous emission linewidth of eq. (2–7), but is instead monochromatic. The molecule coherently scatters the excita-

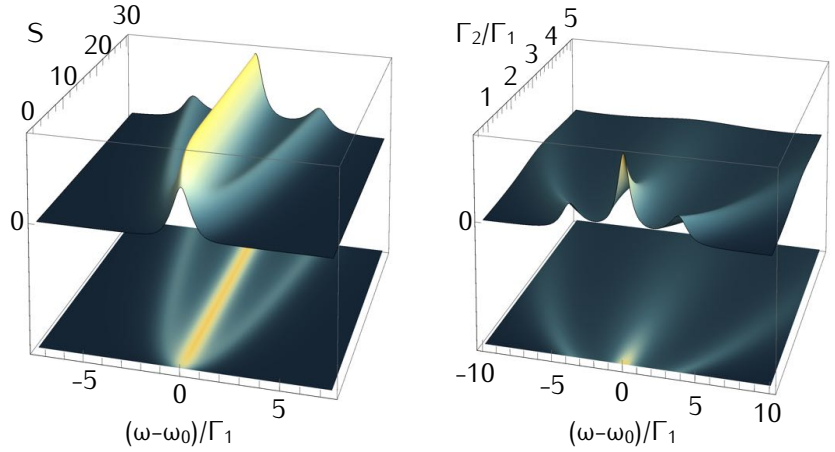


Figure A.2 3D and density plot for $\mathcal{S}_{\text{inc}}(\omega)$ for varying saturation S (left) and dephasing Γ_2 (right). As the excitation intensity increases, the incoherent scattering process prevails and the Mollow sidebands appear. On the other hand, the central peak rapidly vanishes for increasing values of Γ_2, as the coherence is lost from the pumping process.

tion light, and will retain its spectral profile. As the excitation intensity increases, the incoherent process takes over, as

$$\frac{\mathcal{S}_{\text{coh}}}{\mathcal{S}_{\text{inc}}} = \frac{\Gamma_1}{2d} \approx \frac{\Gamma_1^2}{2\Omega_0^2} \tag{A–64}$$

for the case of $\Gamma_2 = \Gamma_1/2$. Already from eq. (2–13) and now from the incoherent spectrum of eq. (A–63c) we see that the field has additional frequency components, due to the splitting of the levels of the molecule. These additional frequencies result in a triplet spectrum, with sidebands at $\omega = \omega_0 \pm \Omega'$. At high intensities we can approximate the spectrum as being composed of three Lorentzian peaks, with FWHM of Γ_2 for the central peak and $3\Gamma_2/2$ for the sidebands. The integrated intensities of the sidebands is half that of the central one. The incoherent process takes over more rapidly if the dephasing rate Γ_2 is increased over the lifetime-limit. We can see from the right panel of figure A.2 that the central peak rapidly loses intensity, to finally disappear completely. While the Mollow triplet spectrum has been observed in several physical systems [164, 238–240], no study of its behaviour as a function of dephasing has been presented.

A.2.4 $G^{(2)}(\tau)$ and antibunching

We can now continue with our analysis, and in particular witness the effect of the particular nature of this harmonic oscillator, that allows only one excitation present at any given time. Already from the matrix representation of σ_i we can see that $\sigma_\pm^2 = 0$, that is the molecule can't be excited twice, nor can two photons be emitted at the same time[2]. We are therefore interested in the state of the system after the emission of one photon.

The procedure to obtain $G^{(2)}(\tau)$ is the same as the one for $G^{(1)}(\tau)$ [234, sec. 2.3.5]. Expanding eq. (A–23b) we have

$$G^{(2)}(\tau) = \frac{1}{2}\left(\langle\sigma_+\sigma_-\rangle_{ss} + \langle\sigma_+(0)\sigma_z(\tau)\sigma_-(0)\rangle\right) \tag{A–65}$$

and applying the quantum regression theorem we get

$$G^{(2)}(\tau) = \frac{1}{2}\langle\sigma_+\sigma_-\rangle_{ss}\left(1 + \langle\sigma_z(\tau)\rangle\right). \tag{A–66}$$

Finally, after inserting eqs. (A–53) and (A–59) and normalising for long times, we have the expression for the *second-order correlation function for resonance fluorescence*

$$g^{(2)}(\tau) = 1 - \frac{p+q}{2q}e^{-(p-q)\tau} + \frac{p-q}{2q}e^{-(p+q)\tau}. \tag{A–67}$$

The expression of eq. (2–14) is equivalent to the expression of the population $\rho_{22}(\tau)$ presented in eq. (2–11b). This is due to the fact that $g^{(2)}(\tau)$ can be interpreted as the probability of detecting a photon at time $t = \tau$, given that a first one was detected at $t = 0$. As the molecule has to transit to the excited state before it can emit a photon, the probability of detection is proportional to the population ρ_{22}.

[2] This of course is valid in our approximation of the molecule as a 2-level system.

B APPENDIX TO CHAPTER 3

I present here the detailed schemes of the optical setup used for the cryogenic analysis of single DBT molecules. The components listed in figure B.1 are

AL1 aspheric lens, Thorlabs C240TME-B or C560TME-B in case of the diode lasers, or the Ti:Sapph laser;

PMF polarisation maintaining fibre, Thorlabs P3-780PM-FC-5;

AL2: aspheric lens, Thorlabs F240APC-780;

L1 AND L2: lenses, Thorlabs LC1715-B and LB1437-B;

P AND HWP: polariser and half-wave-plate, molded;

BP: band-pass filter, Thorlabs FB780-10, FB760-10

BS1: beam splitter, Thorlabs BS017;

BS2: pellicle beam splitter, Thorlabs BP145B2;

PN: pinholes, Thorlabs irises;

BS3: cube beamsplitter;

SM: galvanometric mirrors, Thorlabs GVS002;

LP: long-pass filter, Chroma HQ800LP or 792LP;

AL3: aspheric lens, Thorlabs C560TME-B;

MMF: multimode fibre, Thorlabs with beam splitter FCMM625-50A-FC;

CCD: Andor, Luca 765 MONO;

AL4: collimator, Thorlabs OSL2COL;

WL: liquid light;

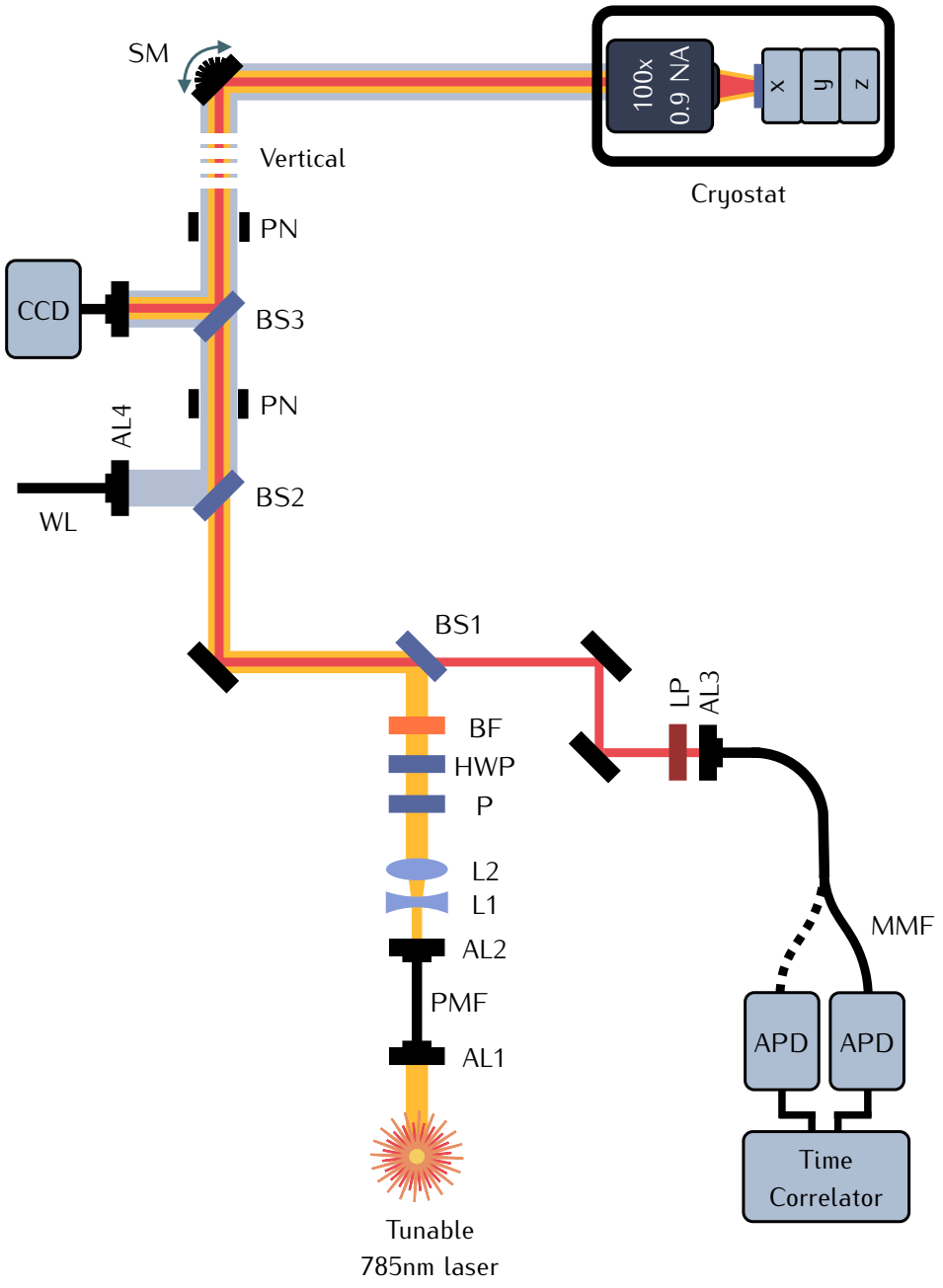


Figure B.1 Detailed scheme of the setup for SMS.

C APPENDIX TO CHAPTER 4

I present here the detailed schemes of the optical setup used for the cryogenic analysis of single DBT molecules. The components listed in figure C.1 are

AL1 aspheric lens, Thorlabs C560TME-B;

PMF polarisation maintaining fibre, Thorlabs P3-780PM-FC-2;

AL2: aspheric lens, Thorlabs C560TME-B;

P: polarising beam splitter, Thorlabs PBS052;

HWP: half-wave plate, Thorlabs WPH10M-780;

BP: band-pass filter, Chroma D780/10X;

BS1: pellicle beam splitter, Thorlabs BP145B2;

SM: galvanometric mirrors, Thorlabs GVS002;

L1 AND L2: lenses, focal lenses 75 and 250 mm;;

BS2: pellicle beam splitter, Thorlabs BP145B2;

BS3: pellicle beam splitter, Thorlabs BP108;

LP: long-pass filter, Chroma HQ800LP or 792LP;

AL3: aspheric lens, Thorlabs C560TME-B;

AL4: aspheric lens, Thorlabs F260APC-780;

MMF: multimode fibre, Thorlabs with beam splitter FCMM625-50A-FC;

CCD: CCD, Andor iXon Ultra camera;

WL: white light source, Thorlabs MCWHL5;

AL5: collimator, Thorlabs ACP2520-A;

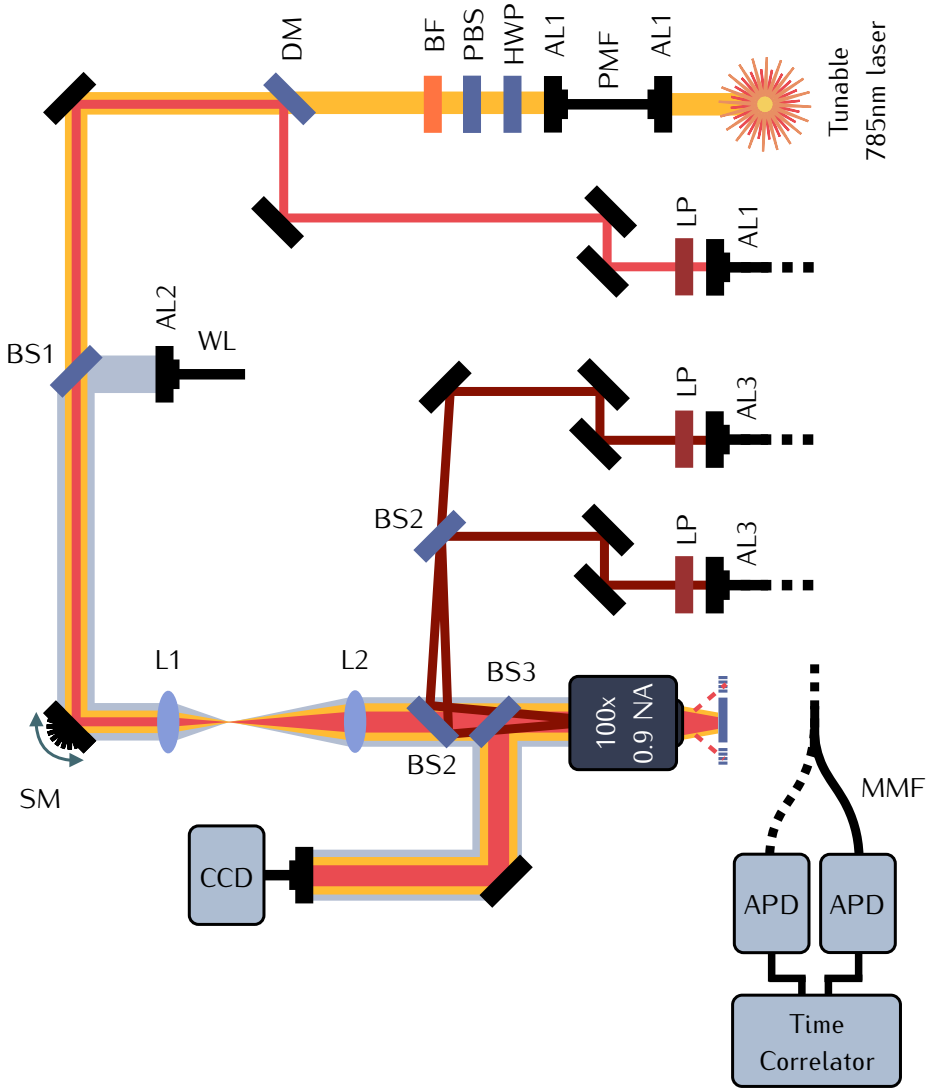


Figure C.1 Detailed scheme of the setup for the HPW.

C.1 LOCAL FIELD CORRECTIONS

It has long been established that the optical transition rate Γ_1 for a 2-level system is strongly dependent on its environment. This is particularly evident in the case of a DBT molecule in an Ac crystal, since it is precisely the interaction between the emitter and the host that allows stable single photon emission. It is also important to consider the host not only as stabilising the emission process, but also as modifying the emission itself. One possible way to understand it is that the medium surrounding the emitter changes the local density of states. Then, from Fermi's golden rule it is possible to calculate the correction to the vacuum

transition rate Γ_1. The general expression for the transition rate, following the notation from [241], is:

$$\Gamma = n^{\alpha} l^{\beta}(n)\Gamma_1 \tag{C–1}$$

where n is the refractive index and $l(n)$ is the local field correction factor. This last term specifies the relationship between the macroscopic electric field in the medium and the field acting on the emitter. The aim of a full analysis is to obtain the expression for the local field correction $l(n)$ and the values for the exponents α and β.

Starting from the direct $n-$dependence, several paths are possible. Through a macroscopic Greens-function approach Barnett, Huttner and Loudon [242] were the first to obtain a result for α, in the particular case of an absorbing dielectric medium. In their work they show that $\Gamma = \Re\{n(\omega_a)\}\Gamma_1$, where $\Re\{n(\omega_a)\}$ is the real part of the refractive index of the medium at the emitter resonant frequency ω_a. The same result was obtained by specifying a microscopic Hamiltonian that included the medium polarisation and the electromagnetic field. This result was then confirmed by other works, based on field quantisation [243] or on reduced density matrix analysis [241]. Barnett *et al.* mention that their calculations are incomplete, since there is no distinction between local and macroscopic field, but at first they do not elaborate their choice of an expression for $l(n)$. The literature seems to be divided on the expression for the local field correction, and three main models are suggested. The first model is referred to as the *Virtual Cavity Mode* (VCM). In this case the 2-level system is thought of as being placed inside a cavity in the dielectric, that is filled with the same medium. The corrected expression for the transition rate is:

$$\Gamma = n\left(\frac{n^2+3}{2}\right)^2\Gamma_1 \tag{C–2}$$

corresponding to a local field correction $l(n) = \frac{n^2+3}{2}$ and values $\alpha = 1$ and $\beta = 2$. This model is based on the work of Lorentz, and was developed considering the interactions of impurity centres in a crystal [244]. The VCM is also the model adopted and later demonstrated by Barnett et al. [245], and received further experimental verification [246].

It was then suggested that the VCM correction is actually valid only for emitters that are embedded into a medium. A new model was developed that considered an isolated emitter placed inside an empty cavity, surrounded by a uniform medium [247, 248]. This *Real Cavity Model*

(RCM) is suited, for example, for emitters substituting lattice atoms, and has been widely verified experimentally and theoretically [249–251]. The corresponding eq. (C–1) obtained in this approach is:

$$\Gamma = n\left(\frac{3n^2}{2n^2+1}\right)^2 \Gamma_1 \tag{C–3}$$

that shows the same values for α and β, but a different expression for $l(n)$ with a heavily reduced dependance on n.

Another model was developed by Crenshaw and Bowden [252], that significantly differs from the RCM and VCM. In their work, the authors point out the lack in previous models of a back action from the emitter onto the dielectric. The model is based on a many body derivation of Langevin-Bloch equations, and implies a much weaker dependence on the refractive index of the transition rate:

$$\Gamma = \left(\frac{n^2+3}{2}\right) \Gamma_1 \tag{C–4}$$

with a similar $l(n)$ as the VCM, but differs with values of $\alpha = 0$ and $\beta = 1$. This model was also validated experimentally [253].

Recently, another correction to the emission rate was obtained, following an adapted version of the chain of Bogoliubov-Born-Green-Kirkwood-Yvon (BBGKY) equations [241]. This model, that resembles the VCM in the form of the local field correction:

$$\Gamma = n\left(\frac{3n^2}{2n^2+1}\right) \Gamma_1 \tag{C–5}$$

was verified on the data from several experimental papers with different type of emitters. A comparison of the different models is presented in figure C.2. Considering the amount of experimental and theoretical proof supporting corrections eqs. (C–2) to (C–5) it is difficult to choose a suitable model for a given experiment. Several papers state that this difficulty is due to the limited conditions accessible in experiments, where, once experimental errors are considered, all three models become acceptable. We plan to perform our own tests on DBT in Ac, and find the model that best suits our case.

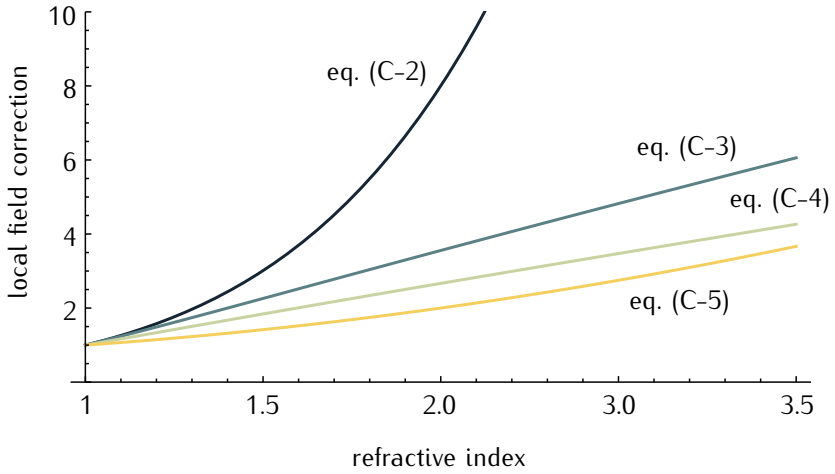


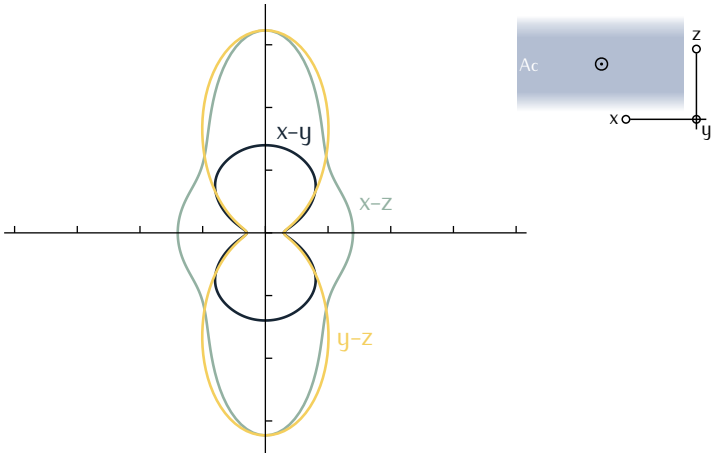
Figure C.2 plot of the local field correction $n^{\alpha}l^{\beta}(n)$ for the presented models of VCM (eq. (C–2)), RCM (eq. (C–3)), the Crenshaw and Bowden model (eq. (C–4)) and the one derived from the BBGKY chain (eq. (C–5)).

C.2 COLLECTION EFFICIENCY: DIPOLE EMISSION

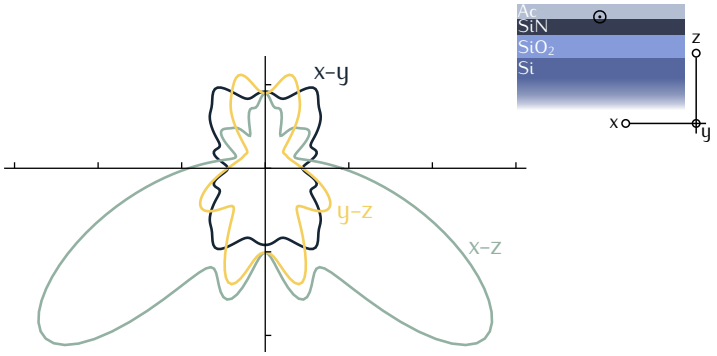
In this section I present the emission patterns of DBT molecules close to several substrates, used to calculate the collection efficiency of the setup. I have used the software Lumerical™ FDTD Solutions software to perform finite-difference time-domain simulations of the emission pattern of a molecule, and to calculate the percentage of field collected by a 0.9 NA objective. Polar plots of the emitted radiation in the three planes are reported in figure C.3, together with a scheme of the substrate and the alignment axes. The dipole was placed along the y-axis.

I studied at first the case of a DBT molecule embedded in bulk Ac. I used the result as a first testbed for the simulations. The result is reported in figure C.3a, that shows the expected asymmetry of the emission pattern for the three axes of anthracene, due to the different refractive indices.

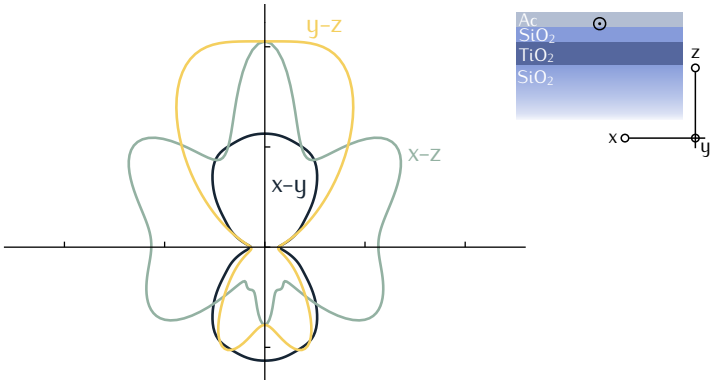
More interesting is the case for an anthracene crystal deposited over a silicon nitride substrate, of the type described in chapter 3 (from top to bottom: 120 nm of silicon nitride and 1 µm of silica, over a silicon substrate). I have started the simulations with an 80 nm layer of anthracene and with the molecule at 20 nm from the silicon nitride surface. This case corresponds to the case of a supersaturation crystal deposited over the substrate.



(a) Projections of the dipole emission patterns for the case of DBT in bulk anthracene.



(b) Projections of the dipole emission patterns for the case of DBT 80 nm of Ac, situated at 20 nm over the silicon nitride substrate described in chapter 3. Only ~ 6% of the emitted radiation is radiated upwards and collected by a cone of NA = 0.9.



(c) Projections of the dipole emission patterns for the case of DBT 80 nm of Ac, situated at 20 nm over the titanium dioxide substrate described in chapter 4. Only ~ 17% of the emitted radiation is radiated upwards and collected by a cone of NA = 0.9.

Figure C.3 Dipole emission patterns of DBT in Ac for various substrates.

The polar plot of the emission is reported in figure C.3b. With respect to the previous case the symmetry is broken by the layered structure. Most of the radiation is emitted towards the high index silicon and silicon nitride, with moderate reflections. Only about 6% of the fluorescence from the dipole is collected from an objective.

As the anthracene layer is increased, and the position of the molecule is changed within the crystal, the simulation showed an oscillatory behaviour of the direction of emission, and therefore of the collected portion of the radiation. From a minimum of 6%, comparable with the previous case, the collection efficiency showed a modulation as a function of the distance between the molecule and the top surface of anthracene, reaching a maximum of $\sim$ 12%. This is the case relevant for the thick co-sublimation crystals presented in chapter 3, where the molecules are evenly distributed inside the anthracene [116, 121]. A careful analysis has to be taken into account when calcuating the collection efficiency for this case.

Finally, figure C.3c reports the dipole emission pattern for a DBT molecule deposited over the titanium dioxide layer used for the HPW (from top to bottom: 80 nm of silica and 300 nm of titanium dioxide, over a silica substrate). The polar plot shows that, in contrast with the previous case, the dipole emission is mostly directed towards the upper half space. The integral showed a collection of $\sim$ 18% of the total radiated emission for the case of 80 nm of Ac, and the molecule sitting at 20 nm from the top surface. By moving the position of the dipole inside the anthracene layer it is possible to obtain a maximum collection efficiency of 21% for a molecule close to the silica surface, and a minimum of 9% for a molecule close to the Ac-air interface. It is important to remember that this simulation is valid only for a molecule on the substrate, away from the gold slabs, as these severely modify the emission pattern.

With this new information it is possible to validate the collection efficiency calculation, presented in figure 4.12. By measuring a saturation trace for a molecule placed on a known substrate like those presented in fig. C.3, it is possible to compare the measured collection efficiency with a theoretical calculation, accounting for every optical element in the system.

LIST OF PUBLICATIONS

- **S.G.**, A. Zavatta, M. Bellini and M. G. A. Paris, *Quantum tomography of a homodyne detector*. New Journal of Physics, (2017).
- **S.G.**, K. D. Major, C. Polisseni, S. Boissier, A. S. Clark and E. A. Hinds, *Quantum dynamics of a driven two-level molecule with variable dephasing*. Physical Review A **94**, 063839 (2016), Editor's Suggestions.
- C. Polisseni, K. D. Major, S. Boissier, **S.G.**, A. S. Clark and E. A. Hinds, *Stable, single-photon emitter in a thin organic crystal for application to quantum-photonic devices*. Optics Express **24**, 5615 (2016)
- K. D. Major, Y.-H. Lien, C. Polisseni, **S.G.**, K. W. Rho, A. S. Clark, J. Hwang and E. A. Hinds, *Growth of optical-quality anthracene crystals doped with dibenzoterrylene for controlled single photon production*. Review of Scientific Instruments **86**, (2015).
- H. Jeong, A. Zavatta, M. Kang, S.-W. Lee, L. S. Costanzo, **S.G.**, T. C. Ralph and M. Bellini, *Generation of hybrid entanglement of light*. Nature Photonics **8**, 564-569 (2014).

REFERENCES

[1] R. Loudon. *The Quantum Theory of Light*. Third Edit. Oxford Science Publications, 2000 (cit. on pp. 1, 21, 22, 28, 30, 137, 143, 155).

[2] H.-A. Bachor and T. C. Ralph. *A Guide to Experiments in Quantum Optics*. Wiley-VCH, 2004 (cit. on p. 1).

[3] C. Cohen-Tannoudji, J. Dupont-Roc and G. Grynberg. *Atom-Photon Interactions: Basic Processes and Applications*. Wiley-VCH, 1992 (cit. on p. 1).

[4] M. Planck. "Über eine Verbesserung der Wienschen Spektralgleichung". In: *Verhandlungen der Deutschen Physikalischen Gesellschaft* 2 (1900), pp. 202–204 (cit. on p. 2).

[5] G. N. Lewis. "The Conservation of Photons". In: *Nature* 118.2981 (1926), pp. 874–875. DOI: 10.1038/118874a0 (cit. on p. 2).

[6] M. A. Nielsen and I. L. Chuang. *Quantum Computation and Quantum Information*. Cambridge: Cambridge University Press, 2010. DOI: 10.1017/CBO9780511976667 (cit. on p. 2).

[7] Q. A. Turchette et al. "Measurement of Conditional Phase Shifts for Quantum Logic". In: *Physical Review Letters* 75.25 (1995), pp. 4710–4713. DOI: 10.1103/PhysRevLett.75.4710 (cit. on p. 3).

[8] P. Domokos et al. "Simple cavity-QED two-bit universal quantum logic gate: The principle and expected performances". In: *Physical Review A* 52.5 (1995), pp. 3554–3559. DOI: 10.1103/PhysRevA.52.3554 (cit. on p. 3).

[9] I. L. Chuang and Y. Yamamoto. "Simple quantum computer". In: *Physical Review A* 52.5 (1995), pp. 3489–3496. DOI: 10.1103/PhysRevA.52.3489 (cit. on p. 3).

[10] E. Knill, R. Laflamme and G. J. Milburn. "A scheme for efficient quantum computation with linear optics". In: *Nature* 409.6816 (2001), pp. 46–52. DOI: 10.1038/35051009 (cit. on pp. 3, 115).

[11] J. I. Cirac and P. Zoller. "Quantum Computations with Cold Trapped Ions". In: *Physical Review Letters* 74.20 (1995), pp. 4091–4094. DOI: 10.1103/PhysRevLett.74.4091 (cit. on p. 3).

[12] Q. A. Turchette et al. "Deterministic Entanglement of Two Trapped Ions". In: *Physical Review Letters* 81.17 (1998), pp. 3631–3634. DOI: 10.1103/PhysRevLett.81.3631 (cit. on p. 3).

[13] Y. Nakamura, Y. A. Pashkin and J. S. Tsai. "Coherent control of macroscopic quantum states in a single-Cooper-pair box". In: *Nature* 398.6730 (1999), pp. 786–788. DOI: 10.1038/19718 (cit. on p. 3).

[14] J. E. Mooij et al. "Josephson Persistent-Current Qubit". In: *Science* 285.5430 (1999), pp. 1036–1039. DOI: 10.1126/science.285.5430.1036 (cit. on p. 3).

[15] D. P. DiVincenzo. "Two-bit gates are universal for quantum computation". In: *Physical Review A* 51.2 (1995), pp. 1015–1022. DOI: 10.1103/PhysRevA.51.1015 (cit. on p. 3).

[16] I. L. Chuang, N. Gershenfeld and M. Kubinec. "Experimental Implementation of Fast Quantum Searching". In: *Physical Review Letters* 80.15 (1998), pp. 3408–3411. DOI: 10.1103/PhysRevLett.80.3408 (cit. on p. 3).

[17] B. Trauzettel et al. "Spin qubits in graphene quantum dots". In: *Nature Physics* 3.3 (2007), pp. 192–196. DOI: 10.1038/nphys544 (cit. on p. 3).

[18] J. J. Pla et al. "A single-atom electron spin qubit in silicon". In: *Nature* 489.7417 (2012), pp. 541–545. DOI: 10.1038/nature11449 (cit. on p. 3).

[19] M. Fuechsle et al. "A single-atom transistor". In: *Nature Nanotechnology* 7.4 (2012), pp. 242–246. DOI: 10.1038/nnano.2012.21 (cit. on p. 3).

[20] O. Gywat, H. J. Krenner and J. Berezovsky. *Spins in Optically Active Quantum Dots*. Wiley-VCH, 2010 (cit. on p. 3).

[21] L. Childress and R. Hanson. "Diamond NV centers for quantum computing and quantum networks". In: *MRS Bulletin* 38.02 (2013), pp. 134–138. DOI: 10.1557/mrs.2013.20 (cit. on pp. 3, 7).

[22] D. J. Christle et al. "Isolated electron spins in silicon carbide with millisecond coherence times". In: *Nature Materials* 14.2 (2014), pp. 160–163. DOI: 10.1038/nmat4144 (cit. on p. 3).

[23] D. J. Reilly. "Engineering the quantum-classical interface of solid-state qubits". In: *npj Quantum Information* 1.April (2015), p. 15011. DOI: 10.1038/npjqi.2015.11 (cit. on p. 3).

[24] H. J. Kimble. "The quantum internet." In: *Nature* 453.7198 (2008), pp. 1023–30. DOI: 10.1038/nature07127 (cit. on p. 3).

[25] B. Lounis and M. Orrit. "Single-photon sources". In: *Reports on Progress in Physics* 68.5 (2005), pp. 1129–1179. DOI: 10.1088/0034-4885/68/5/R04 (cit. on p. 3).

[26] M. D. Eisaman et al. "Invited Review Article: Single-photon sources and detectors". In: *Review of Scientific Instruments* 82.7 (2011), p. 071101. DOI: 10.1063/1.3610677 (cit. on p. 3).

[27] R. Hanbury Brown and R. Q. Twiss. "Correlation between Photons in two Coherent Beams of Light". In: *Nature* 177.4497 (1956), pp. 27–29. DOI: 10.1038/177027a0 (cit. on pp. 3, 29).

[28] N. Gisin et al. "Quantum cryptography". In: *Reviews of Modern Physics* 74.1 (2002), pp. 145–195. DOI: 10.1103/RevModPhys.74.145 (cit. on p. 4).

[29] Y. R. Shen. *The Principles of Nonlinear Optics*. Wiley, 1984 (cit. on p. 4).

[30] C. K. Hong and L. Mandel. "Experimental realization of a localized one-photon state". In: *Physical Review Letters* 56.1 (1986), pp. 58–60. DOI: 10.1103/PhysRevLett.56.58 (cit. on p. 4).

[31] D. C. Burnham and D. L. Weinberg. "Observation of Simultaneity in Parametric Production of Optical Photon Pairs". In: *Physical Review Letters* 25.2 (1970), pp. 84–87. DOI: 10.1103/PhysRevLett.25.84 (cit. on p. 4).

[32] C. K. Hong, Z. Ou and L. Mandel. "Measurement of subpicosecond time intervals between two photons by interference". In: *Physical Review Letters* 59.18 (1987), pp. 2044–2046. DOI: 10.1103/PhysRevLett.59.2044 (cit. on pp. 4, 5).

[33] P. G. Kwiat et al. "New High-Intensity Source of Polarization-Entangled Photon Pairs". In: *Physical Review Letters* 75.24 (1995), pp. 4337–4341. DOI: 10.1103/PhysRevLett.75.4337 (cit. on p. 4).

[34] Y. Shih. "Entangled biphoton source - property and preparation". In: *Reports on Progress in Physics* 66.6 (2003), pp. 1009–1044. DOI: 10.1088/0034-4885/66/6/203 (cit. on p. 4).

[35] J. F. Clauser. "Experimental distinction between the quantum and classical field-theoretic predictions for the photoelectric effect". In: *Physical Review D* 9.4 (1974), pp. 853–860. DOI: 10.1103/PhysRevD.9.853 (cit. on p. 5).

[36] J. F. Clauser and A. Shimony. "Bell's theorem. Experimental tests and implications". In: *Reports on Progress in Physics* 41.12 (1978), pp. 1881–1927. DOI: 10.1088/0034-4885/41/12/002 (cit. on p. 5).

[37] A. Aspect, P. Grangier and G. Roger. "Experimental Tests of Realistic Local Theories via Bell's Theorem". In: *Physical Review Letters* 47.7 (1981), pp. 460–463. DOI: 10.1103/PhysRevLett.47.460 (cit. on p. 5).

[38] P. Grangier, G. Roger and A. Aspect. "Experimental Evidence for a Photon Anticorrelation Effect on a Beam Splitter: A New Light on Single-Photon Interferences". In: *Europhysics Letters (EPL)* 1.4 (1986), pp. 173–179. DOI: 10.1209/0295-5075/1/4/004 (cit. on p. 5).

[39] A. S. Parkins et al. "Synthesis of arbitrary quantum states via adiabatic transfer of Zeeman coherence". In: *Physical Review Letters* 71.19 (1993), pp. 3095–3098. DOI: 10.1103/PhysRevLett.71.3095 (cit. on p. 5).

[40] A. Kuhn, M. Hennrich and G. Rempe. "Deterministic Single-Photon Source for Distributed Quantum Networking". In: *Physical Review Letters* 89.6 (2002), p. 067901. DOI: 10.1103/PhysRevLett.89.067901 (cit. on p. 5).

[41] C. Maurer et al. "A single-photon source based on a single Ca + ion". In: *New Journal of Physics* 6 (2004), pp. 94–94. DOI: 10.1088/1367-2630/6/1/094 (cit. on p. 5).

[42] M. Keller et al. "Continuous generation of single photons with controlled waveform in an ion-trap cavity system". In: *Nature* 431.7012 (2004), pp. 1075–1078. DOI: 10.1038/nature02961 (cit. on p. 5).

[43] M. Trupke et al. "Atom Detection and Photon Production in a Scalable, Open, Optical Microcavity". In: *Physical Review Letters* 99.6 (2007), p. 063601. DOI: 10.1103/PhysRevLett.99.063601 (cit. on p. 5).

[44] M. Hijlkema et al. "A single-photon server with just one atom". In: *Nature Physics* 3.4 (2007), pp. 253–255. DOI: 10.1038/nphys569 (cit. on p. 5).

[45] C. Santori et al. "Indistinguishable photons from a single-photon device". In: *Nature* 419.6907 (2002), pp. 594–597. DOI: 10.1038/nature01086 (cit. on pp. 5, 6).

[46] T. Legero et al. "Quantum Beat of Two Single Photons". In: *Physical Review Letters* 93.7 (2004), p. 070503. DOI: 10.1103/PhysRevLett.93.070503 (cit. on p. 5).

[47] R. B. Patel et al. "Two-photon interference of the emission from electrically tunable remote quantum dots". In: *Nature Photonics* 4.9 (2010), pp. 632–635. DOI: 10.1038/nphoton.2010.161 (cit. on pp. 5, 6).

[48] R. Lettow et al. "Quantum Interference of Tunably Indistinguishable Photons from Remote Organic Molecules". In: *Physical Review Letters* 104.12 (2010), p. 123605. DOI: 10.1103/PhysRevLett.104.123605 (cit. on pp. 5, 12, 73).

[49] H. Bernien et al. "Two-Photon Quantum Interference from Separate Nitrogen Vacancy Centers in Diamond". In: *Physical Review Letters* 108.4 (2012), p. 043604. DOI: 10.1103/PhysRevLett.108.043604 (cit. on p. 5).

[50] A. Sipahigil et al. "Indistinguishable Photons from Separated Silicon-Vacancy Centers in Diamond". In: *Physical Review Letters* 113.11 (2014), p. 113602. DOI: 10.1103/PhysRevLett.113.113602 (cit. on pp. 5, 7).

[51] J. Bylander, I. Robert-Philip and I. Abram. "Interference and correlation of two independent photons". In: *The European Physical Journal D - Atomic, Molecular and Optical Physics* 22.2 (2003), pp. 295–301. DOI: 10.1140/epjd/e2002-00236-6 (cit. on p. 6).

[52] A. Kiraz, M. Atatüre and A. Imamoʃülu. "Quantum-dot single-photon sources: Prospects for applications in linear optics quantum-information processing". In: *Physical Review A* 69.3 (2004), p. 032305. DOI: 10.1103/PhysRevA.69.032305 (cit. on p. 6).

[53] X. Brokmann et al. "Highly efficient triggered emission of single photons by colloidal CdSe/ZnS nanocrystals". In: *Applied Physics Letters* 85.5 (2004), p. 712. DOI: 10.1063/1.1775280 (cit. on p. 6).

[54] B. Lounis et al. "Photon antibunching in single CdSe/ZnS quantum dot fluorescence". In: *Chemical Physics Letters* 329.5-6 (2000), pp. 399–404. DOI: 10.1016/S0009-2614(00)01042-3 (cit. on pp. 6, 51, 67).

[55] D. Gammon et al. "Homogeneous Linewidths in the Optical Spectrum of a Single Gallium Arsenide Quantum Dot". In: *Science* 273.5271 (1996), pp. 87–90. DOI: 10.1126/science.273.5271.87 (cit. on p. 6).

[56] V. Zwiller, T. Aichele and O. Benson. "Quantum optics with single quantum dot devices". In: *New Journal of Physics* 6 (2004), pp. 96–96. DOI: 10.1088/1367-2630/6/1/096 (cit. on p. 6).

[57] P. Lodahl, S. Mahmoodian and S. Stobbe. "Interfacing single photons and single quantum dots with photonic nanostructures". In: *Reviews of Modern Physics* 87.2 (2015), pp. 347–400. DOI: 10.1103/RevModPhys.87.347 (cit. on pp. 6, 109).

[58] N. Somaschi et al. "Near-optimal single-photon sources in the solid state". In: *Nature Photonics* 10.5 (2016), pp. 340–345. DOI: 10.1038/nphoton.2016.23 (cit. on pp. 6, 7).

[59] A. K. Nowak et al. "Deterministic and electrically tunable bright single-photon source". In: *Nature Communications* 5 (2014), p. 3240. DOI: 10.1038/ncomms4240 (cit. on p. 7).

[60] R. N. E. Malein et al. "Screening Nuclear Field Fluctuations in Quantum Dots for Indistinguishable Photon Generation". In: *Physical Review Letters* 116.25 (2016), p. 257401. DOI: 10.1103/PhysRevLett.116.257401 (cit. on p. 7).

[61] G. Kiršanskf ó et al. "Indistinguishable and efficient single photons from a quantum dot in a planar nanobeam waveguide". In: 1.d (2017), pp. 1–11. arXiv: 1701.08131 (cit. on p. 7).

[62] D. Huber et al. "Highly indistinguishable and strongly entangled photons from symmetric GaAs quantum dots". In: (2016). arXiv: 1610.06889 (cit. on p. 7).

[63] Z. H. Peng et al. "Tuneable on-demand single-photon source in the microwave range". In: *Nature Communications* 7.May 2015 (2016), p. 12588. DOI: 10.1038/ncomms12588 (cit. on p. 7).

[64] R. Al-Khuzheyri et al. "Resonance fluorescence from a telecom-wavelength quantum dot". In: *Applied Physics Letters* 109.16 (2016), p. 163104. DOI: 10.1063/1.4965845 (cit. on p. 7).

[65] J.-P. Jahn et al. "An artificial Rb atom in a semiconductor with lifetime-limited linewidth". In: *Physical Review B* 92.24 (2015), p. 245439. DOI: 10.1103/PhysRevB.92.245439 (cit. on pp. 7, 72).

[66] A. Gruber et al. "Scanning Confocal Optical Microscopy and Magnetic Resonance on Single Defect Centers". In: *Science* 276.5321 (1997), pp. 2012–2014. DOI: 10.1126/science.276.5321.2012 (cit. on p. 7).

[67] R. Brouri et al. "Photon antibunching in the fluorescence of individual color centers in diamond". In: *Optics Letters* 25.17 (2000), p. 1294. DOI: 10.1364/OL.25.001294 (cit. on pp. 7, 52).

[68] N. Mizuochi et al. "Electrically driven single-photon source at room temperature in diamond". In: *Nature Photonics* 6.5 (2012), pp. 299–303. DOI: 10.1038/nphoton.2012.75 (cit. on p. 7).

[69] T. Gaebel et al. "Stable single-photon source in the near infrared". In: *New Journal of Physics* 6 (2004), pp. 98–98. DOI: 10.1088/1367-2630/6/1/098 (cit. on p. 7).

[70] E. Wu et al. "Room temperature triggered single-photon source in the near infrared". In: *New Journal of Physics* 9.12 (2007), pp. 434–434. DOI: 10.1088/1367-2630/9/12/434 (cit. on p. 7).

[71] E. Neu et al. "Single photon emission from silicon-vacancy colour centres in chemical vapour deposition nano-diamonds on iridium". In: *New Journal of Physics* 13.2 (2011), p. 025012. DOI: 10.1088/1367-2630/13/2/025012 (cit. on p. 7).

[72] T. Müller et al. "Optical signatures of silicon-vacancy spins in diamond". In: *Nature Communications* 5 (2014). DOI: 10.1038/ncomms4328 (cit. on p. 7).

[73] Y. Zhou et al. "Coherent control of a strongly driven silicon vacancy optical transition in diamond". In: *Nature Communications* 8 (2017), p. 14451. DOI: 10.1038/ncomms14451 (cit. on p. 7).

[74] P. C. Maurer et al. "Room-Temperature Quantum Bit Memory Exceeding One Second". In: *Science* 336.6086 (2012), pp. 1283–1286. DOI: 10.1126/science.1220513 (cit. on pp. 7, 60).

[75] J. Riedrich-Möller et al. "Deterministic Coupling of a Single Silicon-Vacancy Color Center to a Photonic Crystal Cavity in Diamond". In: *Nano Letters* 14.9 (2014), pp. 5281–5287. DOI: 10.1021/nl502327b (cit. on p. 7).

[76] J. Benedikter et al. "Cavity-Enhanced Single-Photon Source Based on the Silicon-Vacancy Center in Diamond". In: *Physical Review Applied* 7.2 (2017), p. 024031. DOI: 10.1103/PhysRevApplied.7.024031 (cit. on p. 7).

[77] S. Pezzagna et al. "Creation and nature of optical centres in diamond for single-photon emission - overview and critical remarks". In: *New Journal of Physics* 13.3 (2011), p. 035024. DOI: 10.1088/1367-2630/13/3/035024 (cit. on p. 7).

[78] S. Castelletto et al. "A silicon carbide room-temperature single-photon source". In: *Nature Materials* 13.2 (2013), pp. 151–156. DOI: 10.1038/nmat3806 (cit. on p. 7).

[79] F. Fuchs et al. “Engineering near-infrared single-photon emitters with optically active spins in ultrapure silicon carbide”. In: *Nature Communications* 6.May (2015), p. 7578. DOI: 10.1038/ncomms8578 (cit. on p. 7).

[80] T. T. Tran et al. “Quantum emission from hexagonal boron nitride monolayers”. In: *Nature Nanotechnology* 11.1 (2015), pp. 37–41. DOI: 10.1038/nnano.2015.242 (cit. on p. 7).

[81] I. Aharonovich, D. Englund and M. Toth. “Solid-state single-photon emitters”. In: *Nature Photonics* 10.10 (2016), pp. 631–641. DOI: 10.1038/nphoton.2016.186 (cit. on p. 7).

[82] J. Bernard et al. “Photon bunching in the fluorescence from single molecules: a probe for intersystem crossing”. In: *The Journal of Chemical Physics* 98.2 (1993), p. 850. DOI: 10.1063/1.464249 (cit. on pp. 8, 30, 33).

[83] C. Brunel et al. “Triggered Source of Single Photons based on Controlled Single Molecule Fluorescence”. In: *Physical Review Letters* 83.14 (1999), pp. 2722–2725. DOI: 10.1103/PhysRevLett.83.2722 (cit. on p. 8).

[84] A. Köhler and H. Bässler. “Triplet states in organic semiconductors”. In: *Materials Science and Engineering: R: Reports* 66.4-6 (2009), pp. 71–109. DOI: 10.1016/j.mser.2009.09.001 (cit. on p. 8).

[85] A. Makarewicz et al. “Vibronic spectra of single dibenzoterrylene molecules in anthracene and 2,3-dimethylanthracene crystals”. In: *Chemical Physics Letters* 535 (2012), pp. 140–145. DOI: 10.1016/j.cplett.2012.03.091 (cit. on pp. 8, 13).

[86] S. Kitson et al. “Intensity fluctuation spectroscopy of small numbers of dye molecules in a microcavity”. In: *Physical Review A* 58.1 (1998), pp. 620–627. DOI: 10.1103/PhysRevA.58.620 (cit. on p. 8).

[87] M. Steiner et al. “Highly efficient, tunable single photon source based on single molecules”. In: *Applied Physics Letters* 90.18 (2007), p. 183122. DOI: 10.1063/1.2736294 (cit. on p. 8).

[88] T. Basché et al. “Photon antibunching in the fluorescence of a single dye molecule trapped in a solid”. In: *Physical Review Letters* 69.10 (1992), pp. 1516–1519. DOI: 10.1103/PhysRevLett.69.1516 (cit. on pp. 8, 24, 30, 33, 140).

[89] B. Lounis and W. E. Moerner. “Single photons on demand from a single molecule at room temperature”. In: *Nature* 407.6803 (2000), pp. 491–493. DOI: 10.1038/35035032 (cit. on p. 8).

[90] J.-B. Trebbia et al. "Efficient generation of near infra-red single photons from the zero-phonon line of a single molecule." In: *Optics express* 17.26 (2009), pp. 23986–23991. DOI: 10.1364/OE.17.023986 (cit. on pp. 8, 12–14, 16, 34, 46, 56).

[91] C. Toninelli et al. "Near-infrared single-photons from aligned molecules in ultrathin crystalline films at room temperature". In: *Optics Express* 18.7 (2010), p. 6577. DOI: 10.1364/OE.18.006577 (cit. on pp. 8, 12, 14, 16, 48, 50, 61, 100, 101).

[92] J. Hwang et al. "A single-molecule optical transistor". In: *Nature* 460.7251 (2009), pp. 76–80. DOI: 10.1038/nature08134 (cit. on p. 8).

[93] A. Maser et al. "Few-photon coherent nonlinear optics with a single molecule". In: *Nature Photonics* 10.7 (2016), pp. 450–453. DOI: 10.1038/nphoton.2016.63 (cit. on p. 8).

[94] C. Polisseni et al. "Stable, single-photon emitter in a thin organic crystal for application to quantum-photonic devices". In: *Optics Express* 24.5 (2016), p. 5615. DOI: 10.1364/OE.24.005615 (cit. on pp. 8, 12, 14, 16, 48, 50, 90, 92, 103).

[95] A. M. Boiron, B. Lounis and M. Orrit. "Single molecules of dibenzanthanthrene in n-hexadecane". In: *Journal of Chemical Physics* 105.10 (1996), pp. 3969–3974. DOI: 10.1063/1.472270 (cit. on p. 8).

[96] A. Walser et al. "Lifetime-limited zero-phonon spectra of single molecules in methyl methacrylate". In: *Chemical Physics Letters* 472.1-3 (2009), pp. 44–47. DOI: 10.1016/j.cplett.2009.02.070 (cit. on p. 8).

[97] J. Hwang and E. A. Hinds. "Dye molecules as single-photon sources and large optical nonlinearities on a chip". In: *New Journal of Physics* 13.8 (2011), p. 85009. DOI: 10.1088/1367-2630/13/8/085009 (cit. on pp. 8, 12, 16).

[98] P. A. M. Dirac. "The Quantum Theory of the Emission and Absorption of Radiation". In: *Proceedings of the Royal Society A: Mathematical, Physical and Engineering Sciences* 114.767 (1927), pp. 243–265. DOI: 10.1098/rspa.1927.0039 (cit. on p. 9).

[99] P. W. Milonni. "Why spontaneous emission?" In: *American Journal of Physics* 52.4 (1984), pp. 340–343. DOI: 10.1119/1.13886 (cit. on p. 9).

[100] V. Weisskopf and E. Wigner. "Berechnung der natürlichen Linienbreite auf Grund der Diracschen Lichttheorie". In: *Zeitschrift für Physik* 63.1-2 (1930), pp. 54–73. DOI: 10.1007/BF01336768 (cit. on p. 9).

[101] E. M. Purcell. "Spontaneous emission probabilities at radio frequencies". In: *Physical Review* 69.11-12 (1946), pp. 674–674. DOI: 10.1103/PhysRev.69.674.2 (cit. on pp. 9, 10, 78).

[102] R. G. Hulet, E. S. Hilfer and D. Kleppner. "Inhibited Spontaneous Emission by a Rydberg Atom". In: *Physical Review Letters* 55.20 (1985), pp. 2137–2140. DOI: 10.1103/PhysRevLett.55.2137 (cit. on p. 9).

[103] W. Jhe et al. "Suppression of spontaneous decay at optical frequencies: Test of vacuum-field anisotropy in confined space". In: *Physical Review Letters* 58.7 (1987), pp. 666–669. DOI: 10.1103/PhysRevLett.58.666 (cit. on p. 9).

[104] M. Pelton. "Modified spontaneous emission in nanophotonic structures". In: *Nature Photonics* 9.7 (2015), pp. 427–435. DOI: 10.1038/nphoton.2015.103 (cit. on pp. 10, 78).

[105] G. Lecamp, P. Lalanne and J. P. Hugonin. "Very Large Spontaneous-Emission β Factors in Photonic-Crystal Waveguides". In: *Physical Review Letters* 99.2 (2007), p. 023902. DOI: 10.1103/PhysRevLett.99.023902 (cit. on p. 11).

[106] M. Arcari et al. "Near-Unity Coupling Efficiency of a Quantum Emitter to a Photonic Crystal Waveguide". In: *Physical Review Letters* 113.9 (2014), p. 093603. DOI: 10.1103/PhysRevLett.113.093603 (cit. on pp. 11, 108).

[107] A. Kinkhabwala et al. "Large single-molecule fluorescence enhancements produced by a bowtie nanoantenna". In: *Nature Photonics* 3.11 (2009), pp. 654–657. DOI: 10.1038/nphoton.2009.187 (cit. on pp. 11, 78).

[108] F. Jelezko et al. "Dibenzoterrylene in Naphthalene: A New Crystalline System for Single Molecule Spectroscopy in the Near Infrared". In: *The Journal of Physical Chemistry* 100.33 (1996), pp. 13892–13894. DOI: 10.1021/jp960845q (cit. on pp. 12, 13).

[109] I. Deperasińska et al. "Single dibenzoterrylene molecules in naphthalene and 2,3-dimethylnaphthalene crystals: vibronic spectra". In: *Physical Chemistry Chemical Physics* 13.5 (2011), p. 1872. DOI: 10.1039/c0cp01730b (cit. on pp. 12, 14).

[110] S. Faez et al. "Design and synthesis of aromatic molecules for probing electric fields at the nanoscale". In: *Faraday Discussion* (2015), pp. 251–262. DOI: 10.1039/C5FD00065C (cit. on pp. 12, 13).

[111] I. Deperasińska et al. "On the photo-stability of single molecules. Dibenzoterrylene in 2,3-dimethylnaphthalene crystals". In: *Chemical Physics Letters* 492.1-3 (2010), pp. 93–97. DOI: 10.1016/j.cplett.2010.04.025 (cit. on pp. 12, 15).

[112] N. R. Verhart, M. Müller and M. Orrit. "Spectroscopy of Single Dibenzoterrylene Molecules in para -Dichlorobenzene". In: *ChemPhysChem* 17.10 (2016), pp. 1524–1529. DOI: 10.1002/cphc.201501087 (cit. on pp. 12, 13, 105).

[113] C. Hofmann et al. "Towards nanoprobes for conduction in molecular crystals: Dibenzoterrylene in anthracene crystals". In: *Chemical Physics* 318.1-2 (2005), pp. 1–6. DOI: 10.1016/j.chemphys.2005.02.003 (cit. on pp. 12, 13).

[114] S. Faez et al. "Coherent Interaction of Light and Single Molecules in a Dielectric Nanoguide". In: *Physical Review Letters* 113.21 (2014), p. 213601. DOI: 10.1103/PhysRevLett.113.213601 (cit. on p. 12).

[115] G. Kewes et al. "A realistic fabrication and design concept for quantum gates based on single emitters integrated in plasmonic-dielectric waveguide structures". In: *Scientific Reports* 6.May (2016), p. 28877. DOI: 10.1038/srep28877 (cit. on p. 12).

[116] K. D. Major. "Coupling Single Molecules to Cryogenic Optical Fibre Microcavities". PhD thesis. Imperial College London, 2016 (cit. on pp. 12, 16, 33, 46, 72, 167).

[117] D. Wang et al. "Coherent Coupling of a Single Molecule to a Scanning Fabry-Perot Microcavity". In: *Physical Review X* 7.2 (2017), p. 021014. DOI: 10.1103/PhysRevX.7.021014. arXiv: 1612.05007 (cit. on pp. 12, 46).

[118] P. E. Lombardi et al. "Photostable molecules on chip: integrated single photon sources for quantum technologies". In: (2017). arXiv: 1701.00459 (cit. on pp. 12, 16).

[119] P. Türschmann et al. "On-chip linear and nonlinear control of single molecules coupled to a nanoguide". In: (2017). arXiv: 1702.05923 (cit. on pp. 12, 16, 105).

[120] G. Witte and C. Wöll. "Growth of aromatic molecules on solid substrates for applications in organic electronics". In: *Journal of Materials Research* 19.07 (2011), pp. 1889–1916. DOI: 10.1557/JMR.2004.0251 (cit. on p. 12).

[121] K. D. Major et al. "Growth of optical-quality anthracene crystals doped with dibenzoterrylene for controlled single photon production". In: *Review of Scientific Instruments* 86.8 (2015), p. 083106. DOI: 10.1063/1.4928500 (cit. on pp. 12, 46, 48, 54, 104, 167).

[122] A. R. Elsharkawi and K. C. Kao. "Study of the optical properties of anthracene thin films by ellipsometry". In: *Journal of the Optical Society of America* 65.11 (1975), p. 1269. DOI: 10.1364/JOSA.65.001269 (cit. on p. 12).

[123] I. Nakada. "The Optical Properties of Anthracene Single Crystals". In: *Journal of the Physical Society of Japan* 17.1 (1962), pp. 113–118. DOI: 10.1143/JPSJ.17.113 (cit. on p. 12).

[124] A. A. L. Nicolet et al. "Single dibenzoterrylene molecules in an anthracene crystal: main insertion sites." In: *ChemPhysChem* 8 (2007), pp. 1929–36. DOI: 10.1002/cphc.200700340 (cit. on pp. 12, 64).

[125] S. Grandi et al. "Quantum dynamics of a driven two-level molecule with variable dephasing". In: *Physical Review A* 94.6 (2016), p. 063839. DOI: 10.1103/PhysRevA.94.063839 (cit. on pp. 13, 16, 36, 62).

[126] A. A. L. Nicolet et al. "Single dibenzoterrylene molecules in an anthracene crystal: spectroscopy and photophysics". In: *ChemPhysChem* 8 (2007), pp. 1215–1220. DOI: 10.1002/cphc.200700091 (cit. on pp. 13, 15, 16, 33, 46, 48, 50, 54, 59, 61).

[127] T. Basché, S. Kummer and C. Bräuchle. "Excitation and Emission Spectroscopy and Quantum Optical Measurement". In: *Single-molecule optical detection, imaging and spectroscopy*. Ed. by W. E. Moerner et al. Wiley, 2008 (cit. on p. 14).

[128] Z. S. Sadeq and J. E. Sipe. "A Simple Hubbard Model for the Excited States of Dibenzoterrylene". In: (2016). arXiv: 1611.09286 (cit. on p. 15).

[129] L. Fleury et al. "High photo-stability of single molecules in an organic crystal at room temperature observed by scanning confocal optical microscopy". In: *Molecular Physics* 95.6 (1998), pp. 1333–1338. DOI: 10.1080/002689798166332 (cit. on p. 15).

[130] M. Kuno et al. "Nonexponential "blinking" kinetics of single CdSe quantum dots: A universal power law behavior". In: *The Journal of Chemical Physics* 112.7 (2000), pp. 3117–3120. DOI: 10.1063/1.480896 (cit. on p. 15).

[131] C. Bradac et al. "Observation and control of blinking nitrogen-vacancy centres in discrete nanodiamonds". In: *Nature Nanotechnology* 5.5 (2010), pp. 345–349. DOI: 10.1038/nnano.2010.56 (cit. on p. 15).

[132] C. Polisseni. "Preparation and testing of dye molecules in anthracene for single photon generation on a waveguide". PhD thesis. Imperial College London, 2017 (cit. on pp. 16, 90, 139).

[133] C. Toninelli et al. "A scanning microcavity for in situ control of single-molecule emission". In: *Applied Physics Letters* 97.2 (2010), p. 021107. DOI: 10.1063/1.3456559 (cit. on p. 16).

[134] H. Wang et al. "Near-Transform-Limited Single Photons from an Efficient Solid-State Quantum Emitter". In: *Physical Review Letters* 116.21 (2016), p. 213601. DOI: 10.1103/PhysRevLett.116.213601. arXiv: 1602.07386 (cit. on p. 16).

[135] P. Siyushev et al. "Molecular photons interfaced with alkali atoms." In: *Nature* 509.7498 (2014), pp. 66–70. DOI: 10.1038/nature13191 (cit. on pp. 16, 72).

[136] H. J. Carmichael and D. F. Walls. "A quantum-mechanical master equation treatment of the dynamical Stark effect". In: *Journal of Physics B: Atomic and Molecular Physics* 9.8 (1976), pp. 1199–1219. DOI: 10.1088/0022-3700/9/8/007 (cit. on pp. 29, 67).

[137] H. J. Carmichael and D. F. Walls. "Proposal for the measurement of the resonant Stark effect by photon correlation techniques". In: *Journal of Physics B: Atomic, Molecular and Optical Physics* 9.4 (1976), pp. L43–L46. DOI: 10.1088/0022-3700/9/4/001 (cit. on p. 29).

[138] H. J. Kimble, M. Dagenais and L. Mandel. "Photon Antibunching in Resonance Fluorescence". In: *Physical Review Letters* 39.11 (1977), pp. 691–695. DOI: 10.1103/PhysRevLett.39.691 (cit. on pp. 29, 67).

[139] W. P. Ambrose et al. "Fluorescence photon antibunching from single molecules on a surface". In: *Chemical Physics Letters* 269.3-4 (1997), pp. 365–370. DOI: 10.1016/S0009-2614(97)00266-2 (cit. on p. 30).

[140] S. Singh. "Antibunching, sub-poissonian photon statistics and finite bandwidth effects in resonance fluorescence". In: *Optics Communications* 44.4 (1983), pp. 254–258. DOI: 10.1016/0030-4018(83)90132-3 (cit. on p. 30).

[141] X. T. Zou and L. Mandel. "Photon-antibunching and sub-Poissonian photon statistics". In: *Physical Review A* 41.1 (1990), pp. 475–476. DOI: 10.1103/PhysRevA.41.475 (cit. on p. 30).

[142] D. F. Walls and G. J. Milburn. *Quantum Optics*. Second. Berlin: Springer, 1994 (cit. on pp. 30, 109).

[143] W. P. Ambrose, T. Basché and W. E. Moerner. "Detection and spectroscopy of single pentacene molecules in a p-terphenyl crystal by means of fluorescence excitation". In: *The Journal of Chemical Physics* 95.10 (1991), p. 7150. DOI: 10.1063/1.461392 (cit. on p. 32).

[144] T. G. Tiecke et al. "Nanophotonic quantum phase switch with a single atom." In: *Nature* 508.7495 (2014), pp. 241–4. DOI: 10.1038/nature13188 (cit. on p. 34).

[145] H. P. Specht et al. "A single-atom quantum memory". In: *Nature* 473.7346 (2011), pp. 190–193. DOI: 10.1038/nature09997 (cit. on p. 34).

[146] W. E. Moerner, M. Orrit and U. P. Wild. *Single-molecule detection, imaging and spectroscopy*. Wiley-VCH, 1996 (cit. on p. 37).

[147] W. E. Moerner and M. Orrit. "Illuminating Single Molecules in Condensed Matter". In: *Science* 283.5408 (1999), pp. 1670–1676. DOI: 10.1126/science.283.5408.1670 (cit. on p. 37).

[148] W. E. Moerner and D. P. Fromm. "Methods of single-molecule fluorescence spectroscopy and microscopy". In: *Review of Scientific Instruments* 74.8 (2003), p. 3597. DOI: 10.1063/1.1589587 (cit. on p. 37).

[149] M. Born and E. Wolf. *Principles of Optics*. 1999 (cit. on p. 38).

[150] L. Novotny and B. Hecht. *Principles of nano-optics*. Cambridge University Press, 2006 (cit. on p. 38).

[151] T. R. Corle and G. S. Kino. "Confocal Scanning Optical Microscopy and Related Imaging Systems". In: *Optical Engineering* 36.6 (1997), p. 1821. DOI: 10.1117/1.601601 (cit. on p. 39).

[152] J.-B. Trebbia, P. Tamarat and B. Lounis. "Indistinguishable near-infrared single photons from an individual organic molecule". In: *Physical Review A* 82.6 (2010), p. 063803. DOI: 10.1103/PhysRevA.82.063803 (cit. on p. 46).

[153] M. Beck. "Comparing measurements of $g^{(2)}(0)$ performed with different coincidence detection techniques". In: *Journal of the Optical Society of America B* 24.12 (2007), p. 2972. DOI: 10.1364/JOSAB.24.002972 (cit. on p. 51).

[154] A. Beveratos et al. "Room temperature stable single-photon source". In: *The European Physical Journal D - Atomic, Molecular and Optical Physics* 18.2 (2002), pp. 191–196. DOI: 10.1140/epjd/e20020023 (cit. on p. 52).

[155] F. Dolde et al. "Room-temperature entanglement between single defect spins in diamond". In: *Nature Physics* 9.3 (2013), pp. 139–143. DOI: 10.1038/nphys2545 (cit. on p. 60).

[156] P. de Bree and D. A. Wiersma. "Application of Redfield theory to optical dephasing and line shape of electronic transitions in molecular mixed crystals". In: *The Journal of Chemical Physics* 70.2 (1979), p. 790. DOI: 10.1063/1.437512 (cit. on p. 62).

[157] W. H. Hesselink and D. A. Wiersma. "Optical dephasing and vibronic relaxation in molecular mixed crystals: A picosecond photon echo and optical study of pentacene in naphthalene and p-terphenyl". In: *The Journal of Chemical Physics* 73.2 (1980), p. 648. DOI: 10.1063/1.440167 (cit. on pp. 62–64).

[158] M. Suzuki, T. Yokoyama and M. Ito. "Polarized Raman spectra of naphthalene and anthracene single crystals". In: *Spectrochimica Acta Part A: Molecular Spectroscopy* 24.8 (1968), pp. 1091–1107. DOI: 10.1016/0584-8539(68)80129-1 (cit. on p. 64).

[159] M. Orrit et al. "Surface Raman spectroscopy and lineshape analysis of monolayer surface phonons of the anthracene crystals". In: *Chemical Physics Letters* 95.4-5 (1983), pp. 315–321. DOI: 10.1016/0009-2614(83)80565-X (cit. on p. 64).

[160] C. Cohen-Tannoudji and S. Reynaud. "Dressed-atom description of resonance fluorescence and absorption spectra of a multi-level atom in an intense laser beam". In: *Journal of Physics B: Atomic and Molecular Physics* 10.3 (1977), pp. 345–363. DOI: 10.1088/0022-3700/10/3/005 (cit. on p. 67).

[161] F. Diedrich and H. Walther. "Nonclassical radiation of a single stored ion". In: *Physical Review Letters* 58.3 (1987), pp. 203–206. DOI: 10.1103/PhysRevLett.58.203 (cit. on p. 67).

[162] A. V. Akimov et al. "Generation of single optical plasmons in metallic nanowires coupled to quantum dots". In: *Nature* 450.7168 (2007), pp. 402–406. DOI: 10.1038/nature06230 (cit. on pp. 67, 77).

[163] A. Batalov et al. "Temporal coherence of photons emitted by single nitrogen-vacancy defect centers in diamond using optical rabi-oscillations". In: *Physical Review Letters* 100.7 (2008), pp. 1–4. DOI: 10.1103/PhysRevLett.100.077401 (cit. on p. 70).

[164] E. B. Flagg et al. "Resonantly driven coherent oscillations in a solid-state quantum emitter". In: *Nature Physics* 5.3 (2009), pp. 203–207. DOI: 10.1038/nphys1184 (cit. on pp. 70, 156).

[165] J. Wolters et al. "Simple atomic quantum memory suitable for semiconductor quantum dot single photons". In: (2017). arXiv: 1703.00489 (cit. on p. 72).

[166] M. Orrit et al. "Stark effect on single molecules in a polymer matrix". In: *Chemical Physics Letters* 196.6 (1992), pp. 595–600. DOI: 10.1016/0009-2614(92)86000-8 (cit. on p. 73).

[167] R. W. Wood. "XLII. On a remarkable case of uneven distribution of light in a diffraction grating spectrum". In: *Philosophical Magazine Series 6* 4.21 (1902), pp. 396–402. DOI: 10.1080/14786440209462857 (cit. on p. 77).

[168] D. Pines. "A Collective Description of Electron Interactions: IV. Electron Interaction in Metals". In: *Physical Review* 92.3 (1953), pp. 626–636. DOI: 10.1103/PhysRev.92.626 (cit. on p. 77).

[169] D. Pines. "Collective Energy Losses in Solids". In: *Reviews of Modern Physics* 28.3 (1956), pp. 184–198. DOI: 10.1103/RevModPhys.28.184 (cit. on p. 77).

[170] S. L. Cunningham, A. A. Maradudin and R. F. Wallis. "Effect of a charge layer on the surface-plasmon-polariton dispersion curve". In: *Physical Review B* 10.8 (1974), pp. 3342–3355. DOI: 10.1103/PhysRevB.10.3342 (cit. on p. 77).

[171] G. Fujii et al. "Preservation of photon indistinguishability after transmission through surface-plasmon-polariton waveguide". In: *Optics Letters* 37.9 (2012), p. 1535. DOI: 10.1364/OL.37.001535 (cit. on p. 77).

[172] G. Di Martino et al. "Observation of Quantum Interference in the Plasmonic Hong-Ou-Mandel Effect". In: *Physical Review Applied* 1.3 (2014), p. 034004. DOI: 10.1103/PhysRevApplied.1.034004 (cit. on p. 77).

[173] F. B. C. Dieleman. "Quantum Properties of Plasmonic Waveguides". PhD Thesis. Imperial College London, 2017 (cit. on p. 77).

[174] R. Kolesov et al. "Wave,Äìparticle duality of single surface plasmon polaritons". In: *Nature Physics* 5.7 (2009), pp. 470–474. DOI: 10.1038/nphys1278 (cit. on p. 77).

[175] E. Altewischer, M. P. van Exter and J. P. Woerdman. "Plasmon-assisted transmission of entangled photons". In: *Nature* 418.6895 (2002), pp. 304–306. DOI: 10.1038/nature00869 (cit. on p. 77).

[176] S. Fasel et al. "Energy-Time Entanglement Preservation in Plasmon-Assisted Light Transmission". In: *Physical Review Letters* 94.11 (2005), p. 110501. DOI: 10.1103/PhysRevLett.94.110501 (cit. on p. 77).

[177] S. Fasel et al. "Quantum superposition and entanglement of mesoscopic plasmons". In: *New Journal of Physics* 8 (2006), pp. 13–13. DOI: 10.1088/1367-2630/8/1/013 (cit. on p. 77).

[178] A. Huck et al. "Demonstration of Quadrature-Squeezed Surface Plasmons in a Gold Waveguide". In: *Physical Review Letters* 102.24 (2009), p. 246802. DOI: 10.1103/PhysRevLett.102.246802 (cit. on p. 77).

[179] J. Takahara et al. "Guiding of a one-dimensional optical beam with nanometer diameter". In: *Optics Letters* 22.7 (1997), p. 475. DOI: 10.1364/OL.22.000475 (cit. on p. 77).

[180] W. L. Barnes. "Fluorescence near interfaces: The role of photonic mode density". In: *Journal of Modern Optics* 45.4 (1998), pp. 661–699. DOI: 10.1080/09500349808230614 (cit. on pp. 77, 78).

[181] N. E. Hecker et al. "Surface plasmon-enhanced photoluminescence from a single quantum well". In: *Applied Physics Letters* 75.11 (1999), pp. 1577–1579. DOI: 10.1063/1.124759 (cit. on p. 77).

[182] D. E. Chang et al. "Quantum Optics with Surface Plasmons". In: *Physical Review Letters* 97.5 (2006), p. 053002. DOI: 10.1103/PhysRevLett.97.053002 (cit. on p. 78).

[183] M. S. Tame et al. "Quantum plasmonics". In: *Nature Physics* 9.6 (2013), pp. 329–340. DOI: 10.1038/nphys2615 (cit. on p. 78).

[184] P. Anger, P. Bharadwaj and L. Novotny. "Enhancement and Quenching of Single-Molecule Fluorescence". In: *Physical Review Letters* 96.11 (2006), p. 113002. DOI: 10.1103/PhysRevLett.96.113002 (cit. on p. 78).

[185] K. M. Birnbaum et al. “Photon blockade in an optical cavity with one trapped atom”. In: *Nature* 436.7047 (2005), pp. 87–90. DOI: 10.1038/nature03804 (cit. on p. 78).

[186] P. Kolchin, R. F. Oulton and X. Zhang. “Nonlinear Quantum Optics in a Waveguide: Distinct Single Photons Strongly Interacting at the Single Atom Level”. In: *Physical Review Letters* 106.11 (2011), p. 113601. DOI: 10.1103/PhysRevLett.106.113601 (cit. on p. 78).

[187] A. Manjavacas, P. Nordlander and F. J. García de Abajo. “Plasmon Blockade in Nanostructured Graphene”. In: *ACS Nano* 6.2 (2012), pp. 1724–1731. DOI: 10.1021/nn204701w (cit. on p. 78).

[188] N. P. de Leon et al. “Tailoring Light-Matter Interaction with a Nanoscale Plasmon Resonator”. In: *Physical Review Letters* 108.22 (2012), p. 226803. DOI: 10.1103/PhysRevLett.108.226803 (cit. on p. 78).

[189] D. E. Chang et al. “A single-photon transistor using nanoscale surface plasmons”. In: *Nature Physics* 3.11 (2007), pp. 807–812. DOI: 10.1038/nphys708 (cit. on p. 78).

[190] R. Chikkaraddy et al. “Single-molecule strong coupling at room temperature in plasmonic nanocavities”. In: *Nature* 535.7610 (2016), pp. 127–130. DOI: 10.1038/nature17974 (cit. on p. 78).

[191] F. H. L. Koppens, D. E. Chang and F. J. García de Abajo. “Graphene Plasmonics: A Platform for Strong Light-Matter Interactions”. In: *Nano Letters* 11.8 (2011), pp. 3370–3377. DOI: 10.1021/nl201771h (cit. on p. 79).

[192] K. G. Lee et al. “A planar dielectric antenna for directional single-photon emission and near-unity collection efficiency”. In: *Nature Photonics* 5.3 (2011), pp. 166–169. DOI: 10.1038/nphoton.2010.312 (cit. on p. 79).

[193] J. Cambiasso et al. “Bridging the Gap between Dielectric Nanophotonics and the Visible Regime with Effectively Lossless Gallium Phosphide Antennas”. In: *Nano Letters* 17.2 (2017), pp. 1219–1225. DOI: 10.1021/acs.nanolett.6b05026 (cit. on p. 79).

[194] L. Lafone, T. P. H. Sidiropoulos and R. F. Oulton. “Silicon-based metal-loaded plasmonic waveguides for low-loss nanofocusing”. In: *Optics Letters* (2014). DOI: 10.1364/OL.39.004356 (cit. on p. 79).

[195] M. P. Nielsen et al. "Adiabatic Nanofocusing in Hybrid Gap Plasmon Waveguides on the Silicon-on-Insulator Platform". In: *Nano Letters* 16.2 (2016), pp. 1410–1414. DOI: 10.1021/acs.nanolett.5b04931 (cit. on p. 79).

[196] J. D. Jackson. *Classical Electrodynamics*. Wiley, 1999 (cit. on p. 81).

[197] D. K. Gramotnev, M. W. Vogel and M. I. Stockman. "Optimized nonadiabatic nanofocusing of plasmons by tapered metal rods". In: *Journal of Applied Physics* 104.3 (2008), p. 034311. DOI: 10.1063/1.2963699 (cit. on p. 83).

[198] B. Gmeiner et al. "Spectroscopy and microscopy of single molecules in nanoscopic channels: spectral behavior vs. confinement depth". In: *Physical Chemistry Chemical Physics* 18.29 (2016), pp. 19588–19594. DOI: 10.1039/C6CP01698G (cit. on p. 104).

[199] R. B. Campbell, J. M. Robertson and J. Trotter. "The crystal structure of hexacene, and a revision of the crystallographic data for tetracene". In: *Acta Crystallographica* 15.3 (1962), pp. 289–290. DOI: 10.1107/S0365110X62000699 (cit. on p. 104).

[200] *Photonic Nanostructure Research Group*. DOI: www.brl.ntt.co.jp/E/group_011/group_011.html (cit. on p. 107).

[201] A. Yariv et al. "Coupled-resonator optical waveguide: a proposal and analysis". In: *Optics Letters* 24.11 (1999), p. 711. DOI: 10.1364/OL.24.000711 (cit. on pp. 107, 109).

[202] S. L. McCall et al. "Whispering-gallery mode microdisk lasers". In: *Applied Physics Letters* 60.3 (1992), pp. 289–291. DOI: 10.1063/1.106688 (cit. on p. 107).

[203] R. D. Meade et al. "Novel applications of photonic band gap materials: Low-loss bends and high Q cavities". In: *Journal of Applied Physics* 75.9 (1994), pp. 4753–4755. DOI: 10.1063/1.355934 (cit. on p. 107).

[204] P. R. Villeneuve, S. Fan and J. D. Joannopoulos. "Microcavities in photonic crystals: Mode symmetry, tunability, and coupling efficiency". In: *Physical Review B* 54.11 (1996), pp. 7837–7842. DOI: 10.1103/PhysRevB.54.7837 (cit. on p. 107).

[205] Y. A. Vlasov et al. "Active control of slow light on a chip with photonic crystal waveguides". In: *Nature* 438.7064 (2005), pp. 65–69. DOI: 10.1038/nature04210 (cit. on p. 108).

[206] E. Kuramochi et al. "Systematic hole-shifting of L-type nanocavity with an ultrahigh Q factor". In: *Optics Letters* 39.19 (2014), p. 5780. DOI: 10.1364/OL.39.005780 (cit. on p. 108).

[207] T. Baba. "Slow light in photonic crystals". In: *Nature Photonics* 2.8 (2008), pp. 465–473. DOI: 10.1038/nphoton.2008.146 (cit. on p. 109).

[208] C. P. Michael et al. "Growth, processing, and optical properties of epitaxial Er_2O_3 on silicon". In: *Optics Express* 16.24 (2008), p. 19649. DOI: 10.1364/OE.16.019649 (cit. on pp. 112, 114).

[209] A. M. Grishin, S. I. Khartsev and D. O. Dzibrou. "Enhanced photoluminescence in $[Er_2O_3/TiO_2]^m$ photonic crystals". In: *Journal of Applied Physics* 105.11 (2009), p. 113122. DOI: 10.1063/1.3143082 (cit. on p. 112).

[210] T.-D. Nguyen, C.-T. Dinh and T.-O. Do. "Shape- and Size-Controlled Synthesis of Monoclinic ErOOH and Cubic Er_2O_3 from Micro- to Nano-structures and Their Upconversion Luminescence". In: *ACS Nano* 4.4 (2010), pp. 2263–2273. DOI: 10.1021/nn100292s (cit. on p. 112).

[211] R. Kolesov et al. "Mapping Spin Coherence of a Single Rare-Earth Ion in a Crystal onto a Single Photon Polarization State". In: *Physical Review Letters* 111.12 (2013), p. 120502. DOI: 10.1103/PhysRevLett.111.120502 (cit. on p. 112).

[212] K. Xia et al. "All-Optical Preparation of Coherent Dark States of a Single Rare Earth Ion Spin in a Crystal". In: *Physical Review Letters* 115.9 (2015), pp. 1–5. DOI: 10.1103/PhysRevLett.115.093602 (cit. on p. 112).

[213] H. Omi and T. Tawara. "Energy Transfers between Er^{3+} Ions Located at the Two Crystalographic Sites of Er_2O_3 Grown on Si(111)". In: *Japanese Journal of Applied Physics* 51.2 (2012), 02BG07. DOI: 10.1143/JJAP.51.02BG07 (cit. on pp. 112, 113).

[214] T. Tawara et al. "Population dynamics in epitaxial Er_2O_3 thin films grown on Si(111)". In: *Applied Physics Letters* 102.24 (2013), p. 241918. DOI: 10.1063/1.4812294 (cit. on pp. 113, 114, 124).

[215] J. B. Gruber et al. "Energy Levels of Single-Crystal Erbium Oxide". In: *The Journal of Chemical Physics* 45.2 (1966), pp. 477–482. DOI: 10.1063/1.1727592 (cit. on p. 114).

[216] K. Nozaki et al. "Sub-femtojoule all-optical switching using a photonic-crystal nanocavity". In: *Nature Photonics* 4.7 (2010), pp. 477–483. DOI: 10.1038/nphoton.2010.89 (cit. on p. 114).

[217] J. D. Franson, B. C. Jacobs and T. B. Pittman. "Quantum computing using single photons and the Zeno effect". In: *Physical Review A* 70.6 (2004), p. 062302. DOI: 10.1103/PhysRevA.70.062302 (cit. on pp. 114, 115).

[218] B. Misra and E. C. G. Sudarshan. "The Zeno's paradox in quantum theory". In: *Journal of Mathematical Physics* 18.4 (1977), pp. 756–763. DOI: 10.1063/1.523304 (cit. on p. 114).

[219] T. B. Pittman, B. C. Jacobs and J. D. Franson. "Probabilistic quantum logic operations using polarizing beam splitters". In: *Physical Review A* 64.6 (2001), p. 062311. DOI: 10.1103/PhysRevA.64.062311 (cit. on p. 115).

[220] S. M. Hendrickson et al. "All-optical-switching demonstration using two-photon absorption and the Zeno effect". In: *Physical Review A* 87.2 (2013), p. 023808. DOI: 10.1103/PhysRevA.87.023808 (cit. on p. 116).

[221] K. T. McCusker et al. "Experimental Demonstration of Interaction-Free All-Optical Switching via the Quantum Zeno Effect". In: *Physical Review Letters* 110.24 (2013), p. 240403. DOI: 10.1103/PhysRevLett.110.240403 (cit. on p. 116).

[222] P. D. Drummond and D. F. Walls. "Quantum theory of optical bistability. I. Nonlinear polarisability model". In: *Journal of Physics A: Mathematical and General* 13.2 (1980), pp. 725–741. DOI: 10.1088/0305-4470/13/2/034 (cit. on p. 117).

[223] B. Cao, K. W. Mahmud and M. Hafezi. "Two coupled nonlinear cavities in a driven-dissipative environment". In: *Physical Review A* 94.6 (2016), p. 063805. DOI: 10.1103/PhysRevA.94.063805 (cit. on p. 117).

[224] A. Le Boité, G. Orso and C. Ciuti. "Steady-State Phases and Tunneling-Induced Instabilities in the Driven Dissipative Bose-Hubbard Model". In: *Physical Review Letters* 110.23 (2013), p. 233601. DOI: 10.1103/PhysRevLett.110.233601 (cit. on p. 117).

[225] N. Bartolo et al. "Exact steady state of a Kerr resonator with one- and two-photon driving and dissipation: Controllable Wigner-function multimodality and dissipative phase transitions". In: *Physical Re-*

view A 94.3 (2016), p. 033841. DOI: 10.1103/PhysRevA.94.033841 (cit. on p. 117).

[226] L. Gilles and P. L. Knight. "Two-photon absorption and nonclassical states of light". In: *Physical Review A* 48.2 (1993), pp. 1582–1593. DOI: 10.1103/PhysRevA.48.1582 (cit. on p. 118).

[227] W. Casteels et al. "Truncated correlation hierarchy schemes for driven-dissipative multimode quantum systems". In: *New Journal of Physics* 18.9 (2016), p. 093007. DOI: 10.1088/1367-2630/18/9/093007 (cit. on pp. 119, 130).

[228] M. Pawlicki et al. "Two-Photon Absorption and the Design of Two-Photon Dyes". In: *Angewandte Chemie International Edition* 48.18 (2009), pp. 3244–3266. DOI: 10.1002/anie.200805257 (cit. on pp. 130, 131).

[229] H. de Vries and D. A. Wiersma. "Fluorescence transient and optical free induction decay spectroscopy of pentacene in mixed crystals at 2 K. Determination of intersystem crossing and internal conversion rates". In: *The Journal of Chemical Physics* 70.12 (1979), p. 5807. DOI: 10.1063/1.437411 (cit. on p. 140).

[230] W. H. Heitler. *The Quantum Theory of Radiation*. Oxford, London, 1954 (cit. on p. 142).

[231] B. R. Mollow. "Power Spectrum of Light Scattered by Two-Level Systems". In: *Physical Review* 188.5 (1969), pp. 1969–1975. DOI: 10.1103/PhysRev.188.1969 (cit. on pp. 142, 155).

[232] B. R. Mollow. "Pure-state analysis of resonant light scattering: Radiative damping, saturation, and multiphoton effects". In: *Physical Review A* 12.5 (1975), pp. 1919–1943. DOI: 10.1103/PhysRevA.12.1919 (cit. on p. 142).

[233] D. F. Walls. "Evidence for the quantum nature of light". In: *Nature* 280.5722 (1979), pp. 451–454. DOI: 10.1038/280451a0 (cit. on p. 142).

[234] H. J. Carmichael. *Statistical Methods in Quantum Optics 1*. Springer, 2002 (cit. on pp. 143, 147, 148, 152, 157).

[235] H. J. Carmichael. *Statistical Methods in Quantum Optics 2*. 2008 (cit. on p. 152).

[236] A. Muller. "Resonance Fluorescence and Cavity Quantum Electrodynamics with Quantum Dots". PhD Thesis. Austin, 2007 (cit. on p. 155).

[237] C. Matthiesen, A. N. Vamivakas and M. Atatüre. "Subnatural linewidth single photons from a quantum dot". In: *Physical Review Letters* 108.9 (2012), p. 093602. DOI: 10.1103/PhysRevLett.108.093602 (cit. on p. 155).

[238] G. Wrigge et al. "Efficient coupling of photons to a single molecule and the observation of its resonance fluorescence". In: *Nature Physics* 4.1 (2008), pp. 60–66. DOI: 10.1038/nphys812 (cit. on p. 156).

[239] M. Baur et al. "Measurement of Autler-Townes and Mollow Transitions in a Strongly Driven Superconducting Qubit". In: *Physical Review Letters* 102.24 (2009), p. 243602. DOI: 10.1103/PhysRevLett.102.243602 (cit. on p. 156).

[240] B. Pigeau et al. "Observation of a phononic Mollow triplet in a multimode hybrid spin-nanomechanical system". In: *Nature Communications* 6 (2015), p. 8603. DOI: 10.1038/ncomms9603 (cit. on p. 156).

[241] D. V. Kuznetsov, V. K. Roerich and M. G. Gladush. "Local field and radiative relaxation rate in a dielectric medium". In: *Journal of Experimental and Theoretical Physics* 113.4 (2011), pp. 647–658. DOI: 10.1134/S1063776111100050 (cit. on pp. 163, 164).

[242] S. M. Barnett, B. Huttner and R. Loudon. "Spontaneous emission in absorbing dielectric media". In: *Physical Review Letters* 68.25 (1992), pp. 3698–3701. DOI: 10.1103/PhysRevLett.68.3698 (cit. on p. 163).

[243] P. W. Milonni. "Field Quantization and Radiative Processes in Dispersive Dielectric Media". In: *Journal of Modern Optics* 42.10 (1995), pp. 1991–2004. DOI: 10.1080/09500349514551741 (cit. on p. 163).

[244] J. Knoester and S. Mukamel. "Intermolecular forces, spontaneous emission, and superradiance in a dielectric medium: Polariton-mediated interactions". In: *Physical Review A* 40.12 (1989), pp. 7065–7080. DOI: 10.1103/PhysRevA.40.7065 (cit. on p. 163).

[245] S. M. Barnett et al. "Decay of excited atoms in absorbing dielectrics". In: *Journal of Physics B: Atomic, Molecular and Optical Physics* 29.16 (1999), pp. 3763–3781. DOI: 10.1088/0953-4075/29/16/019 (cit. on p. 163).

[246] F. A. Inam et al. "Modification of spontaneous emission from nanodiamond colour centres on a structured surface". In: *New Journal of Physics* 13 (2011). DOI: 10.1088/1367-2630/13/7/073012 (cit. on p. 163).

[247] L. Onsager. "Electric Moments of Molecules in Liquids". In: *Journal of the American Chemical Society* 58.8 (1936), pp. 1486–1493. DOI: 10.1021/ja01299a050 (cit. on p. 163).

[248] R. J. Glauber and M. Lewenstein. "Quantum optics of dielectric media". In: *Physical Review A* 43.1 (1991), pp. 467–491. DOI: 10.1103/PhysRevA.43.467 (cit. on p. 163).

[249] G. Kumar, D. Rao and G. S. Agarwal. "Measurement of Local Field Effects of the Host on the Lifetimes of Embedded Emitters". In: *Physical Review Letters* 91.20 (2003). DOI: 10.1103/PhysRevLett.91.203903 (cit. on p. 164).

[250] H. T. Dung, S. Y. Buhmann and D.-G. Welsch. "Local-field correction to the spontaneous decay rate of atoms embedded in bodies of finite size". In: *Physical Review A* 74.2 (2006). DOI: 10.1103/PhysRevA.74.023803 (cit. on p. 164).

[251] L. Zampedri et al. "Evaluation of local field effect on the $^4I_{13/2}$ lifetimes in Er-doped silica-hafnia planar wave". In: *Physical Review B* 75.7 (2007), p. 073105. DOI: 10.1103/PhysRevB.75.073105 (cit. on p. 164).

[252] M. E. Crenshaw and C. M. Bowden. "Effects of Local Fields on Spontaneous Emission in Dielectric Media". In: *Physical Review Letters* 85.9 (2000), pp. 1851–4. DOI: 10.1103/PhysRevLett.85.1851 (cit. on p. 164).

[253] S. F. Wuister, C. de Mello Donega and A. Meijerink. "Local-field effects on the spontaneous emission rate of CdTe and CdSe quantum dots in dielectric media." In: *The Journal of chemical physics* 121.9 (2004), pp. 4310–4315. DOI: 10.1063/1.1773154 (cit. on p. 164).

INDEX

anthracene, 12

Born approximation, 147
broadening
    inhomogeneous, 56

collection efficiency, 102
colour-centres, 7
confocal microscope, 37
correlation function
    first-order, 142, 154
    second-order, 36, 142, 157
CROW, 109, 126

dibenzoterrylene, 12
dipole emission pattern, 165

fluorescence spectrum, 59
    Mollow triplet, 155

input/output formalism, 111

local field corrections, 162

Markov approximation, 147
master equation
    derivation, 146
    resonance fluorescence, 146
    two-photon absorption, 120

optical Bloch equations
    blue-detuned pumping, 34
    steady-state, 23
    triplet state, 32
    two-level system, 22, 137

photon, 1
Purcell factor, 10

quantum dot, 6
qubit, 2

saturation
    room temperature, 48
    theory, 23
single molecules, 7
SPDC, 4
surface plasmon polariton, 77

triplet state, 14
    correlation function, 32
    energy, 15
    lifetime, 61

waveguide coupling
    coupling factor β, 99
    results, 102

PERMISSIONS

Follows here the permissions from the Japanese Journal of Applied Physics and from Applied Physics Letters, equired to reproduce figure 5.3.

[Notice]
If you are the one of the authors of the paper, you don't have to apply for a permission with the following conditions.
1. Follow the Copyright Policy of the Japan Society of Applied Physics
2. A credit line of "Copyright (published year) The Japan Society of Applied Physics" should be added to the end of the figure caption in the Content.
3. The Content must be cited as a reference in the Publication.

30 / 03 / 2017
Day Month Year

To: President of the Japan Society of Applied Physics

Submit to:
Publication Center for Pure and Applied Physics, The Japan Society of Applied Physics
2-31-22-5F, Yushima, Bunkyo-ku, Tokyo 113-0034, Japan
TEL: +81-3-5844-3291 FAX: +81-3-5844-3290 E-mail address: permission@jsap.or.jp

Application for Permission to Reproduce Material

I request permission to reproduce the following material, copyrighted by the Japan Society of Applied Physics.

Publication where material is reproduced (the Publication)

Name of the Publication (e.g., journal title, book title): PhD Thesis - Single Quantum emitters: resonance fluorescence and emission enhancement
Publisher (e.g., publishing company): Imperial College London
Planned date of publication: April 2016
Number of copies:

Content of reproduction (the Content)

Journal title: Japanese Journal of Applied Physics
Volume/Year/ID(starting page): 51 / 2012 / 02BG07
Article title: Energy transfer between Er^{3+} ions located at the two crystallographic sites of EGO_3 grown on Si(111)
Author(s): H. Omi, T. Tawara
Content to be reproduced (please specify): figure 3, panel (a)

Applicant (only to be completed by the author of the Publication)

Name: Samuele Grandi
Affiliation (e.g., university, company, organization): Imperial College London
Centre for Cold Matter
E-mail address: s.grandi@imperial.ac.uk

I will abide by the following conditions of reproduction.
1. A credit line "Copyright *publication year* The Japan Society of Applied Physics" must be added to the Content (in the figure caption(s)). The material containing the Content, copyrighted by the Japan Society of Applied Physics, must be cited in the references of the Publication.
2. The Content will not be modified.
3. The Content will not be reproduced in other materials.

Signature of applicant: Samuele Grandi

* The purpose of reproduction will be considered before permission is granted.

ENDORSEMENT

Dr. Samuele Grandi

I permit the reproduction of the Content in the Publication.

31 / 03 / 2017
Day Month Year

Kazuo Hotta
President, The Japan Society of Applied Physics

Publication Center for Pure and Applied Physics, The Japan Society of Applied Physics
2-31-22-5F, Yushima, Bunkyo-ku, Tokyo 113-0034, Japan /TEL: +81-3-5844-3291/FAX: +81-3-5844-3290/E-mail address: permission@jsap.or.jp

AIP PUBLISHING LLC LICENSE TERMS AND CONDITIONS

Apr 04, 2017

This Agreement between Samuele Grandi ("You") and AIP Publishing LLC ("AIP Publishing LLC") consists of your license details and the terms and conditions provided by AIP Publishing LLC and Copyright Clearance Center.

License Number	4081791017418
License date	Apr 04, 2017
Licensed Content Publisher	AIP Publishing LLC
Licensed Content Publication	Applied Physics Letters
Licensed Content Title	Population dynamics in epitaxial Er2O3 thin films grown on Si(111)
Licensed Content Author	
Licensed Content Date	Jun 17, 2013
Licensed Content Volume	102
Licensed Content Issue	24
Type of Use	Thesis/Dissertation
Requestor type	Student
Format	Print and electronic
Portion	Figure/Table
Number of figures/tables	2
Title of your thesis / dissertation	Single Quantum Emitters: resonance fluorescence and emission enhancements
Expected completion date	Apr 2017
Estimated size (number of pages)	150
Customer Tax ID	GB649926678
Requestor Location	Samuele Grandi Prince Consort Road 20 London, SW7 2AZ United Kingdom Attn: Samuele Grandi
Customer VAT ID	GB649926678
Billing Type	Invoice
Billing Address	Samuele Grandi Prince Consort Road 20 London, United Kingdom SW7 2AZ Attn: Samuele Grandi
Total	0.00 GBP
Terms and Conditions	

AIP Publishing LLC -- Terms and Conditions: Permissions Uses